Electrical Properties of Conductive Electric Roads

Wenander, David

2025

Document Version:
Publisher's PDF, also known as Version of record

Link to publication

Citation for published version (APA):
Wenander, D. (2025). *Electrical Properties of Conductive Electric Roads*. [Doctoral Thesis (monograph), Division for Industrial Electrical Engineering and Automation]. Division of Industrial Electrical Engineering and Automation, Faculty of Engineering, Lund University.

Total number of authors:
1

LUND UNIVERSITY

PO Box 117
221 00 Lund
+46 46-222 00 00

Electrical Properties of Conductive Electric Roads

DAVID WENANDER
FACULTY OF ENGINEERING | LUND UNIVERSITY

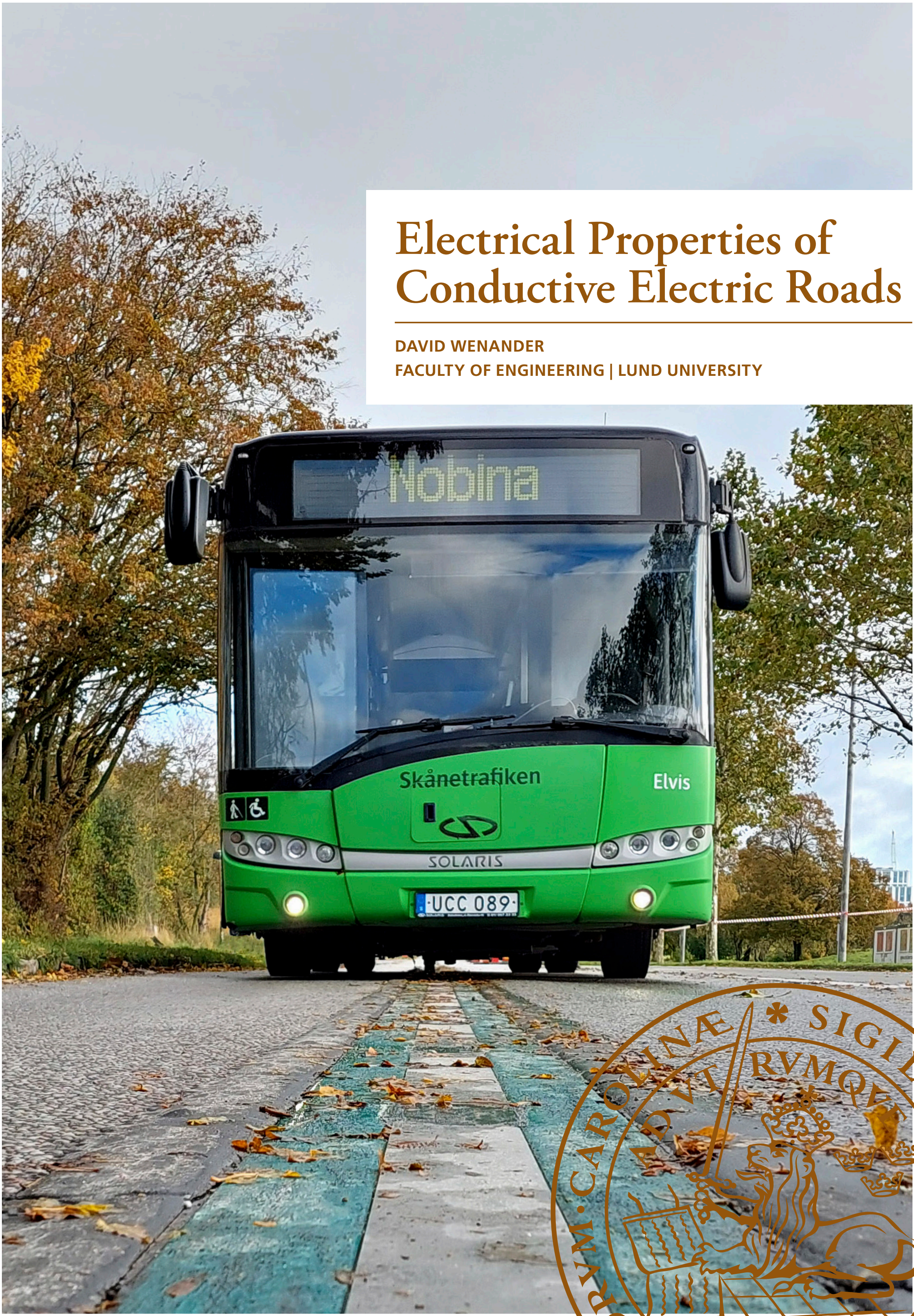

Electrical Properties of Conductive Electric Roads

Electrical Properties of Conductive Electric Roads

by David Wenander

LUND UNIVERSITY

Thesis for the degree of Doctor of Philosophy in Engineering
Thesis advisors: Prof. Mats Alaküla, Assoc. Prof. Francisco J. Márquez-Fernández
Faculty opponent: Dr. Reno Filla

To be presented, with the permission of the Faculty of Engineering of Lund University, for public criticism in the M:B lecture hall, Mechanical Engineering Building, Ole Römers väg 1, on Friday, the 16th of May 2025 at 09:00.

DOKUMENTDATABLAD enl SIS 61 41 21

Organization	Document name
LUND UNIVERSITY Division of Industrial Electrical Engineering and Automation Box 118 SE–221 00 LUND, Sweden	**DOCTORAL DISSERTATION**
	Date of disputation 2025-05-16
Author(s) David Wenander	Sponsoring organization

Title and subtitle

Electrical Properties of Conductive Electric Roads

Abstract

Given the global climate crisis, the electrification of road transport has accelerated in recent decades as a strategy to mitigate global greenhouse gas emissions, with the share of Battery Electric Vehicles (BEVs) increasing exponentially. While BEVs provide substantial environmental advantages during their operational phase compared to combustion-powered vehicles, they require an extensive charging infrastructure due to their limited range. Conductive electric roads have emerged as a promising solution, enabling BEVs to charge while in motion, thereby extending their range and reducing the required battery size when deployed on a large scale.

This thesis examines the electrical properties of conductive electric roads, specifically assessing the electrical sliding contact that facilitates energy transfer between the electric road and the vehicle, as well as evaluating the system's power capabilities, losses, and efficiency in relation to varying traffic characteristics. It also addresses challenges related to conducted Electromagnetic Interference (EMI) within the system and its power grid connection, along with electrical safety concerns related to touch events involving human contact with the vehicles operating on the electric road and the electric road itself.

Key findings show that the electrical sliding contact between the vehicle and the electric road is influenced by numerous factors, making it complex and requiring further research. Preliminary results suggest that the sliding contact design needs improvement, as contact resistance fluctuates and arcing occurs frequently. In terms of the technology's performance regarding losses, the system demonstrates high efficiency, exceeding 93% across urban, rural, and highway deployment scenarios. The impact of conducted EMI within the system and its power grid connection is found to depend largely on the design of the rectifier station. An analysis of electrical safety related to touch events related to human contact with the vehicle chassis reveals that parasitic capacitive coupling can occur between the chassis and the vehicle's onboard high-voltage system, posing a potential safety risk.

Key words

Electric Road System, Charging, Sliding Contact, System Efficiency, Conductive EMC, Electrical Safety

Classification system and/or index terms (if any)

Supplementary bibliographical information		Language English
ISSN and key title		ISBN 978-91-985110-4-8 (print) 978-91-985110-5-5 (pdf)
Recipient's notes	Number of pages 269	Price
	Security classification	

Signature ________________ Date 2025-03-27

Electrical Properties of Conductive Electric Roads

by David Wenander

LUND UNIVERSITY

Cover illustration front: The electric bus at the electric road demonstrator, photographed by the author.

Cover illustration back: The electric road demonstrator, photographed by the author.

Division of Industrial Electrical Engineering and Automation
Department of Biomedical Engineering
Faculty of Engineering
Lund University

ISBN: 978-91-985110-4-8 (PRINT)
ISBN: 978-91-985110-5-5 (PDF)
CODEN: LUTEDX/(TEIE-1100)/1-269/(2025)

Printed in Sweden by Media-Tryck, Lund University, Lund 2025

Messen ist Wissen, aber Messen ohne Wissen ist kein Wissen.

- Werner von Siemens

Contents

Acknowledgements

The general perception of doing a PhD is very mixed in my experience. Some people view it as true hardship, with limited rewards and an excessive workload, while others are more content and passion-driven, cherishing the freedom and independence it offers, even portraying it as a relaxed form of employment. For me, it has definitely been challenging at times, yet it has been the best job I could have imagined during these years of my life. I have truly enjoyed the experience and everything it entails, despite my forgetfulness in expressing this gratitude.

First and foremost, I would like to thank my main supervisor, Professor Mats Alaküla, for giving me the opportunity to pursue a PhD and for believing in me. Mats, I will always be grateful for your support, encouragement, and mentorship in the fascinating world of electrotechnology, as well as for your patience when our opinions have diverged. Thank you, Mats.

Secondly, I would like to express my gratitude to my co-supervisor, Associate Professor Francisco J. Márquez-Fernández, who has been a great support in helping me navigate the day-to-day challenges of my research. Fran, although your superman-like, do-everything-at-once approach sometimes limits your time, I have greatly appreciated your flexibility in making yourself available and engaging in the details of my work, particularly in helping me improve my writing abilities. You have taught me the craft of being a researcher, which I have come to deeply appreciate–thank you for this experience.

Although my supervisors have helped me greatly throughout this journey, I have also had, in my mind, a number of unofficial co-supervisors. Thank you, Dr. Philip "quick and dirty" Abrahamsson, for giving me the most intense crash course on being a PhD student one can imagine during my first year, introducing me to the lab, emphasizing the importance of practical work, and showing me how to do things real quick, and real dirty. Dr. Anton Karlsson, thank you for being so helpful with everything related to my work and for mentoring me through difficult decisions, both technical and non-technical. I cannot stress enough how important your guidance has been for me. Dr. Johan Björnstedt, your expertise and competence in electrical engineering (and beyond) are qualities I greatly admire. Thank you for taking the time to patiently answer my questions and for adhering to my common sense and critical thinking, keeping my feet firmly on the ground when my ideas were too visionary.

My time at the Division of Industrial Electrical Engineering and Automation would not have been as enjoyable without the people I worked with. Without them, this thesis would not have been possible. A special thank you to Getachew Darge, who, regardless of the issue, has always been available to help me in the lab and to get hold of the equipment I needed, in spite of how wild or ridiculous my ideas may have been. Professor Olof Samuelsson, thank you for supporting me and for cherishing my urge for organization and structure. Martin, we both started at IEA around the same time, and although we have worked in different fields of research, I have greatly enjoyed pursuing a PhD alongside you and truly appreciate your humor, advice, and patience with me. Thank you for all of this. Thank you, Dr. Max Collins, for proofreading some of my papers and providing valuable advice when needed. A big thank you to all my colleagues at IEA–Samuel, Alice, Leo, Mattias, Edvin, Hannes, Huan, Akanksha, Gabriel, Imran, and many others–for making the day-to-day work so enjoyable.

I would also like to express my gratitude to the Elonroad team, particularly Joel, Dan, Johan, and Andreas, for helping me conduct measurements and tests at the electric road demonstrator. Without your cooperation and assistance, there would have been no foundation for this thesis.

Although I have pursued a PhD at IEA, there are many who, outside of work, have supported me throughout this endeavor. Firstly, my own little family: Malin, Evy, and Tor. Malin, you are my safe harbor. Thank you for supporting me throughout this pursuit and for being patient with me, allowing me to vent whenever I needed to. I don't think I can give you enough credit for your support. Thank you for being you. My daughter, Evy, you came into this world during the most intense period of work on my thesis; thank you for putting everything in my life into perspective. To my parents and my sister: thank you for your solid support and encouragement. Thank you, Jürgen, for proofreading the thesis. A heartfelt thank you to all my friends, especially Harald and Lasse, for patiently listening to my work-related rants. And finally, thank you, Tor, my dog, who on the days when I've worked from home, has helped me relieve stress and reminded me that work is far from the most important thing in life.

David Wenander
Malmö, March 2025

Popular summary

As the global environmental crisis intensifies, efforts to address it are being carried out across various sectors, including the electrification of road transport. As a result, the proportion of battery electric vehicles in vehicle fleets has increased exponentially over the past decade. Although this strategy has proven effective, as battery electric vehicles produce significantly fewer emissions during operation compared to conventional combustion-powered vehicles, they still have drawbacks. One major issue is the environmental impact of battery production and the mining of the minerals required for their manufacture. Additionally, the range of battery electric vehicles is limited by battery size, and they also require an extensive charging infrastructure to compete with the range offered by conventional combustion-powered vehicles. An electric road is a charging infrastructure that allows electric vehicles to charge while driving, thereby increasing charging opportunities and extending their driving range. If widely implemented, electric roads could enable the use of smaller batteries onboard vehicles, as charging opportunities would become more frequent. From an environmental perspective, the reduced battery size onboard vehicles could also reduce the negative environmental effects associated with the production of battery electric vehicles.

In this thesis, the electrical properties of conductive electric road technology are assessed. In this context, "conductive" refers to the transfer of electrical energy between the vehicle and the electric road via a physical sliding contact, similar to the one used in metro trains. During the last decade, various electric road technologies have been studied and tested at different levels of operational readiness. Although these technologies show promise for large-scale deployment, several technical challenges remain unresolved. This thesis assesses four main aspects of conductive electric road technology: I) the electrical characteristics of the sliding contact, II) the power capabilities and efficiency of the electric road technology from a system perspective, III) conducted electromagnetic interference within the electric road's power supply and grid connection, and IV) electrical safety challenges related to touch events involving human contact between vehicles drawing power from the electric road and the exterior surface of the electric road. The assessment is conducted through measurements and simulations, made possible by access to a conductive electric road demonstrator.

The evaluation of the electrical characteristics of the sliding contact reveals that it is complex and requires further research. The results indicate

that the sliding contact design needs improvement, as the resulting contact resistance varies significantly and exhibits peaks well above 100 mΩ, which could lead to excessive energy losses. Additionally, arcing frequently occurs, which may cause electromagnetic compatibility issues within the electric road and its surrounding area. From a system perspective, the technology shows great promise in terms of power capabilities and efficiency, with system efficiency exceeding 93% in urban, rural, and highway deployment scenarios. In terms of conductive electromagnetic interference, the issue of voltage and current ripple within the electric road supply is highlighted, where alternative designs for the rectifier station are analyzed and recommended as a potential solution. Finally, the electrical safety concerns related to touch events involving human contact are evaluated, with parasitic capacitive coupling identified as an underlying cause of potential hazardous situations when a vehicle draws power from the electric road.

Populärvetenskaplig sammanfattning

I takt med att den globala miljökrisen förvärras vidtas åtgärder inom ett flertal olika områden, bland annat inom elektrifiering av vägtransporter. Detta har lett till att andelen batterielektriska fordon i fordonsflottor har ökat kraftigt under det senaste decenniet. Trots att denna strategi har visat sig vara effektiv, då batterielektriska fordon producerar avsevärt lägre utsläpp under drift jämfört med traditionella förbränningsmotorfordon, finns det fortfarande vissa nackdelar med denna strategi. Ett stort problem är den miljöpåverkan som batteriproduktion och utvinning av de mineraler som behövs för tillverkningen medför. Dessutom är batterielektriska fordons räckvidd begränsad av batteristorleken, och de kräver också en utbyggd laddinfrastruktur för att kunna konkurrera med den räckvidd som traditionella förbränningsmotorfordon erbjuder. Elvägar är en typ av laddningsinfrastruktur som gör det möjligt för elektriska fordon att ladda medan de kör, vilket ökar laddningstillgängligheten och förlänger fordonens räckvidd. Om elvägar implementeras i stor skala skulle det möjliggöra användning av mindre batterier i fordonen, eftersom laddningsmöjligheterna blir betydligt fler. Ur ett miljöperspektiv skulle detta även kunna minska de negativa effekterna på miljön som är kopplade till produktionen av batterierna i elektriska fordon.

I denna avhandling utvärderas konduktiva elvägars elektriska egenskaper. Med "konduktiv" avses att elektrisk energi överförs mellan fordonet och elvägen via en släpkontakt, liknande den teknik som används för tunnelbanetåg. Under det senaste decenniet har olika typer av elvägstekniker utvärderats och testats i varierande operativa nivåer på allmän väg. Även om dessa tekniker visar stor potential för storskalig implementering återstår flera tekniska utmaningar. I denna avhandling analyseras fyra huvudområden inom konduktiva elvägar: I) släpkontaktens elektriska egenskaper, II) effektöverföringskapacitet och verkningsgrad av elvägstekniken utifrån ett systemperspektiv, III) konduktiva elektromagnetiska störningar i elvägens kraftförsörjning och i elvägens elnätsanslutning, samt IV) elektriska säkerhetsproblem som kan uppstå vid mänsklig beröring av både fordon som drar effekt från elvägen och elvägen i sig. Arbetet genomförs med hjälp av mätningar och simuleringar, som möjliggjorts genom tillgång till en konduktiv elvägsdemonstrator.

Utvärderingen av släpkontaktens elektriska egenskaper visar att den är komplex och kräver vidare forskning. Resultaten tyder på att designen av släpkontakten bör förbättras, eftersom den resulterande kontaktresistansen varierar avsevärt och uppvisar toppar som ligger långt över 100 mΩ, vilket kan leda till stora energiförluster. Dessutom uppstår ofta ljusbågar, vilket kan orsaka problem med elektromagnetisk kompatibilitet inom elvägsystemet och dess omgivning. Ur ett systemperspektiv uppvisar tekniken stor potential, då både effektöverföringskapaciteten är god och systemverkningsgraden överstiger 93% i både stadsvägs-, landsvägs- och motorvägsmiljöer. När det gäller konduktiva elektromagnetiska störningar lyfts problemet med spännings- och strömvariationer inom elvägens kraftförsörjning, där olika designförslag för likriktarstationens utformning presenteras och föreslås som en potentiell lösning. Slutligen analyseras elsäkerhetsproblem som kan uppstå vid mänsklig beröring av fordon som matas från elvägen, där parasitiska kapacitiva kopplingar identifieras som rotorsaken till potentiellt farliga beröringsströmssituationer.

Nomenclature

η	Efficiency
C_s	Capacitor representing the skin capacitance of the human body.
I_b	Current through the human body.
k_{ERS}	Electric road coverage factor.
k_p	Ratio of the total power drawn by the vehicle from the ERS that is supplied to the propulsion and auxiliary systems in the vehicle.
L	Electric road length.
R_b	Resistor representing the internal resistance of the human body.
R_s	Resistor representing the skin resistance of the human body.
V_b	Voltage over the internal resistance of the human body.
V_h	Voltage over the entire human body.
AC	Alternating Current
ASSE	Alternating Short Segmented Electric Road
BEV	Battery Electric Vehicle
DAQ	Data Acquisition Device
DC	Direct Current
EMC	Electromagnetic Compatibility
EMI	Electromagnetic Interference

ERS	Electric Road System
EV	Electric Vehicle
Fe_2O_3	Ferric Oxide
FFT	Fast Fourier Transform
HVAC	Heating, Ventilation, and Air Conditioning
IMS	Isolation Monitoring System
m	Measured
RCD	Residual Current Breaker
RMS	Root Mean Square
RTR	Rotating Test Rig
s	Simulated
SER	Sections of Electric Road
SoC	State of Charge
THD	Total Harmonic Distortion
TVS	Traction Voltage System

Chapter 1

Introduction

1.1 Background

Over the past decades, the Intergovernmental Panel on Climate Change has consistently underscored the urgent need to address the global environmental crisis [1]. In 2024, the International Energy Agency reported that the transport sector accounts for 23.7% of global CO_2 emissions, with road transport responsible for 73.8% of these emissions [2], as illustrated in Fig. 1.1. In response to this pressing climate issue, the road transport sector has begun transitioning from traditional combustion-based vehicles to Electric Vehicles (EVs) to mitigate environmental impacts. Over this period, the global stock share of Battery Electric Vehicles (BEVs) in the passenger car sector has increased exponentially, reaching 3.2% of the global passenger car stock by 2023 [2]. While the shift from combustion-based vehicles offers a promising solution to the environmental crisis, EVs also present certain drawbacks.

Firstly, while EVs can be cleaner in terms of noise and emissions during their operational phase compared to internal combustion-based vehicles, the production of EV batteries presents significant challenges. Manufacturing EV batteries requires specific critical minerals such as lithium, cobalt, manganese, nickel, and graphite [3], which are often sourced from developing countries. In these regions, labor conditions may be exploitative, human rights abuses are reported, and mining practices frequently lead to significant local environmental impacts [4–6]. Additionally, the production of EV batteries is associated with substantial CO_2 emissions [7]. Improving

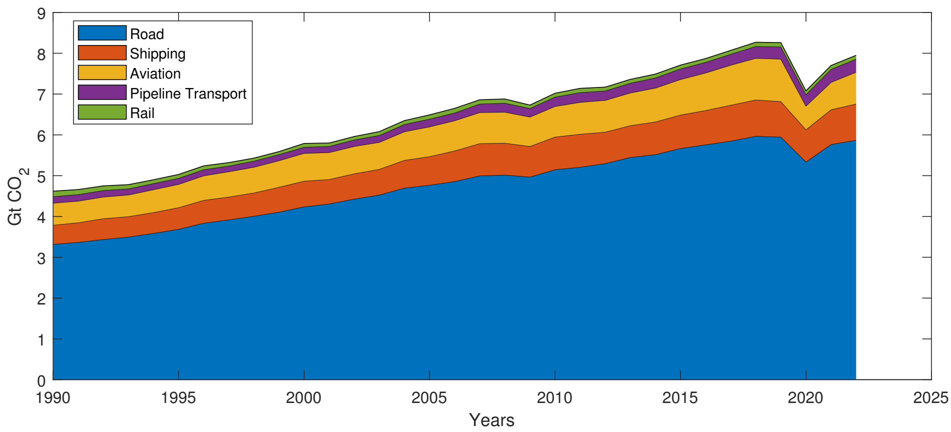

Figure 1.1: Global CO_2 emissions from the transport sector. Data taken from IEA website [2].

the production processes for EV batteries could mitigate these issues; however, reducing the overall demand for EV battery production would more effectively address these environmental and ethical concerns.

Secondly, the range of EVs depends on their battery size. To improve this range, the battery sizes in EVs have increased over the last decade [2], thereby intensifying the environmental strain related to battery production.

Thirdly, EVs take longer to charge compared to refueling conventional internal combustion-based vehicles. In addition, the trend of increasing battery sizes further extends the charging times and heightens the demand for fast charging stations.

Fourthly, the exponential rise of EVs and their accompanying increase in battery size underscores the imperative for the development of charging infrastructure proportional to the expanding EV fleet. This infrastructure must not only accommodate the growing number of EVs but also ensure a level of practicality, availability, and user experience on par with that of conventional internal combustion-based vehicles.

In summary, the transformative potential of EVs in mitigating environmental impacts relies on several factors, with the development of a suitable charging infrastructure being crucial. This infrastructure must not only offer the same level of convenience as conventional internal combustion-based vehicles but also address the limitations associated with EV batteries.

1.2 Charging Infrastructure

There are a number of different charging technologies available to recharge the batteries of EVs, with stationary charging stations (both slow and fast) being the main option to refill your vehicle with energy. In parallel with the global exponential increase in EVs, the number of public charging stations has also increased exponentially, as illustrated in Fig. 1.2. Charging stations can be divided into two main categories I) slow chargers, defined as having a power rating less than or equal to 22 kW II) and fast chargers, defined as having a power rating of more than 22 kW and up to 350 kW [2]. For EVs to remain competitive against combustion-based vehicles for longer trips, fast chargers are essential in reducing charge times. Public charging points are projected to surpass 25 million by 2035, representing a sixfold increase from 2023. China, Europe, and the United States are primary contributors to this growth, with China leading in public charging deployment. While home charging remains critical, public chargers are indispensable for those without home charge access. Moreover, ensuring the access, convenience, reliability, and interoperability of public charging stations is essential in a charging infrastructure adopted for EV users.

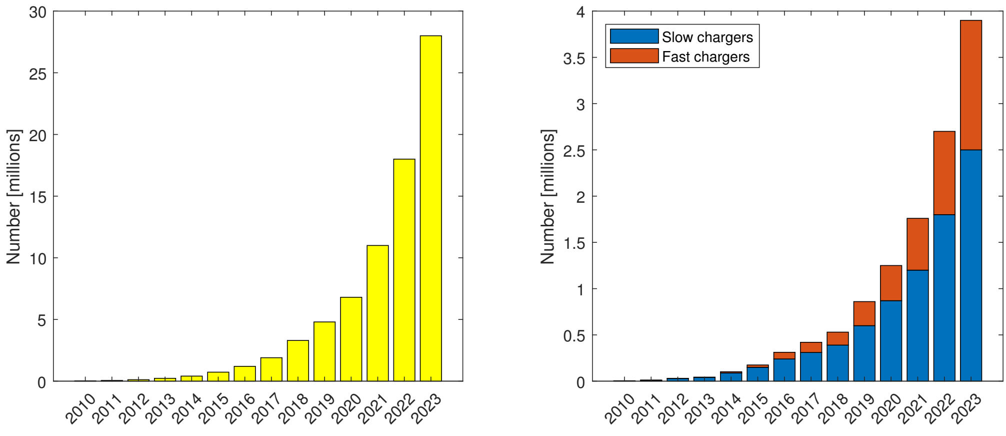

Figure 1.2: Global BEV passenger cars to the left and global publicly available slow and fast chargers to the right. Data taken from the IEA website [2].

Norway, which in many aspects can be considered a global leader in electrifying road transport, had a stock of 689,196 BEVs in 2023, supported by 7,741 fast chargers [8]. This corresponds to a fast-charger-to-BEV ratio of approximately 1:100, suggesting that at least this ratio is required for a fast-charging-based system. However, the charging infrastructure in

Norway primarily relies on slow, overnight charging, which is feasible given that a significant portion of the population lives in single-family homes. This suggests that in a more densely populated country, with fewer slow overnight chargers, a ratio of 1:100 or even denser fast charging stations for BEV passenger cars may be necessary. In Germany, with approximately 49 million cars [9], the 1:100 ratio would translate to around 490,000 fast charging stations distributed along 51,000 km of highways, main, and national roads [10]. This equates to roughly 100 fast charging stations every 50 km on average along German roads. Although approximate, these calculations and assumptions highlight the significant challenge of implementing a fast-charging-based system on a national level, emphasizing the need for a vast number of fast charging stations.

As illustrated in Fig. 1.2, the global increase in fast chargers suggests that the implementation of an extensive fast-charging infrastructure is already underway. However, the formidable task of establishing such a vast number of fast charging stations necessitates exploring additional solutions to support the ongoing electrification of the transport sector. These solutions might include promoting alternative modes of transportation or reflecting on our behavior related to transport and other climate-impacting activities. Regardless of behavioral considerations, technological advancements in reducing climate impact remain critical. For instance, alongside fast charging stations, battery swapping is emerging as a viable option in charging infrastructure.

Battery swapping constitutes an alternative method for replenishing EV batteries, wherein the entire battery unit is exchanged with a fully charged one at battery swapping stations [11]. Compared to charging stations, battery swapping greatly reduces the time required to refill the EV battery, even when compared with fast charging stations that allow for high-power charging. At battery swapping stations, multiple batteries are maintained, undergoing charging at a slower rate compared to conventional stations, thereby mitigating the demand for high-power charging and reducing battery degradation resulting from rapid recharging. Nonetheless, as with fast-charging stations, setting up a network of battery swapping stations on a large scale requires considerable areas of land as well as significant investments.

While acknowledging the benefits of battery swapping and its potential as an effective charging infrastructure if widely adopted, this thesis focuses on electric roads that facilitate vehicle charging while in motion, also known as dynamic charging.

1.3 Dynamic Charging

One approach to alleviate the limited range of EVs and to enhance charging opportunities is the implementation of Electric Road Systems (ERSs). ERSs provide a charging infrastructure that enables vehicles to charge while driving, thereby reducing the dependence on conventional static charging stations and significantly increasing charging availability. With widespread deployment, ERSs could enable smaller onboard battery sizes [12], thus reducing the environmental impact associated with battery production.

From a historical perspective, ERSs are not a new concept. Trolleybuses, which can be regarded as a type of ERS, date back to 1882, when Dr. Ernst Werner von Siemens demonstrated the "Elektromote" [13]. Slightly more than a century later, a number of more modern ERS technologies emerged such as KAIST OLEV [14], Alstom APS [15], Bombardier Primove [16], and Ansaldo Tramwave [17]. As the road transport sector increasingly transitions towards electrification, the demand for a robust and effective charging infrastructure has become more urgent. Consequently, ERSs are emerging as a viable option for widespread implementation, providing an efficient and scalable solution to support electric vehicle charging [18].

Although ERSs can be designed to charge EV batteries at power levels exceeding 200 kW [19, 20], one significant advantage of ERS, provided that the EV's Traction Voltage System (TVS) is appropriately designed, is the direct energy transfer from ERS to the EV propulsion system. This direct energy transfer offers two main benefits. Firstly, EVs can maintain their State of Charge (SoC) during ERS access, resulting in a low total power draw from the vehicle, as power is solely required for propulsion and auxiliary systems, rather than battery charging. Moreover, in the scenario of extensive ERS implementation, battery size and charging power would only need to be optimized for the distances between roads with ERS access. Secondly, the direct energy transfer from the ERS to the EV propulsion system achieves higher efficiency compared to conventional static charging stations, as energy is transferred directly to the propulsion system, avoiding the inefficiencies associated with charging and discharging the battery [21].

1.3.1 Types of Electric Road Technology

ERS technology can be categorized into two main types: wireless and conductive. In wireless ERS technology the energy transfer is facilitated through electromagnetic induction, utilizing coupled high-frequency magnetic fields. The vehicle's underbody is equipped with a receiving coil along with a power electronic interface onboard the BEV, while a transmitting coil with corresponding power electronic equipment is installed in the road, typically beneath the road surface. Several companies produce this type of ERS technology, with notable examples being KAIST OLEV [14], ENRX [22] and Electreon [23] which is shown in Fig. 1.3.

Figure 1.3: A bus line in Balingen, Germany where Electreon's wireless charging technology is implemented.[24].

However, despite the sophistication and effectiveness of wireless energy transfer design, there are limitations associated with this technology. Firstly, the energy transfer capability is somewhat restricted by the surface area beneath the vehicle, potentially making it unsuitable for high-power applications. Secondly, since the technology relies on high-frequency magnetic fields, there is a risk of introducing Electromagnetic Compatibility (EMC) related issues. Thirdly, while wireless ERS can achieve high efficiency, conductive ERSs currently exhibit superior efficiency performance, particularly at higher power levels [20, 25].

In conductive ERS technology the energy transfer is facilitated by using a physical sliding contact between the electric road and the vehicle, similar to the mechanisms used in third-rail systems for metro trains or catenary systems for trolleybuses. The stationary side of the sliding contact can be situated on the road surface, embedded within the road, along the side of the road, or suspended above the road, as depicted in Fig. 1.4.

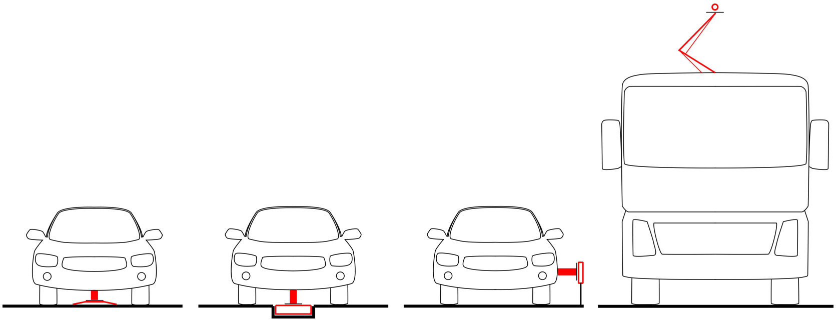

Figure 1.4: Different types of conductive electric road technologies (left to right): mounted on top of the road, embedded within the road, mounted on the side of the road, and suspended above the road.

The surface-mounted conductive electric road supply, developed by Elonroad [26], is notable for its rapid and straightforward installation process. In addition to the surface-mounted supply, Elonroad, as well as the company EVIAS [27] shown in Fig. 1.5, offer embedded electric road designs that do not protrude above the road surface, thereby impacting the vehicle's motion dynamics less than the surface-mounted design.

Honda has developed a side-mounted rail along the road, with the vehicle making contact via a wheel-based mechanism that extends to the side rail. This technology has been successfully tested on a racetrack, achieving power levels of up to 450 kW at speeds of 150 km/h [19].

Figure 1.5: EVIAS embedded electric road design deployed between Arlanda airport and a logistics center outside of Stockholm, Sweden [28].

Siemens eHighway provides conductive energy transfer from overhead catenary lines illustrated in Fig. 1.6, similar to those used in trains and tramways [29]. However, this catenary solution is only suitable for heavier vehicles, as the installation height poses compatibility issues for passenger cars.

Figure 1.6: Siemens eHighway deployed on the autobahn near Frankfurt [30].

Although similar from an electrical perspective, there are significant distinctions among the presented conductive ERS technologies. Firstly, the majority of these technologies employ a Direct Current (DC) voltage supply, requiring a rectifier between the electrical grid and the electric road, whereas the EVIAS design uses an Alternating Current (AC) voltage supply, eliminating the need for a rectifier station due to its different electrical topology [27].

Secondly, in the presented conductive technologies with a DC voltage supply, the negative pole of the supply is grounded to ensure electrical safety, except for Honda's solution, where the ERS power supply is in principle floating with respect to ground. Grounding the negative pole serves to prevent the introduction of harmful voltages or currents to humans or animals in the event of an electrical fault. Chapter 6 offers an in-depth examination of electrical safety concerns pertaining to conductive electric roads.

1.3.2 Challenges of Electric Road System Implementation

While ERSs offer numerous advantages over other charging infrastructures, they also present several challenges. Firstly, all types of ERS technology require specific onboard equipment within the vehicle, including a power electronic interface. In inductive ERS technology, coils are required, whereas in conductive ERS technology, a current collector facilitating physical contact is required for energy transfer. As the onboard equipment must be integrated within the vehicle, major EV manufacturers need to collaborate with ERS manufacturers. This collaboration can introduce issues related to product ownership, standardization, and regulatory compliance concerning infrastructure and vehicle interfaces. Furthermore, EV companies, most of them operating on a global scale, may lack the incentive to engage with ERS technologies until a standard solution is established at an international level.

Secondly, the full potential of ERS is realized through widespread deployment on a large scale, such as across the European road network (TEN-T). However, this necessitates a joint agreement on the selection of a unified technology and is further complicated by the fact that different countries currently promote their own preferred ERS solutions. In addition, such an extensive deployment requires standardization, harmonization of business models, and regulations across national borders, as well as significant capital investment. Moreover, the ownership, operation, and maintenance of ERS infrastructure remain unresolved issues.

Thirdly, in addition to the challenges posed by non-technical issues, several significant technical challenges persist. Maintenance and upkeep of such an extensive infrastructure can be costly, particularly for electric roads exposed to harsh weather conditions. Moreover, as most ERSs have only been deployed on a limited scale, the impact of upscaling the technology remains unknown, particularly regarding how availability and reliability are influenced by factors such as electrical safety, power capabilities, power grid impact, and EMC. Therefore, to gain comprehensive knowledge about the feasibility of ERS on a wide scale, the technology must be tested and evaluated from various perspectives.

All the aforementioned ERS companies [19, 23, 26, 27, 29] have installed demonstrator electric roads at various deployment levels. One such demonstrator, developed by Elonroad, was tested as part of the Evolution Road project [31] in Lund, Sweden. The objective of this project was to gain insights into the specific conductive ERS technology and evaluate its viability for wide deployment. This thesis has been conducted as a part of the Evolution Road project with the objective of assessing the electrical properties of the conductive ERS technology produced by Elonroad (further described in Chapter 2).

1.4 Motivation of Research

To evaluate the feasibility of conductive ERSs as a large-scale charging infrastructure, a deeper understanding of their electrical properties is required. The potential of conductive ERS technologies must be examined from a technical perspective, focusing on efficiency, power transfer capabilities, grid impact, EMC, and electrical safety to gain a comprehensive understanding of ERS benefits and limitations. Additionally, it is essential to evaluate the design and deployment parameters of conductive ERS to identify optimal ERS designs and cost-efficient installation strategies. Although several papers have assessed the viability of the ERS concept and the associated costs at a national level [12, 32, 33], detailed evaluations of the electrical properties of electric roads are relatively scarce.

Previous research has partially evaluated the electrical properties of conductive ERS technology. In [34], the primary focus is on the thermal assessment of a version of Elonroad's conductive ERS technology. This study also presents electrical assessments, including losses and the life expectancy of the semiconductors in the ERS. In addition, [35] analyses and models the design of the ERS infrastructure, particularly the placement of rectifier stations and its correlation with voltage drop in the electric road due to vehicle position and drawn power level. Although this model is relevant, it has not been validated with measurements from an actual ERS.

Electrical safety issues concerning the adoption of the EV's TVS for conductive ERS applications are extensively addressed with multiple TVS topologies in [36, 37]. However, the electrical aspects related to the ERS itself are not considered. In [38] a simulation model is introduced which is used to assess electrical safety concerns related to the voltage potential of the chassis of an EV drawing power from an ERS. Although the validation of this model utilizes measurements obtained from a real ERS demonstrator, a trailer equipped with a resistive load is employed instead of a real EV adapted for ERS operation.

When this thesis work started in October 2019, research on the electrical properties of conductive electric roads was limited. Subsequently, as noted, several papers have emerged assessing various aspects of conductive electric roads. However, since 2019, no presented work has included modelling of the electrical properties of conductive ERS using simulation models validated with measurements from a real conductive ERS, including EVs adapted for ERS operation. Moreover, the increasing number of papers addressing conductive and inductive ERSs since 2019 underscores the existing research gap and the imperative for further investigation into the technical aspects, design, and feasibility of future ERS.

This doctoral thesis presents measurements and results, from validated simulation models, that assess the electrical properties of conductive ERS technology. By utilizing simulation models, which are validated with measurements from an actual conductive ERS demonstrator, a comprehensive understanding of the electrical properties of the ERS is achieved. The insights drawn from the analysis of the demonstrator, in conjunction with the simulations results, serve as the foundation for assessing the technology's potential for widespread deployment. This thesis focuses on evaluating four relevant electrical aspects of conductive ERS:

- The electrical characteristics of the current collector and sliding contact.
- The power flow, losses, and system efficiency of the ERS, from the power grid to the vehicle, in relation to traffic characteristics.
- The conductive EMC within the ERS supply and its impact on the power grid.
- Electrical safety considerations during both normal and fault conditions.

1.5 Objectives and Limitations

The objective of this thesis is to evaluate the electrical properties of conductive ERS technology. This evaluation is conducted through measurements obtained from a conductive ERS demonstrator developed and built by Elonroad. These measurements serve as the basis for developing and validating simulation models, which are employed to analyse electrical aspects that are impractical or infeasible to assess through direct experimentation. Consequently, this research facilitates the examination of electrical phenomena, electrical aspects of large-scale deployment, and electrical design of conductive ERS infrastructure.

The main objectives of this thesis are the following:

- Characterize the critical electrical design parameters for the current collector and associated sliding contact for the considered ERS technology. Measure the voltage drop and current to calculate the contact resistance and evaluate the contact quality of the sliding contacts in the current collector utilized for the considered ERS technology.

- Model ERS deployment in urban, rural and highway scenarios with their associated traffic characteristics to evaluate their impact on power flow, losses, and system efficiency for the specified ERS technology. Assess design alterations of ERS components and subsystems and their impact on power flow and losses within the ERS for each deployment scenario.

- Assess the impact of conductive Electromagnetic Interference (EMI) between vehicles within the ERS supply and the ERS grid connection. Evaluate the influence of conductive EMI on voltage and current quality.

- Evaluate the electrical safety concerns related to touch events involving human contact on the exposed parts of both the ERS and the vehicles drawing power from it. Assess the electrical safety issues arising from touch events in conjunction with isolation faults between the vehicle chassis and the ERS supply.

Since ERSs have not yet been widely deployed, there are no EVs originally designed or adapted for ERS operation. Consequently, this thesis is constrained by this reality.

Firstly, the measurements and, by extension, the validation of simulation models, presented in this thesis are limited to the available adapted vehicles used in the ERS demonstrator. This encompasses the TVS topology, as well as the power electronic interface and current collector between the vehicle and the ERS. The analysis of the EV TVS in this thesis is restricted to three primary subsystems: the traction drive, battery (and its corresponding power electronic interface), and the DC/DC power electronic interface (linking the EV and the ERS). Any additional TVS-connected subsystems are grouped under auxiliary systems.

Second, the amount of vehicles drawing power from the ERS, along with the associated power demand characteristics, relies upon two key factors: I) assumed traffic flow and vehicle types extrapolated from general traffic data sourced from [39], and II) assumptions and modelling concerning power consumption per vehicle, estimated through simulations of relevant driving conditions using a vehicle model from [40].

Third, the time resolution of the presented simulation models is constrained by the sampling frequency of the provided measurements. Furthermore, the analyses in this thesis focus exclusively on the ERS and EV TVS, omitting the associated 12V, 24V, and 48V systems present in the ERS and EV. Additionally, the analysis of power grid impact is confined to the ERS grid connection of a single ERS rectifier station.

Finally, the aim of characterizing the electrical properties of the sliding contact and its corresponding current collector is to understand and identify the underlying factors that influence the quality and performance of the sliding contact. This is achieved by assessing the voltage drop, contact resistance, arcing, and frictional force of the sliding contact through measurements obtained from the demonstrator, which utilizes a resistive load mounted on a trailer, and from a laboratory-installed Rotating Test Rig (RTR). However, the precision of the measurements obtained from the demonstrator is limited, as the trailer's motion dynamics, combined with the uncontrolled environment in which the ERS demonstrator is located, affect the quality of the sliding contact and, ultimately, the precision and accuracy of the results. While these variations are mitigated by utilizing the RTR, as the laboratory environment where it is installed allows for more controlled conditions, the results obtained with the RTR still exhibit variations, as the RTR is not a high-precision device, partly due to the rudimentary design of its mechanical system. To validate that the RTR is capable of replicating the conditions present in a real ERS, the order of magnitude of contact resistance from the ERS demonstrator is compared with the results from the RTR. In addition, the experiments with the trailer and the RTR are limited to speeds of up to 30 and 50 km/h, respectively.

1.6 Contribution

In addition to the author's personal and professional development, this thesis has made contributions to the research field of conductive electric roads from an electrical perspective. The contributions, outlined by chapter, are listed below:

- Chapter 3: The presented results on voltage drop, contact resistance, arcing, and frictional forces should be regarded as an initial exploration into the characterization of the electrical properties of the sliding contact adapted for conductive ERS technology. The conclusions from the analysis indicate that the sliding contact is a complex phenomenon that requires further analysis to better understand the underlying factors influencing its electrical properties, which ultimately affect the quality and performance of the sliding contact. Although this assessment does not provide a complete characterization of the electrical properties of the sliding contact, the results offer an estimate of the contact resistance's order of magnitude in a real ERS and indicate that trends and correlations are present, which require further assessment. Moreover, the results also highlight that the presented sliding contact design requires further improvements as it exhibits arcing as well as fluctuating values of contact resistance, intermittently exceeding 100 mΩ.

  Additionally, measurements presenting the magnitude and distribution of the current in the collector, where the sliding contacts are mounted, highlight both the benefits and drawbacks of a current collector design with multiple sliding contacts. For the ERS technology considered in this thesis, utilizing more than three sliding contacts allows for redundancy. If poor contact occurs in one sliding contact, the current load is redistributed to another parallel sliding contact within the current collector.

- Chapter 4: Assessment of the performance of the considered ERS technology in urban, rural, and highway deployment scenarios, taking into account traffic characteristics, power capabilities, losses, and system efficiency. The assessment was conducted using a simulation model that was developed and validated through measurements from the ERS demonstrator. For each deployment scenario, proposed design alterations are presented, and their impact on losses and system efficiency is simulated and analysed.

- Chapter 5: The impact of conductive EMC within the ERS supply and its effect on the ERS power grid connection is analysed. The analysis focuses on how the design and topology of the rectifier station influence voltage and current ripple within the ERS supply and its power grid connection. Additionally, the influence of the input filters of the vehicles' onboard power electronic ERS interfaces on voltage and current ripple within the ERS supply is examined. The analysis is conducted using a simulation model that was developed and validated through measurements conducted at the ERS demonstrator.

- Chapter 6: The electrical safety concerns related to touch events involving human contact on exposed parts of both the ERS and the vehicles drawing power from it are examined. Through modelling and measurements conducted at the ERS demonstrator, it was discovered that current could flow through a human model in contact with the chassis of a vehicle drawing power from the ERS. This phenomenon occurred due to parasitic capacitive coupling between the vehicle chassis and the vehicle TVS, thereby bypassing the electrical insulation between them. To further assess the impact of this phenomenon, simulations were conducted to examine the effects of parasitic capacitive coupling and the resulting current flow experienced by a human model. Additionally, modelling of touch events related to the exterior surface of the electric road during operation was performed to determine the voltage threshold levels with respect to ground that may lead to hazardous voltage and current exposure for a human model. These simulations were carried out using an extended version of the simulation model from Chapter 5, which was validated through measurements at the ERS demonstrator using a human model.

1.7 List of Publications and Author Contribution

The author, as the writer of this thesis, is the principal researcher and the primary individual responsible for the research, which is based on, but not limited to, the papers listed below. Papers I-VI are presented in chronological order, while Paper VII, despite being published first, is intentionally left outside the scope of this thesis for consistency reasons.

I Measuring electric properties of a conductive electric road [41]
D. Wenander, P. Abrahamsson, F. J. Márquez-Fernández, M. Alaküla
2021 AEIT International Conference on Electrical and Electronic Technologies for Automotive (AEIT AUTOMOTIVE), Torino, Italy, 2021, pp. 1-6

- I took a major role in designing and building the measurement system, as well as developing the measurement software. I conducted numerous measurements, processed and analysed the data, which led to the presentation of the ERS demonstrators' electrical characteristics and performance in terms of losses and efficiency. I also evaluated the validity of the measurements based on the performance of the measurement system.

II Modelling of power flow and losses in a conductive Electric Road System [42]
D. Wenander, F. J. Márquez-Fernández, M. Alaküla
2022 IEEE Vehicle Power and Propulsion Conference (VPPC), Merced, CA, USA, 2022, pp. 1-6

- I developed a simulation model capable of accurately modelling power flow and losses within a conductive ERS. I validated the model thoroughly by utilizing measurements which I obtained from the ERS demonstrator. Furthermore, I expanded the model's capability to accommodate simultaneous modelling of multiple vehicles.

III Modelling Electric Transients in a Conductive Electric Road System [43]
D. Wenander, F. J. Márquez-Fernández, M. Alaküla
2023 AEIT International Annual Conference (AEIT), Rome, Italy, 2023, pp. 1-6

- I established a simulation model with the capacity to accurately simulate voltages and currents in the considered conductive ERS technology. I designed the simulation model so that it was capable of both modelling I) conductive EMI and II) electrical safety issues related to touch current events from the chassis of a vehicle drawing power from a conductive ERS. The model was validated utilizing measurements that I conducted on the ERS demonstrator.

IV Efficiency Evaluation of a Conductive Electric Road System With Respect to Traffic Characteristics [21]
D. Wenander, F. J. Márquez-Fernández, M. Alaküla
IEEE Transactions on Vehicular Technology, vol. 73, no. 4, pp. 4694-4704, April 2024

- I expanded the capabilities of the simulation model presented in paper II to encompass the modelling of ERS performance in various deployment environments, including urban and rural settings with corresponding traffic characteristics. The modelled ERS performance incorporated power flow, losses, and efficiency. Additionally, I conducted a comparative assessment of the efficiency performance of the presented ERS technology against that of a DC fast charger.

V Reducing the Environmental Impact of Large Battery Systems with Conductive Electric Road Systems — A Technical Overview [20]
D. Wenander, M. Alaküla
MDPI World Electric Vehicle Journal. 2024; 15(2):59.

- I revised and extended the original manuscript to incorporate evaluations of ERS efficiency and power performance, as well as an electrical safety analysis concerning the chassis voltage potential of charging vehicles. These assessments incorporated measurements that I had conducted at the ERS demonstrator.

VI Measurements of the Electric Properties of the Current Collector in a Conductive Electric Road [44]
D. Wenander, F. J. Márquez-Fernández, M. Alaküla
2024 ELEKTRO (ELEKTRO), Zakopane, Poland, 2024, pp. 1-6

- I identified the necessity for further measurements of the contact resistance of the sliding contact from an actual conductive ERS to characterize the electrical properties of the sliding contact. I designed the measurement setup, conducted the measurements, and performed an analysis of the results. Regarding the assessment of current distributions within the current collector, I analysed the results, designed the measurement system, and supervised the measurement process.

In addition, for consistency reasons, the following publication has been intentionally excluded from the scope of the thesis.

VII Automatic static charging of electric distribution vehicles using ERS technology [45]
P. Abrahamsson, **D. Wenander**, M. Alaküla, F. J. Márquez-Fernández, G. Domingues-Olavarría
2020 IEEE Transportation Electrification Conference & Expo (ITEC), Chicago, IL, USA, 2020, pp. 1191-1196

- I took part in designing and building the measurement system used to evaluate the charging performance of a distribution vehicle using either I) ERS technology for static charging or II) conventional AC charging. I conducted voltage and current measurements to calculate the charging power, logged the vehicle's position using GPS, and contributed to the analysis and discussion of the final results.

The thesis author is the original draft manuscript writer (together with Anna Wilkens and Mats Alaküla in paper V and with Philip Abrahamsson in paper VII) and the primary person responsible for the research conducted in all of the above papers (in Paper VI, parts of the measurements were conducted together with Lucas Olofsson).

All contents of the papers are reproduced with permission of their respective publishers.

1.8 Disposition

In this thesis, Chapter 1 presents the concept of conductive ERS, while Chapter 2 provides a detailed overview of the specific conductive ERS technology considered in this thesis. Chapters 3-6 explore the four main topics assessed in the thesis:

- Characterization of the electrical properties of the sliding contact (Chapter 3): This chapter provides measurements from the current collector and corresponding sliding contacts from the demonstrator as well as more detailed measurements of the sliding contacts provided by the RTR.
- Modelling power flow, losses, and efficiency (Chapter 4): This chapter investigates the dependency of power flow, losses, and efficiency on traffic characteristics and corresponding urban, rural, and highway deployment scenarios. In addition, for each deployment scenario, the impact of proposed design alterations to selected ERS subsystems and components on the performance of the ERS in terms of losses is analysed.
- Modelling conductive EMC (Chapter 5): This chapter examines the impact of conductive EMC in I) the ERS supply and II) its effect on the power grid.
- Modelling electrical safety (Chapter 6): This chapter entails an assessment of electrical safety concerning touch events involving human contact focusing on I) the chassis of a vehicle drawing power from an ERS and II) the exterior surface of the actual electric road.

Finally, Chapter 7 presents the conclusion of the thesis and suggests directions for future research.

Chapter 2

Description of the Considered Conductive Electric Road Technology

This chapter introduces the conductive ERS technology upon which this thesis is based. The considered conductive ERS technology is manufactured by the company Elonroad [26]. Although this ERS technology is still under development, its basic principles can be considered for wide deployment. The fundamental principle for all DC voltage-based conductive ERS technologies is very similar, differing mainly in the design of the physical sliding contact. Consequently, the basic principles presented in this chapter can be regarded as applicable to any conductive ERS technology. The fundamental principle of a widely deployed conductive ERS involves a grid-connected rectifier station supplying rectified DC voltage to Sections of Electric Road (SER), as illustrated in Fig. 2.1.

Fig. 2.1 does not only illustrate the fundamental deployment principle of a conductive ERS, but, in addition, also an example of a suggested ERS deployment on the European road E20 between Örebro and Hallsberg. This specific section of the E20 was considered for a permanent ERS installation, as proposed by the Swedish Transport Administration [46]. Note that the rectifier stations and their respective connection points to the ERS are strategically positioned at the midpoint of the SER to minimize energy losses. This aspect will be examined in greater detail in Chapter 4.

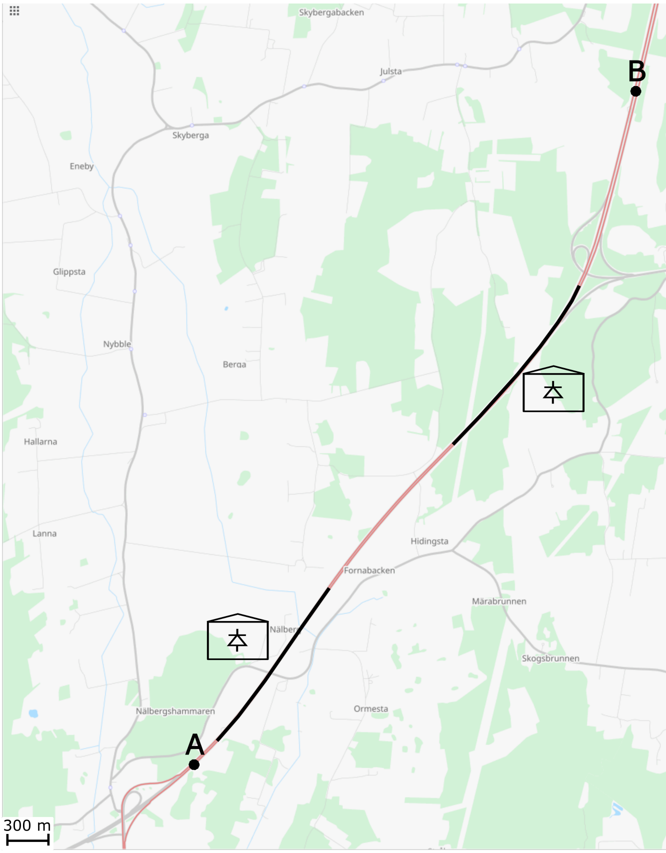

Figure 2.1: An example of suggested ERS deployment on the E20 road between Hallsberg and Örebro in Sweden.

When implementing ERS along a designated road segment, for instance between points A and B in Fig. 2.1, SER are typically installed in certain fractions of the road rather than covering the entire distance. Two primary reasons account for this practice: I) inherent obstacles in the road infrastructure, such as roundabouts, curves, intersections or similar features, and II) findings from prior studies indicate that it is more effective to selectively deploy SER along the chosen road section [36], for instance in uphill sections of a road where the power consumption is higher. The extent of ERS coverage for a given road is described by Eq. (2.1), where k_{ERS} represents the coverage factor, s_{ERS} the length of the road actually covered by ERS, and d_{ERS} the total length of the considered road section.

$$k_{ERS} = \frac{s_{ERS}}{d_{ERS}} \tag{2.1}$$

Depending on the design objectives, business model, and application of ERS, its implementation along a designated road segment can pursue one of three approaches: (i) maintaining a constant SoC for the EV battery throughout the road segment, (ii) charging the EV battery to a desired state of charge, or (iii) complementing the energy already existing in the battery to slow down the reduction of SoC, similar to a range extender. The final approach allows the vehicle to travel significantly longer distances on a single charge, even if it will eventually run out of energy.

Regardless of the chosen charging strategy, the partial deployment of ERS along road segments necessitates that EVs draw additional energy while connected to the ERS. This supplementary energy compensates for the fractions of the road lacking ERS coverage, thereby maintaining or increasing the SoC of the EV battery. The required amount of extra power is determined by the coverage factor, denoted as k_{ERS}. Lower values of k_{ERS}, indicating reduced ERS coverage along the road segment, compel EVs to draw more power during ERS access periods to offset the extended distances traveled without ERS access. Thus, balancing k_{ERS} with the power drawn per vehicle is a pivotal ERS design parameter, significantly influencing both the peak power demand from the grid and the efficiency of the ERS. Chapter 4 delves deeper into the effects of power drawn per vehicle and its impact on system losses.

2.1 The Intended Conductive Electric Road System

The ERS technology evaluated in this thesis is developed by the company Elonroad [26]. This section outlines the envisioned large-scale deployment of this considered ERS technology. Fig. 2.2 illustrates a potential future implementation of an ERS in a rural environment in Sweden. The integrated LEDs within the SER in the figure are designed to indicate the directional movement of vehicles.

Figure 2.2: A visual example of how a conductive ERS can be deployed in a rural environment in Sweden. Picture taken from Evolution Road project website [31].

In Fig. 2.3, an overview of the considered ERS technology is presented, comprising a grid-connected rectifier station, SER, and a vehicle drawing power from the ERS. Subsequent subsections elaborate on each subsystem of the ERS explicitly, whereas this section provides an overview of the entire system.

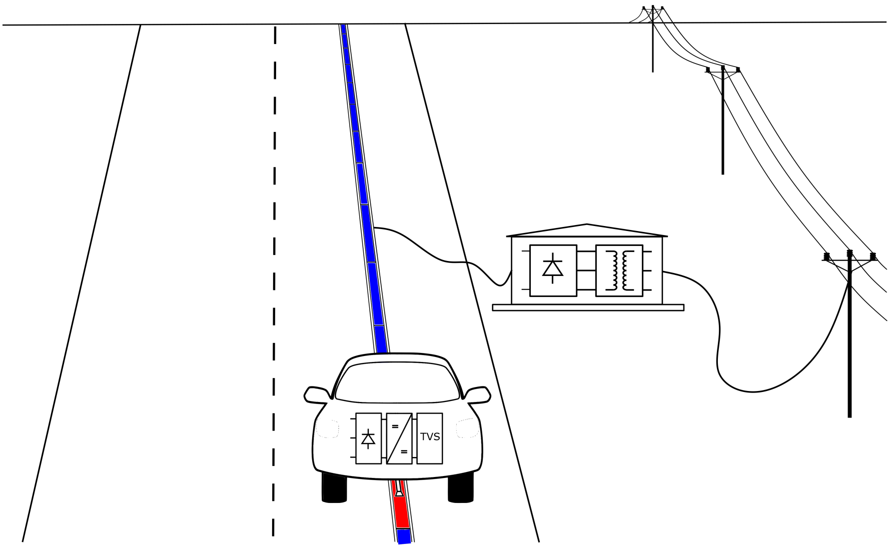

Figure 2.3: An overview of the considered ERS technology comprising a grid connected rectifier station, SER, and a vehicle adapted for ERS operation.

The rectifier station comprises two primary components: the transformer and the rectifier. The transformer is connected to the local distribution grid (10-20 kV). Given that the expected grid power load from each rectifier station is projected to range between 400-3200 kVA, depending on traffic flow and drawn power per vehicle as discussed further in Chapter 4, the rectifier stations should be dimensioned accordingly. In some cases, multiple transformers in parallel may be required to meet the power demand. The secondary winding of the transformer is designed to supply an AC voltage of approximately 480 V AC to the rectifier, resulting in an unregulated rectified DC voltage of 650 V DC to the SER.

The SER are connected to the rectifier station with underground cables. One rectifier station ideally feeds two equally long SER branches, one at each side. This configuration minimizes losses in the SER by reducing its total length from the feeding point. The SER feature a segmented structure, comprising 1 m long segments, to ensure electrical safety by activating only the segments located directly beneath an EV. This segmented design requires that vehicles be equipped with a current collector incorporating at least three sliding contacts, an onboard rectifier, and a DC/DC converter. The following subsections provide a detailed presentation of the required onboard equipment, the rectifier station, and the SER.

2.1.1 The Rectifier Station

Although subject to assumptions and dependent upon factors such as design objectives, business model, and ERS application the expected load from vehicles drawing power from the rectifier station ranges from 0.4 to 3.5 MW. This variation is influenced by factors such as traffic intensity, vehicle type, and the demanded power drawn per vehicle. Consequently, the transformer in the rectifier station must be designed to accommodate these power levels. With this in mind, standard transformer sizes of 400 and 800 kVA, connected to the local distribution grid (10-20 kV), are suitable for ERS applications [47]. For power demands exceeding 800 kVA, additional transformers can be connected in parallel within the rectifier station. Power demands exceeding 3.2 MVA are considered impractical and are out of the scope of this thesis.

The rectifier can be configured as either a 6-pulse or a 12-pulse passive rectifier. However, depending on the power load and grid operator requirements, active rectification, albeit costly, may also be considered. To attain a rectified DC voltage of 600-670 V supplied to the SER, a D/Y transformer design is used. The transformer's secondary winding (Y) is configured to provide a secondary voltage of approximately 450–500 V AC. As a result, the rectifier outputs a DC voltage in the range of 600–670 V, corresponding to the Root Mean Square (RMS) value of the line-to-line voltage, 450–500 V AC, on the transformer's secondary side. Assuming that the SER can accommodate higher voltage levels, there is potential to increase the DC voltage level further, possibly up to 1 kV. The negative pole of the rectifier's output is connected to the electrical ground, thereby the voltage of the negative pole of the SER is close to 0 V, assuming negligible voltage drop in the negative conductors of the SER.

2.1.2 Sections of Electric Road

Since the start of this thesis work in 2019, Elonroad has developed two primary design versions of the considered electric road: an embedded design and an elevated design, as shown in Fig. 2.4. The lower left corner in each picture presents a conceptual cross-sectional drawing of each design, where red elements represent the cross-sectional area of the designs, black outlines the road, and blue indicates the contact surface for the sliding contact. The elevated design is supposed to be installed on top of the road surface. This imposes strict limitations on its physical size, as it must not protrude excessively above the road surface and affect the vehicle's motion dynamics. Moreover, this size restriction results in a constrained cross-sectional area for the main conductors. In contrast, the embedded design permits larger cross-sectional areas due to less stringent volume constraints, as it is only limited by the depth and width of the groove in the road where the SER are installed. Nonetheless, for both designs, the cross-sectional conductor areas and corresponding volumes can be adjusted to a certain extent based on specific design requirements and deployment criteria.

(a) The embedded design version.

(b) The elevated design version.

Figure 2.4: The two design versions of the electric road manufactured by Elonroad, each with a cross-sectional drawing in the lower-left corner in each picture.

Though the elevated design has constraints regarding conductor size, it offers the advantage of easy installation, with minimal impact on the road layers, as illustrated in Fig. 2.5. Conversely, the embedded design is installed using bitumen mass filled into a milled groove in the road, which is 40 cm wide and 6 cm deep, as shown in Fig. 2.6. This thesis focuses on the embedded design of the presented ERS technology.

Figure 2.5: Installation of the elevated design.

(a) A 10 m long subsection of electric road being installed in a groove in the road.

(b) Moulding a 10 m long subsection of electric road into the groove in the road using bitumen mass.

Figure 2.6: Installation of the embedded design. Figures taken from [20].

The structure of the electric road under consideration is illustrated in Fig. 2.7. The exterior is constructed from aluminium and serves as a negative conductor, non-coloured in the figure. This design ensures that the electric road is safe to touch, disregarding potential minor voltage drops in the negative conductor (examined in detail in Chapter 6), since the negative pole (0 V) is connected to the electrical ground at the rectifier station. The positive pole (650 V), in red colour, comprises two conductors that extend along the entire length of the electric road.

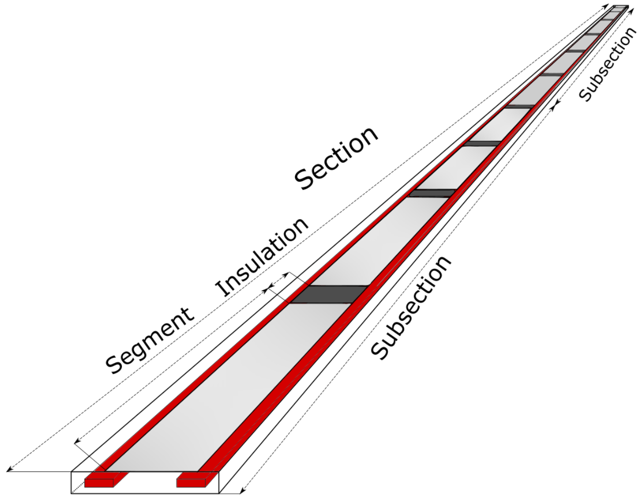

Figure 2.7: The electric road design in detail.

Upon deployment, the electric road is divided into sections of variable lengths along the designated route. These sections are then subdivided into subsections, each measuring 10 meters. This length is considered appropriate for maintenance and installation. Each subsection comprises segments, with each segment extending 1 meter in length. Isolating segments, spanning 0.2 meters each, separate these segments. These isolating segments serve to provide isolation between adjacent segments, ensuring smooth traversal of the sliding contacts across them.

The considered electric road is a type of conductive ERS known as an Alternating Short Segmented Electric Road (ASSE). In order to ensure electrical safety, the fundamental design of the electric road is based on short segments that are activated only when a vehicle drawing power from the SER is located directly above the segment. A schematic overview of the electric circuit of a SER is shown in Fig. 2.8. Every other segment features solid-state switches that allow the segment to connect to either the positive conductor (650 V) or the negative conductor (0 V) within the electric road. The remaining segments in the SER are permanently connected to the negative conductor (0 V). Segments are only activated if the EV is granted access to draw power from the electric road, which is facilitated by wireless communication.

To facilitate energy transfer between an electric road and an EV, the vehicle must be equipped with a current collector. This mechatronic device, mounted on the vehicle's underbody, establishes a physical sliding connec-

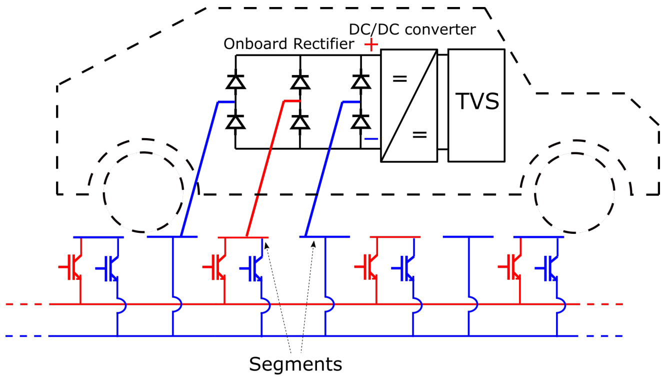

Figure 2.8: A schematic overview of the fundamental functionality of the electric road.

tion with the electric road via arms that can be raised and lowered, and automatically follow the SER laterally. These arms are equipped with sliding contacts. To ensure smooth energy transfer between the vehicle and the electric road, the current collector must have a minimum of three sliding contacts. As illustrated in Fig. 2.8, only the segments directly beneath the vehicle are activated (horizontal red lines). As the vehicle traverses these segments, the sliding contacts in the current collector continuously establish contact with new segments. Thus, in a three-arm current collector, one of the following situations is always valid when the EV is in contact with the electric road:

- Two arms are connected to the positive pole and one arm to the negative pole.
- Two arms are connected to the negative pole and one arm to the positive pole.
- One arm is connected to the positive pole, one arm to the negative pole, and the remaining arm to an isolating segment.

Consequently, the voltage potential of the current collector arms, as perceived by the vehicle, continuously alternates between 0 V DC and 650 V DC as the vehicle drives over the segments. By connecting the arms of the current collector to an onboard rectifier, the vehicle perceives a stable, constant voltage polarity. By increasing the number of sliding contacts in the current collector, additional segments in the SER can be activated under the vehicle, and, consequently, the total power drawn by the vehicle can be increased without imposing excessive strain on individual segments, as the drawn power will be distributed among multiple segments.

2.1.3 Interface between Electric Road and Vehicle

For an EV to be adapted for ERS operation, it must be equipped with three primary components: a current collector, an onboard rectifier, and a DC/DC converter. The current collector consists of a mechatronic system housed within a frame mounted on the vehicle's underbody. The sliding contacts of the current collector are connected to arms that lower when the EV has ERS access and rise when ERS access is unavailable. Additionally, to guarantee smooth alignment and dependable contact with the electric road, the mechanical system of the current collector can move both laterally and rotationally, and apply a precise contact force to the segments. Furthermore, with the aid of motion sensors, the current collector can autonomously track the SER, minimizing the need for driver intervention. Fig. 2.9 illustrates a simplified top-view of a three arm current collector. The outer frame, shown in black, is fixed to the vehicle's underbody. Mechanical components, depicted in blue, enable the rotation and translation of the inner translating framework, highlighted in red, which houses three arms, shown in green, with corresponding sliding contacts in grey. The inner mechanical components, also in blue, facilitate the rotation of the arms of the current collector, which are mounted on axles, allowing them to make contact with the segments and exert the resulting contact force.

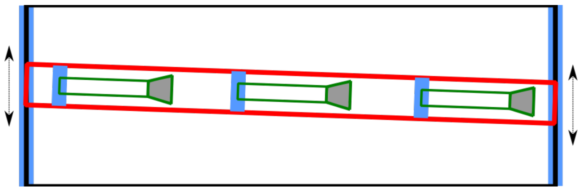

Figure 2.9: Simplified top-view drawing of a current collector. Black elements illustrate the framework, blue elements represent mechanical components, red elements indicate the translating framework, green elements depict the arms of the sliding contacts, and grey elements show the sliding contacts.

As previously mentioned, the alternating voltage polarity (-650, 0, 650 V DC) between the arms of the current collector necessitates an onboard rectifier in the EV to ensure a stable and constant voltage polarity for the EV's TVS. Additionally, due to variations in TVS and battery voltage levels within a vehicle, as well as differences among various EVs, a DC/DC converter is required onboard to match the ERS supply voltage with the EV's TVS voltage. Hence, the cost and potential volume constraints of the DC/DC converter are expected to be the primary limiting factors for its power capacity and, consequently, the amount of power that can be transferred to the TVS. This is because the DC/DC converter is considered the most complex component in terms of electrical energy transfer compared to the current collector and onboard rectifier. Unlike the current collector and onboard rectifier, which are relatively passive, the DC/DC converter is an active component that requires intricate control and seamless integration into the vehicle's TVS.

One significant advantage of ERS is the direct transfer of power to the vehicle's propulsion system without passing through the battery. In Fig. 2.10, the TVS of an arbitrary BEV adapted for ERS application is presented. In this context, the TVS comprises the DC/DC converter, which regulates the drawn power from the ERS supply, a traction motor with an inverter, a battery with a converter, and an auxiliary system. The auxiliary system encompasses additional loads connected to the TVS, such as Heating, Ventilation, and Air Conditioning (HVAC) systems, 12/24 V DC systems, and other onboard auxiliary systems. As shown in Fig. 2.10, power can be directly transferred to the traction motor and auxiliary systems without passing through the battery. Compared to conventional static charging stations, direct power transfer offers higher efficiency, provided that the DC/DC converter efficiency is high, as the losses associated with battery charging and discharging can be eliminated. However, given that the DC/DC converter is always present in an ERS application, its efficiency plays a crucial role in achieving a high system efficiency, as all transferred power passes through it.

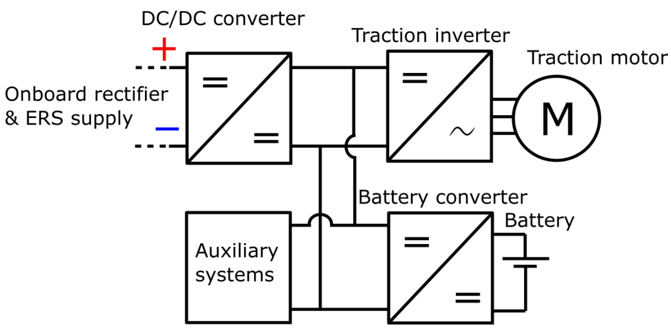

Figure 2.10: Traction voltage system of an arbitrary BEV adopted for ERS operation.

2.1.4 Electrical Safety Issues Related to the Vehicle's Chassis

While extensive electrical systems like a conductive electric road pose numerous challenges regarding electrical safety, this thesis primarily addresses two areas: touch events and isolation faults concerning the chassis of a vehicle drawing power from the ERS, and touch events related to the exposed exterior of the electric road. This subsection provides a brief overview of the fundamental concept concerning a human body touching a vehicle chassis that may carry a harmful voltage.

In contrast to conventional static charging stations, a conductive ERS does not offer a reliable enough option to connect the vehicle chassis to electrical ground. When the BEV chassis is connected to electrical ground, the risk of electric shock is mitigated. In the event of an isolation fault between the charger and BEV chassis, the current would flow through the chassis to the ground connection in the charging port, thereby triggering the Residual Current Breaker (RCD) in the facility where the static charging station is installed.

However, in general, road-bound conductive ERSs have the electrical ground connected to the negative pole of the ERS supply [15, 26, 29], except for Honda, which utilizes a floating two-pole supply [19]. If a conductive object or debris, possibly combined with salt water from the road, comes into contact with an active segment or arm in the current collector and the vehicle chassis, there is a risk of a high voltage on the vehicle chassis, as illustrated in 1) in Fig. 2.11. Additionally, the risk of an elevated chassis voltage could occur due to an isolation fault onboard the vehicle TVS between the positive pole in the vehicle and the vehicle chassis, as shown in 2). In the event of an isolation fault resulting in the BEV chassis carrying an elevated voltage, when a human body touches the chassis, current will flow through the human body to electrical ground, returning to the rectifier station.

To mitigate risks associated with hazardous touch events caused by an elevated chassis voltage, appropriate levels of isolation are required [48]. For conductive ERS applications, implementing strategies to ensure adequate levels of isolation between the ERS supply, from segment to current collector and TVS poles, and the vehicle chassis is paramount. Special attention during the design phase of the current collector is necessary to minimize the risk of objects from the road or salted water or ice coming into contact with the vehicle chassis and high-voltage poles. To mitigate the necessity for strict isolation measures across the entire vehicle, an isolated DC/DC

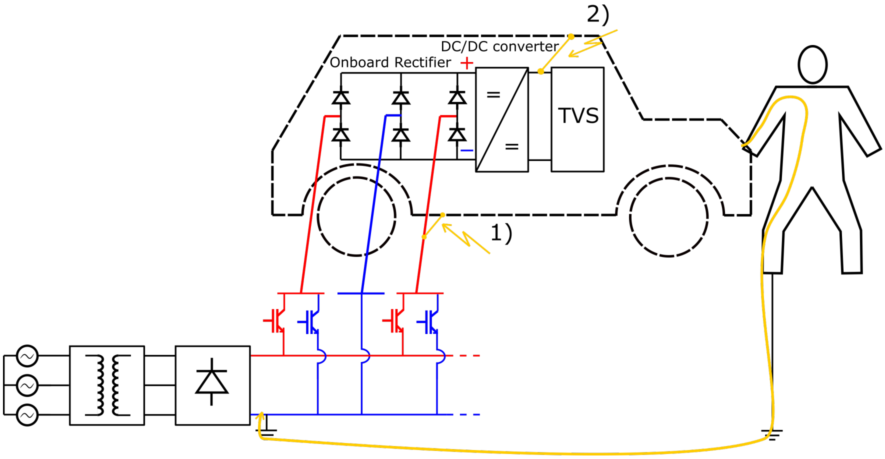

Figure 2.11: Electrical safety issue related to the voltage of the chassis of a BEV while the BEV is drawing power from the ERS: 1) represents an isolation fault between the chassis and ERS supply, and 2) represents an isolation fault between the chassis and TVS. In the event of an isolation fault to the BEV chassis current may flow through the human body to ground in the rectifier station.

converter can be introduced between the onboard rectifier and TVS. This setup effectively separates the TVS from the ERS supply, allowing for less stringent isolation requirements on the isolated TVS [48]. Thus, in the event of an isolation fault within the isolated TVS, no current will pass through the human body.

BEVs typically feature an Isolation Monitoring System (IMS) designed to identify isolation faults between high-voltage poles and the vehicle chassis. The IMS could be reconfigured for application in conductive ERS setups. Its adaptation would involve monitoring impedance variations between the high-voltage poles, extending from the arms in the current collector to the TVS. Upon detection of an isolation fault, whereby the impedance between the chassis and pole undergoes drastic alteration, the IMS would activate, thereby disconnecting the vehicle from the ERS supply. Prompt detection and disconnection are vital aspects of IMS operation, given that time is essential in mitigating harmful electric hazards, as emphasized in [49].

2.2 Experimental Setup - The Electric Road Demonstrator

The main experimental setup in this thesis is the conductive electric road demonstrator built by Elonroad, located on a public road in an urban environment in Lund, Sweden. Measurements from the demonstrator serve as the foundation for all analyses, including the presented measurement results and established simulation models. Fig. 2.12 presents a satellite map from Google Maps showing where the demonstrator was located in Lund. The red colour represents the location of the rectifier station and corresponding grid connection. The turquoise colour indicates where the embedded design was installed, and the purple colour shows where the elevated design was installed. The demonstrator was installed in May 2020 and decommissioned in May 2024.

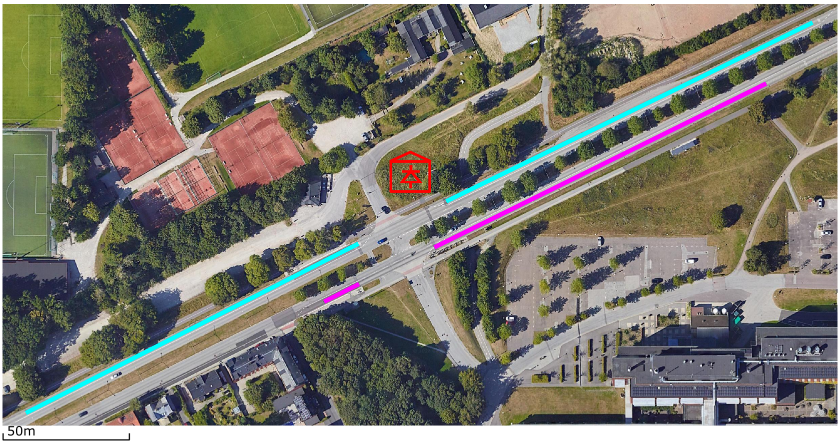

Figure 2.12: Satellite map of where the demonstrator was located. The location of the rectifier station is shown in red, the embedded electric road in turquoise and the elevated electric road in purple.

The demonstrator comprises a 400 kVA 400/450 V three-phase D/Y transformer, a six-pulse passive rectifier, and two distinct designs of SER: one elevated and one embedded. Detailed descriptions of these design variations are provided in the preceding subsection. While several vehicles have been adapted for ERS operation to varying extents, the primary vehicle considered in this thesis is a modified trolleybus. Measurements involving this electric bus drawing power from the demonstrator are utilized for establishing and validating the simulation models presented in this thesis. To evaluate the electrical characteristics of the current collector, a trailer equipped with a resistive load, which was towed by a car over the demonstrator, was employed. In Chapter 3 the design and structure of the trailer is explained in detail.

Fig. 2.13 illustrates a simplified overview of the demonstrator's electrical circuit, highlighting the rectifier station in red, the electric road in turquoise, and the electric bus in green. Note that the current collector within the vehicle is equipped with six sliding contacts, mirroring the configuration of the installed current collector in the electric bus. A-D denote measurement interfaces for voltage and current. These measurements serve to validate and calibrate the simulation models which are based on the demonstrator.

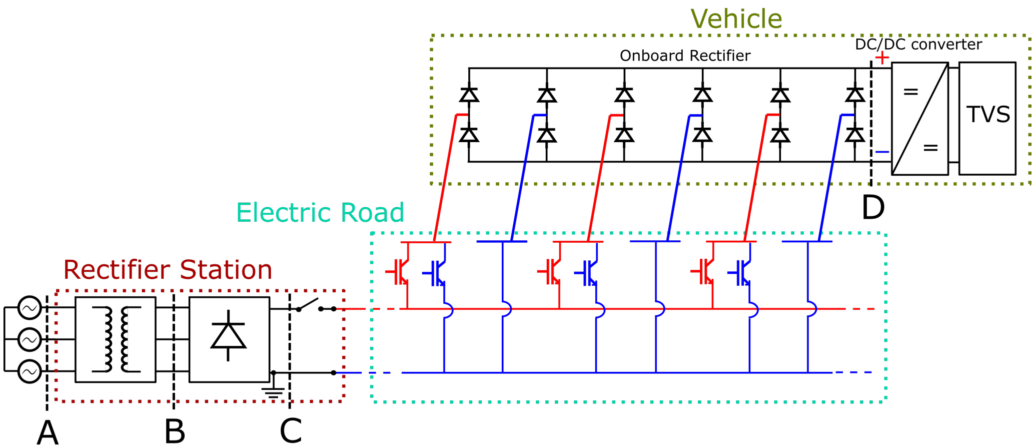

Figure 2.13: Simplified schematic of the demonstrators electrical circuit.

The subsequent subsections feature schematics of the demonstrator's electrical circuits. These presented circuits do not constitute complete schematics of every subsystem within the demonstrator. Instead, they represent the essential components of the demonstrator. Furthermore, these schematics are further simplified and subsequently utilized in this thesis for the development of simulation models.

2.2.1 The Rectifier Station

The schematic of the rectifier station is presented in Fig. 2.14. The rectifier station comprises a 400 kVA 400/450 V three-phase D/Y dry transformer, which is connected upstream the grid to another transformer via 210 meters of cable. A passive six-pulse rectifier is connected to the output of the transformer, followed by various filters and a solid-state switch that can be used to connect and disconnect the SER. A 41 meter underground cable connects the rectifier station and the SER. Interface x) denotes where the SER connects to the rectifier station. This connection is known as the feeding point of the SER. At interfaces A, B and C voltage and current are measured.

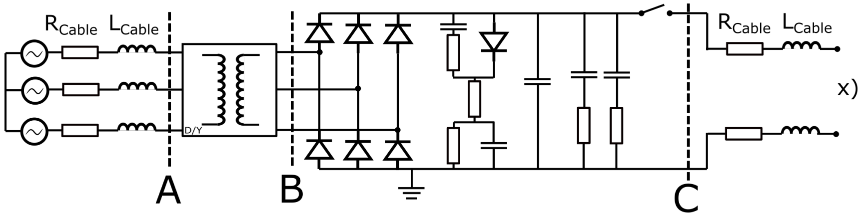

Figure 2.14: Schematic of the rectifier station, including its connection to the power grid.

2.2.2 Sections of Electric Road

Although the demonstrator featured two design versions of the electric road (see Fig. 2.12), this thesis focuses on the embedded design, since this has been the preferred alternative for the Swedish Transport Administration due to its less protrusive impact. Nonetheless, from an electrical perspective, the primary difference between the two designs lies in the cross-sectional area of the main conductors. Therefore, by altering this parameter in the simulation models presented in Chapters 4 and 5, the conceptual differences between the two designs are still evaluated in this thesis from an electrical perspective.

The SER consists of 1-meter segments controlled by transistors, as illustrated in Fig. 2.15. Although these transistors are complemented by various filters and corresponding snubber circuits, they are omitted to simplify the circuit, as the modelling in this thesis does not include the switching of these particular transistors.

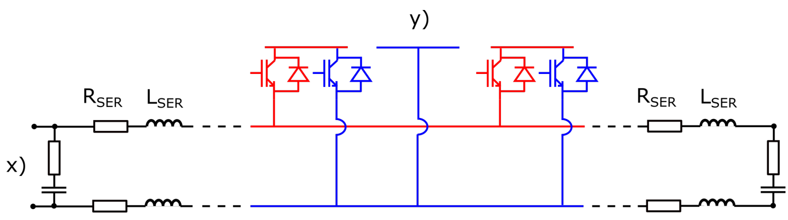

Figure 2.15: Schematic of the SER. Red and blue elements represent segments and the positive and negative poles of the SER, respectively. The schematic illustrates the circuit's configuration with two activated segments along a SER.

The schematic also includes the impedance of the main positive and negative conductors of the SER, labeled as "SER" in the figure. At the beginning (feeding point) and end of each SER segment, an RC filter is deployed. Interface x) represents the connection between the SER and the rectifier station. Interface y) indicates the connection between the vehicle and the electric road, facilitated by the sliding contacts of the current collector.

2.2.3 Vehicle Integration and Testing

A Solaris Trollino 12 trolleybus, equipped with a high-voltage battery designed for traction applications and additionally outfitted with a current collector and onboard rectifier, served as the primary vehicle for testing the ERS demonstrator [50]. Fig. 2.16 shows the bus during testing at the demonstrator.

Figure 2.16: The primary vehicle, a Solaris Trollino 12 electric bus, during testing at the demonstrator.

The current collector installed on the bus features six arms to prevent excessive power draw per segment in the SER. Fig. 2.17 illustrates the current collector installed on the bus during operation. The sliding contacts consist of braided wires made of copper and stainless steel, positioned at the tip of each arm in the current collector, as depicted in Fig. 2.17b. Additionally, each arm is connected to a branch of the passive rectifier to ensure a constant polarity to the TVS of the bus.

(a) Current collector installed on the electric bus during operation.

(b) Sliding contact at the tip of the arm in the current collector, featuring a metallic brush.

Figure 2.17: Left: Current collector in operation on the electric bus. Right: Zoomed-in view of the sliding contact with a metallic brush. Figures taken from [20, 44].

Figure 2.18 provides a schematic of the electric bus' TVS circuitry. The term "TVS" encompasses all electrical loads connected to the high-voltage battery in the electric vehicle. However, this thesis solely considers the high-voltage battery with its corresponding battery converter, the traction motor with its corresponding inverter, and the DC/DC converter between the onboard rectifier as the TVS. Additional subsystems connected to the TVS, such as HVAC, the 24 V system, and the compressor, are summarized as "Auxiliary". Interface D depicts the measurement interface where current and voltage are measured.

Within this schematic, the voltage drop across the sliding contact is represented as a resistor. Following the rectifier in the TVS, a differential mode filter is integrated, comprising an inductor and two capacitors. Situated between these capacitors is a common mode filter, which features a common mode choke.

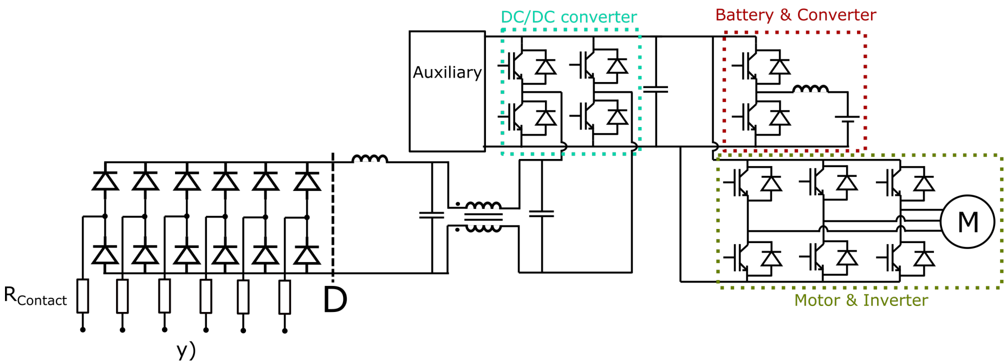

Figure 2.18: Schematic of the bus' TVS. Turquoise colour represents the DC/DC converter, red the high-voltage battery with corresponding converter and green traction motor with corresponding inverter. Auxiliary summarizes all additional loads that are connected to the bus' TVS.

One of the primary reasons the bus was chosen as the test vehicle for the demonstrator is its suitability for ERS applications, owing to its trolley system configuration. The bus's TVS topology is particularly advantageous for ERS applications because the DC/DC converter between the ERS supply and the bus's TVS is designed to meet the bus's power demands without limitations. This offers several benefits:

- The bus can draw power directly from the ERS supply to the motor and corresponding inverter without passing it through the battery, thereby reducing energy losses associated with battery charging and discharging cycles.
- The DC/DC converter's power capability enables the bus to simultaneously charge its battery and draw power for the motor and all additional auxiliary systems in the TVS, thereby maximizing the utilization of the ERS supply.

As detailed in Chapter 4, which presents measurements from the testing of the demonstrator, the battery converter in the bus was configured to draw 40 kW during static charging and 80 kW during dynamic charging to the high-voltage battery. The power drawn during static charging is limited to 40 kW to prevent overheating of the brushes in the sliding contact shown in Fig. 2.17. The total power drawn, encompassing both battery charging, propulsion during acceleration, and auxiliary loads, can peak at nearly 200 kW, as demonstrated in Chapter 4. While this setup is effective for testing the demonstrator's power capabilities, BEVs adapted for ERS operation may face restrictions regarding their power electronic ERS interfaces. These restrictions arise due to two main factors:

1. Allowing unrestricted power draw from all BEVs could overload the ERS supply if multiple heavy vehicles accelerate simultaneously, as the power draw during acceleration significantly exceeds that required for cruising. To prevent oversizing of the ERS, the additional power demands from vehicles during intense accelerations should be drawn from the BEV battery rather than the ERS supply.

2. Volume constraints within BEVs limit the space available for onboard ERS interface equipment. This limitation may restrict the power capacity of the required DC/DC converter, especially if the converter must support high power levels and be isolated due to previously discussed electrical safety mitigation strategies related to the vehicle's chassis.

These considerations underscore the necessity of managing power draw and equipment volume in BEVs adapted for ERS operation and will be further evaluated in Chapter 4.

2.2.4 The Measurement System

The conductive ERS demonstrator played a fundamental role in conducting the work presented in this thesis. The development, calibration and validation of the models presented are based on comprehensive experimental measurement sets obtained during the different tests conducted within the project. Therefore, the equipment and measurement setup presented in this subsection are essential for ensuring the validity and reliability of this research.

This subsection presents the primary measurement system employed throughout this thesis, with a specific focus on evaluating the demonstrator's voltage and current characteristics, power flow, losses, and system efficiency. These parameters are crucial for assessing the overall effectiveness and operational dynamics of the ERS. Moreover, in Chapters 4 and 5, this measurement system plays a pivotal role in providing empirical data that enables the development and subsequent validation of simulation models. To comprehensively evaluate the electrical properties of the demonstrator and, by extension, the properties of the considered ERS technology, it is essential to measure voltage and current across multiple interfaces of the demonstrator. These measurements are then used to calculate and assess electrical characteristics such as voltage and current quality, power flow, losses, and efficiency.

As illustrated in Fig. 2.13, interfaces A-D have been designated for voltage and current measurements. Interface A, shown in Fig. 2.19a, represents the power grid connection of the demonstrator, where voltage and current are measured at every phase. Interface B, located at the input to the rectifier with voltage and current measured at every phase, and Interface C, which corresponds to the output of the rectifier, are shown in Fig. 2.19b. The picture is blurred due to non-disclosure agreements with Elonroad. The voltage sensor at interface D is shown in Fig. 2.20. Interface D represents the input of the bus' TVS, located on the bus roof, after the current collector and onboard rectifier.

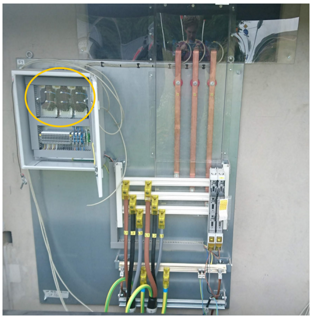

(a) Voltage sensors at interface A (cabinet to the left) and the grid connection of the transformer.

(b) The cabinet in the rectifier station contains the rectifier, corresponding filters, circuit breakers, and control equipment. The circles indicate the locations of current sensors at interfaces B and C.

Figure 2.19: Location of the sensors at interfaces A, B, and C in the rectifier station.

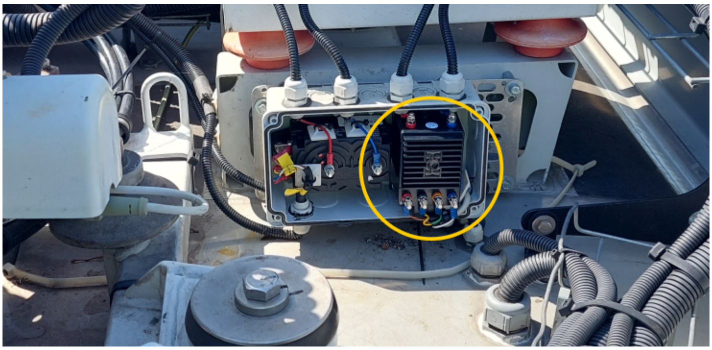

Figure 2.20: LEM CV 3 voltage sensor installed on the roof of the electric bus at measurement interface D.

In order to assess power, efficiency, and conductive EMI, the measurement system was requested to provide high bandwidth, high sampling rate, and high precision and accuracy. This required a careful selection of sensors, measurement resistors, and data loggers, which resulted in a preference for sensors primarily manufactured by LEM. Data logging is performed using two MCC USB-1808X Data Acquisition Devices (DAQs) [51]. Table 2.1 outlines a comprehensive overview of the measurement system's accuracy, detailing both the total error at each interface and the individual contributions from each component, including associated errors and bandwidth [51–57].

Table 2.1: Specifications of error and bandwidth concerning the components in the measurement system.

Measurement System Specifications				
Parameter	*Measurement Interface*			
	A	**B**	**C**	**D**
DAQ				
DAQ sample frequency [kHz]	200			
DAQ error [%]	0.036			
Current measurement				
Sensor model	LEM LF 505-S		LEM IT 605-S	LEM IT 405-S
Sensor Bandwidth [kHZ] (@ -1 dB)	100		200	200
Sensor error [%]	0.6		0.0016	0.0043
Resistor error [%]	0.04		0.012	0.012
Current error [%]	0.68		0.049	0.052
Voltage measurement				
Sensor model	DVL 250	CV 3-500	Resistor	CV 3-1000
Sensor Bandwidth [kHZ] (@ -1 dB)	8 kHz	300 kHz	-	500 kHz
Sensor error [%]	0.5	0.6	0.16	0.6
Resistor error [%]	0.03	-	-	-
Voltage error [%]	0.57	0.64	0.19	0.64

As the chosen LEM current sensors output a current, a measurement resistor used as a shunt is connected to the sensor's output, and the voltage drop across this measurement resistor is used as an input to the DAQs. To calculate the total current error, the error of the data logger, the measurement resistor, and the sensors must be accounted for, as presented in the table. The errors of the resistors are calculated by considering both the tolerance value, as specified by the manufacturer, and the resistance temperature coefficient of the resistors. All chosen resistors are high-precision resistors, characterized by low tolerance deviation and minimal temperature drift [58, 59].

The bandwidth in the measurement system is defined at a 1 dB change at the cut-off frequency. For the voltage measurement in interface C, a shunt resistor design was used, in which no cut-off frequency was found [58, 59]. However, through calculations, the cut-off frequency was determined to be above the data logger sample frequency and thus does not affect the total bandwidth of the measurement system. In contrast to the other LEM sensors in the measurement system, the CV 3 sensors output a voltage rather than a current and therefore do not require additional measurement resistors. All LEM sensor errors are defined as the deviation of current or voltage at the specified nominal value according to the datasheet. The total errors presented and the corresponding bandwidth of the interfaces are deemed adequate for assessing the electrical properties of the considered ERS technology.

However, one of the main challenges in the performance of measurement system is that the accuracy of power and efficiency calculations is highly influenced by the measurement accuracy of voltage and current at the individual interfaces. To illustrate this, two arbitrary measurement interfaces are introduced: interface 1 and interface 2, where voltage and current are measured. Interface 1 is assumed to be located at the ERS power grid connection, and interface 2 is assumed to be located in the vehicle. At these interfaces, we introduce measurement errors for each measured voltage and current individually, as presented in Eqs. (2.2) to (2.5). These measurement errors are represented by $\delta_{V_1}, \delta_{I_1}, \delta_{V_2}, \delta_{I_2}$, which are the total errors for each respective measurement and can be either positive or negative, depending on whether the measurement is overestimated or underestimated. Parameters V_1, I_1, V_2, and I_2 represent the true voltage and current values at each interface, respectively. The measured values at these interfaces are given by:

$$V_1^{\text{meas}} = (1 + \delta_{V_1})V_1 \tag{2.2}$$

$$I_1^{\text{meas}} = (1 + \delta_{I_1})I_1 \tag{2.3}$$

$$V_2^{\text{meas}} = (1 + \delta_{V_2})V_2 \tag{2.4}$$

$$I_2^{\text{meas}} = (1 + \delta_{I_2})I_2 \tag{2.5}$$

The power at interfaces 1 and 2, calculated from the measured values in Eqs. (2.2) to (2.5), are presented in Eqs. (2.6) and (2.7):

$$P_1^{\text{meas}} = (1 + \delta_{V_1})(1 + \delta_{I_1})P_1 \tag{2.6}$$

$$P_2^{\text{meas}} = (1 + \delta_{V_2})(1 + \delta_{I_2})P_2 \tag{2.7}$$

Finally, the efficiency η^{meas} is calculated based on the ratio of the power calculated at interfaces 1 and 2 from Eqs. (2.6) and (2.7), and are presented in Eq. (2.8):

$$\eta^{\text{meas}} = \frac{P_2^{\text{meas}}}{P_1^{\text{meas}}} = \frac{(1 + \delta_{V_2})(1 + \delta_{I_2})}{(1 + \delta_{V_1})(1 + \delta_{I_1})} \times \eta \tag{2.8}$$

Thus, the efficiency η^{meas}, calculated from the measured values, will differ from the theoretical efficiency η unless the measurement errors at interfaces 1 and 2 cancel out in a specific way. For instance, this results in a possible error of -0.55% between interfaces A–D by incorporating the calculated positive errors of voltage and current from Table 2.1. Although this might appear insufficient, this accuracy is considered acceptable given the inherent nature of the mathematical procedures and the constraints of time and budget in the EVR project for improving it.

Furthermore, the performance of the measurement systems in terms of accuracy varies among the measurement interfaces. Notably, the current sensors in interfaces C and D exhibit significantly better performance in terms of error compared to interfaces A and B. This is because, in the initial stages of this thesis work, there was a greater focus on interfaces C and D, as interfaces A and B represent transformer and rectifier components, which at the time were deemed to have well-known losses. Nonetheless, as shown in Chapter 4, the impact of varying traffic intensity significantly affects the entire ERS system, including the losses and design of the rectifier station.

2.2.5 Measurement System Validation

To further enhance the credibility of the measurement system, its performance was validated. Although it was challenging to find instruments that exceeded the accuracy of certain components in the measurement system, such as the current sensors in interfaces C and D, a Rigol DM 3068 high-accuracy multimeter [60] was available. This multimeter was deemed sufficient for validating the system's performance. Prior to installation in the rectifier station, the system was tested in a laboratory setting. This testing revealed that installation factors such as cable lengths and power supply choices affected the measurement results. Consequently, despite the practical difficulties of performing the validation outdoors, including uncontrolled ambient temperature at the rectifier station, the decision was made to validate the measurement system under real conditions. This approach accounted for cable lengths and power supply choices, but also introduced potential accuracy issues for the high-accuracy multimeter.

To validate the accuracy performance of the system's voltage measurements, an Oltronix A2,5K-10 power supply was connected to the voltage sensors in interfaces A and B and the shunt resistor in interface C. The terminals of the sensors were disconnected from their respective connections in the rectifier station and connected in parallel with the power supply and the high-accuracy multimeter. In Table 2.2, the results of the voltage measurement validation are presented for interfaces A, B, and C. Four measurements were conducted at each interface, aiming to cover the full voltage range at which the sensors were expected to operate. The first column of the table presents the measurements conducted for each interface. The second column presents the value measured with the high-accuracy multimeter and the third column presents the maximum possible measurement error according to the multimeter's datasheet [60].

Table 2.2: Validation of the voltage measurement accuracy of the measurement system.

Voltage Measurement Validation			
Device	Rigol DM3068		Demonstrator Measurement System
Parameter	Value [V]	Error [%]	Maximum Error [%]
Interface A			
Measurement 1	-224	0.032	0.27
Measurement 2	-112	0.023	0.26
Measurement 3	32	0.038	0.19
Measurement 4	352	0.026	0.24
Average			0.24
Interface B			
Measurement 1	-266	0.029	0.18
Measurement 2	-133	0.028	0.25
Measurement 3	38	0.058	1.21
Measurement 4	350	0.026	0.22
Average			0.47
Interface C			
Measurement 1	65	0.027	0.13
Measurement 2	260	0.030	0.054
Measurement 3	585	0.022	0.033
Measurement 4	715	0.021	0.031
Average			0.063

The fourth column presents the calculated maximum error for each measurement value provided by the demonstrator's measurement system. This maximum error calculation originate from Eqs. (2.9) and (2.10). Eq. (2.9) presents the maximum possible error that the measured values from the high-accuracy multimeter can exhibit, according to the instrument's datasheet [60]. Here, X_{HA} is the value measured with the high-accuracy multimeter (shown in column two of Table 2.2), and $\delta_{\mathrm{max,HA}}$ is the maximum error (positive or negative) of the high-accuracy multimeter (shown in column three of Table 2.2). $X_{\mathrm{max,HA}}$ represents the calculated value provided by the high-accuracy multimeter, including its maximum possible error.

$$X_{\mathrm{max,HA}} = \frac{X_{\mathrm{HA}}}{(1 \pm \delta_{\mathrm{max,HA}})} \tag{2.9}$$

In Eq. (2.10), X_{demo} represents the measured value from the demonstrator, and $X_{\mathrm{max,HA}}$ represents the value provided by the high-accuracy multimeter, including its maximum possible error. E_{demo} represents the calculated maximum relative error provided by the demonstrator's measurement system (shown in column four of Table 2.2).

$$E_{\mathrm{demo}} = \left| \frac{X_{\mathrm{max,HA}} - X_{\mathrm{demo}}}{X_{\mathrm{max,HA}}} \right| \tag{2.10}$$

For interfaces A and B, the maximum error for each measurement presented in the fourth column from the measurement system is the average maximum error calculated from all three sensors across the three phases. The row labeled 'Average' presents the average value of the maximum errors from measurements 1 to 4 of the measurement system.

When comparing the accuracy performance in terms of voltage of the measurement system, as presented in column four in Table 2.2, with the calculated accuracy in Table 2.1, it is evident that the system outperforms the calculations based on datasheets. The error percentage is lower in Table 2.2, particularly in interface C, where the average maximum error percentage is 0.063%, compared to the calculated error of 0.19% of voltage measurements provided by the measurement system. The calculated accuracy of the high-accuracy multimeter with an error as low as 0.021%, verifies its performance and suitability as a reliable reference.

The accuracy of the current sensors was validated by connecting a Velleman PS3010 power supply [61] in series with a resistive load, the same high-accuracy multimeter used in the previous validation, and a thin cable wound around the core of the current sensors. Figure 2.21a presents the circuit of the setup used for validating the current sensors in the measurement system, where the current source represents the power supply, R_{load} represents the resistor, A represents the high-accuracy multimeter used as an ammeter, the thin cable is shown in red, and the current sensor is shown in blue. By applying this method, as illustrated in Fig. 2.21b, the current detected by the current sensor was linearly proportional to the number of winding turns around the sensor, thereby eliminating the need for a high-current power supply.

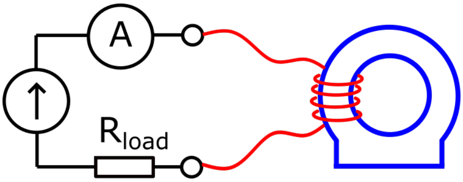

(a) Circuit of the setup used for validating the current sensors in the measurement system, where a thin cable (in red) was wound around the current sensor (in blue).

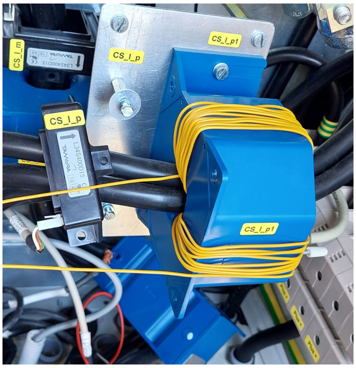

(b) The method of winding a thin cable (the yellow cable in the picture) around the current sensor was applied during the validation of the measurement system.

Figure 2.21: Measurement setup for validating the current sensors.

The multimeter's accuracy in measuring current is significantly lower than its accuracy in measuring voltage [60]. However, it remained the most suitable instrument available as a reference for assessing the measurement system's accuracy in measuring current. Consequently, the current sensors in interfaces C and D were not evaluated, as their expected accuracy far exceeded that of the high-accuracy multimeter, making it unsuitable as a reference for these interfaces. In addition, due to practical limitations, validation was conducted only on two current sensors in interface B. Although sub-optimal, this approach was deemed acceptable since the sensors in interfaces A and B are identical models, making the evaluation of a subset of sensors justifiable.

Using the same equations and type of data as in Table 2.2, Table 2.3 presents the results of the current measurement validation for interface B. The first column lists the measurements 1-4, the second column presents the values measured by the high-accuracy multimeter, the third column provides the multimeter's error, and the fourth column presents the calculated maximum error in current for the demonstrator's measurement system, determined using Eqs. (2.9) and (2.10). Similar to the validation results of the voltage performance, the measured current performance of the measurement system, as shown in Table 2.3, surpasses the calculated performance presented in Table 2.1. The average maximum possible measurement error is 0.48%, compared to the calculated error of 0.68% for interfaces A and B.

Table 2.3: Validation of the current measurement accuracy of the measurement system.

Current Measurement Validation			
Device	Rigol DM3068		Demonstrator Measurement System
Parameter	Value [A]	Error [%]	Maximum Error [%]
Interface B			
Measurement 1	-135	0.27	0.65
Measurement 2	-55	0.30	0.40
Measurement 3	79	0.29	0.36
Measurement 4	159	0.27	0.49
Average			0.48

While this experimental validation could be improved by encompassing a larger number of measurements per interface, including all sensors in the system, and utilizing even more accurate instruments as references, the conducted validation indicates that the measurement system generally performs at least according to the datasheet specifications. In many instances, it even performs better than prescribed.

Chapter 3

Experimental Characterization of the Sliding Contact

3.1 Introduction

The electric sliding contact is a well-known technology for transferring energy that has been studied in a wide range of applications [62–64]. Trains, trams, metro trains, and trolleybuses are just a few examples where sliding contacts are successfully used. However, conductive ERS presents a new application for sliding contacts, differing from previous ones. In road-bound conductive ERS, not only are the geometries different, but the contact surfaces are also more exposed to dirt, snow, rain, and other debris that may obstruct or affect the quality of energy transfer. Moreover, similar to trolley applications, the current collector must be designed to accommodate the motion dynamics of the vehicle to maintain stable and reliable contact.

Since the sliding contact is the most crucial element for energy transfer between the road and the vehicle in a conductive ERS, this chapter focuses on the experimental characterization of its electrical properties. Different designs of sliding contacts and current collectors have been developed across various conductive ERS [15, 19, 26, 27, 29]. Among these, Honda's design is particularly noteworthy, as it employs an electrically conducting rotating wheel in contrast to conventional sliding contact designs. As outlined in Section 2.2, the ERS demonstrator presented in this thesis employs a sliding contact design based on a metallic brush-based contact mechanism. During the tests conducted at the ERS demonstrator the performance of the sliding contact exhibited significant variations in terms of stability and reliability. Therefore, further assessment is required to determine the optimal current collector and sliding contact configuration for conductive ERS. Published work on sliding contacts for conductive ERS applications is sparse. To address this research gap, this chapter presents an experimental approach utilizing three distinct setups, located both in laboratory settings and at the ERS demonstrator, aimed at expanding the understanding of this technical solution.

A reliable electrical contact between the ERS and the vehicle is essential, as it ensures a continuous and stable energy transfer to the vehicles using the ERS. If the supplied current from the ERS to the vehicle is disrupted, the primary purpose of the ERS is compromised. Therefore, the sliding contact must be reliable. However, poor contact is inevitable at some point. While it may not completely disrupt the energy transfer, poor contact may increase the voltage drop across the sliding contact, leading to excessive losses. If the contact quality deteriorates further, intermittent contact loss can occur, posing a significant risk of arcing. Although such arcing may be brief and intermittent, it can lead to severe issues, particularly in terms of radiated and conducted emissions within the ERS and its surroundings. This phenomenon is well-documented in railroad networks [65]. Thus, during the design process of the current collector and sliding contacts, it is essential to implement strategies to minimize arcing and to adopt methods to maintain stable contact, thereby reducing losses and decreasing both radiated and conducted electromagnetic emissions.

To delve deeper into the design of the sliding contact with respect to its availability and reliability, it is necessary to understand its underlying electrical properties. This involves investigating characteristics such as voltage drop, contact resistance, friction force, and arcing, all of which are expected to have a significant impact on the contact's quality and stability. By attempting to measure and assess these properties, valuable insights can be obtained into which factors, such as current levels, vehicle speed, contact force, and weather conditions, influence the electrical properties of the sliding contact. Additionally, the results from these measurements can facilitate the parametrization of sliding contact behavior within simulation models, such as those presented in Chapters 4 and 5 of this thesis, thereby enabling the simulation of various performance characteristics of conductive ERS technology across a wide range of applications.

The first section of this chapter presents measurements from the ERS demonstrator, covering both the magnitude and distribution of current within the different arms in the current collector. This is crucial for gaining a deeper understanding of how the design of the current collector affects the characteristics of the current flowing through a single sliding contact, as well as the resulting supplied current to the vehicle. Subsequently, the findings regarding the characteristics of the current per arm in the current collector are used to conduct a more detailed examination of the electrical properties of an individual sliding contact.

The second section of this chapter presents experiments designed to assess the contact resistance, friction forces, and arcing of a single sliding contact. These experiments are conducted in a controlled laboratory environment using an RTR. This experimental setup facilitates the manipulation of parameters such as contact force, current level, and speed, enabling a thorough examination of their effects on voltage drop over the sliding contact, contact resistance, friction forces, and arcing. Moreover, the controlled nature of the laboratory environment eliminates external factors that could potentially influence similar measurements taken at the ERS demonstrator.

Finally, the third section of this chapter presents experimental results from the ERS demonstrator, focusing on the voltage drop and resistance of two sliding contacts at varying speeds and current levels. These measurements are subsequently used to calculate the mean contact resistance of a single sliding contact from the ERS demonstrator. While the conducted measurements at the demonstrator are more rudimentary in nature and less accurate than those obtained from the RTR, they provide an order of magnitude for contact resistance of a sliding contact from a real ERS. Moreover, these results, in terms of their order of magnitude, validate the ability of the RTR to assess the characteristics of the sliding contact from a real ERS in terms of their order of magnitude. All experimental work related to the demonstrator presented in this chapter is based on [44].

3.2 Experimental Assessment of the Magnitude and Distribution of Currents in the Current Collector

In order to assess the quality of the sliding contact, including properties such as voltage drop over the sliding contact, contact resistance and frictional forces, comprehensive measurements are necessary. As the vehicle traverses the electric road drawing power dynamically, the current drawn by each sliding contact in the current collector alternates continuously and is influenced by the vehicle's power draw, speed, and the quality of the sliding contacts.

A thorough understanding of contact quality, voltage drop, contact resistance, arcing, and forces exerted on the contacts necessitates an initial evaluation of the current flowing through each sliding contact. This is due to the fact that all of these parameters are influenced by both the waveform shape of the current and its magnitude. To assess the distribution and magnitude of the currents in the sliding contacts of a current collector, a trailer is used that is specifically designed to test current collector designs, sliding contact designs, and to demonstrate the demonstrator's capability of supplying power to vehicles.

3.2.1 Experimental Setup

Fig. 3.1 presents the trailer which is equipped with a current collector, an onboard rectifier as well as a resistive load. The trailer is designed to draw 300 kW from the SER and is equipped with 10 sliding contacts, each mounted on an arm in the current collector, to distribute the power drawn across multiple segments of the SER. During the testing procedure, the trailer is towed by a vehicle along the SER.

The current collector mounted on the trailer comprises a mechatronic system that integrates actuators, pulleys, wires, and springs. This system controls the movement of the arms of the current collector, where the sliding contacts are mounted, allowing them to be raised and lowered as charging is initiated or terminated. In addition, the arms are designed to automatically follow the electric road as the longitudinal frame on which the arms are mounted can both rotate and traverse across the electric road, as originally presented in Fig. 2.9 in Chapter 2, thus ensuring continuous energy transfer. The current collector is also engineered to apply a consistent con-

(a) Overview of the trailer.

(b) The underbody of the trailer, where the current collector is mounted. Figure taken from [20].

Figure 3.1: The trailer specifically designed for testing at the ERS demonstrator.

tact force on the segments. The trailer is equipped with a communication system that enables wireless activation of the segments in the electric road as it traverses over them.

To assess how the currents in the sliding contacts of the current collector depend on vehicle speed and contact quality over time, measurements were conducted with the trailer. In theory, assuming stable contact, the current should be evenly divided among each segment and sliding contact in the current collector. However, in reality, the quality of contact is not continuously stable, resulting in a changing distribution of currents within the current collector over time. To validate this expected outcome, the current is measured in each arm of the current collector to evaluate the distribution and magnitude of currents, which in turn allows for an assessment of contact quality per sliding contact.

Fig. 3.2 presents a basic schematic of the trailer with n arms, including the placement of current sensors. Note that the load current of the load resistor is also measured, allowing for an assessment of how the current and contact quality of each individual arm impact the total load current. Tamura current sensors [66] were employed to measure the current, and the data was logged using a DATAQ data logger [67]. Before the measurements were conducted, the contact forces on the sliding contacts were measured using a scale, with contact forces varying between 5 and 10 N among the sliding contacts.

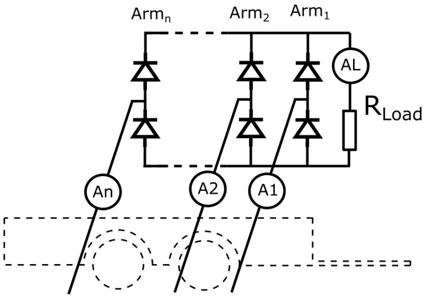

Figure 3.2: Conceptual schematic of the trailer with n arms.

3.2.2 Results of Magnitude and Distribution of Currents in the Current Collector

Fig. 3.3 presents the current for each arm in the current collector (A1-A3 top, A4-A6 middle, A7-A10 bottom), as well as the load current (AL). The trailer is towed by a car at a speed of approximately 18 km/h. As the trailer moves along the SER, the sliding contacts alternate between contact with segments that are either a) isolated, resulting in zero current flow, b) connected to the negative pole, resulting in negative current flow, or c) connected to the positive pole, resulting in positive current flow. The resulting rectified load current (AL) originates from the sum of currents of each sliding contact with the same segment polarity. The presented 10-arm current collector design demonstrates the advantage of using multiple arms in applications requiring high power, as the total power draw is distributed across multiple segments and sliding contacts.

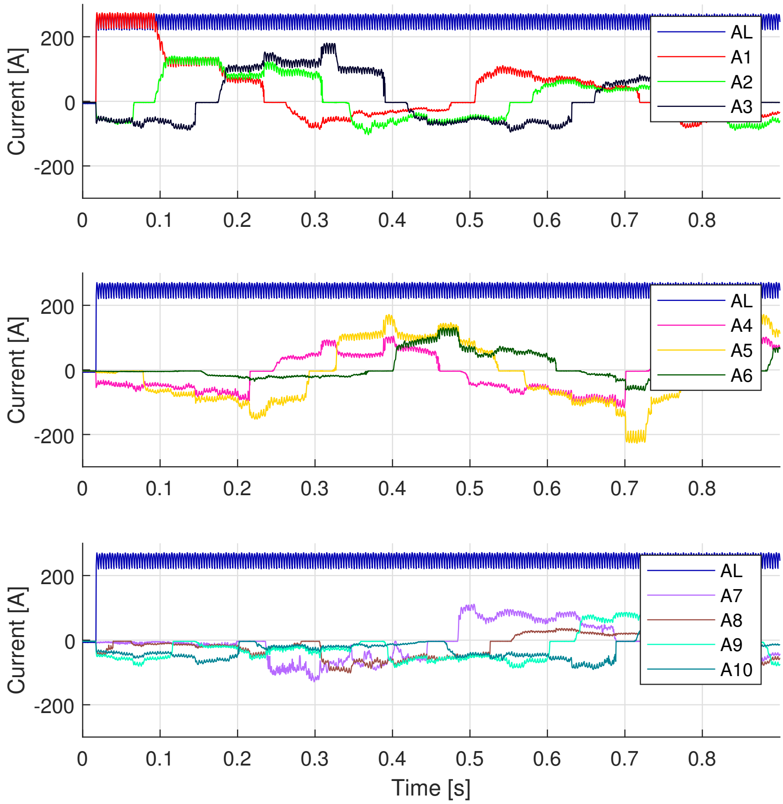

Figure 3.3: Measured current for each sliding contact in the current collector (A1–A3: top, A4–A6: middle, A7–A10: bottom) and the resulting rectified load current (AL). The figure is taken from [44].

After 0.02 s, arm A1 makes contact with the first active segment, enabling the full load current (positive current) to flow through the first arm of the current collector. Simultaneously, the return path for the current is shared between arms A2-A4 and A8-A10 (negative current), as these arms are in contact with segments connected to the negative pole of the SER at this time. Given that the distance between the arms in the current collector is 0.45 m and the length of each segment is 1 m, a maximum of three arms can maintain contact with a single segment (for example, A8-A10 at 0.02 seconds). After 0.13 seconds, the trailer has moved, allowing arm A2 to make contact with the same active segment as A1. As a result, the load current is now divided between A1 and A2. The return current is now distributed among arms A3-A5, which are on the same segment connected to the negative pole, and arm A10, which is in contact with a negative segment located further behind the segment that arms A3-A5 are in contact with.

In theory, if optimal contact is maintained, the current in a single sliding contact is expected to exhibit a repeating waveform. This is partially observed in currents A2 and A3, which can be considered examples of this repeating waveform under adequate contact conditions. The magnitude of currents A2 and A3 alternates periodically, depending on the varying contact status of other sliding contacts connected in parallel to segments with the same voltage.

Although the load current (AL) remains unaltered, local instances of poor contact occur. From 0.23 to 0.44 s in the bottom plot, current A7 appears to exhibit poor contact. Fig. 3.4 presents a zoomed-in view of currents AL, A2, A3, and A7 during this time duration. Current A7 has a discontinuous waveform shape, fluctuating greatly and even reaching zero at 0.405 s, despite that the corresponding arm of A7 is still located on the same segment. An additional indication of poor contact is that the waveform shape of current A7 does not resemble that of a rectified current, as observed in currents A2 and A3, which demonstrate adequate contact. While local variations in amplitude and waveform shape occur to varying extents in almost all arms shown in Fig. 3.3, it is noteworthy that the rectified load current (AL) remains unaffected

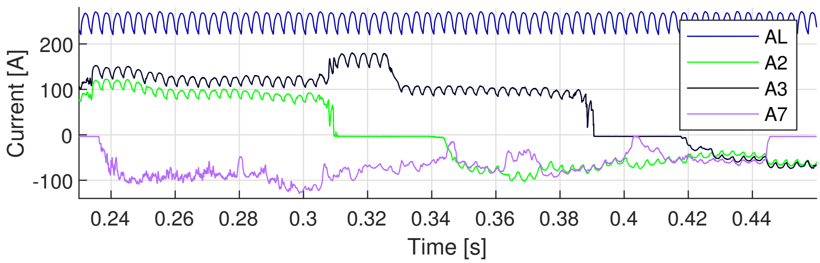

Figure 3.4: Zoomed-in view from Fig. 3.3 of measured currents for sliding contacts A2, A3, A7 and the load current AL between 0.23-0.44 s.

The fact that the load current (AL) remains constant and continuous highlights the benefits of the redundant design of a current collector with more than three arms. Not only does a larger number of adequately spaced contact points reduce the current load on each segment of the electric road, but it also decreases the risk of introducing conductive EMI into the load current. However, as shown in Fig. 3.3, poor contact can still occur within the arms of the current collector, increasing the risk of excessive contact losses and potential arcing that may go unnoticed in the load current. Although the load current itself remains unaffected, this localized poor contact can lead to issues with radiated EMI, impacting the ERS and its vicinity.

In Fig. 3.3, the risk associated with having only three sliding contact points is highlighted during the first 0.1 s, as the entire current load is dependent on the contact quality of arm A1 at this time. Consequently, if arm A1 experiences poor contact during this period, the power supplied to the trailer may be compromised.

To conclude, as demonstrated in Figs. 3.3 and 3.4, poor contact can easily occur. While it may not always affect the load current, it can still lead to severe consequences such as arcing and radiated emissions. Although the current collector in the trailer is still considered a prototype, which accounts for its partially imperfect performance, the measurements clearly indicate that substantial design improvements are required to establish more stable contact across all sliding contacts in the current collector. To improve the overall performance of the current collector, a deeper understanding of the characteristics of a single sliding contact is required, along with the identification of the factors that impact its performance the most.

3.3 Experimental Assessment of the Sliding Contact under Laboratory Conditions

To further evaluate the characteristics of a single sliding contact, this section examines the voltage drop, contact resistance, and frictional force of a sliding contact, as well as their dependence on speed, current, contact force, and contact material in a controlled laboratory environment. Performing the experiments in a laboratory setting allows for more practical, detailed and time-efficient testing, enabling a greater number of measurements to be conducted within a given time frame.

This section introduces an RTR that allows for the characterization of two sliding contacts at the same time. While the RTR is expected to deliver more refined measurements compared to those obtained from the ERS demonstrator, its primary objective is not to achieve high precision and accuracy in measuring voltage drop, arcing, or frictional force in relation to the detailed properties of the brushes or the contact surface of the segments. Rather, the RTR is intended to emulate the sliding contact and its behavior under conditions similar to those in the ERS demonstrator while eliminating uncontrollable factors inherent to the ERS demonstrator, as it is located on a public road. In previous work, various aspects of electrical contacts have been investigated, as outlined in [62]. Studies have been conducted on both static contact resistance [62, 68] and sliding contacts [62–64, 69], often in conjunction with contact wear. In [34], results are presented for the calculated contact resistance and the coefficient of friction using an earlier version of the same RTR as introduced in this thesis. These measurements were limited to speeds of up to 7.5 km/h and were carried out with solid metal blocks instead of metallic brushes. Moreover, the experiments included only one measurement per combination of material, contact force, speed, and current level, thus failing to account for variations of contact resistance, which, as discussed in the subsequent sections of this chapter, are inherent to sliding contacts in conductive ERS.

During the design of the experiments with the RTR, various efforts were made to minimize variability in the results by adjusting the experimental setup. Even minor mechanical adjustments, such as variations in contact force (ranging from 0.5 to 1 N) or small changes in the mounting angles of the brushes (in the order of a few degrees), were found to have a considerable impact on the observed contact resistance, arcing and friction force. As the mechanical system in the RTR was not sophisticated enough to handle these minor alterations, repeated measurements were conducted to partially mitigate their effects and highlight the natural variations in the results. Since conducting measurements with a large number of varying parameters becomes time-consuming, the experiments were limited to five consecutive measurements for each combination of contact force, current, and speed in order to capture the inherent variability in the results. Moreover, it became apparent that contact resistance and friction force are influenced by numerous factors, and the interactions between these factors remain unclear. Therefore, a comprehensive understanding of the factors influencing these phenomena necessitates further research, employing more advanced experimental methods and a greater number of measurements than those presented in this chapter. More sophisticated measurements, in combination with additional data collection, are the subject of future work and are beyond the scope of this thesis, as these experiments cannot be conducted with the RTR in its current state. Consequently, the experiments and results presented in this thesis should be regarded as preliminary with respect to a full understanding of the factors influencing contact resistance and friction forces in conductive ERS. The presented findings are intended to serve as a foundation for future research in the field of sliding contacts adapted for conductive ERS technology.

While the RTR offers multiple advantages over the demonstrator, measurements of voltage drop and current across the sliding contacts at the ERS demonstrator remain vital for assessing the contact conditions in a real-life ERS. Measurements conducted at the ERS demonstrator serve as a reference to determine whether the RTR can appropriately replicate the sliding contact conditions present in a real-life ERS. To account for the differences that may arise between the RTR and actual ERS conditions, the validity of the contact resistance obtained with the RTR is verified in terms of order of magnitude by comparing it with contact resistance derived from voltage drop and current measurements made using the trailer at the demonstrator. The comparison of resulting contact resistance originating from the RTR and the ERS demonstrator is outlined in the final section of this chapter.

3.3.1 Experimental Setup

Fig. 3.5 presents the RTR, which consists of a rotating disk equipped with a steel ring having the same cross-sectional area as the segments in the ERS demonstrator. The RTR is fitted with two sliding contacts in the form of steel brushes, similar to those used in the current collectors of the ERS demonstrator. A DC current source is connected between the two sliding contacts, enabling current to flow through one sliding contact, across the steel ring, to the other sliding contact, and back to the current source. The required contact force on each sliding contact is applied by placing weights on them using a seesaw-based mechanical system.

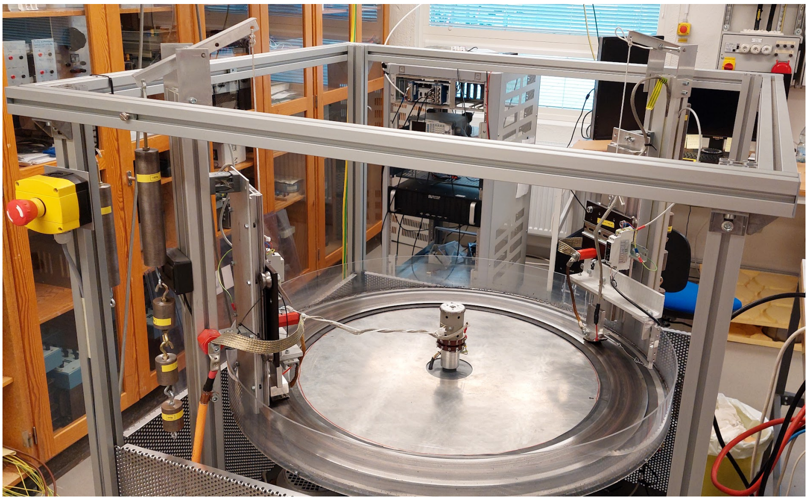

Figure 3.5: The RTR located in a laboratory environment.

Fig. 3.6 presents a conceptual overview of the selected parameters influencing the RTR. The red elements represent the sliding contacts. The circular symbol with an arrow connected between the sliding contacts represents the current source connected to them. The green arrows indicate the selected mechanical parameters that are assessed and influence the sliding contacts. The vertical arrows represent the applied downward forces on the sliding contacts, corresponding to the counteracting contact forces exerted to them, while the tangential arrows denote the measured pulling forces, which directly correspond to the counteracting frictional forces exerted on the sliding contacts. Finally, the green arc-shaped arrow represents the rotation of the entire rotating disk.

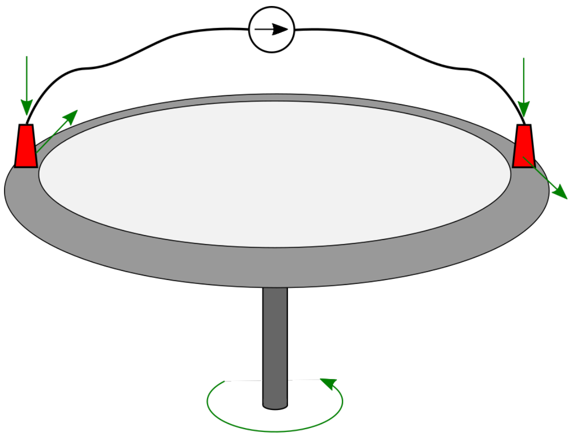

Figure 3.6: Conceptual overview of the considered parameters in the RTR. Red elements represent the sliding contacts and green arrows mechanical parameters.

In order to provide a stable continuous contact between vehicle and electric road, a specific contact force is necessary. However, the exact magnitude of the required contact force remains uncertain and is potentially influenced by several factors, including vehicle speed, contact material, surface area, current, and road unevenness. Additionally, the vertical motion dynamics of the vehicle, in conjunction with the behavior of its suspension system, must be considered when selecting the appropriate contact force. For the 10-arm current collector used in the trailer, the contact force ranged from 5 to 10 N among the sliding contacts. When using the RTR, the forces exerted to the sliding contacts are limited compared to those experienced in the ERS demonstrator, as dynamic forces resulting from the motion dynamics of the vehicle and its corresponding current collector are excluded. The RTR is specifically designed to allow the contact force to be set to predetermined values, thereby facilitating detailed measurements of the resulting contact resistance and friction force.

In the RTR, the contact force is controlled by employing a mechanical seesaw-based construction, as illustrated in Fig. 3.7, where counterweights are suspended to exert a constant downward force on the sliding contacts. The sliding contacts are mounted on a mechanical system with sliding bearings, allowing free vertical motion, thereby maintaining a constant contact force. The contact force is not logged continuously during a measurement but is measured prior to each measurement using a scale. Although transients may occur in the vertical forces over time due to unevenness in the surface or the steel ring and mechanical oscillations caused by the RTR, the mean value of the contact force is assumed to remain constant throughout the measurement procedure. This assumption is considered adequate, as only the mean values of voltage drop, current, and friction force are relevant for the assessment of contact resistance and friction force.

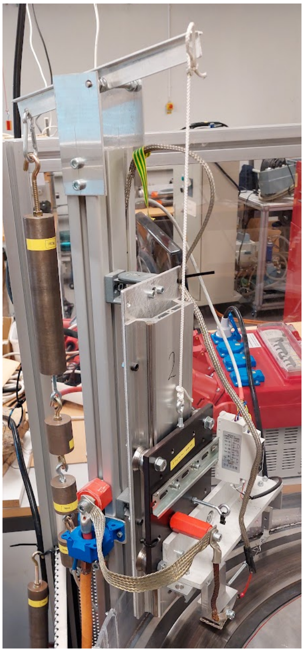

Figure 3.7: One of the two mechanical systems in the RTR where the sliding contacts are mounted. The sliding contact is attached to a vertical sliding bearing, and a downward force is applied to it using a seesaw-based mechanism.

The frictional forces originating from the sliding contacts are assessed by mounting the sliding contacts on a horizontally installed sliding bearing, as illustrated in Fig. 3.8. The sliding contacts themselves are attached horizontally to a steel wire, which is connected to a load cell (with the corresponding load cell amplifier [70, 71]). The mount for the brush of the sliding contact is attached to the sliding bearing via a smooth cylinder, allowing the sliding contact to rotate freely as it is pulled by the steel wire when the disk of the RTR is rotating. This setup is designed to isolate the frictional force to the steel wire.

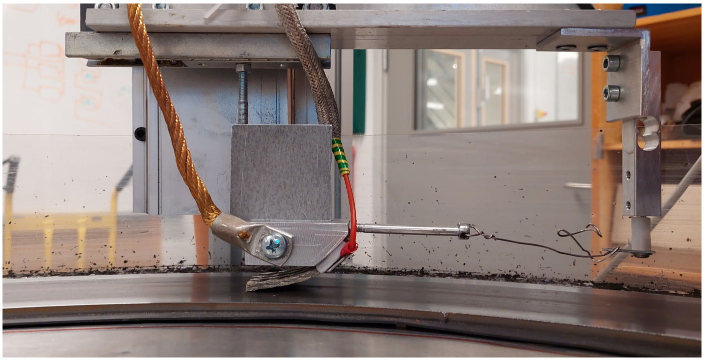

Figure 3.8: One of the two sliding contacts in the RTR. The sliding contact mount is attached to a horizontal sliding bearing and connected to a load cell via a steel wire, enabling the measurement of the friction force.

The exposed copper cable in Fig. 3.8 is the connection from the current source to the sliding contacts, and the red thinner cable is the connection for the voltage measurement. The voltage drop across the contact is measured between the brush, at the mounting point of the brush as shown in Fig. 3.8, and the steel ring. The connection for the voltage measurement point on the steel ring is facilitated by a slip ring, as seen in the middle of the disk in Fig. 3.5. To minimize the impact of the added resistance from the steel ring, copper wires were installed underneath the steel ring's circumference every 15 cm, resulting in minimal added resistance between the steel ring and the sliding contacts. The resistance of the brushes themselves is considered negligible compared to the resulting values of contact resistance.

Throughout the testing at the ERS demonstrator, two types of materials were used for the metallic brushes: copper and stainless steel. These materials were tested both separately and in combination as sliding contacts in various current collector configurations. The brushes were mounted in two different orientations, either across the threads or along the threads, relative to the segments. For the measurements conducted with the RTR, the brushes were aligned with their threads in the direction of the tangential motion of the rotating steel ring. This configuration was chosen because it resulted in the least variation in contact resistance.

During the establishment of the experiments with the RTR, it was discovered that the structural integrity of the brushes was sensitive to mechanical impact. The arbitrary nature of the brushes contributed significantly to variations in the results, as each measurement introduced distinct mechanical structures in every brush sample. This occurred because the bond between the threads would disperse unpredictably, resulting in each brush having a unique composition and shape. The alteration of the brushes structure also occurred during the preparation of the brush specimens and their attachment to the mounting positions on the RTR. This inherent variation led to significant differences between measurements, despite the same contact force, rotational speed, and current being set in the RTR. To mitigate this issue, each brush sample was taped at the attachment point (white tape, as seen in Fig. 3.9) to retain its structural integrity. The method of applying tape at the tip of every brush sample and aligning them parallel with the rotation of the steel ring was selected for the experiments conducted with the RTR, as this configuration resulted in the least variation in contact resistance between samples.

(a) Contact surface of 1 cm^2.

(b) Contact surface of 6 cm^2.

Figure 3.9: Two different surface areas of the sliding contact assessed using the RTR.

For each brush material, two contact surface areas were selected: 1 cm^2 and 6 cm^2. As the copper and stainless steel brushes had different moduli of elasticity and ductility, different downforces were applied to achieve the same contact area. For a surface area of 1 cm^2, a downforce of 7 N was required for the copper brush, while for the stainless steel brush, a downforce of 17 N was required. For the surface area of 6 cm^2, a downforce of 14 N was required for the copper brush, and 31 N for the stainless steel brush. In Fig. 3.9, the contact surfaces of 1 cm^2 and 6 cm^2 for the stainless steel brushes are shown. Note, that although the contact surface area was selected prior to the measurements, this surface area will be altered during the measurements, as heat due to current and friction will increase the mechanical ductility of the brushes, thus expanding their surface area. The brushes have a cross-sectional area of $50\,\mathrm{mm}^2$, a width of 30 mm, and a length of 55 mm.

The voltage drop across the contacts, speed, current, and frictional forces were logged using a NI CompactRIO-based system [72, 73]. The current was measured using a LEM LF 505-S current sensor [54], and the voltage was measured using an isolated voltage amplifier [74]. The rotational speed of the rotating disk was measured using an inductive sensor.

Although the RTR was deemed adequate in emulating the sliding contact conditions present at the ERS demonstrator during the establishment of the experiments, it remains a compromise due to the following limitations:

1. **Radial Contact Surface**: The basic construction of the RTR is based on a rotating disk, in contrast to the longitudinal arrangement of segments used in the ERS demonstrator. This difference in design accelerates the effects of contamination on the surface of the steel ring. During the design of the experiments, it was observed that a metallic oxide formed on the surface of the steel ring during testing, particularly under poor contact conditions and arcing phenomena. These oxides exhibited lower electrical conductivity than the metallic brushes and surface of the steel ring, leading to an increase in contact resistance. As the same surfaces on the steel ring and brush becomes repeatedly contaminated with metallic oxides, a snowball effect occurs, causing rapid accumulation of contamination, which is different from the more gradual contamination that would occur in the longitudinal electric road.

2. **Mechanical Oscillations**: The RTR is not a high-precision setup, and its limited radius of 0.4 meters requires rotational speeds greater than 333 rpm to simulate vehicle speeds of 50 km/h or more. At these rotational speeds, the RTR becomes unbalanced, causing vibrations within its mechanical structure. These vibrations inherently affect the forces exerted on the sliding contacts, and, consequently, the measurements of voltage drop, current, and friction force. At speeds exceeding 333 rpm, the impact of mechanical oscillations becomes so excessive that the sliding contacts become unstable, rendering them unrealistic compared to the sliding contact conditions in the

ERS demonstrator. As a result, the RTR experiments are limited to vehicle speeds corresponding to approximately 50 km/h.

3. **Absence of a Suspension System**: For a BEV equipped for ERS operation, vehicle dynamics inherently influence the forces exerted on the current collector, which in turn affect the sliding contacts. The suspension system of the vehicle, its current collector, and the evenness of the road where the ERS is installed all contribute to these forces. In contrast, the only factors influencing the results in the RTR, in terms of suspension, is the inherent elasticity of the brushes and the weight of the sliding contact mount, which holds the brushes and weighs approximately 350 g.

4. **Limitations of the Current Source**: In a real ERS, in the event of contact loss, the voltage across the sliding contact is equal to the ERS DC voltage (650 V DC for the demonstrator). When poor contact occurs, the voltage across the contact will intermittently be equal to this DC voltage, provided no other sliding contact in the current collector is in contact with a segment of the same voltage. However, in the RTR, a power supply is used as a current source, which means that when contact loss occurs, the voltage across the contact is altered only as quickly as the control circuit of the power supply allows. Moreover, the open-circuit voltage of the power supply is limited to 30 V DC [79]. Consequently, the RTR does not fully replicate the complete electrical dynamics of the real ERS demonstrator during contact loss.

Despite these limitations and the fact that the RTR is not a high-precision experimental setup, it is still expected to adequately emulate the sliding contact conditions present in a real ERS. As such, it is expected to be used to assess contact resistance and friction force in detail. This is in line with the aim of the RTR, as in real-life scenarios, the sliding contacts are far from a controlled environment, and the current collectors where the sliding contacts are mounted are not high-precision mechanical systems.

3.3.2 Methodology and Parameter Selection

The primary aim of the presented measurements using the RTR is to characterize the contact resistance and friction force under varying speeds, currents, and contact surface areas. Although the RTR does not have the capability to directly measure arcing, qualitative observations of arcing events during the tests were noted and are presented as part of the results. The assessed sliding contacts consist of metallic brushes made of copper and stainless steel. For each material, two levels of contact force were applied, resulting in contact areas of either 1 cm^2 or 6 cm^2. Measurements were carried out at speeds of 10, 30, and 50 km/h under current levels of 10, 30, 50, and 80 A.

The current flowing through a single sliding contact in a current collector is an AC current that depends on speed, as observed in the previous section of this chapter and shown in Fig. 3.3. However, due to limitations in time, no power supply capable of replicating this AC current was available when the experiments with the RTR were conducted. As a result, a constant DC current was selected as a means of simplification and was deemed adequate to emulate the sliding contact conditions present at the ERS demonstrator. Moreover, during the setup of the experiments with the RTR, a constant current was preferred, as the voltage drop across the sliding contacts oscillated due to mechanical vibrations of the RTR, and thus a constant current contributed in providing results with less variation.

Fig. 3.10 illustrates the simulated current from a three-arm current collector on a vehicle drawing 40 kW at a speed of 20 km/h, simulated using the simulation model described in detail in Chapter 5. This simulation highlights the waveform shape of a current flowing through one sliding contact during favorable contact conditions. The current flowing through one arm of the current collector is AC and its corresponding RMS value is theoretically approximately 0.78 times the mean rectified total DC current after the onboard rectifier for a 3-arm current collector, based on the simulated currents shown in Fig. 3.10, assuming a 6-pulse passive rectifier is used in the rectifier station.

The DC current levels of 10, 30, 50, and 80 A were selected as they represent the current flowing through a single sliding contact for a BEV drawing powers of approximately 9, 25, 42, and 67 kW, respectively, using a three-arm current collector. For example, a DC current of 10 A, representing the RMS value of the AC current through a single sliding contact, results in a total rectified current of 13 A after the onboard rectifier, leading to a

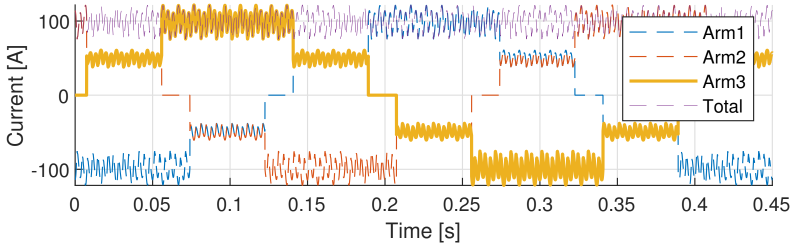

Figure 3.10: Simulated currents in a three-arm current collector. Arm 1-3 are represented in blue, red (dashed lines), and yellow (solid highlighted lines), respectively, along with the load current, labeled 'Total' (purple dashed lines), after the onboard rectifier.

power draw of approximately 9 kW at an electric road DC voltage of 650 V. Similarly, an RMS current of 80 A through one sliding contact yields a rectified current of 103 A, corresponding to a power draw of 67 kW. A power level of 9 kW corresponds to the magnitude of power consumption that a passenger car might require when cruising at urban speeds or even on rural roads, considering only propulsion and auxiliary systems. In contrast, a power draw of 67 kW is more representative of a passenger EV operating on highways, with energy supplied to propulsion, auxiliary systems, and battery charging. These assumptions are discussed in greater detail in Section 4.4 in Chapter 4. A heavier BEV, such as a truck, is expected to require significantly higher power levels than 67 kW from an ERS. However, for such vehicles, the current collector can be extended by increasing the number of arms, provided the vehicle's underbody surface area is sufficient to accommodate larger current collectors, as a greater number of arms facilitates a higher power draw.

While a single sliding contact in a three-arm current collector and corresponding segment in the electric road is capable of handling peak currents exceeding 200 A, distributing the energy transfer across multiple segments offers two main advantages. Firstly, it reduces the risk of contact loss between the BEV and the ERS, as multiple sliding contacts provide greater redundancy in maintaining continuous contact. Secondly, using more than three sliding contacts in a current collector reduces overall losses, since the current per arm decreases and the losses are proportional to the square of the current, as elaborated in the introduction in Chapter 4. Consequently, for vehicles with sufficient space in their underbody to accommodate a current collector with more than three sliding contacts, especially when high power demands are involved, using additional arms can lower the current per segment and reduce total losses. This is particularly relevant for heavier BEVs, such as buses and trucks, which typically have larger batteries and higher power consumption compared to passenger cars. To sum up, the selected DC current levels of 10, 30, 50, and 80 A are appropriate, as they represent a reasonable range of currents for one arm in a current collector, relevant for both passenger cars and heavier BEVs operating on an ERS.

The rotational speeds were selected to correspond to 15, 30, and 50 km/h. The speeds of 15 and 30 km/h were chosen because they fall within the range of speeds that could be validated using the ERS demonstrator, while 50 km/h was selected to assess how contact resistance, frictional force, and arcing are influenced at higher speeds beyond the demonstrator's limitations. Although investigating speeds above 50 km/h is relevant, the RTR is constrained to rotational speeds equivalent to a maximum of 50 km/h, as higher speeds caused excessive mechanical oscillations, which inherently affected the measurements.

For each combination of speed, current, and contact force five consecutive measurements were conducted using the same set of brushes. During each measurement, the current was set to the predetermined level, and the RTR was rotated for 1 minute and 30 seconds. After stopping the rotation, the current was switched off after a few seconds. A logging time of 1 minute and 30 seconds was sufficient in order to obtain stable values of friction force, voltage drop, and current, which were then used to calculate mean values for contact resistance and friction force based on the logged variations.

3.3.3 Experimental Results of the Sliding Contact

Fig. 3.11 presents the fifth measurement for the combination of a copper brush with a 14 N contact force (corresponding to a 6 cm^2 contact area), current set to 30 A, and a rotational speed equivalent to 15 km/h. The upper plot presents the voltage drop across contact 1 (blue) and contact 2 (red) which are related to the left y-axis, and the current in the circuit (green) is related to the right y-axis. The middle plot presents the calculated contact resistance for contact 1 (blue) and contact 2 (red), derived from the voltage drop divided by the current. In the lower plot, the friction forces from sliding contact 1 (blue) and contact 2 (red) are shown along with the emulated speed of the RTR (green). The friction forces are related to the left y-axis and the emulated speed of the RTR is related to the right y-axis. The voltage drop, current, calculated contact resistance, and friction forces are presented with a 100 ms moving average filter. As voltage and current were continuously logged throughout the measurement, the static contact resistance is calculated both before and after the rotation of the RTR. For each measurement, the mean value of the static contact resistance was computed by including a few seconds of logged voltage and current taken before and after the rotation was conducted. This approach is considered an adequate method for emulating the static contact conditions from a real ERS, as it partially accounts for wear on the brushes.

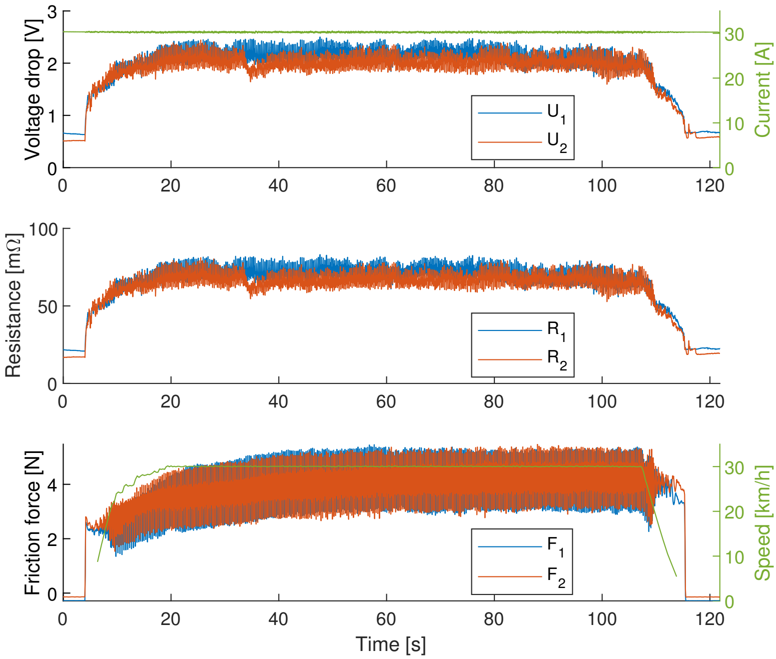

Figure 3.11: The upper plot shows the voltage drop across the two sliding contacts (blue line for Contact 1 and red line for Contact 2, corresponding to the left y-axis) and the current (green line, corresponding to the right y-axis) as measured by the RTR. The middle plot presents the calculated contact resistance for Contacts 1 (blue) and 2 (red), derived from the data in the upper plot. The bottom plot displays the measured friction forces for Contacts 1 and 2 (blue and red lines, corresponding to the left y-axis) and the calculated emulated speed (green line, corresponding to the right y-axis).

In this thesis, contact resistance is defined as the voltage drop across the sliding contact divided by the current. Previous research, including [69], has demonstrated that the voltage drop over the sliding contact in carbon brushes for slip rings is not linearly proportional to the current. Although this phenomenon is particularly relevant for sliding contacts in a conductive ERS, it remains an area for future research as the RTR is focused on producing more order-of-magnitude-oriented results. Given the generalized nature of the results provided by the RTR, contact resistance in this thesis is simplified as the voltage drop over the contact divided by the current.

As mentioned at the end of Section 3.3.1, a suspected metal-oxide layer accumulates on both the surface of the steel ring and the contact surfaces of the stainless steel and copper brushes. The occurrence of this contamination was more prominent under poor contact conditions, intense arcing, and prolonged operation. Additionally, for the copper brushes, smearing of copper onto the ring surface was observed. Fig. 3.12 presents the copper brushes used after five consecutive measurements from Fig. 3.11, which were conducted with a contact force of 14 N, a current of 30 A, and a rotational speed of 30 km/h. The darker regions on the brush surfaces correspond to areas where the suspected metal-oxide deposits were most prominent.

(a) Brush 1 **(b)** Brush 2

Figure 3.12: One set of sliding contacts in the form of copper brushes after five consecutive measurements.

To analyze the materials formed and deposited on the brushes, a preliminary Scanning Electron Microscopy analysis was conducted using a Tescan Mira-based setup [75]. The analysis revealed that material from the steel ring had adhered to the contact surfaces of both the copper and stainless steel brushes. The adhered material consisted primarily of ferric oxide (Fe_2O_3), along with residual sliding contact materials that remained on the surface of the steel ring from previous experiments.

As ferric oxide exhibits a significantly higher resistivity (in the range of $10^{-3}\,\Omega$m) [76] compared to copper and stainless steel (1.68×10^{-8} Ωm and 6.9×10^{-7} Ωm, respectively) [77], this confirms the hypothesis that the contamination of the contact surfaces increases the contact resistance. This observation provides a credible hypothesis for the increase in contact resistance over time during the measurements, which was more rapid under poor contact conditions and even more pronounced in the presence of arcing. The heat generated under these conditions is believed to accelerate the formation of ferric oxide. This adhesive process between the brushes and the steel ring, driven by heat from poor contact, arcing, and prolonged use, is believed to play a critical role in the degradation of contact performance.

To mitigate this contamination during the experiments, the surface of the steel ring was cleaned with a 100 grit sandpaper between each measurement combination, while the brushes remained unaltered throughout the five consecutive measurements. This method was deployed to minimize exaggerated contamination effects caused by the radial design of the RTR, as discussed in the previous subsection. The brushes were kept unchanged to replicate the conditions present in the ERS demonstrator, where the brushes would have experienced wear over time. Moreover, this approach was selected to capture any variations in contact resistance over time, including observations of potential phenomena such as wear-in trends and drifts in the results. It was concluded, by means of testing, that five consecutive measurements with the same brush would be sufficient to determine whether such trends were present. Although performing additional measurements for each combination of current, speed, contact force, and material could potentially yield more conclusive evidence of these trends, it was deemed impractical due to the significant extra time it would require.

The wear on the brushes and the surface of the steel ring resulting from the experiments is considered insignificant compared to the expected wear that the brushes and the contact surfaces of the segments in a real ERS would be subjected to. The total duration of a single measurement corresponds to an estimated travel distance of approximately 0.4 to 1.4 km, depending on speed. This suggests that the observed wear, as well as the contaminating effects of oxidation, on the brushes in the RTR is expected to be significantly more pronounced during ERS operation in real-world applications. Similarly, regarding the contact surface of the steel ring, a rotational speed of 100 rpm (15 km/h) during the measurement period is equivalent to approximately 180 vehicle passages, while 333 rpm (50 km/h) corresponds to about 600 vehicle passages, based on the assumption that one rotation represents a single vehicle traversing a segment. Therefore, the cumulative surface wear measured during the experiments remains minimal compared to the expected wear that a segment would be subjected to in a real ERS.

In the remaining figures of this subsection (Figs. 3.13 to 3.20), two figures are presented for each combination of material and contact force. The first figure shows the resulting contact resistance, while the second illustrates the frictional forces of the two sliding contacts in the RTR, denoted as contact 1 (blue) and contact 2 (red). In the figures, "1" represents the first measurement, and "5" denotes the final measurement. This numbering convention was chosen because an increase in contact resistance over time was commonly observed during the measurements. However, both contact resistance and arcing exhibited highly variable behavior. In some instances, an increase occurred during one of the five consecutive measurements and persisted throughout the remaining series. Conversely, there were also instances where a decrease in contact resistance and/or arcing intermittently appeared in one of the five measurements, and then in the remaining measurements, the results of contact resistance and/or arcing reverted to the original value in the subsequent measurements.

In the process of establishing the experimental setup and conducting initial tests, arcing was frequently observed. Arcing was subjectively graded on a scale from 1 to 3 based on visual observations, as no direct method for measuring arcing intensity was available. The grading of arcing is illustrated in the figures using varying line lengths: 1 represents minimal arcing (shortest line), 2 signifies moderate arcing, and 3 denotes severe arcing (longest line), with noticeable detachment of brush threads.

In the top plot of each figure presenting contact resistance, the static contact resistance is shown. Since the static contact resistance was calculated from measurements taken before and after each dynamic contact resistance measurement, the figure also includes information about the arcing intensity that occurred during each dynamic contact resistance measurement, which impacts the corresponding static contact resistance. The arcing intensity after each calculated static contact resistance is illustrated using the previously described grading system, with longer lines indicating that more intense arcing occurred during the corresponding dynamic contact resistance measurement. This representation aims to highlight any potential correlation between the degree of arcing to which a brush is subjected (and, by extension, the resulting wear and oxide formation caused by the arcing) and its resulting static contact resistance.

Copper Brushes

In Fig. 3.13, the results of the calculated contact resistance for copper brushes with a contact force of 7 N (corresponding to a contact surface area of 1 cm^2) and current levels of 10, 30, 50, and 80 A are presented. The first plot displays the static contact resistance, while the second, third, and fourth plots correspond to rotational speeds of 15 km/h, 30 km/h, and 50 km/h, respectively.

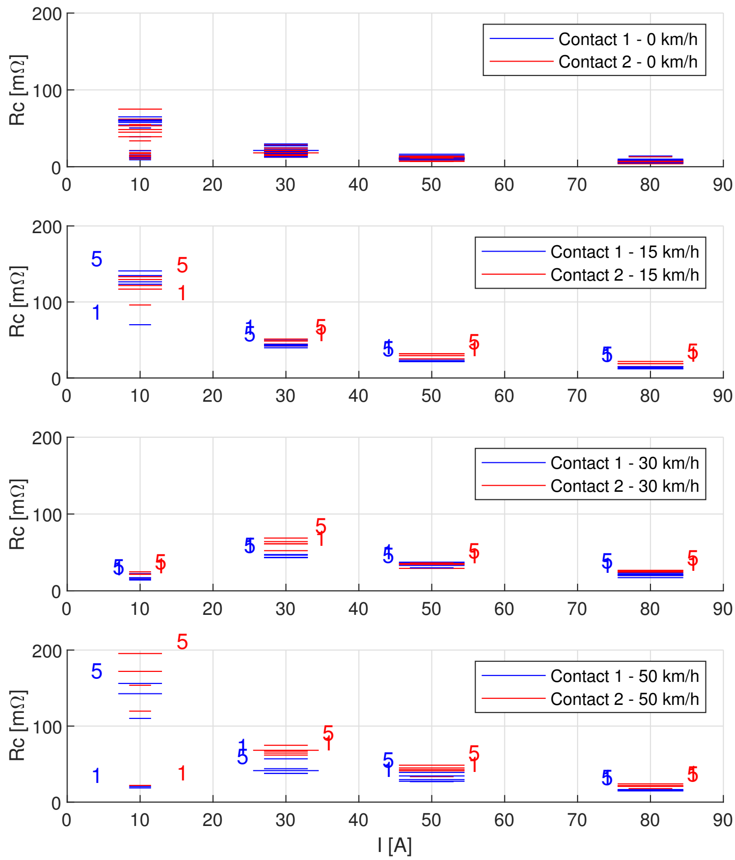

Figure 3.13: Calculated contact resistance for copper brushes (contact 1 in blue and contact 2 in red) with a contact force of 7 N corresponding to a 1 cm^2 contact area. The horizontal length of the lines represents the observed arcing intensity.

In the second and fourth plots, which present contact resistance at speeds of 15 and 50 km/h, at currents of 10 A both contact resistance and arcing increase gradually with each measurement. As the calculated static contact resistance is influenced by arcing and wear occurring during the dynamic experiments this trend can also be observed in the static contact resistance indicating that the wear and contamination of the brushes increases both static and dynamic contact resistance. In contrast, the third plot, which represents a current of 10 A at a speed of 30 km/h, does not display the same behavior, as contact resistance remains fairly constant and no arcing occurs, resulting in lower contact resistance of 14-25 mΩ. Consequently, the results for the static measurements in this case also showed low contact resistance of 11-20 mΩ, as minimal wear and oxide formation were generally associated with good contact and reduced arcing. A general trend is noted when the current exceeds 30 A: regardless of speed, more intense arcing is observed, occurring either continuously throughout the measurements or intermittently.

Overall, higher currents result in lower contact resistance. Higher speeds tend to result in both higher contact resistance and greater variability for currents of 10, 30, and 50 A, with the exception of 10 A at 30 km/h, as previously mentioned. However, for currents of 80 A less variation and approximately constant contact resistance is observed with increasing speed, with static contact resistance values ranging from 5-13 mΩ. For speeds ranging from 15 to 50 km/h, contact resistance remains relatively stable, varying between 12 and 27 mΩ. Although arcing persists, improved contact resistance is observed. This is believed to be due to the fact that higher currents and speeds contribute to increased heat, which leads to greater mechanical ductility of the brushes, resulting in larger contact surfaces and consequently reduced contact resistance. In terms of arcing, all combinations except for a speed of 30 km/h and a current of 10 A exhibit arcing. The reason behind the anomaly observed in contact resistance and arcing for the combination of 10 A current at a speed of 30 km/h remains unknown. One possibility is that this behavior stems from the arbitrariness of the brushes. Another theory is that the mechanical oscillations of the RTR associated with this particular combination of speed and current were favorable for the quality of contact in this case.

Fig. 3.14 presents the corresponding measurements of friction force for the dynamic contact resistance shown in Fig. 3.13. In general no clear trends are observed in relation to current, arcing, or speed with respect to friction force. Additionally, no significant variations in friction force are observed which can be attributed to wear or contamination of ferric oxide on the contacts. It is possible that trends may emerge if additional measurements per brush pair are conducted. With a contact force of 7 N, the friction force between the brush and the contact surface ranges from 1.5–3.5 N.

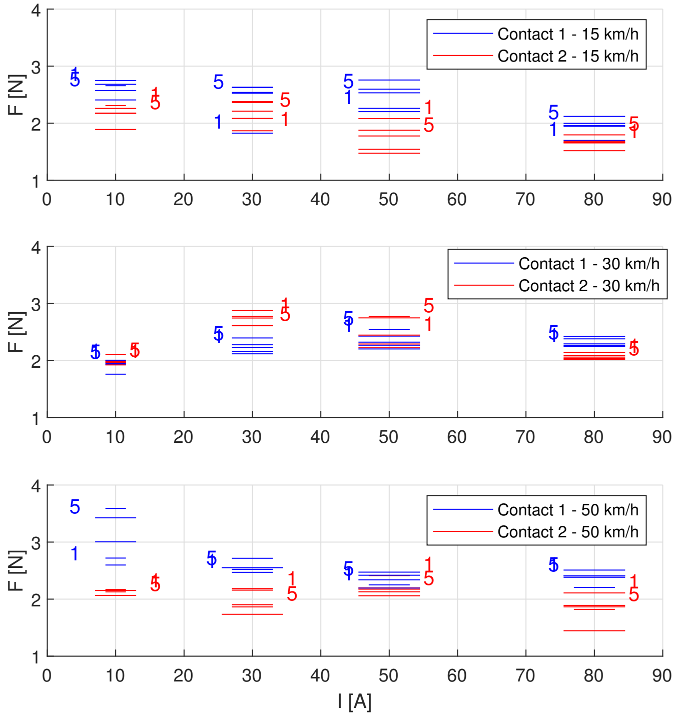

Figure 3.14: Measured frictional force for copper brushes (contact 1 in blue and contact 2 in red) with a contact force of 7 N corresponding to a 1 cm^2 contact area. The horizontal length of the lines represents the observed arcing intensity.

Fig. 3.15 presents the calculated contact resistance for copper brushes under a contact force of 14 N (corresponding to a contact surface area of 6 cm^2) at speeds of 0, 15, 30, and 50 km/h and currents of 10, 30, 50, and 80 A. In general, the increased contact force reduces variations in contact resistance, particularly evident for currents of 30 and 50 A at speeds of 15, 30, and 50 km/h. In addition, arcing is overall also slightly reduced under these combinations of currents and speeds. However, for currents of 10 A and speeds of 15 and 50 km/h the calculated contact resistance still exhibits significant variations.

At a speed of 15 km/h and a current of 10 A, the first measurement shows significantly more arcing than the subsequent ones, with the contact resistance gradually increasing for each measurement. This highlights that during the wear-in phase of the sliding contact, arcing can initially occur and then decrease as resistance gradually increases. In contrast, at a speed

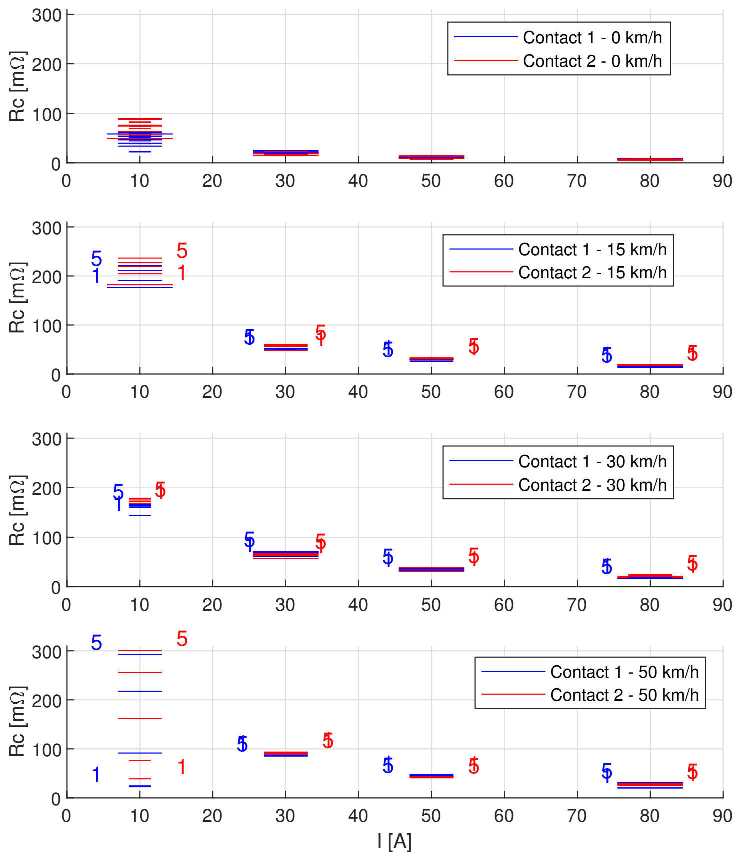

Figure 3.15: Calculated contact resistance for copper brushes (contact 1 in blue and contact 2 in red) with a contact force of 14 N corresponding to a 6 cm^2 contact area. The horizontal length of the lines represents the observed arcing intensity.

of 50 km/h, the opposite is observed: no arcing is present during the initial measurements, but it occurs in later ones, coinciding with a significant increase in contact resistance from 30 mΩ to 300 mΩ. This rapid increase in contact resistance highlights a so-called 'snowball effect,' where poor contact quality over time leads to a greater buildup of contamination (in the form of ferric oxide), which accelerates arcing, increases contact resistance and heating, and causes further contamination and degradation of the contact.

The wear-in phase of the sliding contact at currents of 10 A is believed to result from the fact that the brushes are not sufficiently heated to mold their contact surface against the contact surface as effectively as they do at higher currents which produce more heat. This results in poorer contact and greater variations in contact resistance at currents of 10 A. However, the combination of 10 A and a speed of 30 km/h, as previously discussed and observed in Fig. 3.13, demonstrates an anomalous stable contact with no arcing.

In general, the values of contact resistance for currents of 50 A and 80 A do not differ significantly under varying applied contact forces, as seen when comparing Fig. 3.15 and Fig. 3.13. For currents of 80 A with a contact force of 14 N, the static contact resistance is as low as 5–8 mΩ, while at a speed of 15 km/h, the resistance ranges between 14–20 mΩ. At speeds of 30–50 km/h, the contact resistance stabilizes at approximately 16–30 mΩ. Whereas in Fig. 3.13 with a contact force of 7 N for currents of 80 A the static contact resistance is 5-13 mΩ, while at a speed of 15 km/h, the resistance ranges between 12–22 mΩ. At higher speeds of 30–50 km/h, the contact resistance ranges between 16–27 mΩ.

However, the increased contact force appears to contribute to a reduction in the intensity of arcing. As shown in Fig. 3.15, only moderate arcing is observed at currents of 50 A and speeds of 15 and 50 km/h, compared to Fig. 3.13 with a contact force of 7 N, where most measurements with 50 A present severe arcing. This might be attributed to the impact that the increased contact force has on mitigating the mechanical oscillations that occur at higher speeds, thereby dampening arcing effects and minimizing variations in contact resistance at these speeds.

The corresponding friction forces for a contact force of 14 N, under the combinations of currents and speeds illustrated in Fig. 3.15, are shown in Fig. 3.16. As previously noted, no apparent trends in friction force can be observed in relation to speed and current. With an increased contact force of 14 N, the friction forces are within the range of 3–7 N.

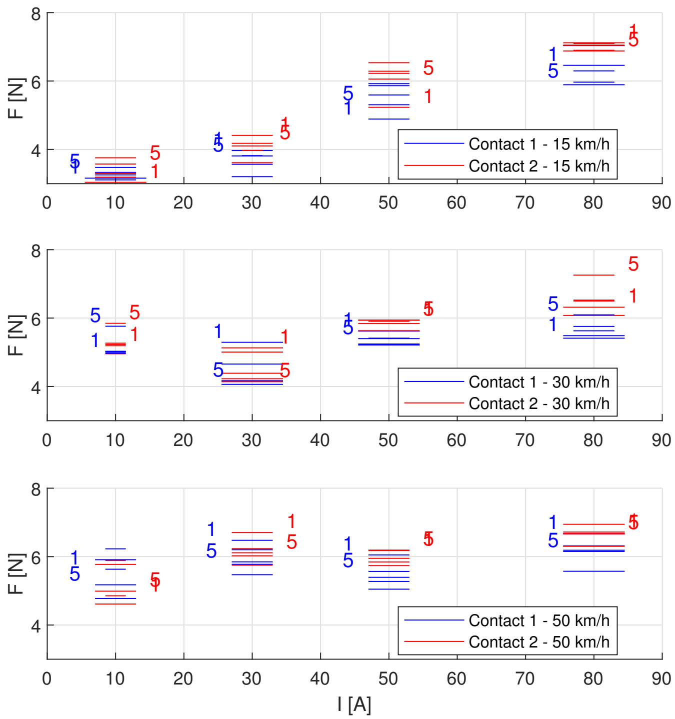

Figure 3.16: Measured frictional forces for copper brushes (contact 1 in blue and contact 2 in red) with a contact force of 14 N corresponding to a 6 cm^2 contact area. The horizontal length of the lines represents the observed arcing intensity.

Stainless Steel Brushes

Fig. 3.17 presents the calculated contact resistance for stainless steel brushes with a contact force of 17 N (corresponding to a contact surface area of 1 cm^2), currents of 10, 30, and 50 A and speeds of 0, 15, 30, and 50 km/h. Compared to copper brushes, stainless steel brushes generally performed better in terms of arcing, with no arcing observed at 10 A and with lower variations in contact resistance. However, arcing intensified rapidly at 30 A and speeds of 15–50 km/h. At currents of 50 A and speed of 30 km/h, the experiments had to be terminated due to excessive arcing, which posed a fire hazard. Measurements at 50 A and 50 km/h, as well as at 80 A, could not be conducted for the same reasons.

In general the contact resistance is higher compared to Figs. 3.13 and 3.15. Despite the occurrence of arcing, the contact resistance values remained

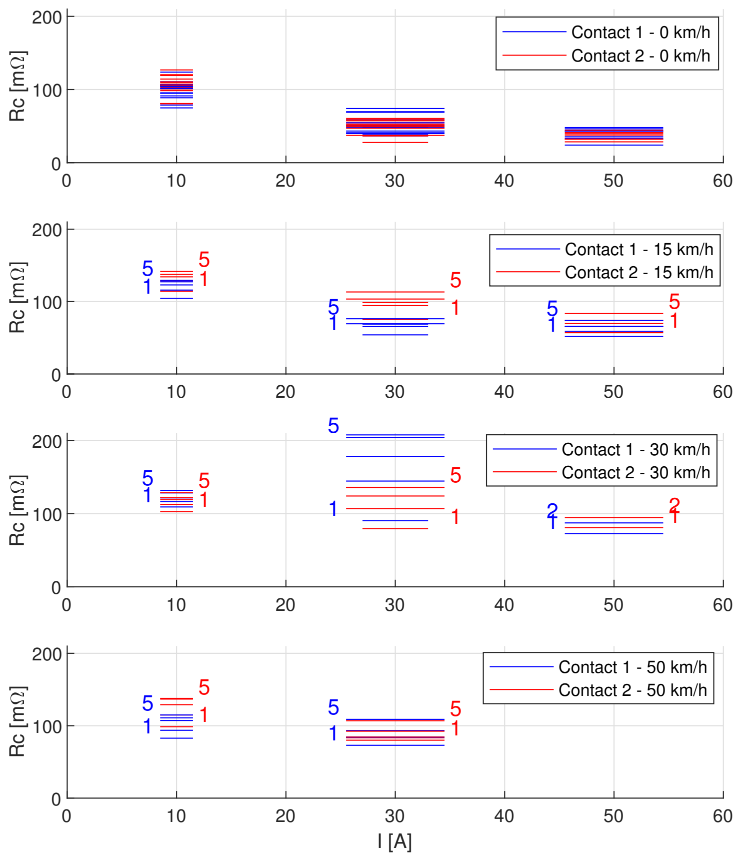

Figure 3.17: Calculated contact resistance for stainless steel brushes (contact 1 in blue and contact 2 in red) with a contact force of 17 N corresponding to a 1 cm^2 contact area. The horizontal length of the lines represents the observed arcing intensity.

within a similar order of magnitude to those observed for copper brushes in some cases, such as 60–90 mΩ for 50 A at a speed of 15 km/h. This suggests that while arcing does not necessarily lead to excessively high contact resistance, it still poses significant risks, including excessive heating, potential fire hazards, and the generation of radiated electromagnetic emissions. Although the heat generated by arcing is expected to promote oxide formation and thereby increase contact resistance, the observed increase in contact resistance is not significant in this case. The underlying reasons for this discrepancy remain unclear.

Fig. 3.18 presents the corresponding friction forces for the steel brushes with a contact force of 17 N. Once again, no clear trends in friction force related to speed and current can be observed. The resulting frictional forces range from 4 to 7.5 N.

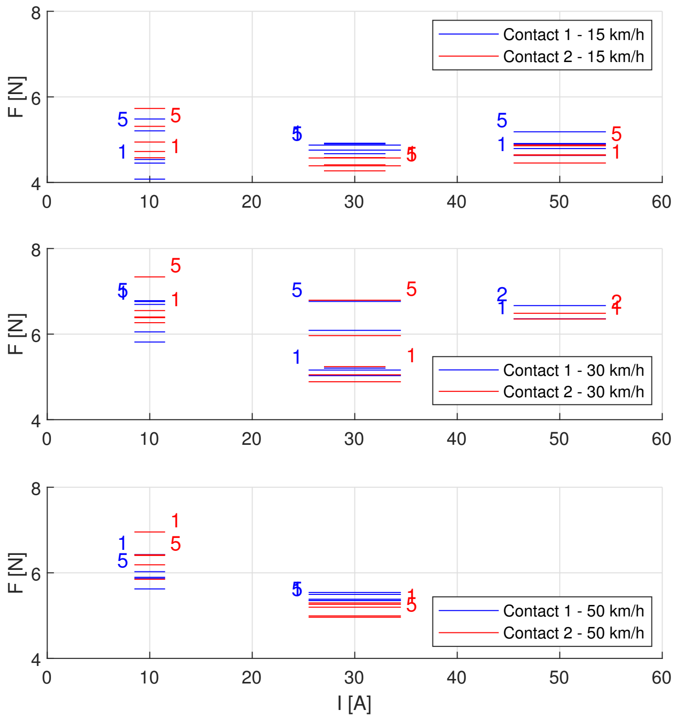

Figure 3.18: Measured frictional forces for stainless steel brushes (contact 1 in blue and contact 2 in red) with a contact force of 17 N corresponding to a 1 cm^2 contact area. The horizontal length of the lines represents the observed arcing intensity.

Fig. 3.19 presents the calculated contact resistance for stainless steel brushes with an applied contact force of 31 N (corresponding to a contact surface area of 6 cm^2), evaluated at currents of 10, 30, 50, and 80 A, with speeds of 0, 15, 30, and 50 km/h. Stainless steel brushes with a contact force of 31 N demonstrate superior performance in mitigating arcing compared to the other combinations of brush material and contact force. At a current of 10 A, no arcing is observed, and the contact resistance decreases on average from approximately 125 to 90 mΩ with increasing speeds of 15 to 50 km/h. Similarly, for 30 A, no arcing is detected. The average contact resistance at this current level is lower than at 10 A, ranging from 25 to 75 mΩ.

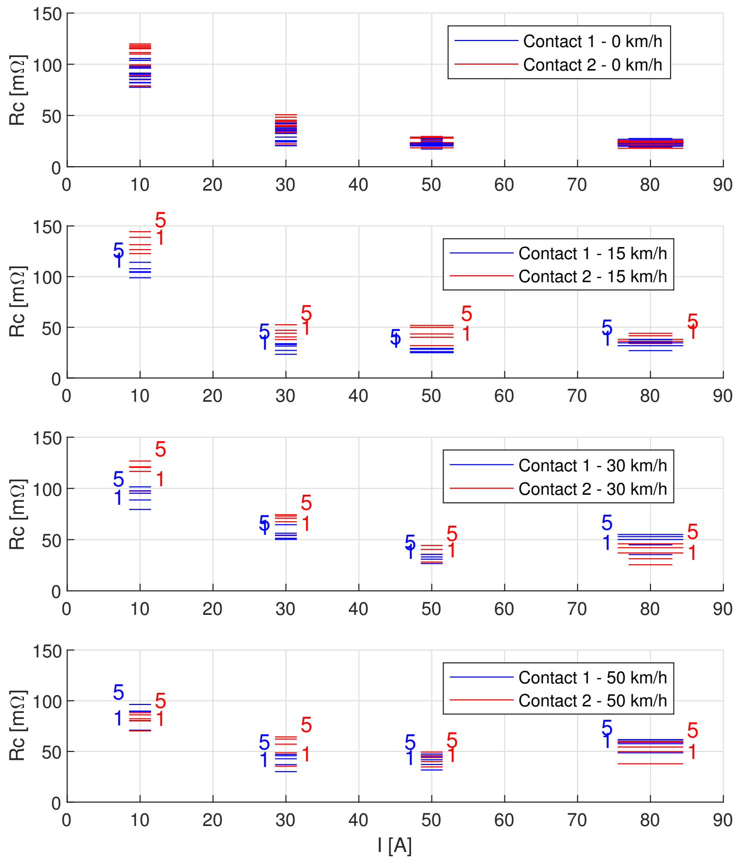

Figure 3.19: Calculated contact resistance for stainless steel brushes (contact 1 in blue and contact 2 in red) with a contact force of 31 N corresponding to a 6 cm^2 contact area. The horizontal length of the lines represents the observed arcing intensity.

At 50 A, arcing occurs only at a speed of 15 km/h, and the range of contact resistance is very similar to that observed at 30 A. At 80 A, however, arcing occurs, accompanied by a slight increase in contact resistance at speeds of 30 and 50 km/h. This suggests that higher current levels require more stable contact conditions than lower current levels to prevent arcing. The phenomenon of increased contact resistance at these high current levels is believed to be attributed to the excessive heating caused by the increased current, which accelerates the oxidation of the contacts.

Although stainless steel brushes may not achieve the lowest contact resistance, their performance in the speed range of 15–50 km/h and currents of 50 and 80 A with a contact force of 31 N yields contact resistance values between 25–50 mΩ. This low contact resistance is comparable to that of copper brushes with a contact force of 14 N, which exhibit slightly lower contact resistance values ranging from 13 to 30 mΩ under the same conditions, although with more frequent arcing.

The corresponding friction forces associated with the stainless steel brushes with a contact force of 31 N are presented in Fig. 3.20. As expected, given that the contact force of 31 N is significant compared to the other materials and contact force values presented, the corresponding friction forces are also considerable, ranging from approximately 8 to 15.5 N.

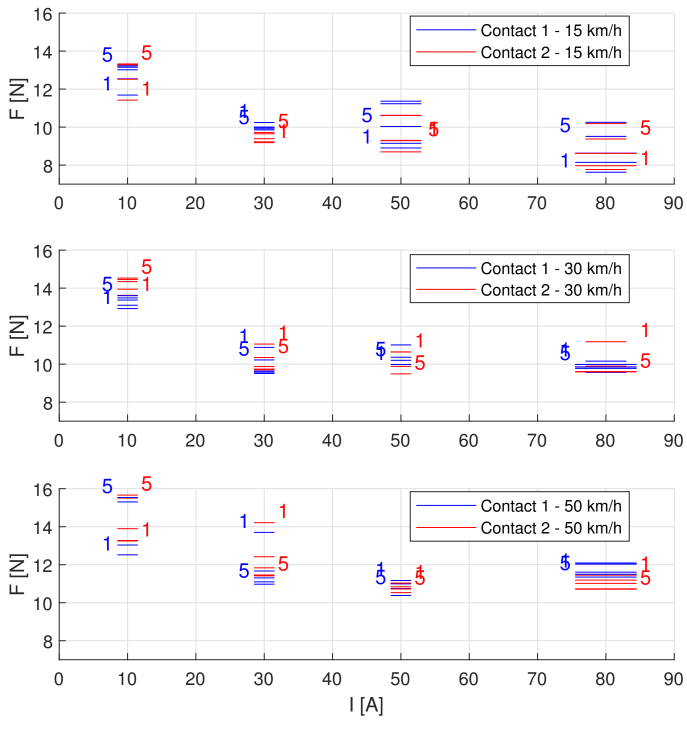

Figure 3.20: Measured frictional forces for stainless steel brushes (contact 1 in blue and contact 2 in red) with a contact force of 31 N corresponding to a 6 cm^2 contact area. The horizontal length of the lines represents the observed arcing intensity.

In general, the results highlight three key observations:

1. The combination of higher speeds (50 km/h), low currents (10 A, and notably 30 A for stainless steel brushes at 17 N), and lower contact forces (7 and 17 N) corresponding to 1 cm^2, tends to create more unstable contact for each brush material. This instability leads to increased arcing, greater variation in contact resistance, and generally higher contact resistance. At higher current levels, as more heat is generated in the brushes, they are believed to become more ductile. This increased ductility allows the brushes to adapt their shape, improving the contact surface area and consequently reducing contact resistance.

2. Despite the varying contact materials and contact force, certain trends remain consistent across all conditions. Specifically, increasing currents appear to decrease contact resistance. This trend has also been observed in static contact cases [68]. This is generally valid, as long as the contact is somewhat stable and consistent, which appears to be accurate for cases involving higher contact force and lower speeds.

3. The results exhibit variations, which are believed to be attributed to both the inherent mechanical nature and dynamics of the RTR, as well as the brushes themselves. The brushes, by their nature, easily change their structure and shape when subjected to mechanical forces. As such, simply mounting the brushes in the RTR could inherently affect their shape and, consequently, their performance. Moreover, these results indicate that the quality of the sliding contact is highly dependent on mechanical dynamics and forces.

Although copper has over 40 times lower resistivity than stainless steel [77], stainless steel brushes, in some of the presented cases, exhibit a contact resistance of a similar order of magnitude. This is believed to be due to mechanical factors, particularly the elasticity and ductility of the brushes, which impact the resulting contact resistance significantly more than the resistivity of the brush materials themselves. These properties allow the brushes to conform to the surface of the steel ring, improving contact. Their significant impact on contact resistance in the experiments is believed to partly stem from the absence of springs or dampers in the RTR. As the copper and stainless steel brushes exhibited a similar order of magnitude in contact resistance in some cases, it is believed that both materials were able to conform to the contact surface of the steel ring in a similarly effective manner.

To sum up, material choice in terms of resistivity may be secondary to the mechanical properties of the contact interface, as contact resistance appears to be more closely related to the mechanical dynamics of the sliding contact than to the resistivity of the materials. Therefore, future sliding contact designs should prioritize the integration of dampers and spring mechanisms, as these features could significantly improve both contact quality and resistance. Additionally, material selection for the sliding contact should also consider durability, the coefficient of friction, and resistivity.

In general, no clear trends or patterns can be observed from Figs. 3.14, 3.16, 3.18 and 3.20 in terms of force as a function of current or speed. This topic is further discussed in [63, 64], which examines the impact of the coefficient of friction, current, and speed on contact wear. In this thesis, however, this subject is not the primary focus, as the RTR currently lacks the precision required to yield reliable results in this context. While it may be possible to identify trends by using multiple brush samples per measurement combination, allowing for the application of statistical methods, such an approach was not within the scope of this thesis. The primary focus of the friction force measurements in this thesis is rather on the magnitude range of the respective friction forces, as these forces have a direct impact on the overall efficiency of the ERS.

The greatest friction force was observed with the stainless steel brushes with a contact force of 31 N, resulting in friction forces ranging from 8 to 15.5 N. In contrast, the smallest friction forces were found with the copper brushes with a contact force of 7 N, yielding friction forces between 1.5 and 3.7 N. For a current collector with three arms, this would result in aggregated total friction forces of 24 to 46.5 N for the stainless steel brushes, and 4.5

to 11 N for copper brushes. The rolling resistance force of a passenger car's tires is typically in the range of 130 to 160 N, assuming a mass of 1500 kg and a rolling resistance coefficient of 0.009 to 0.011 on paved roads [78]. Consequently, this comparison highlights that the friction force generated by the sliding contacts in the current collector may have a non-negligible impact on the overall efficiency of the BEV and ERS. A six-arm current collector with steel brushes, for instance, can result in aggregated friction forces approaching half of the rolling resistance force of a passenger car. Therefore, if these friction forces are not accounted for during the design of the sliding contact system, the expected efficiency of a conductive ERS (as presented in Chapter 4) may be reduced due to the design of the sliding contacts and current collector.

In terms of keeping the losses low from the sliding contacts a low contact resistance is preferred which could be impacted by contamination of the brushes and the contact surface of the electric road. The copper brushes, compared to the stainless steel brushes, appear to have experienced less contamination (ferric oxides accumulating on both the contact surface of the segment and the sliding contacts) over time. This was observed during both the individual 1.5-minute measurements and the five consecutive measurement tests. When comparing Figs. 3.13 and 3.15 with Figs. 3.17 and 3.19, the contact resistance is generally higher after each consecutive measurement for the stainless steel brushes. This is believed to be due to the stainless steel brushes, in combination with the steel ring, creating more favorable oxidation conditions for the formation of ferric oxide compared to the copper brushes. This results in more rapid degradation of contact quality and increase in contact resistance.

The occurrence of arcing appears to have been somewhat arbitrary and intermittent, and further design improvements of the sliding contact are necessary to mitigate it. Arcing inherently poses a risk of introducing issues related to radiated electromagnetic interference within the ERS and its vicinity. The stainless steel brushes with a contact force of 31 N performed the best in this regard, although their performance was far from perfect. This performance is believed to be due to the mechanical elasticity of the stainless steel brushes, which, in combination with the specific applied contact force, resulted in particularly favorable mechanical dynamics of the sliding contact. Finally, it is evident that arcing does not necessarily correlate with poor contact resistance. Arcing can occur without significant performance degradation in terms of contact resistance, and conversely, poor contact resistance does not inherently imply that arcing will occur.

To conclude, the RTR should not be regarded as a high-precision experimental setup, but rather as a setup designed to replicate the contact resistance and friction forces present in a real ERS. In real-world scenarios, the sliding contacts operate in environments that are far from controlled, and the current collector, where the sliding contacts are mounted, is not designed as a high-precision mechanical system. However, to fully capture trends and understand how factors such as contact force, material properties, currents, and speed interact, additional measurements per pair of brushes are required with the RTR. By further reducing the inherent variations introduced by the RTR, such as minimizing mechanical oscillations through the installation of dampers or springs for the brush mounting, and utilizing statistical methods (such as ANOVA or t-tests), more evident trends and correlations can be identified.

3.4 Experimental Assessment of Contact Resistance on the ERS Demonstrator

In an effort to determine the contact resistance in a real-life ERS, the voltage drop and current across two sliding contacts are measured using the trailer, originally presented in Section 3.2.1, at the ERS demonstrator. While the RTR enables detailed assessments of the sliding contact and eliminates external factors present at the ERS demonstrator, it remains unclear to what extent this more detailed approach translates to the conditions present in a real-life ERS, as discussed previously in Section 3.1 in the introduction of this chapter.

Nevertheless, the incorporation of real-life conditions and external factors into the assessment can be considered an advantage, as these conditions may provide valuable context for comparison with the results obtained from the RTR. Such a comparison can serve as the basis for initiating a discussion regarding potential limitations of the RTR and aspects it may fail to capture. Despite these expected uncertainties and differences in results between the ERS demonstrator and the RTR, the measurements from the demonstrator will provide a reliable approximation of the order of magnitude of contact resistance in a real-life ERS.

3.4.1 Experimental Setup

The trailer presented in Section 3.2.1 is modified to include a current source, using a power supply [79], allowing current levels of 10, 30, 50, and 80 A to be assessed through the two front sliding contacts, as illustrated in Fig. 3.21. The selected current levels of 10, 30, 50, and 80 A are the same as those chosen for the experiments with the RTR and are based on assumed power draw levels of 9, 24, 42, and 67 kW for BEVs with a three-arm current collector drawing power from an ERS. While conducting the experiments, the ERS demonstrator is deactivated, which also deactivates the high voltage of the electric road, making the experiment safer and practically easier to perform, while the trailer is pulled by a car over the electric road. Both static (0 km/h) and dynamic contact resistance at speeds of 10, 20, and 30 km/h are evaluated for each current level, resulting in a total of 12 measurements. When the experiments were conducted, the maximum speed was limited to 30 km/h due to a malfunction in the automatic control system of the current collector that aligns the sliding contacts with the electric road. This speed restriction was necessary to maintain stable contact between the sliding contacts and the segments while the trailer traversed the electric road. While these speeds do not match those selected in the RTR, they still provide a variation in speed, allowing for the examination of how speed influences the resulting contact resistance.

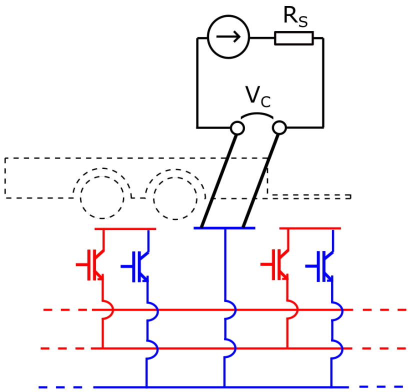

Figure 3.21: Overview of the setup for measuring the voltage drop, V_C, over two sliding contacts on the trailer. The setup consists of two arms in the current collector connected to a current source, with a shunt resistor, R_S, in series.

The measurement setup allows for the measurement of the voltage drop across the sliding contacts as long as the brushes of the two front arms are in contact with the same segment in the electric road. At this time, current flows from the current source through the first arm's sliding contact, through the segment, and back through the second arm's sliding contact. The duration of this period depends on the trailer's speed. Once the first brush makes contact with an isolating segment, the circuit is disrupted, and current can no longer flow, preventing any further measurements until both brushes comes into contact with the next segment. The current in the circuit is measured using a shunt resistor [80], denoted as R_S in Fig. 3.21, and the voltage drop across the two sliding contacts, V_C, and the shunt is measured and logged with a PicoScope [81].

In the trailer, the sliding contacts consist of a combination of two types of brushes: one made of copper and the other of stainless steel. These two types of brushes, which consist of braided metallic wire threads, are stacked alternately and pressed together to form a thicker brush, as shown in Fig. 3.22. Unlike the brushes assessed in the RTR, the wires of the brushes in the trailer are oriented perpendicular to the segments of the electric road rather than being aligned with the segment. Although this is expected to affect the contact surface and the sliding contact dynamics, ultimately influencing the contact resistance during the operation of the electric road, various orientations and sliding contact designs have been tested. Throughout the testing with the ERS demonstrator, different brush designs and orientations were evaluated in multiple configurations. However, this setup was selected as it was deemed the most representative for the ERS demonstrator. Before conducting the experiments, the contact force of the two front sliding contacts was measured using a scale, resulting in values of 6.7 N for both contacts. While this is on the lower end of the contact force range, it is comparable to the contact forces of 7, 14, 17, and 31 N applied in the RTR. During the experiments with the trailer no observations of arcing were conducted, and as a result, the impact of the low contact force on arcing were not be assessed.

Figure 3.22: The sliding contact in the trailer. Figure taken from [44].

3.4.2 Experimental Results of Contact Resistance

The contact resistance is calculated based on the measured voltage drop across two sliding contacts divided by the current flowing through them while the trailer is towed over the electric road demonstrator. To illustrate how contact quality varies over time, the measurement conducted at a current of 80 A and a speed of 30 km/h is selected, as it provides evidence of intermittent poor contact. The upper plot in Fig. 3.23 presents the measurements of voltage drop over the two sliding contacts, including the segment and cables in the measurement setup (blue line, associated with the left y-axis) and the current (red line, associated with the right y-axis) in the circuit. The lower plot presents the corresponding contact resistance which is calculated by dividing the voltage drop V_C by the measured current obtained from the shunt in Fig. 3.21, representing the total resistance across the entire setup rather than a single sliding contact. The calculated resistance is filtered using a moving average filter with a window of 0.2 ms.

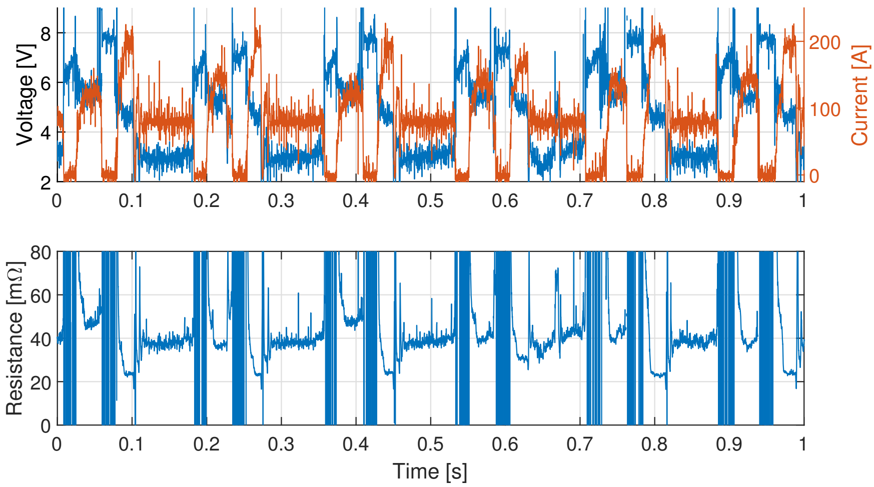

Figure 3.23: Upper plot: Measured voltage drop across the two front sliding contacts in the trailer (blue line, associated with the left y-axis) and the current (red line, associated with the right y-axis) flowing through these contacts while the trailer is being towed at a speed of 30 km/h with the current set to 80 A.
Lower plot: Corresponding calculated contact resistance derived from the measurements in the upper plot.

In the measurements, the voltage drop and calculated contact resistance vary over time. When adequate contact is established, the voltage drop is as low as 3 V, and the current remains relatively constant at the predefined value of 80 A, as observed during the periods between 0.11 and 0.18 s. This suggests stable contact, facilitating smooth energy transfer. During these intervals, the corresponding calculated resistance is approximately 40 mΩ across both sliding contacts, as depicted in the lower plot. In contrast, when the voltage drop fluctuates, such as between 0.62 and 0.7 s, the contact quality is imperfect. During this period, an intermittent peak in the voltage drop reaches over 7 V, resulting in a corresponding peak in contact resistance of 70 mΩ. This indicates that the contact is partly unstable as the voltage drop is fluctuating over time. Moreover, the measurement highlights that the voltage drop may fluctuate over time, serving as an example of the variable nature of contact resistance in a sliding contact within an ERS.

At times when the current is zero, such as between 0.18-0.2 s, the contact cannot be assessed, as one of the sliding contacts is assumed to be in contact with an isolating segment. However, at 0.8 s, the current exceeds 80 A, reaching nearly 200 A. This increase is due to the power supply's control system's inability to adjust the current to the selected level. This is believed to be caused by the resistance of the system changing too rapidly for the power supply's control system to provide a stable current. During this brief moment, the contact resistance cannot be assessed, as the predefined current is not attained. Moreover, since the sliding contacts were not be visually observed during the experiments, it is unclear what conditions were present at this time.

The selected experimental setup can only assess the total resistance across two sliding contacts, including the resistance of the segment and cables in the experimental setup. To estimate the resistance of a single sliding contact, the mean contact resistance of the two sliding contacts was calculated by first subtracting the resistance of the segment and cables and then dividing the remaining resistance by two. Figure 3.24 shows an equivalent circuit of the measurement setup from Fig. 3.21, which is used to determine the mean contact resistance of the two sliding contacts. In Eq. (3.1), the calculation of the voltage drop across two sliding contacts is presented. The circuit includes R_{Cables}, representing the resistance of the cables in the setup; R_{Segment}, representing the segment resistance of the electric road; and $R_{\text{Contact 1}}$ and $R_{\text{Contact 2}}$, representing the resistances of the two sliding contacts. V_C denotes the voltage drop across the two arms of the current collector, and I represents the current in the circuit. The resistance of the cables in the system was measured using the same power supply [79], shunt resistor [80] and Picoscope [81] as those employed during the experiments. The resistances of the cables (R_{Cables}) and segment (R_{Segment}) were 10 mΩ (measured by short-circuiting the cables with the power supply) and 0.4 mΩ (measured by short-circuiting a segment of the electric road with the power supply), respectively. The resistance of each sliding contact is assumed to be equivalent, as both exhibited a contact force of 6.7 N.

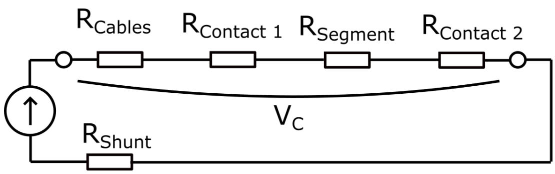

Figure 3.24: Equivalent circuit of the measurement setup, taken from [44]. The circuit includes resistances for the cables, R_{cables}, the segment, R_{Segment}, and the two sliding contacts, $R_{\text{Contact 1}}$ and $R_{\text{Contact 2}}$.

$$\frac{V_C}{I} - R_{Cables} - R_{Segment} = R_{Contact1} + R_{Contact2} \tag{3.1}$$

Fig. 3.25 presents the contact resistance of one sliding contact, based on Eq. (3.1) and Fig. 3.24, at currents of 10, 30, 50, and 80 A. The upper plot shows the dynamic contact resistance at speeds of 10, 20, and 30 km/h, while the lower plot presents three individual measurement samples of static contact resistance for each current level. In the dynamic case the contact resistance varies between 8-20 mΩ, while for the static, it varies between 3-17 mΩ.

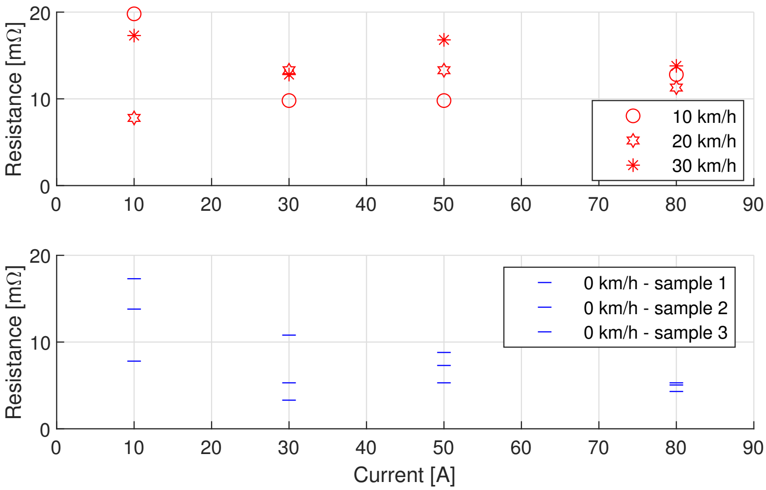

Figure 3.25: Upper plot: Contact resistance from one sliding contact during dynamic operation at speeds of 10, 20, and 30 km/h.
Lower plot: Contact resistance from one sliding contact during static operation with three distinct results per current level.
Figure taken from [44].

The results of both static and dynamic contact resistance indicate that the sample size is too small to assess any definitive trends or draw conclusions about how the calculated contact resistance varies with current and speed. This is not unexpected, as the inherent nature of the trailer and demonstrator leads to significant variations in contact resistance for each measurement. The variation in contact resistance observed in the results are believed to originate from external factors, such as the trailer's motion dynamics and the uncontrolled environment where the ERS demonstrator is located. For example, the asphalt road where the electric road demonstrator is installed presents an uneven surface, which directly impact the trailer's motion dynamics and, consequently, the forces exerted on the sliding contacts, thus affecting the resulting contact resistance. Although the sample size is too limited to draw definitive conclusions, the measurements show fewer variations at higher current levels, aligning with the observations from the RTR at higher currents. As in the RTR, this can be explained by the fact that higher current levels generate more heat, which causes the brushes to heat up, allowing them to conform better to the contact surface. This improved contact surface leads to fewer fluctuations in the measurements and, consequently, more stable contact resistance results.

In general, the results obtained from the experiments with the trailer present lower values of contact resistance compared to those from the RTR. Due to the controlled laboratory environment where the RTR is located, its results might initially be expected to yield lower values of contact resistance compared to the trailer, which, in contrast, was subjected to various uncontrolled factors encountered on the public road where the demonstrator is located. The differences between the results from the trailer and the RTR are suspected to be caused by the following:

1. The suspension provided by the current collector and trailer is suspected to have contributed to the lower contact resistance values in the trailer compared to the RTR. The sliding contacts in the trailer are mounted within the current collector, which consists of a mechanical system of springs and pulleys. As a result, the sliding contacts in the trailer are subjected to entirely different mechanical motion dynamics compared to those in the RTR. In contrast, the sliding contacts in the RTR are mounted completely unsprung, with the only source of suspension being the elasticity of the brushes themselves. This difference is expected to have had a significant impact on the results obtained from the trailer and the RTR.

This hypothesis is supported by one of the main conclusions from the RTR experiments, which suggests that the mechanical properties of the brushes, particularly their elasticity (acting as a spring-like element) and ductility, can be far more central in achieving low contact resistance than the difference in resistivity between stainless steel and copper brushes.

2. The lower contact resistance values obtained with the trailer, compared to the RTR, could be partially attributed to the accuracy of the measurement setup. In the trailer, the measurement setup was more rudimentary compared to that of the RTR. The voltage drop across two sliding contacts, cables, and the segment of electric road was measured, and the resulting mean contact resistance for one sliding contact was then calculated based on these results. The calculated resistance in the cables and the segment of electric road had a significant influence on the resulting mean contact resistance for one sliding contact in the trailer. Consequently, the resulting mean contact resistance obtained with the trailer was based on multiple measurements and is therefore considered less accurate compared to the measurements conducted with the RTR. Since the voltage drop across each sliding contact was measured individually using more accurate equipment in the RTR, these measurements achieved greater accuracy.

3. The difference in the design of the sliding contacts, in terms of orientation and stacking of brushes, might have contributed to the lower contact resistance obtained with the trailer compared to that obtained with the RTR. In the trailer, the design of the sliding contacts involved orienting the brushes across the segments, rather than aligning with the segments as in the RTR. Additionally, the copper and stainless steel braided brushes were stacked alternately in the trailer, whereas in the RTR, only one braided brush was assessed at a time.

In terms of reliable results, the RTR is suspected to yield the most consistent and accurate results due to the controlled lab environment and its more sophisticated measurement system. Although the results deviate between the trailer and the RTR for the aforementioned suspected reasons, the results remain within the same order of magnitude. Thus, the RTR is deemed appropriate for evaluating the contact resistance present in a real-life ERS. Additionally, the RTR provides the capability to observe arcing phenomena and offers estimates of frictional forces related to the sliding contact. Nevertheless, the differences in the methodologies employed for assessing the properties of the sliding contact with the RTR and trailer need to be further assessed to continue the evaluation of the characteristics of sliding contacts adopted for conductive ERS technology.

As demonstrated and discussed, based on the results from the RTR and the trailer, there are inherent differences between conducting measurements with the RTR in a controlled lab environment and on a public road with the trailer on the ERS demonstrator. Future work is required to further assess which aspects and factors cause the differences and deviations in results between the RTR and the trailer. This can be achieved by:

1. Improving the measurement setup in the trailer to obtain more accurate and reliable results.
2. Replicating measurements for combinations of speed, current, and contact force with the trailer, and employing statistical methods to assess how contact resistance and contact quality are impacted by these parameters.
3. Deploying some means to quantify arcing phenomena in the trailer, possibly by using a camera, to assess the impact of arcing in the sliding contacts on a real-life ERS.
4. Exploring the possibility of emulating the same type of sliding contact design as well as suspension in both the RTR and the trailer.

Until these factors are isolated and fully explained, the results highlight that when assessing the characteristics of the sliding contact, both measurements conducted in a lab, possibly with an RTR, and real-life measurements from an ERS are required to fully assess all aspects of the sliding contact. This is motivated by the fact that assessing the underlying factors affecting the sliding contact in detail is practically challenging under the uncontrolled conditions of a real ERS. Meanwhile, emulating the sliding contact behavior in a laboratory setting poses the risk of unintentionally overlooking crucial factors that could impact the results, such as the specific forces exerted on the sliding contact during ERS operation.

In summary, the findings of this chapter should be regarded as providing an initial exploration into the evaluation of the characteristics of the sliding contact used in conductive ERS technology. Although the exact factors affecting contact resistance are not yet fully understood and will require further research, the order of magnitude of the contact resistance has been examined. The results from the trailer and the RTR provide valuable data that will facilitate the setting of parameters and the calibration of simulation models in subsequent chapters, particularly regarding the contact resistance parameters discussed in Chapter 4.

Chapter 4

Modelling Power Flow and Losses

4.1 Introduction

As previously discussed in Section 1.4 in Chapter 1, the performance of the considered ERS technology must be analyzed in terms of power flow capabilities, loss distribution, and system efficiency to determine its potential for widespread deployment. In this chapter, these factors are assessed for ERS deployment in three environments: urban, rural, and highway. This assessment is conducted using a simulation model validated by experimental results from the demonstrator introduced in Section 2.2. The assessment is focused on the impact of a range of parameters including the length of the electric road, type and number of vehicles drawing power from the system, and design choices related to specific ERS subsystems and components. The results presented in this chapter show that the distribution of losses within the ERS is highly dependent on both the traffic characteristics of the considered deployment environments as well as design choices related to specific ERS components. The work presented in this chapter extends the work presented in [21].

In this thesis, the electrical losses within the ERS and its corresponding components are divided into two main categories: 1) resistive losses, which occur when electric current flows through a non-ideal conductor and are therefore valid for essentially all current-carrying components except for semiconductor devices. These losses are proportional to the actual resistance of all components in the circuit (cables, connection points, etc.) and to the square of the current flowing through these components [82]. 2) Semiconductor losses, which are specific to semiconductor devices in the circuit (such as diodes and switches). These losses comprise both resistive losses within the semiconductor material and additional losses associated with the voltage required to forward bias the semiconductor junctions for conduction [82].

To highlight the key phenomena that impact electrical losses in the presented ERS technology, a vastly simplified circuit model of the ERS, shown in Fig. 4.1, is introduced. The model represents a vehicle charging on an electric road. In this circuit, U_{DC} denotes the DC voltage supplied by the rectifier station, R_{ER} represents the resistance in the main conductors of the electric road, and R_V indicates the variable electrical load of the vehicle drawing power from the ERS. The electrical losses within the ERS are described in Eq. (4.1), where P_V, defined by Eq. (4.3), is the power consumed by the vehicle, and P is the total power in the circuit, defined in Eq. (4.2). The current in the circuit is determined according to Eq. (4.4). The equivalent resistance of the electric road, represented as a variable resistor denoted R_{ER}, depends on the distance between the rectifier station (the feeding point) and the vehicle drawing power from the electric road. The drawn power of a vehicle in an ERS is a design choice, as it may be limited by the vehicle's onboard ERS interface. In this thesis, as well as in this particular case, the drawn power of a vehicle is assumed to be a predetermined constant value. Consequently, the current and the variable resistor R_V must be continuously adjusted to maintain the predetermined constant power draw according to Eqs. (4.3) and (4.4) as a vehicle traverses the electric road, since the parameter R_{ER} depends on the vehicle's position on the electric road relative to the feeding point.

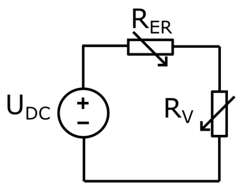

Figure 4.1: Equivalent circuit of a simplified ERS circuit pertaining a voltage source U_{DC}, the resistance of an electric road - R_{ER}, and a vehicle load R_V.

$$P_{loss} = P - P_V \tag{4.1}$$

$$P = I^2(R_V + R_{ER}) \tag{4.2}$$

$$P_V = I^2 R_V = I U_V \tag{4.3}$$

$$I = \frac{U_{DC}}{R_V + R_{ER}} \tag{4.4}$$

Ultimately, the losses in the ERS increase with increasing current and resistance, as detailed in Eqs. (4.1) to (4.3). Fig. 4.2 illustrates the impact of these two parameters on losses (upper plot) and efficiency (lower plot) of the simplified ERS circuit, where P_V (y-axis) and R_{ER} (x-axis) are varied, with U_{DC} fixed at 650 V. The x-axis is presented in meters, reflecting that R_{ER} is given as resistance per unit length, specifically $0.042\,\mathrm{m\Omega/m}$, which is similar to the resistance of the SER conductors in the demonstrator. It is noteworthy that losses increase proportionally to the square of the current and linearly with the electric road length. To maintain low losses and high ERS system efficiency, it is crucial to limit both the total drawn power by the vehicle and the length of the electric road. To thoroughly evaluate the losses in the complete electrical system of the considered ERS technology, a comprehensive simulation model is employed, which incorporates the ERS components and subsystems in detail. Yet, the results of the simplified circuit model in Fig. 4.2 still demonstrate the basic principles and trends concerning losses in an ERS, as shown throughout this chapter.

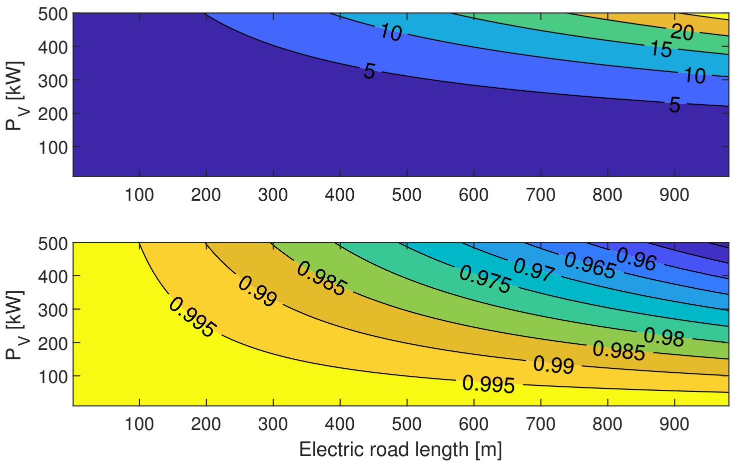

Figure 4.2: Calculated losses (upper plot) and efficiency (lower plot) of the simplified ERS circuit from Fig. 4.1.

4.2 Modelling

The models and simulations presented in this chapter focus on a single rectifier station positioned at the midpoint of one electric road. The vehicles connected to the electric road can vary in type, number, speed, drawn power and position. The simulation model is designed to produce accurate results within a time resolution of seconds; therefore, transient occurrences in the millisecond range are not considered. The simulations are typically executed over several seconds. After the simulation is finalized, power flow, losses, and efficiency are calculated in a post-processing phase.

A block diagram of the simulation model is presented in Fig. 4.3. The blocks represent components and subsystems of the ERS and include circuit models for the power grid, cables between the transformer and the power grid connection, the transformer, the rectifier, the cables connecting the rectifier to the SER, the SER, and the vehicles. The dashed colored lines indicate the three primary circuit models: the grid and rectifier station model, the section of the electric road model (SER), and the vehicle model (BEV). These three circuit models are derived from the original circuits of the demonstrator, as presented in Section 2.2 and illustrated in Figs. 2.14, 2.15 and 2.18. For each simulated vehicle, a SER circuit model, along with the corresponding BEV circuit model, is incorporated. Dashed black lines denote the locations where additional BEV and SER circuit models can be integrated into the simulation model.

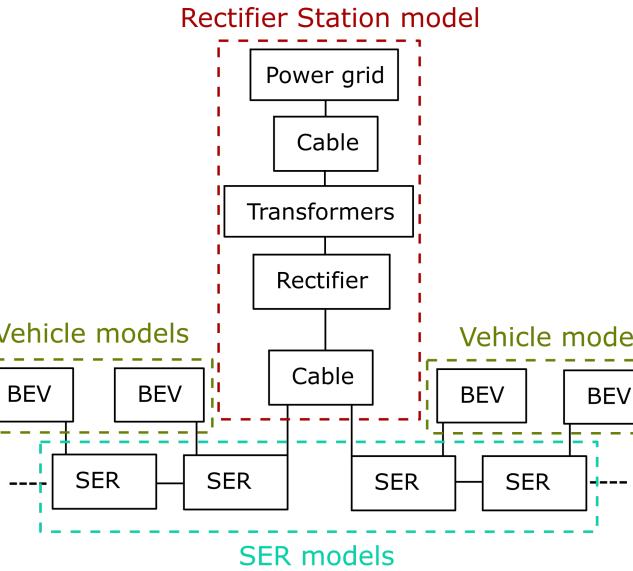

Figure 4.3: Block diagram of the simulation model displayed for an arbitrary simulation case with four vehicles.

To accurately model the losses in the ERS, the simulation model was designed to maintain a maximum error margin of 15%. Although this limit might initially appear relatively tolerant, it is essential to consider that the accuracy of the loss measurements is constrained by the measurement system's accuracy in voltage and current. As the same voltage and current measurement setup is used both to calculate losses between measurement interfaces and determine power at a measurement interface, accurately obtaining these losses is challenging. This difficulty arises from the requirement for voltage and current measurements to maintain high accuracy across their entire measurement range.

Specifically, interface B exhibits the highest average error: 0.47% for voltage and 0.48% for current, as detailed in Tables 2.2 and 2.3 in Chapter 2. This results in a maximum error of approximately 0.95% in the calculated measured power, according to Eqs. (2.6) and (2.7) in Chapter 2. For instance, in the case of a drawn power of 100 kW, this corresponds to a possible maximum error in power of 950 W. As the losses are calculated by the difference in power between interfaces, assuming an efficiency of 98%, the true calculated output power is 98 kW, resulting in 2 kW of losses. However, when accounting for the maximum error of 950 W in the input power, the resulting calculated losses increase to 2.95 kW. In contrast, a 15% maximum error margin in the simulation model, for the same drawn power of 100 kW and an assumed efficiency of 98%, leads to a maximum deviation of ±300 W in the calculated losses. Since the measurement system itself introduces a greater maximum deviation in the calculated measured losses (950 W in this example), a 15% error margin between modelled and measured losses (300 W in this example) is reasonable and constitutes an acceptable constraint for the simulation model.

4.2.1 Model Development

Due to the extensive and complex nature of the ERS demonstrator, it was necessary to introduce simplifications during the development of the simulation model to balance accuracy and simulation time. These simplifications are detailed for each circuit model in the subsequent subsections of this chapter. The simulations are executed using MathWorks® Simulink™ software, along with the Simscape Electrical™ library.

The power flow and losses in an ERS are fundamentally determined by the vehicles that draw power from it. Consequently, the power draw is dependent on the motion dynamics of these vehicles, which vary on a timescale of seconds. Therefore, the timescale selected for the simulation model is in the magnitude of seconds. However, during the heuristic development of the simulation model, it was discovered that accurately replicating the overall waveform shapes of currents and voltages in both amplitude and time was essential to reach the predetermined error margin of 15% in losses and power flow. This requirement increased the complexity of the model, resulting in challenges for the simulation software to execute the model within a reasonable timeframe. Thus, a balance was sought by simplifying the model sufficiently to allow for execution while retaining the overall waveform shapes of voltage and current as provided by the measurements, thereby achieving the predetermined accuracy.

As a result, the level of detail for each and every circuit of ERS components, originally presented in Figs. 2.14, 2.15 and 2.18, was achieved through multiple iterative refinements. The parameters for all electrical elements from the original circuits were obtained either from electrical schematics provided through collaboration with Elonroad and other partners in the Evolution Road project or measured using a Hioki IM3570 impedance analyzer [83]. The subsequent subsections provide a detailed description of the three main circuit models, including a thorough discussion of the selection and origin of parameters. All parameter values outlined in these subsections were utilized for the validation of the simulation model. For the succeeding simulation cases representing ERS deployment in urban, rural, and highway environments, the model parameters and circuits are adjusted to accurately represent each scenario.

4.2.2 The Rectifier Station

The circuit model for the grid and rectifier station includes a 400 V three-phase voltage source, 210 meters of grid cable, a D/Y 400 kVA 400/450 V transformer, a 6-pulse passive rectifier, a solid-state switch (modelled as a diode) situated straight after the rectifier station, 41 meters of cable connecting the rectifier station to the SER, and an RC filter positioned immediately prior to the SER, as illustrated in Fig. 4.4. Interfaces A, B, C represents where voltage and currents are measured in the model which is then used to calculate power, losses and efficiency.

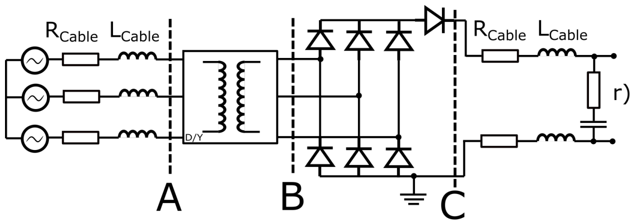

Figure 4.4: Circuit model of the power grid, rectifier station and corresponding connections.

Compared to the original circuit introduced in Section 2.2 in Fig. 2.14, all the filters on the output of the rectifier have been omitted as they do not have a considerable impact on the waveform-shape of voltage and current. The parameters of the circuit model are detailed in Table 4.1. The resistance and capacitance values of the RC-filter are in a range due to non-disclosure agreements with Elonroad.

In the model, all cables, including those for the grid and the connection between the rectifier station and the SER, are represented as resistors in series with inductors, with their resistance and inductance defined per unit length of cable. Throughout the demonstrator, the resistance of the negative main conductors after the rectifier station is significantly lower than that of the positive main conductors. Given that the negative main conductors are exposed externally, it is crucial to maintain low resistance throughout the system to prevent voltage drops that could lead to hazardous touch events, as more fully examined in Chapter 6.

Table 4.1: Simulation parameters for the rectifier station circuit model.

Rectifier station circuit model parameters		
Parameter	*Unit*	*Value*
Grid Cable		
Grid cable resistance	mΩ/km	41.7
Grid cable inductance	mH/km	0.23
Transformer		
Nominal power	kVA	400
Nominal line-line voltages (prim, sec)	V_{RMS}	404, 455
Winding resistance	p.u.	0.01, 0.008
Positive-sequence no-load excitation current	% of I_{nominal}	1.217
Positive-sequence no-load losses	W	1362
Positive-sequence short-circuit reactance	p.u.	0.04
Rectifier		
Rectifier diodes on-state resistance	mΩ	2
Rectifier diodes forward voltage drop	V	0.8
Solid state switch on-state resistance	mΩ	0.1
Solid state switch forward voltage drop	V	0.9
SER Cable		
Rectifier-SER cable resistance positive conductor	mΩ/km	125
Rectifier-SER cable resistance negative conductor	mΩ/km	62.5
Rectifier-SER cable inductance	mH/km	0.23
Filter resistance	Ω	0.1-10
Filter capacitance	mF	0.001-0.1

The D/Y 400 kVA 400/450 V transformer is modelled using the three-phase transformer inductance matrix type (two windings) Simulink block [84]. The diodes within the six-pulse passive rectifier are represented with forward voltage drops and constant resistive on-loss components during conduction. Similarly, the solid-state switch following the six-pulse passive rectifier is also modelled as a diode with corresponding values of forward voltage drop and constant resistive on-loss components.

An RC filter is connected to the SER cable immediately before the connection point (interface r)) with the electric road. This connection point, known as the feeding point, is where the total current flow in the ERS, regardless of the number of vehicles or the power drawn by each vehicle. It is defined as the physical distance between a vehicle connected to the ERS and the electric road connection to the rectifier station that feeds it.

4.2.3 Sections of Electric Road

The circuit model for the SER comprises the main positive and negative conductors, as well as the semiconductors that facilitate the activation of the segments as illustrated in Fig. 4.5, with corresponding parameter values presented in Table 4.2.

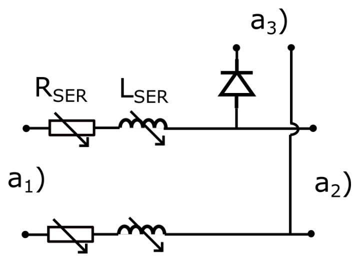

Figure 4.5: Circuit model of a section of electric road.

Table 4.2: Simulation parameters for the section of electric road model.

Section of electric road circuit model parameters		
Parameter	*Unit*	*Value*
SER		
SER resistance positive conductor	mΩ/km	42
SER resistance negative conductor	mΩ/km	4.1
SER inductance	mH/km	0.02
Transistor forward voltage drop	V	1.4
Transistor on-state resistance	mΩ	0.1

The main positive and negative conductors of the SER are modelled with variable resistance and inductance, with their resistance and inductance values defined per unit length. Similar to the cables between the rectifier station and the SER, the resistance of the negative main conductors after the rectifier station is significantly lower than that of the positive main conductors. As previously mentioned, this measure is implemented to mitigate voltage drops in the exposed negative conductors, thereby reducing the risk of potentially hazardous touch events. In the demonstrator, Elonroad did not utilize the full potential of the positive conductor of the SER, as only one of the two positive conductors was deployed. The resistance of one positive conductor is 42 mΩ/km. However, by deploying both conductors, the design allows for a value as low as 21 mΩ/km, which is beneficial in a highly utilized system. The resistance and inductance values per unit length of the SER conductors were obtained through measurements using the Hioki IM3570 impedance analyzer [83], and the semiconductor parameters were sourced from datasheets.

During the simulation, the impedance of each SER conductor is continuously recalculated based on the vehicle's position on the electric road. As the vehicle moves along the road, its distance from the feeding point (interface r, as shown in Fig. 4.4) changes, which in turn causes the effective length of the SER conductors perceived by the ERS to to change continuously.

In comparison to the original circuit detailed in Section 2.2 and illustrated in Fig. 2.15, the model circuit has been simplified by representing the semiconductors that activate the segments with a single diode. As a vehicle traverses the electric road, it sequentially activates new segments, each facilitating a current flow through the associated semiconductors and the positive main conductor of the SER. Although new segments are activated, the corresponding conduction losses of the semiconductors that momentarily conduct current as the vehicle traverses the segments are assumed to remain constant. Consequently, the assumption of constant semiconductor losses in the segments and the onboard rectifier is justified, and the switches can be modelled by using a single diode that incorporates a forward voltage drop and a resistive on-loss component during conduction.

Interface a_1) in Fig. 4.5 connects to the feeding point of the rectifier station model from Fig. 4.4 at interface r), where two SER circuit models are connected in parallel, thereby establishing the midpoint of the electric road. The SER circuit model is connected to a vehicle circuit model at interface a_3). For simulating multiple vehicles drawing power from the ERS, additional SER circuit models with corresponding vehicle circuit models can be connected in series at interface a_2) to the right.

4.2.4 The Vehicle

The vehicle model includes the contact resistance of the sliding contacts, represented as two resistors—one in each pole—along with an onboard rectifier, an LC filter, and a resistive load representing the vehicles power consumption, as shown in Fig. 4.6, with corresponding parameters presented in Table 4.3. The DC/DC converter originally shown in the bus schematic (see Fig. 2.18) is omitted from the model because it does not perform voltage conversion via switching to the bus TVS. Instead, it functions merely as a switch, allowing connection and disconnection of the bus' TVS from the ERS supply. The sections of electric road circuit model is connected to the vehicle model at interface v). Interface D represents where voltage and current are measured in the model which is then used to calculate power, losses and efficiency.

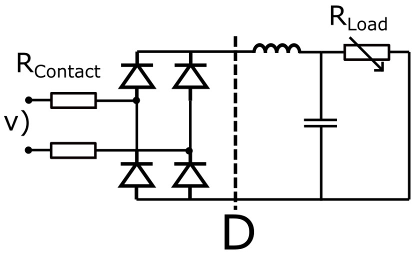

Figure 4.6: Circuit model for a vehicle.

Table 4.3: Simulation parameters for the vehicle model

Vehivle circuit model parameters		
Parameter	*Unit*	*Value*
Vehicle		
Contact resistance	mΩ	16
Diodes on-state resistance	mΩ	0.4
Diodes forward voltage drop	V	0.8
Filter inductance	mH	1.15
Filter capacitance	mF	5

Compared to the original circuit defined in Section 2.2 and illustrated in Fig. 2.18, the contact resistance in the vehicle circuit model is simplified to include only two resistances, despite the presence of six sliding contacts in the original circuit. As previously discussed in Section 2.1 in Chapter 2, a current collector is required to have a minimum of three arms. However, for the sake of simplicity, this thesis mainly focuses on current collectors with a number of arms that are multiples of three. The theoretical basis for this simplification is that for each additional set of three sliding contacts, the current is equally divided among the sliding contacts due to parallel coupling.

For a current collector with three arms, for the majority of the time, as illustrated in Fig. 3.10 in Chapter 3 and discussed in Chapter 2, two arms are connected to the same segment, while the remaining arm is connected to another segment. Only during a small fraction of the time, approximately 8%, is one of the arms in contact with an isolating segment, resulting in the current collector having only two arms connected to the ERS supply. By omitting this brief period, it is assumed that, at all times, two sliding contacts are connected to the same segment in parallel. Thus, the total contact resistance perceived by the vehicle, denoted R_{ceq}, can be described by Eq. (4.5), where y and z denote the two arms in contact with the same segment and x the remaining arm.

$$R_{ceq} = R_x + \frac{R_y R_z}{R_y + R_z} \tag{4.5}$$

The average contact resistance for one pole is defined by the parameter R_{contact}, as presented in Fig. 4.6, and is obtained by dividing R_{ceq} by two for a current collector configuration with three arms. If a vehicle has additional multiples of three arms in the current collector, R_{ceq} is further divided by the number of arms divided by three, reflecting that with each additional set of three arms, the current is equally divided due to parallel coupling. Although Eq. (4.5) can be used to assess the total contact resistance perceived by the vehicle, it is still dependent on the contact resistance of the individual sliding contacts, R_x, R_y, R_z, of the current collector, which exhibit significant variation over time, as presented and discussed in Chapter 3.

Due to the arbitrary nature of these variations in contact resistance and the complexity involved in modelling a full current collector with varying contact quality, the parameter R_{contact} is assumed to be constant over time for simplicity. As there was no means of measuring the contact resistance of the sliding contacts in the current collector on the bus during the tests at the demonstrator, the value of R_{contact} was determined by adjusting this parameter to fit the measurements during model validation. This process resulted in a value of 16 mΩ for R_{contact}, which corresponds to a contact resistance of 42 mΩ per sliding contact point, according to Eq. (4.5), assuming that all six arms of the current collector exhibit the same contact resistance.

To verify that this method of determining the parameter R_{contact} yielded credible results, the order of magnitude of 42 mΩ for one sliding contact was compared with the results from the RTR and the trailer in Chapter

3. The results obtained from the RTR are, on average, 30–100 mΩ, and the results from the trailer are 8–20 mΩ. Although 42 mΩ is higher than the experimental results from the trailer (8–20 mΩ), the current collector and corresponding sliding contacts in the bus differ slightly in design from those in the trailer, which could explain the discrepancy. Therefore, the result of 42 mΩ is still considered credible.

The onboard rectifier is modelled using four diodes to represent the total semiconductor losses, although the original circuit comprises 12 diodes, as illustrated in Fig. 2.18. In the complete onboard rectifier, the diodes alternate to conduct the current based on the vehicle's position over the segments. Moreover, the current amplitude varies depending on the number of arms connected in parallel at any given moment, as shown in Fig. 3.3 in Chapter 3. The model is simplified so that only two diodes are constantly conducting all the current to model the losses.

A variable resistor, denoted as R_{Load}, is utilized to simulate the power consumption of the vehicle. This power consumption fluctuates based on factors such as vehicle dynamics, auxiliary power requirements, and battery charging. For the model validation, the measured load current from the bus, filtered using a 500 ms moving average filter, is used as an input to the model. This input allows for the continuous calculation of R_{Load} and, consequently, the reproduction of the power consumption associated with the vehicle's dynamic motion. R_{Load} is computed by dividing the voltage across R_{Load} with the load current. In the simulation cases presented in subsequent subsections in this chapter, the variable resistor R_{Load} is continuously updated based on the predetermined constant total drawn power by the vehicle.

4.3 Model Validation

The simulation model is validated using two sets of measurements conducted on 2022-09-07 and 2022-09-13, during which the bus draws power from the ERS demonstrator, illustrated in the upper plots of Figs. 4.7 and 4.8. The lower plots presents the relative error between simulated and measured losses. In both sets of measurements 100 meters of electric road were available. The model is initially calibrated using the data from the first set of measurements from 2022-09-07. Subsequently, without modifying any parameters, the model is validated against the second set of measurements from 2022-09-13. Voltages and currents from interfaces A-D from model and measurements were used to calculate power and losses.

The model composition adapted for the validation comprises a grid and rectifier station circuit model and a section of electric road circuit model connected to a vehicle circuit model. As described in the introduction of the vehicle circuit model, the measured load current of the bus from interface D is utilized as an input to continuously calculate the load resistor R_{Load}. This approach is applied to ensure accurate replication of the bus' power consumption related to its motion dynamics from the specific measurement event.

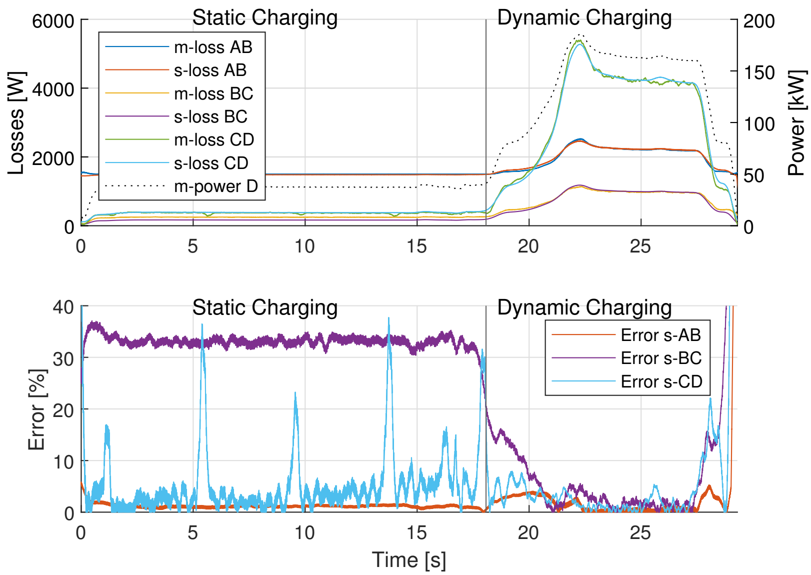

Figure 4.7: Upper plot: Simulated (s) and measured (m) losses for the charging event from 2022-09-07. Losses between interfaces A-B, B-C and C-D in W are associated with the left y-axis. Vehicle power from interface D, m-power D, in kW is presented as a dotted black line related to the right y-axis.
Lower plot: Relative error between simulated and measured losses for interfaces A–B, B–C, and C–D.

In the upper plots of Figs. 4.7 and 4.8 the total drawn power of the bus is represented by the dotted black line associated with the right y-axis in the figures. In both sets of measurements the bus starts at standstill, drawing power from the demonstrator, statically charging. This static charging phase is followed by a dynamic charging phase, during which the bus increases its charging power from 40 kW to 80 kW. As dynamic charging begins and the bus accelerates, the power consumption of the bus's propulsion system is added, increasing the total power to approximately 160 kW in both cases. This power level is maintained until the bus reaches a final speed of 30 km/h, after which it decelerates and disconnects from the

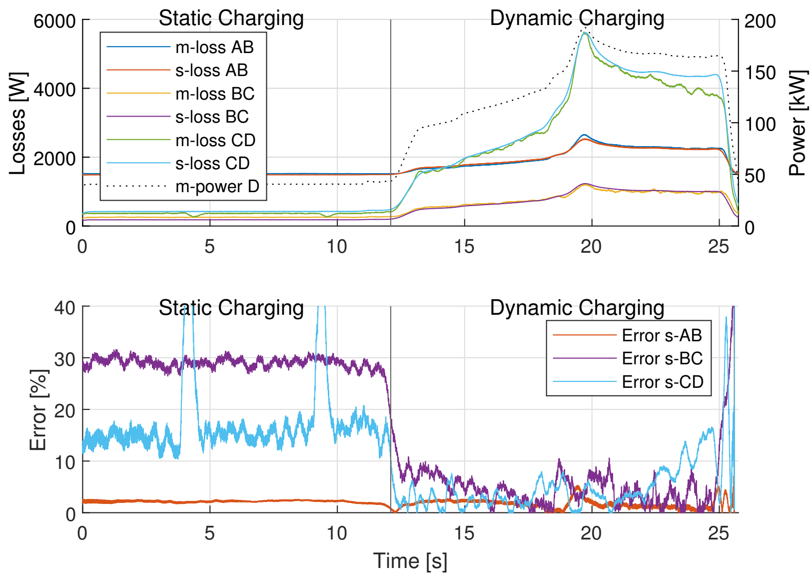

Figure 4.8: Upper plot: Simulated (s) and measured (m) losses for the charging event from 2022-09-13. Losses between interfaces A-B, B-C and C-D in W are associated with the left y-axis. Vehicle power from interface D, m-power D, in kW is presented as a dotted black line related to the right y-axis.
Lower plot: Relative error between simulated and measured losses for interfaces A–B, B–C, and C–D.

electric road. The measured (denoted as m) and simulated (denoted as s) losses, with a 500 ms moving average filter, are presented for interfaces A-B, B-C, and C-D and are associated with the left y-axis. Although the bus' speed was not logged during the measurements, direct observation of the speedometer showed that the bus reached a speed of approximately 30 km/h shortly after the peak power is achieved during dynamic charging.

In the measurement from 2022-09-07, as depicted in the upper plot of Fig. 4.7, the bus starts to draw 40 kW statically from the electric road after 1 s. After 18 s, the bus starts to accelerate and dynamic charging is initiated. At this point, the power increases to 100 kW after 19 s and reaches a peak value of 180 kW at 22 s. From 22 to 28 s, the bus maintains a speed of 30 km/h. Subsequently, after 28 s, the bus begins to decelerate, resulting in a decrease in power.

In the upper plot of Fig. 4.8, the measurement from 2022-09-13 is depicted. At 0 s, the bus is already statically charging with a power of 40 kW. After 12 s, the bus begins to accelerate and transitions to dynamic charging, reaching a peak of 195 kW after 19.4 s. Following this peak, the bus attains a final speed of 30 km/h. At 25 s, the bus initiates braking, resulting in a subsequent decrease in power.

During static charging, the losses in the transformer (interface A-B) are the most substantial. This is due to the relatively large no-load losses of the transformer, which, being rated at 400 kVA, reach approximately 1.5 kW in comparison to the modest drawn power of 40 kW. In contrast, during dynamic charging, the losses between the rectifier station (interface C) and the vehicle (interface D) surpass the losses at interfaces A-C, with peak values exceeding 5 kW. This phenomenon arises due to the significantly higher aggregated resistance present between interfaces C-D relative to the other interfaces. As a result, these components incur greater losses as the power increases, since these losses are proportional to the square of the current, as previously shown in Eqs. (4.1) to (4.3).

As explained in Section 4.2.1, an error margin of 15% is deemed sufficient for the purpose of this study. In the lower plots of Figs. 4.7 and 4.8 the relative error between simulated and measured losses of interfaces A-B, B-C and C-D is presented. Overall, the prescribed maximum error margin of 15% is achieved with the exception of interface B-C during static charging. The intermittent peaks in relative error, which occur for instance at 5.2 s in Fig. 4.7 and 4 s in Fig. 4.8, are caused by the simulation model's inability to fully replicate the fluctuations in power consumption of the bus, as observed in the measurements. Therefore, these peaks should not be considered representative of the simulation model's overall accuracy.

For interfaces A-B and C-D the average relative error is below 5% compared to the measurements, as presented in the lower plot of Fig. 4.7, for which the model was calibrated. When validating the model against the second measurement set (without altering any parameters), shown in the lower plot of Fig. 4.8, the error for interface A-B does not exceed 5%. However, for interface C-D, during static charging, the error averages just below 15%, and during dynamic charging, the error remains under 10%, except for a peak of 15% at 24.9 s. For interface B-C, the relative error margin greatly exceeds the prescribed maximum error margin of 15%, reaching approximately 30% during static charging in both figures. In contrast, during dynamic charging when the total power draw greatly exceed 40 kW, the error remains below 10% for interface B-C in both figures.

As the model is intended to assess ERS deployment scenarios with multiple vehicles operating on the ERS, the total drawn power greatly exceeds 40 kW, reaching levels of several hundred kW. The drawn power in the calibration and validation measurements ranges from 40 kW to nearly 200 kW. With the presented model structure, it is difficult to tune the model parameters to achieve the same level of accuracy across the entire power range for all interfaces. Consequently, accuracy at higher power levels has been prioritized, given the model's original purpose. As observed in the lower plots of Figs. 4.7 and 4.8, during dynamic charging, when power levels exceed 100 kW, the relative error of the simulated losses meets the prescribed maximum error margin of 15%. The fact that the model error increases to nearly 30% for the losses at interface B-C while static charging at 40 kW indicates that there is room for improvement in the model between these interfaces. However, at the target power levels above 100 kW, the error remains below 10% at all times, even in the B-C interface. Based in this, the overall error margin for all interfaces is deemed sufficient for assessing power flow, losses, and efficiency across different ERS deployment scenarios.

4.4 Predictions of Vehicle Power Consumption via Modelling

Although the experimental results from the demonstrator provide data from a real ERS in operation, the number and type of available vehicles drawing power from it are limited. To assess the performance and capability of the considered ERS technology in different deployment environments, it is necessary to estimate the power drawn by different vehicles when using the electric road. Given that ERS are not deployed to the extent where deployment scenarios with adhering traffic characteristics are available, predictions and estimations are required. In this thesis, the power consumption of vehicles drawing power from the ERS is estimated using a modified version of the vehicle simulation models presented in [36, 40]. This model is employed to assess and predict the vehicles' power consumption during ERS operation.

As observed during simulations with the vehicle model, the power consumption of a BEV, whether a car or a truck, varies significantly depending on numerous factors and conditions such as mass, drag coefficient, rolling resistance, inclination and acceleration. However, to simplify the various conditions that can occur for a vehicle in motion drawing power from an ERS, the following simplifications are made:

1. The road where the ERS is deployed is assumed to have no inclination.
2. During the simulation, the total power drawn from each vehicle is considered constant. This assumption is based on the vehicle maintaining a constant speed, resulting in constant power required for propulsion. Additionally, the charging power to the battery and the power required for auxiliary systems are also assumed to be constant.

While the ERS has the potential to supply power to BEVs for propulsion during acceleration, as demonstrated in the validation of the model in Figs. 4.7 and 4.8, the power drawn during acceleration significantly exceeds the power required for cruising. Rather than having the ERS provide the vehicles with the transient power peaks associated with acceleration, these power peaks are managed by the BEVs' batteries rather than the ERS supply. As a result, the ERS is not required to be engineered to handle these power peaks and can be used to provide steady energy to multiple vehicles under constant speed conditions. In this thesis, the ERS main operational functionality is considered to be provide a constant power to BEVs with ERS access.

Two types of vehicles are considered for the vehicle model: a passenger car with parameters derived from a Nissan Leaf [85], and a truck with parameters obtained from a Tesla Semi-Truck [86]. The simulation parameters for the vehicle model and each vehicle type are detailed in Table 4.4, where some parameters are estimated due to the lack of publicly available information. Note that the electric traction power represents the available traction power and does not correspond to the continuously drawn power for consumption. In [85], the power consumption of the Nissan Leaf is reported as 163 Wh/km, and in [87], the power consumption of the Tesla Semi Truck is reported as 1.1 kWh/km. These values align well with the simulated power consumption for each vehicle type in the presented ERS deployment cases.

The battery size for each vehicle has been intentionally omitted, as this parameter is closely related to the concept of ERS. By implementing ERSs, the battery size of vehicles can be reduced. Consequently, the battery size is dependent on the ERS coverage factor k_{ERS}, which is introduced at the beginning in Chapter 2. The concept of k_{ERS} and the direct power transfer to the vehicle's propulsion system are further elaborated in subsequent

Table 4.4: Simulation parameters for the vehicle model.

Vehicle model parameters			
Parameter	*Unit*	*Value*	
		Truck	**Car**
Wheel radius	m	0.506*	0.3
Drag coefficient	-	0.7*	0.32*
Roll resistance coefficient	-	0.0032*	0.01*
Front area	m^2	9.7*	2.28
Mass	kg	37000	1600
Electric traction power	kW	384*	80
Maximum auxiliary power	kW	20 *	10*

* Estimated values

subsections of this chapter. Although the sizing of the battery in relation to k_{ERS} is beyond the scope of this thesis, the charging power to the battery is considered.

In this thesis, it is assumed that the power transfer capabilities of the vehicles are constrained by volume limitations onboard. Although not specified in Table 4.4, it is anticipated that passenger cars will have a maximum total transfer capability of 50-60 kW. In contrast, trucks may have a total power draw that exceeds their transfer capability limit, depending on design choices as extensively discussed in [36].

The total drawn power per vehicle is determined by the vehicle model, considering the following factors:

1. The power consumption for propulsion and its dependency on vehicle parameters, such as weight, rolling resistance, frontal area, and average speed.
2. The estimated power consumption of the vehicle's auxiliary systems.
3. The estimated charging power to the vehicle battery.

The total power consumption per vehicle, for both the car and the truck as modelled by the vehicle model, is used as an input parameter when assessing the performance of the considered ERS technologies in terms of power flow, losses, and efficiency across various deployment environments.

4.5 Model Composition

To accurately replicate the proposed deployment environments for the considered ERS technology, it is necessary to consider not only the power consumption of vehicles utilizing the ERS but also the number and distribution of vehicle types. Given the complexity of this task, which encompasses a broad field of research in itself, assumptions are made regarding traffic intensity and vehicle distribution. The assumed number of vehicles and the distribution of vehicle types are sourced from data provided by the Swedish Transport Administration [39]. Since the power, losses, and efficiency of the ERS, as well as the distribution of losses across its components and subsystems, are highly dependent on these assumptions, the focus of these simulations is not on the accuracy of the assumed traffic characteristics nor on the exact values of their corresponding simulated results for power, losses, and efficiency. Rather, the emphasis is on the trends in power, losses, and efficiency influenced by these assumptions.

To assess how the performance of the considered ERS technology relates to and depends on different deployment environments and associated traffic conditions, three deployment scenarios are introduced in this chapter: urban, rural, and highway. To represent traffic for each deployment scenario, including the types and number of vehicles, assumptions are made based on data from [39], examining urban, rural, and highway roads. The composition of vehicles in each deployment case is based on hourly traffic data, with a conservative approach of selecting hours with intense traffic conditions at roads with overall high traffic intensity. Generally, trucks are less common on urban roads compared to highways, where they are more prevalent, with rural roads falling somewhere in between. However, to make more conservative choices regarding power draw from vehicles to the ERS, the rural scenario includes 8 cars and 1 truck, while the highway scenario comprises 2 trucks and 7 cars. The urban scenario features 16 cars to represent the more traffic-intensive environments of cities, which are dominated by passenger cars.

The model is configured such that each simulation case is represented by a single rectifier station and grid-connected circuit model, as illustrated in Fig. 4.4, along with two branches of series-connected SER circuit models, as depicted in Fig. 4.5 and shown in Fig. 4.3. Each SER circuit model is connected to a vehicle circuit model, where the SER circuit model accounts for the losses and total impedance between the vehicle and the preceding vehicle in the cluster. The point of connection between the rectifier and the series-connected SER circuit models is referred to as the feeding point. The SER circuit model closest to the feeding point is utilized to evaluate the impedance and losses of the SER relative to the vehicle nearest to this feeding point.

On both sides of the feeding point, clusters of vehicles are powered by the electric road, as illustrated in Fig. 4.9 and Fig. 4.10. The first cluster is positioned at the far end of the electric road, to the left of the rectifier station, defined by d_1, and is moving towards the feeding point. The second cluster is located at the feeding point, defined by d_2, and is moving away from it. The distance between vehicles within each cluster is uniform and predetermined to be equivalent to 3 seconds, meaning the distance between vehicles varies with their speed.

From a loss perspective, placing a cluster of vehicles at the very end of the electric road is a conservative approach. As discussed in the introduction of this chapter, this configuration results in the highest losses for the vehicle cluster because the maximum length of the electric road from the feeding point introduces maximum resistance. To balance this, the first cluster draws power from the farthest point from the feeding point (d_1), while the second cluster starts at the feeding point (d_2). As one cluster approaches the feeding point and the other moves away, with both clusters traveling at the same constant speed, the total resistance in the system remains relatively constant. However, to account for potential variations in losses due to this setup, all simulation results are based on mean values derived from at least 3 seconds of simulation, corresponding to a traveled distance of 30-90 meters, depending on vehicle speed.

4.5.1 Deployment Parameters

For each deployment case, the original parameters from the validation, as presented in Tables 4.1 to 4.3, are used with the following exceptions:

- The original 400 kVA transformer specified in Table 4.1 is replaced by a similar transformer rated at 800 kVA, as detailed in Table 4.5, with parameters obtained from [47]. This adjustment is necessary because the power drawn in all deployment cases exceeds 400 kW, requiring a transformer with a higher power rating to prevent issues such as voltage collapse or excessive transformer losses. In simulation scenarios where the power drawn surpasses 800 kW, an additional 800 kVA transformer is connected in parallel to manage the total power demand effectively.

- The resistance values per unit length for the SER cable parameters are adjusted according to the total drawn power to avoid excessive losses in this component. This adjustment is made to shift the simulation's focus towards the electric road components and to maintain realistic design considerations. The reduced resistance values per unit length are determined using integer division, which indicates the installation of an additional parallel cable.

  As previously mentioned, the resistance of the negative conductor in the SER cable is maintained at half the value of the positive conductor. This design choice is intended to mitigate potential voltage drops in the negative conductor, as the negative pole of the electric road is exposed externally.

- Regardless of the vehicle type, the same vehicle circuit model, as illustrated in Fig. 4.6, with parameters specified in Table 4.3, is utilized consistently across all vehicle types.

- The resistance per unit length of the positive conductors in the SER is halved (from 42 to 21 mΩ/km) to represent that both of the two positive conductors are deployed. The original demonstrator design did not fully exploit this capacity, as only one of the two positive conductors was installed.

Table 4.5: Parameters for the transformer used for the deployment cases.

Transformer parameters		
Parameter	*Unit*	*Value*
Nominal power	kVA	800
Nominal line-line voltages	$\mathrm{kV_{RMS}}$	11, 0.45
Winding resistance	p.u.	0.004, 0.0024
Positive-sequence no-load excitation current	% of I_{nominal}	0.09
Positive-sequence no-load losses	W	595
Positive-sequence short-circuit reactance	p.u.	0.044

4.5.2 Power Allocation Between Vehicle Subsystems

Given practical and economic constraints, it is not feasible to cover the entire length of a road with electric road when deploying an ERS [33, 37]. Consequently, the parameter k_{ERS}, introduced in Chapter 2, quantifies the ratio of the length of the electric road to the total road length. For instance, a k_{ERS} value of 0.5 means that 50% of the road is equipped with electric road infrastructure. Typical theoretical values for k_{ERS} are around 0.5, as this ratio is generally the most cost-efficient [33].

The parameter k_p, as discussed in Section 2.1.3 in Chapter 2, represents the ratio of the total power drawn from the ERS that is allocated directly to the vehicle's propulsion system and auxiliary systems. The remaining power is used to charge the battery. To sustain the SoC of a BEV throughout a trip, the battery must be sufficiently charged to cover the distance traveled when ERS access is unavailable. Thus, k_{ERS} should equal k_p. However, if an ERS with $k_{\mathrm{ERS}} = 0.5$ is utilized primarily to fill the BEV's battery rather than maintaining its SoC, then k_p must be less than 0.5 to achieve a higher SoC by the end of the trip. This scenario could involve a shorter journey that prepares the BEV for a subsequent trip with limited or no charging opportunities. To achieve a specific SoC level, the parameter k_p may need to be adjusted dynamically during the trip, depending on ERS availability, to ensure the desired SoC level is reached by the end of the trip.

In this thesis, the selected values for $k_{\mathrm{ERS}} = k_p$ are consistently set below 0.5 across all simulation scenarios for the following conservative reasons:

1. Values of $k_{\text{ERS}} = k_p = 0.5$ necessitate extensive deployment of ERS infrastructure, which entails substantial capital costs and significant logistical efforts. Therefore, opting for lower values of k_{ERS} reflects a more cautious approach.

2. As detailed in Section 2.1.3 of Chapter 2, a key benefit of ERS is its capability to deliver power directly to the BEV's propulsion and auxiliary systems, thereby facilitating high efficiency, as will be shown in the results presented in this chapter. By selecting lower values for k_p, this chapter adopts a more conservative approach in optimizing the efficiency benefits of ERS.

An additional factor influencing the choice of k_{ERS} is the availability of grid connections, as this indirectly affects the length of the electric road and the total power drawn per vehicle as well as the cumulative power drawn by all vehicles. This, in turn, impacts k_{ERS} and k_p. For each ERS deployment scenario—urban, rural, and highway—the motivation behind the choice of k_{ERS} and $k_{\text{ERS}} = k_p$ is loosely based on a publicly available infrastructure map of Sweden from [88] and a publicly available map indicating the current locations of conventional static chargers from [89].

4.5.3 Urban Deployment of Electric Roads - Parameters

In Fig. 4.9, an overview of the urban simulation case is presented with an arbitrary number of cars, denoted n. The modelled urban deployment case includes 16 cars ($n = 16$) each drawing 40 kW at a speed of 40 km/h on 1020 m of electric road (L), as detailed in Table 4.6. These parameter choices represent a typical urban ERS deployment with a congested traffic load comprising solely passenger cars.

The initial position of the left cluster of vehicles is 300 m from the feeding point (d_1), while the right cluster is positioned at the feeding point ($d_2 = 0$ m). The distance between the vehicles within each cluster is maintained at 30 meters. To ensure that the system can accommodate a total power draw of 640 kW, an 800 kVA transformer, with the parameters specified in Table 4.5, is used. The positive conductor of the cable between the rectifier station and the electric road is characterized by a resistance of 31.25 mΩ/km, while the negative conductor exhibits a resistance of 15.63 mΩ/km. These cable parameters are chosen to facilitate the total power draw of the vehicles while avoiding excessive losses in the cable.

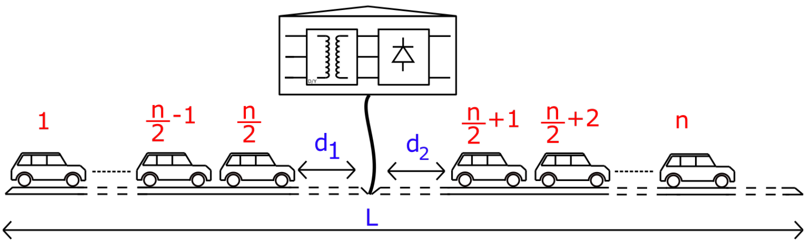

Figure 4.9: Overview of the urban simulation case with a total of *n* vehicles. One rectifier station supplies two connected electric road sections. Each electric road section has a cluster of cars in movement, either approaching or leaving the rectifier station. The distances between the rectifier station and the clusters are denoted d_1 and d_2. The total electric road length for the simulation case is *L*. Figure taken from [21].

Table 4.6: Simulation parameters for urban deployment.

Simulation parameters Urban		
Parameter	*Unit*	*Value*
Infrastructure		
Transformer	kVA	800
Cable positive conductor	mΩ/km	31.25
Electric road length, L	m	1020
Left distance feeding point, d_1	m	300
Right distance feeding point, d_2	m	0
Vehicles		
		Car
Number of vehicles		16
Distance between vehicles	m	30
Speed	km/h	40
Total Power	kW	40
Auxiliary & Propulsion Power	kW	6
Battery Power	kW	34
Ratio of power to Auxiliary & Propulsion, k_p		0.15

The total power drawn per vehicle is 40 kW, of which 6 kW is allocated for auxiliary systems and propulsion, and the remaining 34 kW is dedicated to charging the battery. This corresponds to a mean value of $k_p = 0.15$. This low value of k_p and ERS length (L) of 1020 m is motivated by the following assumptions:

1. In cities, the ERS length is constrained by space limitations related to road planning and other obstructions in the urban infrastructure.

2. The presence of multiple potential grid connections for rectifier stations allows for a denser distribution of rectifier stations along the ERS.
3. Due to the low power consumption at the low speeds typical of urban environments, there is an opportunity to utilize the available power for battery charging. Which means that BEVs can charge their batteries in preparation for a subsequent journey where the excess energy is required.

4.5.4 Rural Deployment of Electric Roads - Parameters

The rural simulation case represents an ERS deployed in a rural environment, accommodating 8 cars and 1 truck driving at 70 km/h on 3360 meters of electric road (L), as detailed in Table 4.7. The rural deployment case is characterized by a long electric road with limited power draw for vehicles with higher power consumption, such as trucks, due to the assumption of scarce and weak grid connections in rural areas.

Table 4.7: Simulation parameters for rural deployment.

Simulation parameters Rural			
Parameter	*Unit*	*Value*	
Infrastructure			
Transformer	kVA	800	
Cable positive conductor	mΩ/km	31.25	
Electric road length, L	m	3360	
Left distance feeding point, d_1	m	1500	
Right distance feeding point, d_2	m	0	
Vehicles			
		Car	**Truck**
Number of vehicles		8	1
Distance between vehicles	m	60	60
Speed	km/h	70	70
Total Power	kW	50	150
Auxiliary & Propulsion Power	kW	10	68
Battery Power	kW	40	82
Ratio of power to Auxiliary & Propulsion, k_p		0.23	

Fig. 4.10 provides an overview of the rural simulation case. In this scenario, the left cluster of vehicles starts 1500 m (d_1) from the feeding point, while the right cluster starts at the feeding point ($d_1 = 0$ m). The distance between vehicles within each cluster is maintained at 60 m. The rural simulation case employs the same parameters for transformer power rating and cable dimensions between the electric road and rectifier station as the urban case. The truck draws a total power of 150 kW, with 82 kW allocated to battery charging. Each car draws 50 kW, with 40 kW allocated to battery charging. This yields a mean value of the direct power transfer to propulsion and auxiliary systems of $k_p = 0.23$.

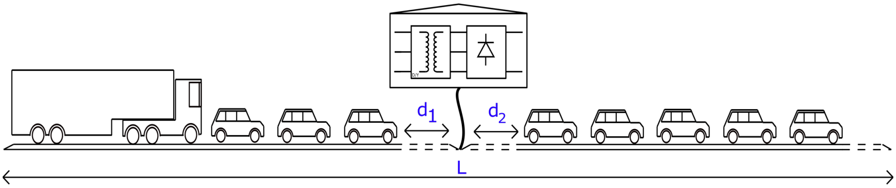

Figure 4.10: Overview of simulated rural deployment. One rectifier station supplies two connected electric road sections. Each electric road section has a cluster of vehicles in movement, either approaching or leaving the rectifier station. The distances between the rectifier station and the clusters are denoted d_1 and d_2. The total electric road length for the simulation case is L. Figure taken from [21].

In the context of the rural deployment case discussed in this chapter, it is anticipated that grid connections in rural areas will be scarce and characterized by weak grid connections. This leads to low values of $k_{ERS} = k_p$ and necessitates the use of long electric roads, such as 3.4 km. Although the truck could potentially benefit from drawing a higher power to accelerate battery charging, the grid connection for the ERS in this scenario is assumed to be insufficient for such an increase.

4.5.5 Highway Deployment of Electric Roads - Parameters

In the highway deployment case, the model features seven passenger cars, each drawing 50 kW at a speed of 110 km/h, and two trucks, each drawing 300 kW at a speed of 90 km/h, accessing an electric road with a length of 2642 meters (L), as detailed in Fig. 4.11 and Table 4.8. Due to the significantly higher speeds compared to the urban scenario, the spacing between vehicles, the length of the electric road (L), and the distance of the left vehicle cluster (d_1=1000 m) from the feeding point are all increased, while the distance of the right vehicle cluster from the feeding point (d_2) remains at 0 meters. To accommodate the total power draw of 950 kW, two 800 kVA transformers, as specified in Table 4.5, are required. To minimize cable losses between the rectifier station and the electric road, the resistance of the positive conductor is reduced to 20.8 mΩ/km, with the negative conductor having half of this resistance value.

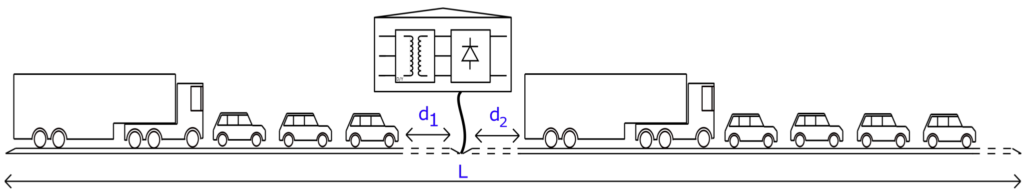

Figure 4.11: Overview of simulated highway deployment. One rectifier station supplies two connected electric road sections. Each electric road section has a cluster of vehicles in movement, either approaching or leaving the rectifier station. The distances between the rectifier station and the clusters are denoted *d1* and *d2*. The total electric road length for the simulation case is *L*.

Table 4.8: Simulation parameters for highway deployment.

Simulation parameters Highway			
Parameter	*Unit*	*Value*	
Infrastructure			
Transformer	kVA	$2 \cdot 800$	
Cable positive conductor	mΩ/km	20.8	
Electric road length, L	m	2642	
Left distance feeding point, d_1	m	1000	
Right distance feeding point, d_2	m	0	
Vehicles			
		Car	**Truck**
Number of vehicles		7	2
Distance between vehicles	m	107	107
Speed	km/h	110	90
Total Power	kW	50	300
Auxiliary & Propulsion Power	kW	21	108
Battery Power	kW	29	192
Ratio of power to Auxiliary & Propulsion, k_p		0.41	

For highway deployment, the average value of power directly transferred to vehicle propulsion and auxiliary systems, is 0.41 where $k_{ers} = k_p$ is assumed. This is based on that highway ERS deployments are expected to require more robust and numerous grid connections compared to the presented rural case, leading to higher power draw per vehicle and shorter electric road lengths per rectifier station. However, an examination of publicly available infrastructure maps of Sweden [88] and the locations of conventional static charging stations [89] does not distinctly indicate a significantly greater number of grid connections along highway roads compared to rural roads. Nevertheless, due to higher traffic intensity of highway environments, the initiative to expand grid connections along highways is expected to be greater compared to rural roads.

4.6 Simulation Results

The simulations for each modelled deployment case yield voltage and current data at interfaces A to D (see Fig. 2.13). These data are used to calculate power, losses, and efficiency at these interfaces. For interfaces C-D, additional measurements are included in the simulation to provide data to assess the distribution of losses in each ERS component between these interfaces. This allows for a detailed evaluation of losses in the cable between the rectifier and the electric road, the SER conductors, the SER semiconductors, the contact resistance, and the onboard rectifier losses.

4.6.1 Urban Deployment of Electric Roads - Results

In Table 4.9 power and efficiency between interfaces A-D are detailed for the urban deployment case. Fig. 4.12 illustrates the distribution of losses in each ERS component at interfaces A-D. Overall, the considered ERS technology demonstrates excellent performance in this deployment scenario, with total losses amounting to 24 kW across interfaces A-D and achieving an efficiency of 96.7%. This performance is attributed, in part, to the relatively short length of the electric road and modest total power draw of 640 kW.

Table 4.9: Simulation results for urban deployment.

Simulation results Urban					
Simulation case	*Unit*	*Value*			
		Power			
		A	**B**	**C**	**D**
Urban Nominal	kW	664	659	651	640
		Efficiency			
		A-B	**B-C**	**C-D**	**A-D**
Urban Nominal	%	99.4%	98.9%	98.3%	96.7%

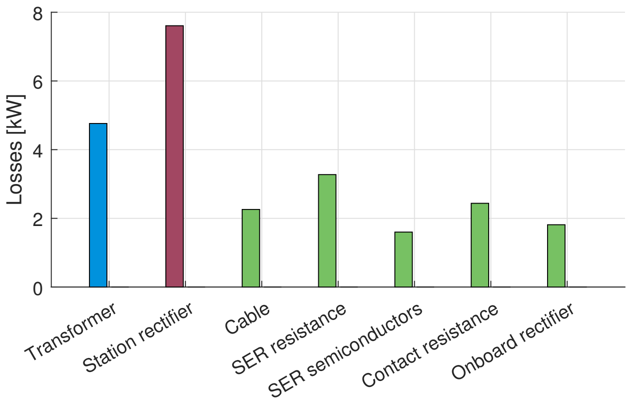

Figure 4.12: Simulated losses per component in the ERS for urban deployment. Blue color represents components at interface A-B. Red color represents components at interface B-C. Green color represents components at interface C-D.

The primary factors contributing to the low losses are the length of the electric road and the relatively low power draw per vehicle. This suggests that the ERS technology is well-suited for urban applications given the proposed electric road length and traffic intensity. Notably, the semiconductors (diodes and solid-state switches) in the rectifier station, as illustrated in Fig. 4.4, represent the largest portion of the losses. This is because, with a high number of vehicles drawing relatively low power and a short electric road length, the predominant losses occur at the rectifier station, where the total current flows through the rectifier and solid-state switch components. Since losses are proportional to I^2, the total current passing through the rectifier station is significantly higher than the current distributed among individual vehicle circuits.

Given the generally low losses and high efficiency of the ERS in the urban deployment case, it is challenging to justify the need for improvements to specific components or to identify any component as a significant source of excessive losses. All ERS components exhibit very low losses relative to the total power draw. However, the resistive losses in the SER conductors is less than half of the losses in the station rectifier. Therefore, it may be more cost-effective to reduce the overall losses by reducing the semiconductor losses associated with the semiconductors in the rectifier station than reduce the cross-sectional area of the conductors in the electric road.

It should be noted that the semiconductor components collectively (including the station rectifier, SER semiconductors, and onboard rectifier) account for almost half of the total losses when compared to the purely resistive components (the transformer, cable between rectifier station and SER, SER resistance, and contact resistance). This is a consequence of the extensive use of semiconductors in the considered ERS technology, both for activating individual segments and for rectifying the current supplied to the vehicle. As a result, the losses in these semiconductors may impact the overall system efficiency, especially when the number of vehicles is high and the power per vehicle is relatively low. From the perspective of improving system efficiency, this approach might seem counterintuitive, as semiconductor losses may not be the first aspect to consider. This will be further examined in Section 4.7.3.

4.6.2 Rural Deployment of Electric Roads - Results

The rural deployment case is characterized by scarce and weak grid connections, resulting in a long electric road and fewer vehicles than the urban case. Consequently, this leads to poorer efficiency and loss performance compared to the urban scenario, as detailed in Table 4.10. Despite the increased length of the electric road and fewer vehicles, the total losses in the rural case (28 kW) are similar to those in the urban case (24 kW). However, considering the lower total power draw in the rural scenario, the efficiency is lower, at 95.3%.

Table 4.10: Simulation results for rural deployment.

Simulation results Rural					
Simulation case	*Unit*	*Value*			
		Power			
		A	**B**	**C**	**D**
Rural Nominal	kW	578	574	568	550
		Efficiency			
		A-B	**B-C**	**C-D**	**A-D**
Rural Nominal	%	99.5	99	96.8	95.3

Fig. 4.13 presents the distribution of losses among the ERS components in the rural deployment case. The primary contributor to losses is the resistive losses in the main conductors of the SER, attributed to the extensive length of the electric road. For deployment environments involving long electric road lengths, design improvements in the material and/or the cross-sectional area of the SER conductors could be considered to enhance overall system efficiency.

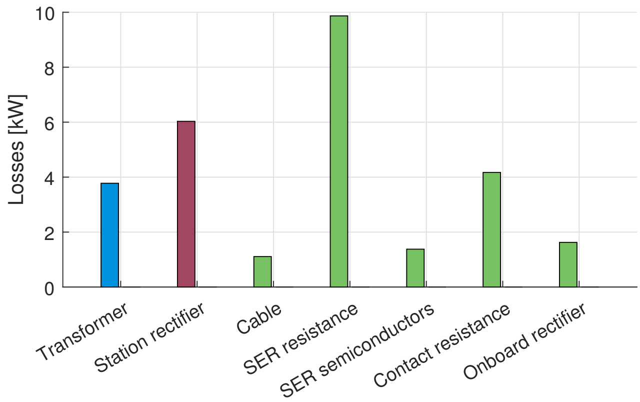

Figure 4.13: Simulated losses per component in the ERS for rural deployment. Blue color represents components at interface A-B. Red color represents components at interface B-C. Green color represents components at interface C-D.

Although the efficiency in the rural simulation case is lower than in the urban simulation case, the simulated rural case efficiency might still be adequate for rural ERS deployment. Nonetheless, it is evident that to achieve greater efficiency, improvements are needed in the resistance per unit length of the SER conductors and possibly in the rectifier station, as illustrated in Fig. 4.13.

4.6.3 Highway Deployment of Electric Roads - Results

In Table 4.11, the simulated power and efficiency for the highway deployment case are presented, along with the distribution of losses between ERS components, as shown in Fig. 4.14. This scenario is characterized by a relatively long electric road length of 2642 meters and a high total power draw of 950 kW, primarily due to the relative high number of trucks drawing 300 kW each. Consequently, this simulation case corresponds to the greatest total losses of all three simulation cases resulting in 70 kW. The system efficiency is as low as 93.7%, with the largest portion of the losses attributed to the contact resistance, the station rectifier, and the resistance of conductors in the SER, as shown in Table 4.11, where losses at interface C-D reach 43 kW. A system efficiency of 93.7% might seem low compared to other simulation cases; nevertheless, it could still be adequate for deployment. However, it is important to consider the overall efficiency of the charging system, including the battery efficiency, rather than focusing solely on the ERS efficiency, as discussed in the subsequent section.

Table 4.11: Simulation results for highway deployment.

Simulation results Highway					
Simulation case	*Unit*	*Value*			
Power					
		A	**B**	**C**	**D**
Highway Nominal	kW	1020	1010	993	950
Efficiency					
		A-B	**B-C**	**C-D**	**A-D**
Highway Nominal	%	99.5	98.5	95.6	93.7

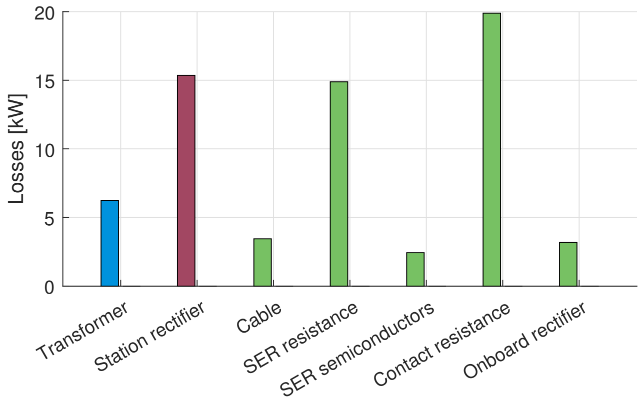

Figure 4.14: Simulated losses per component in the ERS for highway deployment. Blue color represents components at interface A-B. Red color represents components at interface B-C. Green color represents components at interface C-D.

The contact resistance is identified as the most prominent source of losses among the ERS components in the highway deployment case, as detailed in Fig. 4.14. Given the lack of available measurements for contact resistance or losses associated with the sliding contact of the considered ERS technology at speeds above 50 km/h, as presented and discussed in Chapter 3, the results concerning the losses of the sliding contact in the model should be interpreted with caution for deployment cases with vehicle speeds surpassing 50 km/h. Since the sliding contact is still in the development phase for the considered ERS technology, it is possible that the presented results may either overestimate or underestimate the actual losses. Nonetheless, the findings indicate that further development and research are necessary to enhance the performance of the sliding contact in terms of reducing losses and, consequently, improving the overall system efficiency.

In the highway deployment scenario, significant losses are observed due to the resistance of the SER conductors, similar to the rural case. Specifically, the highway case demonstrates losses of 15 kW in the SER resistance, compared to 10 kW observed in the rural deployment case. This highlights the necessity for increased cross-sectional area of the SER conductors, particularly in high-power scenarios and extended electric road lengths.

Additionally, the station rectifier in the highway case also contributes notable losses of 15 kW. This indicates a potential need for re-evaluating the topology and semiconductor components used in the rectifier station to enhance overall system efficiency. The subsequent section will conduct an analysis to explore these significant loss components and assess potential improvements through parameter sweeps.

4.6.4 Implications of Power Allocation Between Vehicle Subsystems

When evaluating the system efficiency of the ERS technology under consideration, it is essential to account for the deployment strategy of the technology. While the results presented in the preceding subsections reflect ERS efficiency values associated with a fixed k_p, these values pertain only to scenarios where vehicles have access to the ERS. As detailed in the introduction in Chapter 2 and in Section 4.5.2 of this chapter, the ERS is designed to be sectioned, as defined by the coverage factor parameter k_{ERS}.

In this context, the overall system efficiency is influenced not only by the efficiency of the ERS itself but also by the efficiency of the system when vehicles lack ERS access. This includes considerations for the efficiency of the BEV battery. In this section, the system efficiency for a charging infrastructure—whether ERS or conventional static charging stations—is defined as the ratio between the energy effectively used to propel the vehicle and the total energy drawn from the power grid during a trip. While no specific strategies for sectioning the ERS are proposed, a detailed discussion on this topic is available in [36]. Instead, this work focuses on evaluating the impact of the parameter k_p, which specifies the amount of power allocated directly to vehicle propulsion and auxiliary systems.

To evaluate the system efficiency and its correlation with k_p, the efficiency results presented in the previous subsections are compared with those of a conventional static charger. The system efficiency for conventional static charging stations, denoted as η_{SC}, is calculated according to Eq. (4.6). The parameter $\eta_B = 0.97$ represents the battery efficiency, assumed to be the same for both charging and discharging, as cited in [90]. The parameter $\eta_{Ch} = 0.95$ indicates the efficiency of a DC fast charger, obtained from [91].

$$\eta_{SC} = \eta_{Ch} \cdot \eta_B^2 \tag{4.6}$$

The ERS system efficiency, denoted as η_{ERSS}, is calculated for all considered deployment cases—urban, rural, and highway—according to Eq. (4.7). In this calculation, the ERS efficiency η_{ERS} is derived from Tables 4.9 to 4.11. The battery efficiency $\eta_B = 0.97$ remains consistent with previous assumptions, obtained from [90]. Additionally, the efficiency of the onboard DC/DC converter, which acts as the power electronic interface between the ERS supply and the vehicle's TVS, is assumed to be $\eta_{DC/DC} = 0.97$, as cited from [92]. The parameter k_p denotes the fraction of the total power drawn from the ERS that is directly allocated to the vehicle's propulsion and auxiliary systems. For simplicity, it is assumed that this parameter remains uniform across all vehicles and does not affect the ERS efficiency η_{ERS} for each deployment case.

$$\eta_{ERSS} = \eta_{DC/DC} \cdot \eta_{ERS} \cdot (k_p + (1 - k_p) \cdot \eta_B^2) \tag{4.7}$$

In Fig. 4.15 the ERS system efficincy for the urban, rural and highway deployment cases is compared to the system efficiency of a conventional static fast charger at different values of k_p by applying Eqs. (4.6) and (4.7). The pink area represents values for $k_p > 0.7$ that would require $k_{ERS} > 0.7$ to maintain the SoC level in a BEV for a trip. $k_{ERS} > 0.7$ is not considered realistic in this thesis, as there are practical limitations regarding where ERS can be installed in reality (e.g., crossroads, curves, etc.). The vertical lines show the corresponding mean values of k_p from the urban, rural and highway deployment cases from Tables 4.6 to 4.8. The yellow horizontal line illustrates the system efficiency for conventional static charging from Eq. (4.6).

This comparison reveals that the efficiency of the charging infrastructure varies significantly with different values of k_p, depending on how the supplied ERS power is distributed between battery charging and remaining subsystems of the TVS. Although a higher k_p can enhance efficiency, it is constrained by the efficiency of the ERS during its operational period. This limitation is particularly evident in the highway deployment scenario, where the efficiency of the highway ERS only exceeds that of the static

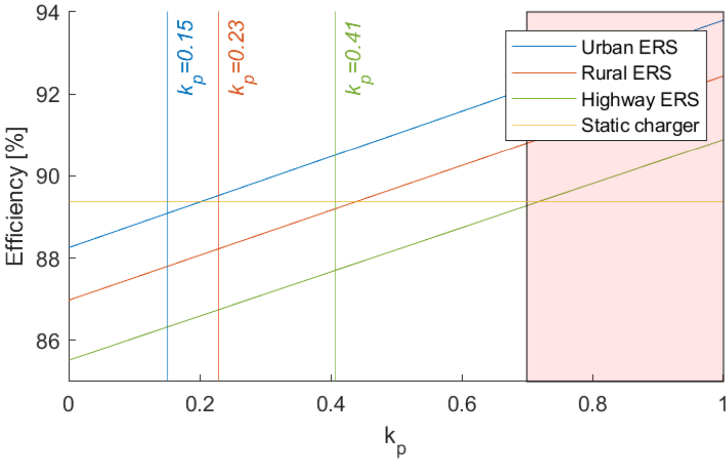

Figure 4.15: Efficiency for calculated urban (blue lines), rural (red lines) and highway deployment (green lines) with varying ratio of power transferred directly to the vehicles propulsion systems, k_p. The pink area represents values of k_p which are assumed to be unrealistic. The yellow line shows the efficiency of the DC fast charger in conjunction with the battery efficiency.

charger when k_p exceeds 0.7 (with $k_{ERS} = 0.7$), which is at the upper boundary of what is considered feasible for the considered ERS technology in this thesis. Note that in none of the urban, rural, or highway deployment cases, with the selected values of k_p, does their respective system efficiency surpass that of the conventional static charger.

Although this may be perceived as an indication of sub-optimal system efficiency when compared to conventional static chargers, it highlights the necessity for thorough consideration in the design of ERS. Specifically, the ERS efficiency, in conjunction with the direct power transfer factor (k_p) and the coverage factor (k_{ERS}), must be rigorously evaluated for future ERS deployments. In the urban and rural cases the overall system efficiency can surpass the system efficiency of the static charger by adjusting the parameter k_p. Regardless of the overall system efficiency of ERS, from a practical perspective, ERS can still offer advantages over conventional static chargers. ERS offers dynamic charging, thereby mitigating risks concerning congestion and queues at static charging stations.

4.7 Influence of Selected Parameters

As previously stated in Section 4.5, the presented deployment cases are intended to be indicative and not regarded as absolute truths in the context of traffic intensity and conditions. To further evaluate the factors affecting power flow, losses, and efficiency, a parameter analysis is performed on the deployment cases. The analysis in the urban case focuses on varying the total power drawn per vehicle and the number of vehicles. In contrast, the highway case examines improvements or alterations to ERS components, namely the sliding contact, the semiconductors in the rectifier station, and the conductors of the SER, as well as the impact of reducing the power drawn per vehicle. These ERS component parameters are selected due to that they are associated with the greatest losses as illustrated in Fig. 4.14. Additionally, the practical feasibility of implementing the suggested parameter variations is discussed. The simulation cases presented in this section are executed with the same parameters as those in the original deployment cases, with only the considered parameters being altered.

4.7.1 Urban Deployment of Electric Roads - Considered Parameters

The original urban simulation case demonstrated excellent performance in terms of losses and efficiency, but also highlighted the distribution of semiconductor losses and pure resistive losses. By simulating this case again, with different numbers of vehicles and varying values of the power drawn per vehicle, the performance of the ERS deployment in the urban case is assessed in terms of both losses and efficiency, and the loss distribution between semiconductor and resistive losses is characterized.

16 different simulations are presented, involving a sweep where the number of vehicles (n) is assessed at 4, 8, 12, and 16 at power levels of 10, 20, 40, and 60 kW, as detailed in Table 4.12. Each simulation case has the same configuration as previously presented in Section 4.5.3 and Fig. 4.9 and Table 4.6 with 1020 m of electric road and the left vehicle cluster starting at 300 m left of the feeding point (d_1). The number of vehicles, (n), is equally split between the left and right clusters.

Table 4.12: Simulation parameters for urban deployment with adjusted vehicle load parameters.

Simulation parameters Urban adjusted vehicle load		
Parameter	*Unit*	*Value*
	Vehicle load 1-4	
Number of vehicles	-	4
Power per vehicle	kW	10, 20, 40, 60
	Vehicle load 5-8	
Number of vehicles	-	8
Power per vehicle	kW	10, 20, 40, 60
	Vehicle load 9-12	
Number of vehicles	-	12
Power per vehicle	kW	10, 20, 40, 60
	Vehicle load 13-16	
Number of vehicles	-	16
Power per vehicle	kW	10, 20, 40, 60

4.7.2 Highway Deployment of Electric Roads - Considered Parameters

Three distinct analyses are conducted on the highway deployment case to evaluate potential improvements in the design and performance of the ERS for this scenario. In the first analysis, the contact resistance is considered. The second analysis examines the combined impact of contact resistance, the semiconductors in the rectifier station, and the SER resistance. Finally, the third analysis assesses the impact of reducing the power drawn per vehicle.

In the highway simulation, the initial parameter assessed is the contact resistance, which is related to the performance of losses associated with the sliding contact. The simplified contact resistance parameter used in the vehicle circuit model, as presented in Section 4.2.4, which considers only two sliding contacts, might not accurately model current collector designs with 6 or more sliding contacts. Moreover, as presented and discussed in Chapter 3, the contact resistance for one sliding contact varies greatly over time and can intermittently increase by a factor of 10 in some cases. Nonetheless, the model validation shows that this simplification can reasonably describe sliding contact losses up to speeds of 30 km/h. To address uncertainties related to the contact resistance parameter, an analysis is conducted to assess its impact.

The contact resistance is adjusted to 5, 10, 30, and 50 mΩ, as detailed in Table 4.13. As previously noted, there is limited knowledge regarding contact resistance in current collectors adapted for conductive ERS. The values of 5 and 10 mΩ reflect anticipated improvements in future sliding contact development, with 5 mΩ being considered more extreme and less realistic, while 10 mΩ is regarded as more achievable based on experimental results from the validation of the simulation model, where the contact resistance was set to 16 mΩ, albeit at speeds of only 30 km/h. The contact resistance parameters of 30 and 50 mΩ represent scenarios in which resistance increases with speed. This increase is based on the assumption that the design of the current collector and corresponding sliding contacts may not maintain a stable connection at higher speeds due to the anticipated elevated forces exerted on the sliding contacts.

Table 4.13: Simulation parameters for highway deployment with adjusted contact resistance parameters.

Simulation parameters Highway adjusted design		
Parameter	*Unit*	*Value*
	Contact resistance design 1	
Contact resistance	mΩ	5
	Contact resistance design 2	
Contact resistance	mΩ	10
	Contact resistance design 3	
Contact resistance	mΩ	30
	Contact resistance design 4	
Contact resistance	mΩ	50

For the second analysis the combination of improved semiconductors in the rectifier station, thicker positive SER conductors, and reduced contact resistance are evaluated. Two simulations are conducted to demonstrate potential design modifications that could reduce the losses in these specific ERS components with parameter values detailed in Table 4.14.

- Firstly, the resistive on-losses in the diodes of the passive 6-pulse rectifier are adjusted to 0.5 and 1 mΩ to reduce losses in the rectifier station. This improvement can be achieved by selecting diodes with lower resistive conducting on-losses [93].

- Secondly, the contact resistance is adjusted to 5 and 10 mΩ. These values reflect anticipated improvements in future sliding contact development, with 5 mΩ considered more extreme and less realistic, while 10 mΩ is deemed more achievable.
- Thirdly, to improve the resistance of the SER conductors, two strategies can be applied: I) altering the material used in the SER conductors to one with higher conductivity, such as replacing aluminum with copper, and II) increasing the cross-sectional area of the conductors.

However, increasing the cross-sectional area of the positive conductor, which already has significantly higher resistance compared to the negative conductor, will have a greater impact on the road surface and underlying road layers. The resistance value of the positive SER conductor is 21 mΩ/km, corresponding to a cross-sectional area of 1266 mm^2 for the positive conductors and a combined cross-sectional area of 8888 mm^2 for both poles.

Although it is feasible to increase the ratio of the positive cross-sectional conductor area relative to the negative cross-sectional area without compromising the dielectric properties between the two poles or inducing excessive voltage drops in the negative conductor due to its external exposure, such design modifications are limited. Ultimately, the total combined cross-sectional area must be improved.

Without further evaluation of these design requirements, which are beyond the scope of this thesis, an improved resistance value per unit length for the SER positive conductor is assumed to be 5 and 10 mΩ/km. Implementing SER resistance values of 5 and 10 mΩ/km for the positive conductor is expected to require considerable modifications to the road layers where the SER is installed. This would also lead to increased costs due to the need for superior materials or larger conductor cross-sectional areas.

Table 4.14: Simulation parameters for highway deployment with adjusted design parameters.

Simulation parameters Highway adjusted design		
Parameter	*Unit*	*Value*
Design alternatives 1		
Diode on-state resistance	mΩ	0.5
SER positive conductor resistance	mΩ/km	5
Contact resistance	mΩ	5
Design alternatives 2		
Diode on-state resistance	mΩ	1
SER positive conductor resistance	mΩ/km	10
Contact resistance	mΩ	10

In the third and final sensitivity analysis, the proposed power draw levels are selected to represent lower degrees of power supplied to the trucks' batteries, as detailed in Table 4.15, compared to the original total drawn power of 300 kW for one truck. This reduction in power provided to the trucks' batteries impacts the parameters k_p and k_{ERS}. Specifically, the lowest total power draw for the trucks, 150 kW, corresponds to $k_p = 0.72$, while a slightly higher total power draw of 225 kW corresponds to $k_p = 0.48$ for the trucks.

Table 4.15: Simulation parameters for highway deployment with adjusted power per vehicle.

Simulation parameters Highway adjusted vehicle power		
Parameter	*Unit*	*Value*
Adjusted power per vehicle 1		
Power per vehicle	kW	150
Adjusted power per vehicle 2		
Power per vehicle	kW	225

These design alterations suggest that if the total power drawn by the vehicle is limited, the ERS will be less strained, and consequently, no costly design alterations need to be considered for specific ERS components and subsystems. This strategy can be regarded in terms of quantity over quality—by limiting the power drawn per vehicle, the ERS development, installation, and possibly also the production costs are lowered. Consequently, ERS investments can be focused on wider deployments rather than implementing potentially costly development measures. These assumptions can be regarded as an attempt to shift the focus of investments and measures from the batteries installed in vehicles to wide deployment of the ERS infrastructure by increasing k_p and k_{ERS}.

4.7.3 Urban Deployment of Electric Roads - Influence of Traffic Intensity and Power Flow

As the original efficiency of the urban case performed exceptionally well, with a total efficiency surpassing 97%, and given that the specific losses for each ERS component are significantly low, no design improvements of any specific ERS components are suggested for this analysis. Instead, the focus is on how the efficiency and distribution of semiconductor and resistive losses are altered depending on the number of vehicles and the power drawn by the vehicles using the ERS.

In the urban case, 16 different simulations are presented in Fig. 4.16, involving an analysis where the number of vehicles (n) is assessed at 4, 8, 12, and 16, at power levels of 10, 20, 40, and 60 kW, as detailed in Table 4.12. The results are presented as follows: the total system losses between interfaces A-D (upper plot), the system efficiency between interfaces A-D (middle plot), and the share of semiconductor losses (comprising the semiconductors in the rectifier station, SER semiconductors, and onboard rectifier) in relation to the total losses (bottom plot). These results are shown as a function of the number of vehicles and the power drawn per vehicle.

The analysis indicates that losses are generally low, regardless of the power drawn and the number of vehicles. However, an exception occur in scenarios with a high number of vehicles (12-16) and relatively high drawn power per vehicle (40-60 kW), where losses peak at 40-45 kW. Notably, these losses correspond to a total drawn power of 960 kW, resulting in an efficiency of over 95%.

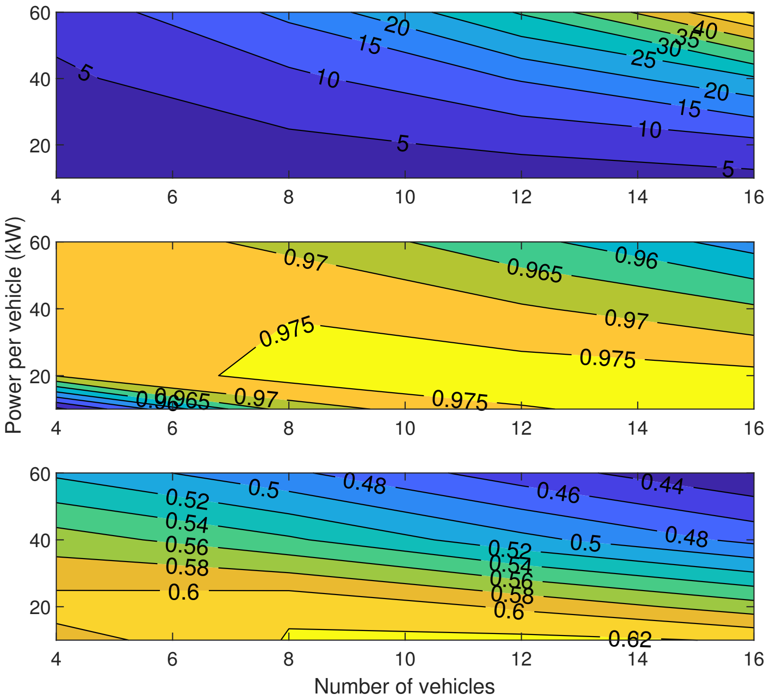

Figure 4.16: Simulated values between interfaces A-D: Losses [kW] (upper plot), efficiency (middle plot) and semiconductor losses divided by total losses (lower plot).

In the specific case of 960 kW total power draw, the use of a transformer rated for 800 kVA, chosen to maintain consistency across simulations, leads to slightly higher losses compared to other combinations in the analysis. Despite this, the additional losses attributable to the transformer are minimal and do not significantly impact the overall system performance.

The highest efficiency levels (97.5%) in the middle plot are obtained under two conditions: either with low power per vehicle (10-20 kW) and a high number of vehicles (12-16), or with slightly higher power per vehicle (15-35 kW) and 7-12 vehicles. Conversely, if the ERS is used by a low number of vehicles (4-6), each drawing relatively low power (10-20 kW), the efficiency decreases to approximately 95%.

This reduction in efficiency is attributed to increased open-circuit losses in the transformer (interfaces A-B) relative to the remaining losses in the ERS (interfaces B-D). In summary, the efficiency performance of the urban deployment, as indicated by the analysis, is generally high, reaching values over 96.5% for the majority of the presented simulation cases.

In the bottom plot, the share of semiconductor losses (comprising the semiconductors in the rectifier station, SER semiconductors, and onboard rectifier) divided by the total losses of the ERS is presented. It is observed that over 50% of the losses are attributed to the semiconductors for all combinations, except when the power per vehicle exceeds 40 kW and the number of vehicles exceeds 10, represented by the upper right corner of the plot. The increase in resistive losses for these combinations is due to the losses being proportional to the square of the current, which increase with higher drawn power. Additionally, with an increased number of vehicles, the total electric road length is extended, adding more aggregated resistance to the system. This result underscores the importance of accounting for semiconductor losses when optimizing the efficiency of the ERS design, as numerous semiconductors are a part of the system. This consideration becomes particularly significant in scenarios such as traffic congestion or queues, which are characterized by low power drawn per vehicle and a high number of vehicles.

Given that the efficiency exceeds 96.5% in most cases, it may be more advantageous to focus on improving the cost-effectiveness of the design rather than solely on enhancing efficiency. By prioritizing the reduction of semiconductor losses (from components such as the rectifier station, onboard rectifier, and SER semiconductors) and accepting a potential increase in resistive losses within the SER by using conductors with smaller cross-sectional area, a more cost-effective design could be achieved. This approach assumes that the cost of the SER conductors is higher compared to the cost of semiconductor components. Given these assumptions, it is possible to maintain high efficiency while lowering the overall costs of the ERS deployed in an urban setting.

4.7.4 Highway Deployment of Electric Roads - Influence of Design Parameters

As illustrated in Fig. 4.17 and Table 4.16, the impact of contact resistance significantly affects the efficiency performance of the ERS. In the original highway deployment case, with a contact resistance of 16 mΩ, the efficiency between interfaces A-D is 93.7% with contact resistance losses amounting to 20 kW, as shown in Fig. 4.14 and Table 4.11. For *contact resistance design 1 and 2*, these losses are notably reduced to values of 5 kW and 8 kW, respectively. Consequently, the efficiency between interfaces A-D improves to 95.1% and 94.5%, respectively. These results indicate that, for high-speed applications where contact resistance is expected to exceed the original value of 16 mΩ (see Table 4.3), reducing contact resistance losses is crucial for future conductive ERS deployments. For *contact resistance design 3 and 4*, which represent worst-case scenarios at higher speeds, the losses are significant, reaching 40 kW and 75 kW, resulting in efficiencies between interfaces A-D of 91.7% and 88.7%, respectively. These results highlight the necessity for further research and development of sliding contacts for the considered ERS technology presented in this thesis.

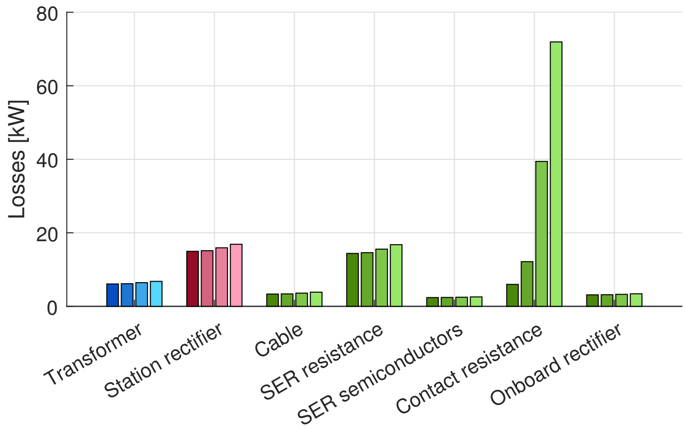

Figure 4.17: Simulated losses per component in the ERS for highway deployment with adjusted contact resistance. The darkest color represents Contact resistance design 1 (far left bars) and gradual lighter colors represents Contact resistance design 2-4. Blue color represents components at interface A-B. Red color represents components at interface B-C. Green color represents components at interface C-D.

Table 4.16: Simulation results for highway deployment with adjusted contact resistance design parameters.

Simulation results Highway adjusted contact resistance					
Simulation case	*Unit*	*Value*			
		Power			
		A	**B**	**C**	**D**
Contact resistance design 1	kW	1000	994	979	950
Contact resistance design 2	kW	1007	1000	985	950
Contact resistance design 3	kW	1036	1030	1014	950
Contact resistance design 4	kW	1072	1065	1048	950
		Efficiency			
		A-B	**B-C**	**C-D**	**A-D**
Contact resistance design 1	%	99.5	98.5	97.1	95.1
Contact resistance design 2	%	99.5	98.5	96.4	94.5
Contact resistance design 3	%	99.5	98.5	93.7	91.7
Contact resistance design 4	%	99.4	98.4	90.6	88.7

As demonstrated in the original highway case, there are additional loss factors beyond those attributed to contact resistance, suggesting that further design adjustments for additional ERS components could be implemented. Two simulation cases are conducted presenting *design alternatives 1 and 2* in which the SER resistance, the resistive on-losses of the diodes in the rectifier station, and the contact resistance of the current collector are varied as detailed in Table 4.14. The resulting power, losses, and efficiency from these simulations are presented in Fig. 4.18 and Table 4.17.

Table 4.17: Simulation results for highway deployment with adjusted design parameters.

Simulation results Highway adjusted design parameters					
Simulation case	*Unit*	*Value*			
		Power			
		A	**B**	**C**	**D**
Design alternatives 1	kW	982	976	969	950
Design alternatives 2	kW	994	988	978	950
		Efficiency			
		A-B	**B-C**	**C-D**	**A-D**
Design alternatives 1	%	99.5	99.3	98.0	96.9
Design alternatives 2	%	99.5	99.1	97.1	95.7

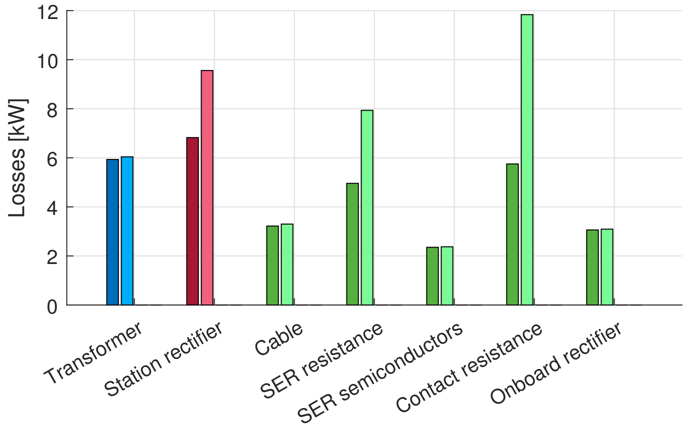

Figure 4.18: Simulated losses per component in the ERS for highway deployment with adjusted parameters. The darkest color represents design alternative 1 (left bar in each pair), and the lighter color represents design alternative 2. Blue represents components at interface A-B, red represents components at interface B-C, and green represents components at interface C-D.

In comparison to the original design presented in Fig. 4.14, these design alternatives result in a significant reduction of losses. For instance, losses due to SER resistance decreased from 15 kW to 5 kW in *design alternatives 1* and to 8 kW in *design alternatives 2*. As previously discussed, the most significant design change in reducing losses is lowering the contact resistance. This adjustment reduces the losses from 20 kW in the original design to 6 kW for *design alternative 1* and 12 kW for *design alternative 2*. The total losses in these simulations were reduced to 32 kW for *design alternatives 1* and 44 kW for *design alternatives 2*, compared to the initial total losses of 70 kW. Furthermore, the system efficiency, initially below 93.7% in the original design, improved to 96.9% in *design alternatives 1* and 95.7% in *design alternatives 2*.

The analysis demonstrates that the proposed design alterations can enhance efficiency and reduce losses. However, some of these design alterations are anticipated to incur additional costs related to development. It is important to note that, depending on specific deployment cases and corresponding requirements, some design alterations are presumed to be more cost-effective than others. For example, reducing the losses in the rectifier station by selecting another topology for the rectifier [94, 95] could potentially be a more cost-effective strategy than increasing the cross-sectional area of the SER conductors, as the latter would impact the road structure more and potentially increase installation costs. In order to avoid the high costs and development efforts associated with improving the ERS components, another solution to mitigate excessive losses is to limit the power drawn per vehicle.

Fig. 4.19 and Table 4.18 presents the power, losses, and efficiency for the analysis of the simulation cases where the power drawn by the trucks in the original highway case is reduced from 300 kW to 150 kW in case 1, and 225 kW in case 2. As a consequence, the losses are reduced, despite all other ERS design parameters remaining unaltered. In *adjusted power per vehicle 1*, with a total power of 650 kW, the efficiency between interface A-D is at 95.9%, and in *adjusted power per vehicle 2*, with a total power of 800 kW, the efficiency between interface A-D is 94.7%. Both these results are improvements compared to the original highway deployment case efficiency of 93.7%.

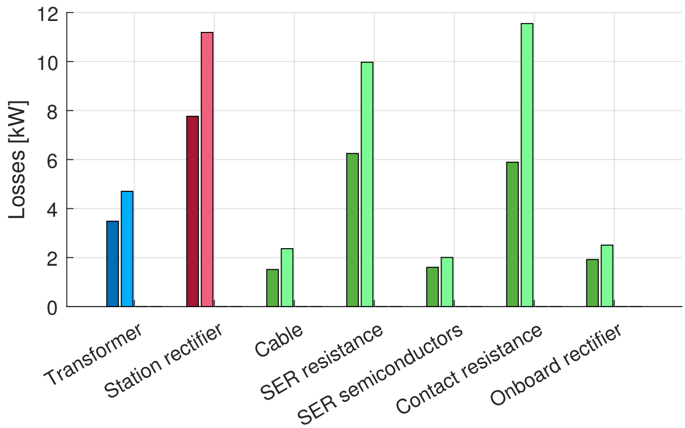

Figure 4.19: Simulated losses per component in the ERS for highway deployment with adjusted drawn power per truck. The darkest color represents design alternative 1 (left bar in each pair), and the lighter color represents design alternative 2. Blue represents components at interface A-B, red represents components at interface B-C, and green represents components at interface C-D.

Table 4.18: Simulation results for highway deployment with adjusted power per vehicle parameters.

Simulation results Highway adjusted vehicle power parameters					
Simulation case	*Unit*	*Value*			
	Power				
		A	**B**	**C**	**D**
Adjusted power per vehicle 1	kW	678	675	667	650
Adjusted power per vehicle 2	kW	844	839	828	800
	Efficiency				
		A-B	**B-C**	**C-D**	**A-D**
Adjusted power per vehicle 1	%	99.5	98.9	97.5	95.9
Adjusted power per vehicle 2	%	99.5	98.7	96.6	94.7

The proposed design alterations to the rectifier station, SER conductors, and contact resistance can result in an ERS with reduced losses and improved efficiency. However, since ERS losses are proportional to the square of the current, substantial reductions in losses can also be achieved by decreasing the power drawn per vehicle. Both strategies improve the technology's performance similarly, and the choice and combination between them should be dependent on deployment requirements.

For some deployment cases where a high value of $k_{\mathrm{ers}} = k_{\mathrm{p}}$ is suitable, the power drawn by trucks can be limited, thereby achieving high efficiency. If the power drawn per vehicle is reduced, the available power to charge the vehicle battery decreases, necessitating an increase in the availability of ERS infrastructure to maintain the SoC of the battery and the vehicle's range. In other cases, where strict constraints related to the extent of ERS deployment result in low values of $k_{\mathrm{p}} = k_{\mathrm{ers}}$, necessitating a higher power draw per vehicle, design alterations to the ERS components might be actually necessary to maintain high system efficiency. Alternatively, a combination of both strategies may prove to be the most effective measure for improving system efficiency in an additional scenario.

To conclude this chapter, it is crucial to assess the deployment environment and the corresponding traffic characteristics for the specific ERS deployment case, and to design the ERS specifically for this case. The design of the ERS must account for parameters such as k_{ERS} and k_{p}, and identify which ERS components require special design considerations to achieve high system efficiency. Additionally, regardless of the ERS deployment environment, it is essential to reduce the contact resistance of the current collector for high-speed applications. Inadequate measures to improve the performance of future current collector designs may have a significant negative impact on ERS performance.

Among design alterations, adopting the most cost-effective approach is crucial. In some cases, expanding the ERS network may be more economical than investing in improvements to components and subsystems, such as the SER conductors. Consequently, to achieve cost savings and improve the efficiency of conductive ERS, a combined strategy of optimizing design and reducing power consumption per vehicle may offer the best solution. Moreover, enabling the ERS operator to actively control the power draw per vehicle is likely to be an even more cost-effective approach to minimizing losses.

4.7.5 Suggested Strategies for the ERS Operator

As presented in Fig. 4.2 and confirmed by Figs. 4.13 and 4.14, two major contributors to ERS losses are the resistance in the SER conductors and the power drawn per vehicle. In the analyses presented in this chapter, a constant power draw is assumed for each vehicle throughout the simulations. An alternative, though beyond the scope of this thesis, would be to implement a system allowing the ERS operator to actively manage the total power drawn by each vehicle operating on the ERS. This approach could be facilitated through wireless communication and software implementation, enabling real-time adjustments to the power draw per vehicle to maintain optimal ERS efficiency while continuously monitoring vehicle position and SoC. Such a system could be integrated into the ERS business model, providing premium ERS users with priority access or the option to pay a fee for higher charging power, thereby enhancing overall system efficiency and management.

Chapter 5

Modelling Conductive Electromagnetic Interference

5.1 Introduction

Vehicles drawing power from the ERS must operate without interfering with each other electrically and without disrupting nearby electrical devices. Additionally, the ERS power grid connection must not introduce any conductive EMI that could cause functional disturbances in the power grid, and it must adhere to established standards for power grid quality.

This chapter evaluates the conductive EMI within the ERS supply at interfaces C-D and the effects of conductive EMI caused by the ERS at its grid connection at interface A. The analysis is conducted using a simulation model, validated using experimental results from the ERS demonstrator presented in Section 2.2. Given the absence of multiple vehicles in the ERS demonstrator, the conductive EMI arising from the interaction of multiple vehicles is examined through modelling. Specifically, the analysis focuses on the issues of conductive EMI within the ERS DC voltage supply, which is influenced by the input filters of the vehicle's onboard ERS interface. An expected outcome of this evaluation is the conclusion that there is a need for standardization concerning the ERS supply, as the EMI interaction between each BEV's ERS interface and the ERS supply is expected to influence the voltage and current within the system. The evaluation also considers the impact of conductive EMI related to the rectifier topology in the rectifier station, specifically evaluating the implementation of a 12-

pulse passive rectifier and its influence on both the ERS supply and the power grid. The validation of the simulation model in this chapter was first presented in [43].

5.2 Modelling

To assess the effects of conductive EMI within an ERS and its grid connection, a simulation model was developed. This simulation model is designed to replicate the waveform shapes and amplitudes of voltage and current observed in measurements from the demonstrator at interfaces A-D.

A relative error margin of 10% in amplitude between the measurements and the model is selected. This choice is motivated by the fact that the model's accuracy is limited by the information available in datasheets, which often specify tolerance deviations of 5–10% in passive components such as resistors, inductors, and capacitors. As a result, an error margin of 10% for the simulation model is considered acceptable.

In contrast to the simulation model developed for power flow and loss analysis presented in Chapter 4, this simulation model is specifically designed to accurately simulate the waveform shapes and magnitudes of voltages and currents at interfaces A-D. This model is also required to simulate voltage and current on a significantly finer timescale, specifically in the order of 0.1 ms. The choice of a 0.1 ms timescale is motivated by two main reasons:

- The sampling frequency of the measurement system, which provided experimental results for model validation, is limited to 200 kHz. Theoretically, according to the Nyquist theorem, this would result in reliable measurements up to 100 kHz. However, to ensure data reliability, a target time resolution of 0.1 ms was selected, corresponding to a frequency of 10 kHz. This choice is based on the assumption that the sampling frequency should be at least 20 times higher than the measured frequency. Although the model is capable of simulating phenomena occurring at shorter timescales, which can be useful and adequate in terms of reliability, simulated results at this resolution should be interpreted with caution.

- The switching frequencies of the subsystems within the vehicle TVS range from 1 to 10 kHz. Since these represent the highest frequencies that the model is designed to account for, a 0.1 ms timescale is suitable for accurately modelling these loads.

The simulations in this chapter are conducted using the PLECS© software, which was selected for its capabilities in handling complex electrical simulations.

5.2.1 Model Development

The development of this simulation model employed an iterative heuristic approach, where simulation results were repeatedly compared with experimental results from the ERS demonstrator. The aim of this iterative process was to achieve a balance between simulation accuracy and execution time. During the process, the impact of each component and its corresponding parameters on the resulting waveform shape and magnitude of voltages and currents at interfaces A-D was evaluated for each sub-circuit. Similar to the power flow and loss simulation model presented in Chapter 4, the parameters for all electrical elements in the original circuits were sourced either from electrical schematics and datasheets provided by Elonroad and other project partners in the Evolution Road project, or measured using an impedance analyzer [83]. Where not otherwise specified, parameter values were obtained from project partners or datasheets. The switching frequencies of the battery converter and the traction inverter were determined through measurements conducted with a Picoscope [81]. The following subsections provide a detailed discussion of the circuit models, including the selection and impact of parameters. All parameter values presented were used for the validation of the simulation model.

5.2.2 The Rectifier Station

In Fig. 5.1, the circuit model of the grid and rectifier station is presented, comprising the ERS grid connection, transformer, and passive 6-pulse rectifier, along with the associated filters and solid-state switches. The parameter values for the circuit model of the grid and rectifier station are detailed in Table 5.1.

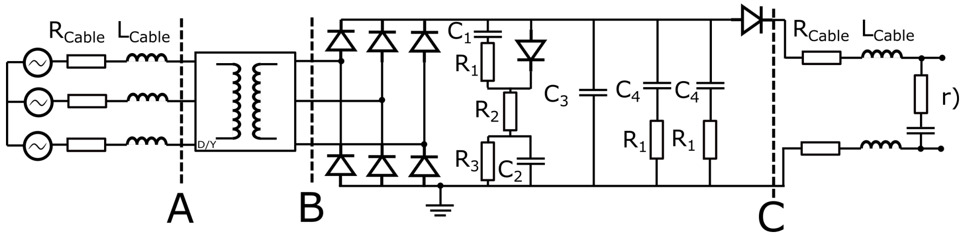

Figure 5.1: Circuit model of the power grid, rectifier station and corresponding connections.

Table 5.1: Simulation parameters for the grid and rectifier station circuit model.

Rectifier station circuit model parameters		
Parameter	*Unit*	*Value*
Three-phase voltage source		
Phase voltages	V_{RMS}	238, 234, 233
Cable grid		
Grid cable R	mΩ/km	41.7
Grid cable L	mH/km	0.23
Transformer		
Nominal power	kVA	400
Nominal line-line voltages	V_{RMS}	400, 482
Leakage inductance 1, 2	μH	30, 30
Winding resistance 1, 2	mΩ	50, 50
Vector group	-	Dyn11
Magnetizing current values	A	0.1
Magnetizing flux values	Vs	1.4
Core loss resistance Rfe	Ω	650
Rectifier		
Rectifier diodes on-state resistance	mΩ	5
Rectifier diodes forward voltage drop	V	0.8
C_1	nF	88
C_2	mF	6.8
C_3	μF	0.66
C_4	nF	22
R_1	Ω	3.3
R_2	Ω	0.09
R_3	kΩ	6
Filter diode on-state resistance	mΩ	0.2
Filter diode forward voltage drop	V	0.8
Solid state switch on-state resistance	mΩ	10
Solid state switch forward voltage drop	V	1.3
SER Cable		
Rectifier-SER cable resistance positive conductor	mΩ/km	125
Rectifier-SER cable resistance negative conductor	mΩ/km	62.5
Rectifier-SER cable inductance	mH/km	0.23
RC filter resistance	Ω	0.1-10
RC filter capacitance	mF	0.001-0.1

The ERS connection, upstream the power grid is represented by a 400 V three-phase voltage source, simulating the transformer upstream the power grid. To accurately replicate the measured voltages at interface A, each phase of the grid voltage is individually defined, as detailed in Table 5.1. The 210 m cable between this grid connection and the ERS transformer is modelled as resistors and inductors, with values specified per kilometer. The transformer is modelled using the PLECS© "Transformer (3ph, 2 Windings)" block (for further details, refer to [96]). The passive 6-pulse rectifier is represented by diodes, with on-state resistance and forward voltage drop values.

All filters from Fig. 2.14 are included in the model after the rectifier. The solid-state switch, which remains continuously conducting during the simulations, is modelled as a diode with corresponding on-state resistance and forward voltage drop values. Note that the on-state resistance for the diodes in the rectifier and the solid-state switch are higher compared to the corresponding values presented in Table 4.1. This is because these resistance values were deliberately set to elevated levels to account for additional resistive elements in the circuits, such as connection joints and other components that introduce resistance but are not specified in the datasheet. The 41 m cable between the rectifier station and the SER is modelled as resistors in series with inductors, with values specified per kilometer. The resistance and capacitance values of the RC-filter are in a range due to non-disclosure agreements with Elonroad.

Interfaces A, B, and C represent measurement points where voltages and currents are measured in the model. The model of the grid and rectifier station in Fig. 5.1 and the model of the SER in Fig. 5.2 are connected at interface r). This interface is known as the feeding point of the ERS.

5.2.3 Sections of Electric Road

Fig. 5.2 presents the model of the SER, which includes positive and negative conductors, solid-state switches that activate the segments (modelled as a diode), an RC-filter, and a switching array used to emulate the duration of vehicle contact with segments in the electric road. The corresponding parameter values for the SER circuit model are presented in Table 5.2.

The positive and negative conductors in the SER are modelled as variable resistors and inductors, as the effective impedance of the conductors relative to the feeding point changes depending on the vehicle's position. How-

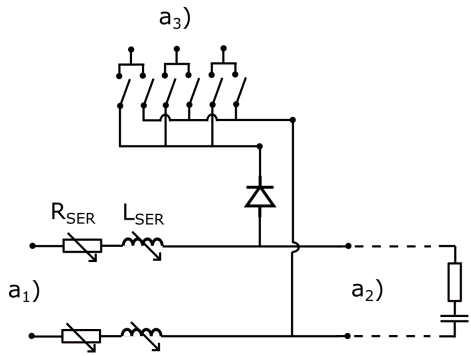

Figure 5.2: Circuit model for the SER.

Table 5.2: Simulation parameters for the sections of electric road circuit model.

Sections of electric road circuit model parameters		
Parameter	*Unit*	*Value*
SER		
SER resistance positive conductor	mΩ/km	42
SER resistance negative conductor	mΩ/km	4.1
SER inductance	mH/km	0.02
Switch Array		
Transistor forward voltage drop	V	1.4
Transistor on-state resistance	mΩ	0.1
Frequency vehicle speed emulation	Hz	7.5

ever, since the timescale of the model is in ms, the impedance alterations due to vehicle movement within this timeframe are negligible. Therefore, the impedance remains constant during the simulation as these minimal alterations have no impact on the simulated voltages and currents. The inductance and resistance of the SER conductors were determined through measurements using an impedance analyzer [83]. As mentioned in Chapter 4, during the deployment of the ERS demonstrator, only one of the two possible positive conductors was installed. As a result, the full potential of the positive conductors in the SER was not fully utilized, leading to a resistance of 42 mΩ/km. For the validation of the model, this parameter value is used. However, in the subsequent simulations in this chapter, both positive conductors are deployed, and therefore, the corresponding resistance parameter is adjusted to 21 mΩ/km.

To mimic the alternating voltage polarity experienced by each sliding contact due to the vehicle's movement along the SER, an array of ideal switches is used. In contrast to the impedance of the SER conductors, the segments which are in contact with the vehicle during the simulation change depending on the vehicle's speed. Each sliding contact point is represented by two switches, connecting it to either a positive (650 V DC) or negative conductor (0 V DC). By altering the switching frequency of these switches, the effect of a vehicle traversing the electric road is emulated. A switching frequency of 7.5 Hz corresponds to vehicle speed of approximately 30 km/h.

The transistors responsible for activating the segments in the SER, modelled as a diode, is located on the positive pole of the switching array and incorporate an on-state resistance and a forward voltage drop. This modelling approach is appropriate because, from the vehicle's viewpoint, these transistors are always in a conducting state.

Since the model focuses on conductive EMI rather than the design and behavior of the current collector, the current collector and switching array are simplified to consist of three sliding contact points, rather than the six used on the bus in the demonstrator. Although the switching dynamics of the segments and the current collector are relevant, the fundamental phenomena affecting conductive EMI and electrical safety are adequately modelled by using a current collector with three sliding contacts instead of six. The model assumes a stable, continuous contact, resulting in constant contact resistance.

The circuit model of the SER is connected to the vehicle model at interface a_3). The SER circuit model is connected to the grid and rectifier station at interface a_1), at the connection r) in the grid and rectifier station circuit model in Fig. 5.1. To simulate multiple vehicles drawing power from the ERS, additional SER circuit models can be connected in series, coupling interface a_1) of the new segment to a_2) of the existing one and with corresponding vehicle circuit models connected at interface a_3). The RC-filter connected to the far right in the model indicates that the last SER circuit model in a series of connected models will have an RC-filter connected to it with the same parameters as presented in Table 5.1.

5.2.4 The Vehicle

The vehicle's TVS model comprises three integrated yet separate circuit models: the vehicle's ERS interface, the high-voltage battery system, and the drivetrain. Fig. 5.3 illustrates the circuit model for the vehicle's ERS interface which consists of an onboard rectifier and corresponding filters from the bus used for the demonstrator, with parameters specified in Table 5.3.

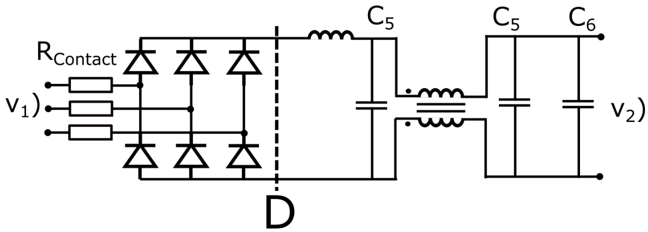

Figure 5.3: Circuit model for the vehicle's ERS interface.

Table 5.3: Simulation parameters for the vehicle's ERS interface.

Vehicle's ERS interface simulation parameters		
Parameter	*Unit*	*Value*
Current collector		
Contact resistance	mΩ	20
Onboard rectifier		
Diode R	mΩ	0.8
Diode Vf	V	0.8
Filters		
Common mode L	mH	1
Filter C_5	μF	1
Filter L	mH	1.15
Filter C_6	mF	5

Interface v_1) of the vehicle ERS interface is connected to interface a_3) of the switching array in the SER circuit model. The sliding contacts between the segments of the SER and the vehicle's current collector are modelled as resistors. The values for contact resistance are estimated based on the results presented in Chapter 3. The diodes within the onboard rectifier are also modelled with their corresponding values of forward voltage drop and on-state resistance. Similar to Chapter 4, the DC/DC converter originally shown in the bus schematic (see Fig. 2.18) is omitted from the model because it functions merely as a switch, allowing connection and disconnection of the bus' TVS from the ERS supply. After interface D, where voltage and current are measured in the model, there is an inductor (L) followed by two capacitors with identical values (C_5), one positioned before a common-mode filter and one after, as shown in the original bus circuit in Fig. 2.18. Following the second capacitor, there is an additional larger capacitor (C_6).

The circuit model of the high-voltage battery system is presented in Fig. 5.4, with parameters outlined in Table 5.4. The model for the drivetrain is shown in Fig. 5.5, with parameters detailed in Table 5.5. Both the high-voltage battery circuit model at interface b) and the drivetrain circuit model at interface t) are connected in parallel to interface v_2 of the vehicle ERS interface circuit model.

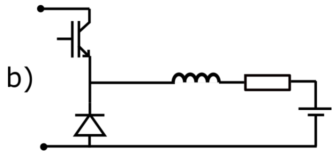

Figure 5.4: Circuit model for the high-voltage battery system.

Table 5.4: Simulation parameters for the high-voltage battery system.

Battery system simulation parameters		
Parameter	*Unit*	*Value*
Switching frequency	kHz	3.8
	Load	
R	mΩ	40
L	mH	1.3
Battery voltage	V	500

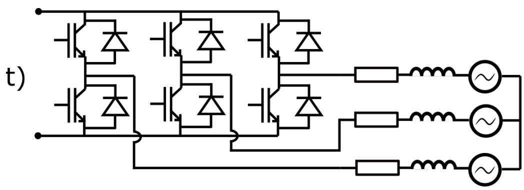

Figure 5.5: Circuit model for the drivetrain.

Table 5.5: Simulation parameters for the drivetrain.

Drivetrain simulation parameters		
Parameter	*Unit*	*Value*
Switching frequency	kHz	3.4
Load		
Rated Power	kW	160
R	mΩ	50
L	mH	0.6
E	V_{RMS}	250
Load frequency	Hz	60

The high-voltage battery system is represented as a buck converter since the model only considers unidirectional power flow for charging the battery. An inductor is located on the load side of the converter, along with a simple battery model comprising a resistor representing the battery's internal resistance and a DC voltage source. The drivetrain is modeled as a three-phase inverter with an electric motor on the load side, represented as a three-phase resistor-inductor-electromotive force load. The resistance and inductance values of the motor were estimated due to the lack of available data for these parameters.

5.3 Model Validation

The model validation is based on experimental results from the ERS demonstrator which were obtained using the measurement system outlined in Section 2.2.4 in Chapter 2. These measurements were conducted while the bus traversed a 100-meter section of the electric road, either charging while stationary or while moving at an approximate speed of 30 km/h. To replicate these conditions and validate the results, the simulation model comprises a grid and rectifier circuit model connected to an SER circuit model, along with a vehicle model that includes the vehicle's ERS interface, battery system, and drivetrain circuit models. Validation was performed at two distinct power levels: 40 kW for stationary charging and 100 kW for dynamic charging, both from the ERS demonstrator.

Figs. 5.6 to 5.9 present the measured (denoted as ”m”, solid lines) and simulated (denoted as ”s”, dashed lines) voltages and currents at interfaces A–D. The measurement interfaces are specified in Fig. 2.13 in Chapter 2. The upper plots correspond to the 40 kW load level, while the lower plots correspond to the 100 kW load level. The blue and red lines represent voltages, corresponding to the left y-axis, while the green and yellow lines represent currents, corresponding to the right y-axis.

Fig. 5.6 presents the simulated and measured voltages and currents for one phase at interface A. The simulated values agree well with the measurements, both in terms of amplitude and waveform shape. The shape of the current waveform is a consequence of the 6-pulse passive rectifier connected downstream of the ERS transformer. Fig. 5.7 presents the same results for interface B, which also shows a high degree of similarity between simulations and measurements. Note that the phase voltages between interfaces A and B are shifted by 30 degrees due to the D-Y transformer between these interfaces.

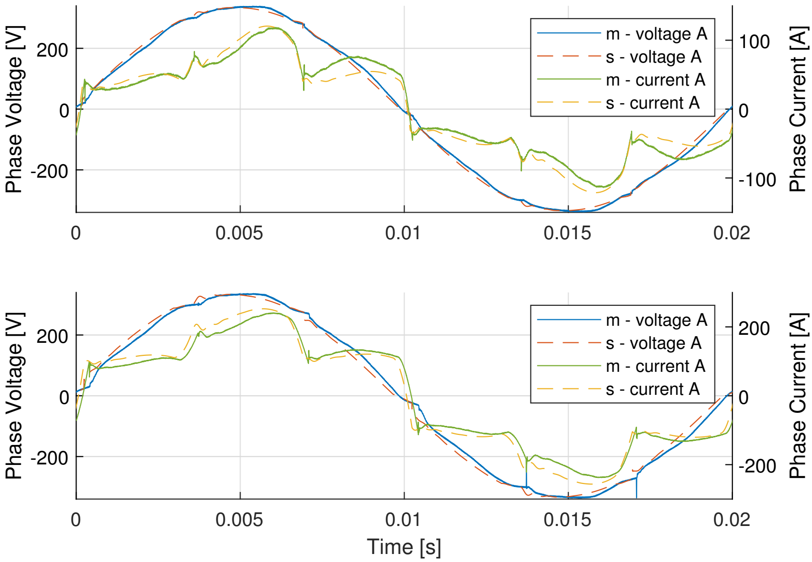

Figure 5.6: Measured (m, solid lines) and simulated (s, dashed lines) phase voltage (blue and red, left y-axis) and phase current (green and yellow, right y-axis) at interface A. The upper plot represents a 40 kW load, while the lower plot represents a 100 kW load. Figure taken from [43].

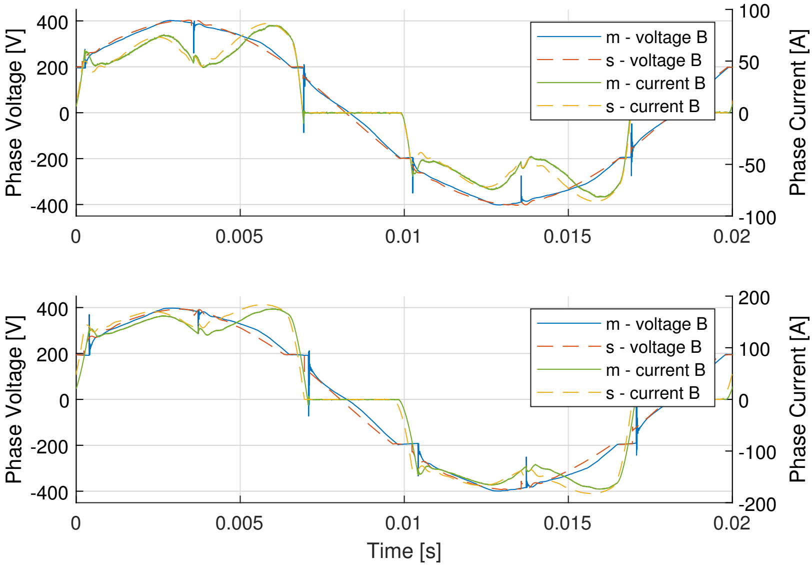

Figure 5.7: Measured (m, solid lines) and simulated (s, dashed lines) phase voltage (blue and red, left y-axis) and phase current (green and yellow, right y-axis) at interface B. The upper plot represents a 40 kW load, while the lower plot represents a 100 kW load. Figure taken from [43].

Figs. 5.8 and 5.9 illustrate the measured and simulated rectified voltages at interfaces C and D. Both the measured and simulated voltages and currents show a high degree of similarity in waveform shape and amplitude. The observed variations in the amplitude of voltage and current at interfaces C and D can be attributed to the unbalanced three-phase grid voltage. The model accounts for this unbalance, as detailed in Table 5.1, and, consequently, these variations affect the rectified voltage and current. Despite adjusting the modelled three-phase voltage source, the measured voltages still show additional variations due to inherent fluctuations in the grid. These variations make it difficult to fully calibrate the model to the measurements.

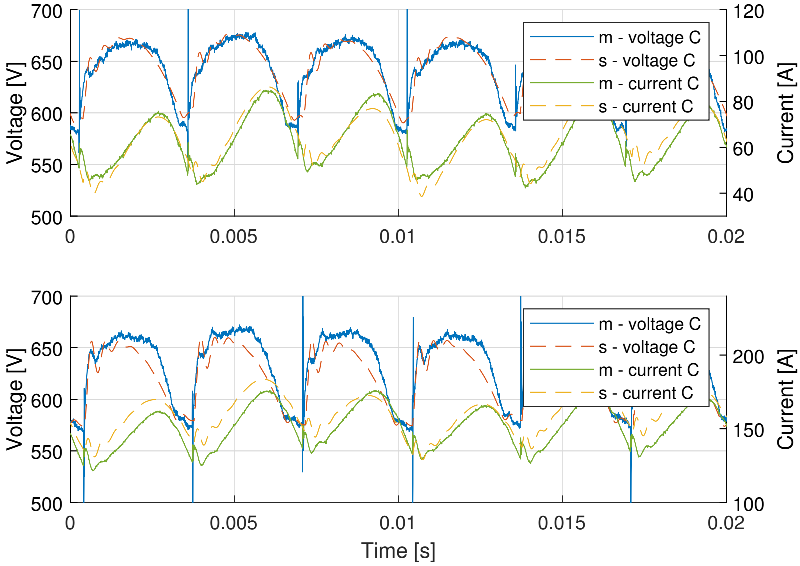

Figure 5.8: Measured (m, solid lines) and simulated (s, dashed lines) voltage (blue and red, left y-axis) and current (green and yellow, right y-axis) at interface C. The upper plot corresponds to a 40 kW load, while the lower plot corresponds to a 100 kW load. Figure taken from [43].

At interface D, shown in Fig. 5.9, the current waveforms exhibit less oscillation at the start of a rectified current period compared to interface C, presented in Fig. 5.8. This reduction in oscillation is likely due to the additional impedance present between interfaces C and D. Additionally, the simulated voltages at interfaces C and D display slight variations in waveform shape when comparing lower power levels (40 kW) to higher power levels (100 kW). Specifically, at 40 kW, the first half-period of the rectified voltage appears to oscillate more compared to 100 kW, which may suggest that the model does not account for additional impedance that exists in reality at these interfaces.

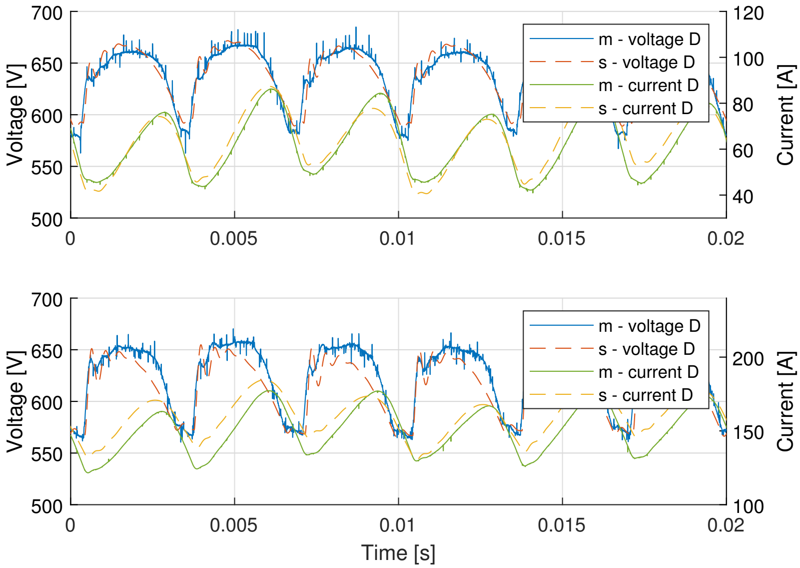

Figure 5.9: Measured (m, solid lines) and simulated (s, dashed lines) voltage (blue and red, left y-axis) and current (green and yellow, right y-axis) at interface D. The upper plot corresponds to a 40 kW load, while the lower plot corresponds to a 100 kW load. Figure taken from [43].

The voltage transients on the timescale of 10 μs, observed at interfaces A-C (Figs. 5.6 to 5.8), are suspected to be caused by the reverse recovery phenomenon of the diodes in the rectifier station. These transients appear within the time interval of 3.33 ms, which corresponds to the period when a diode in the rectifier becomes reverse-biased. However, the sampling frequency of the measurements is insufficient to definitively confirm this hypothesis. Despite this, since the model is intended to simulate electrical transients at a time resolution of 0.1 ms, these short transients are considered negligible for the modelling of conductive EMI in this thesis.

Table 5.6 presents the relative error of the simulation model between measurements and simulations for interfaces A–D, calculated from Figs. 5.6 to 5.9. Overall, the simulation model's accuracy at interfaces B, C, and D fulfills the predetermined maximum error margin of 10% at both simulated power levels of 40 and 100 kW, with interfaces C and D showing significantly lower errors, where the relative errors of simulated voltage and current are as low as 1.3-5.2%.

However, at interface A, the error for the simulated current at a power of 40 kW is 14.9%, and the error for the simulated voltage at 100 kW is 11.2%. Although these values exceed the target maximum error of 10%, this deviation likely results from the model's limitations in representing grid voltage and current. As previously discussed for interfaces C and D, similar issues are suspected to also apply to interface A. These variations likely stem from additional power grid loads and impedance fluctuations occurring further upstream. Since the model is not specifically designed to account for these factors, lower accuracy at interface A is considered acceptable.

Table 5.6: Relative errors for each interface in the simulation model at two different power levels.

Simulation Model Error				
Parameter	*Relative Error [%]*			
	Interface			
	A	B	C	D
40 kW Simulated power				
Simulated voltage	8.5	6.0	1.4	1.3
Simulated current	14.9	8.3	4.9	5.1
100 kW Simulated power				
Simulated voltage	11.2	9.2	1.5	1.6
Simulated current	8.7	3.4	5.2	4.9

5.4 Model Composition

The conducted simulations involve two vehicles drawing power from the ERS: one at 100 kW (vehicle 1, representing a heavier vehicle) and the other at 50 kW (vehicle 2, representing a larger passenger car). In Fig. 5.10 a conceptual overview of the simulation setup is presented. The primary objective of using two vehicles with different power draws is to emulate and investigate the impact of a high-power vehicle on the ERS supply and, consequently, how its conductive emissions affect a vehicle with a lower power draw. This approach aims to explore how multiple vehicles drawing power from the ERS are influenced by conductive EMI in the ERS supply and how such EMI occurs.

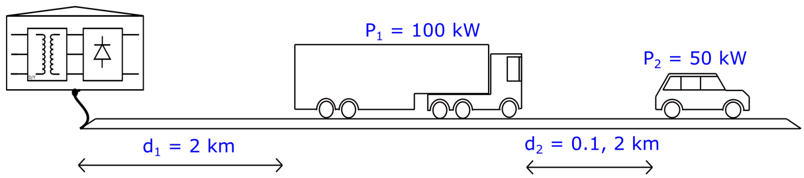

Figure 5.10: Conceptual overview of the simulation setup for assessing the impact of conductive EMI within the ERS supply, the vehicles' onboard ERS interfaces, and the ERS grid connection. P_1 and P_2 denote the power drawn by vehicle 1 and vehicle 2, respectively, and d_1 denotes the distance between vehicle 1 and the feeding point of the ERS, while d_2 denotes the distance between vehicle 1 and vehicle 2.

By varying the input filter parameter L in the onboard ERS interface of vehicle 1, as detailed in Table 5.3 and Fig. 5.3, the impact of this adjustment on voltage and current ripple within the ERS supply at interface C and the onboard ERS interfaces at interface D for both vehicles is evaluated. In real-world scenarios, the power electronic interfaces of BEVs drawing power from the ERS are expected to differ more significantly than merely varying the value of the inductor L. However, this approach is selected to highlight the concept of how each BEV's ERS interface can affect both other vehicles and the ERS supply.

In addition to evaluating the design of the input filters in the vehicles' onboard ERS interfaces, the impact of the electric road length between vehicles 1 and 2, d_2, on the voltage and current ripple at interfaces C and D in both vehicles is also assessed. The same simulation setup is used to assess the impact of conductive EMI on the ERS power grid connection. However, for this assessment, no alterations are made to the filter parameter L or the electric road length between vehicles 1 and 2, d_2, as conducted simulations show that these parameter adjustments mainly impact the ERS supply and have an insignificant effect on the ERS grid connection.

Fig. 5.11 illustrates the block diagram of the simulation model structure used to assess conductive EMI within the ERS supply and its impact on the power grid connection. Each block in the diagram represents a component or subsystem of the ERS. The full circuit models for the grid and rectifier station (depicted in red), the SER (in turquoise), and the vehicle (in green) are highlighted with dashed lines, as previously presented in Section 5.2. For the simulation of conductive EMI, the model structure comprises a single grid and rectifier circuit model connected to the first SER circuit model and its corresponding first vehicle circuit model. At interface a_2) of the first SER circuit model, a second SER circuit model is connected in series with its corresponding second vehicle circuit model. This model structure enables the simulation of two vehicles with different power draws and varying distances between them.

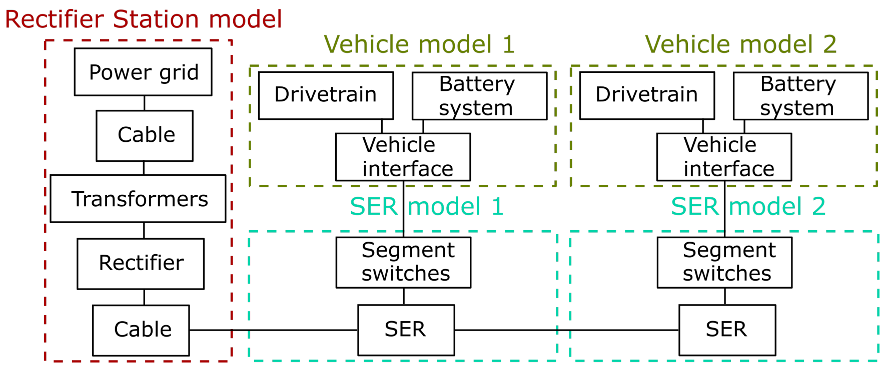

Figure 5.11: Block diagram of the simulation model structure for the subsequent simulation scenarios, consisting of two vehicles drawing power from an ERS, with an SER between the rectifier station and another SER between the vehicles.

Table 5.7 details the simulation parameters used for investigating conductive EMI. Apart from the parameters listed in the table and the reduced resistance of the positive SER conductor, as described previously in relation to Table 5.2, no other values are modified from those originally presented in Section 5.2. In the simulation, the input filter parameter L in the ERS interface of vehicle 1 is varied among three different values: 0.92 mH, the original value of 1.15 mH, and 2.07 mH. Rather than representing different vehicle models, these adjustments are made to assess how small variations in L can influence the ERS supply voltage and current and, consequently, affect other vehicles drawing power from the ERS. To signify that voltage and current within the ERS supply are affected by the length of the electric road, the distance between vehicle 1 and the feeding point, d_1, is set relatively long at 2 km. The distance between vehicles 1 and 2, d_2, is varied in the simulation cases between 0.1 km and 2 km. This adjustment is intended to assess how increased impedance between the vehicles influences conductive EMI in the supply and the EMI perceived between the vehicles.

Table 5.7: Simulation parameters for simulations evaluating conductive EMI within the ERS supply.

Simulation parameters		
Parameter	*Unit*	*Value*
Vehicle 1		
Power draw	kW	100
Distance between vehicle 1 and the feeding point, d_1	km	2
Input inductor, L	mH	0.92, 1.15, 2.07
Vehicle 2		
Power draw	kW	50
Distance between vehicle 1 and 2, d_2	km	0.1, 2

5.4.1 Incorporation of a 12-Pulse Passive Rectifier

An alternative rectifier topology is adopted in the rectifier station to asses its impact on conductive EMI. By replacing the original 6-pulse passive rectifier with a 12-pulse passive rectifier, the harmonics, as well as the ripple, in both voltage and current are expected to be reduced. This modification aims to minimize the impact of EMI on both the ERS supply and the power grid at the ERS grid connection.

Figure 5.12 illustrates the topology of the 12-pulse passive rectifier station circuit model. In order to achieve 12-pulse rectification, the original circuit is modified by incorporating the same three-phase transformer from Fig. 5.1 but extended with two secondary windings—one configured in delta and the other in wye. The specific parameters of this transformer are provided in Table 5.8. All other parameters of the original grid and rectifier circuit model remain unchanged.

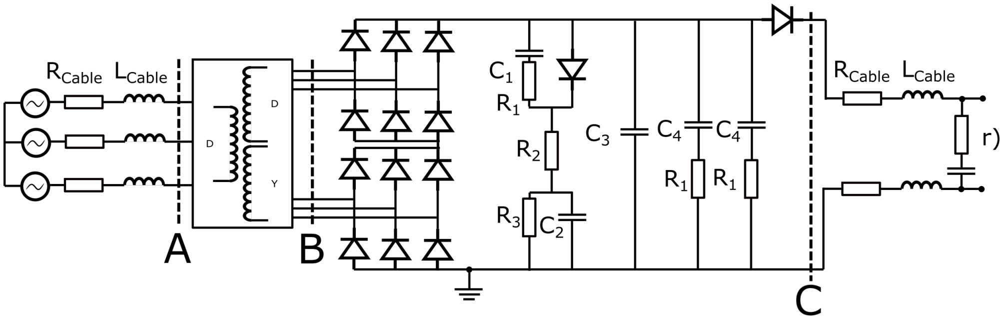

Figure 5.12: Circuit model of the grid and rectifier station with a 12-pulse passive rectifier implemented.

Table 5.8: Simulation parameters for transformer for the 12-pulse passive rectifier station model.

Transformer simulation parameters		
Parameter	*Unit*	*Value*
Nominal power	kVA	400
Nominal line-line voltages	V_{RMS}	400, 245, 245
Leakage inductance 1, 2, 3	μH	30, 30, 30
Winding resistance 1, 2, 3	mΩ	50, 50, 50
Magnetizing current values	A	0.1
Magnetizing flux values	Vs	1.4
Core loss resistance Rfe	Ω	650

5.5 Simulation Results

This section presents the simulation results analyzing the effects of vehicle's ERS interfaces on the ERS supply, as well as on other vehicles drawing power from the ERS, with respect to voltage and current ripple. Additionally, the length of the electric road between the vehicles is varied to evaluate its influence on these phenomena.

The first subsection, 5.5.1, "Influence of Vehicle Interface Design on Voltage and Current Ripple with 6-Pulse Passive Rectification", provides simulations based on a model incorporating a 6-pulse passive rectifier. The second subsection, 5.5.2, "Influence of Vehicle Interface Design on Voltage and Current Ripple with 12-Pulse Passive Rectification" expands this analysis with simulations involving a 12-pulse passive rectifier. The third subsection, 5.5.3, "Assessment of ERS-Induced Harmonics on the Power Grid", investigates the impact of ERS on the power grid in terms of harmonics and rectification type, evaluating both 6-pulse and 12-pulse passive rectifiers.

5.5.1 Influence of Vehicle Interface Design on Voltage and Current Ripple with 6-Pulse Passive Rectification

Figure 5.13 presents the simulated voltages and currents at interfaces C and D, with two vehicles drawing power from an ERS, as described in Table 5.7 and Fig. 5.10. The upper plot shows the voltage, while the lower plot displays the current. Interface C is located after the rectifier but before the cables to the SER (see Fig. 5.1), whereas D1 and D2 are the measurement interfaces within the vehicles, after the onboard rectifiers (see Fig. 5.3). In this simulation, the distance between the feeding point and vehicle 1, d_1, is 2 km and the distance between the two vehicles, denoted as d_2, is 0.1 km. The inductance L in vehicle 1 (100 kW) and 2 (50 kW) is set to 1.15 mH.

In the upper plot, the simulated voltages indicate that the voltage in vehicles 1 and 2 (DV1 and DV2) drops compared to the voltage in interface C, CV. This voltage drop is a result of the resistance between interfaces C and D1-D2, influenced by the length of the electric road between the feeding point and the first vehicle, denoted as d_1. Given that the distance between the vehicles (d_2) is only 0.1 km, the voltage drop between the vehicles (D1-D2) is minimal.

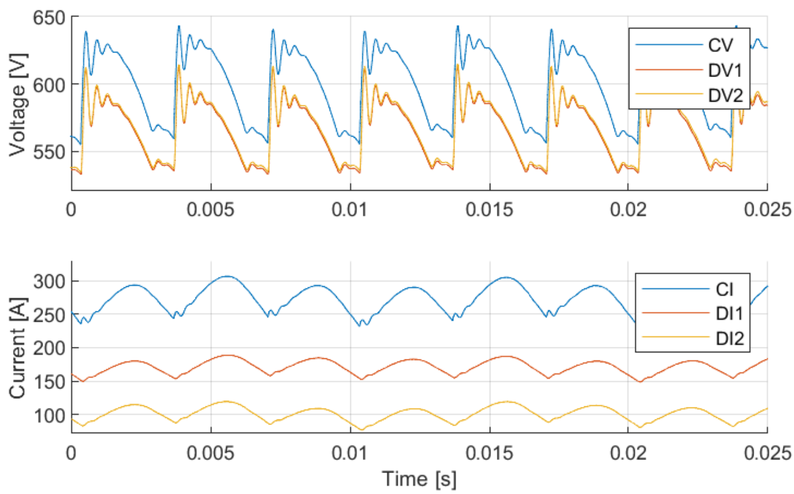

Figure 5.13: Simulated voltage (upper plot) and currents (lower plot) at interfaces C (blue), D1 (red), and D2 (yellow), where vehicle 1 (interface D1) draws 100 kW and vehicle 2 (interface D2) draws 50 kW. The parameter for the input filter is $L = 1.15\,\text{mH}$ in vehicle 1, $L = 1.15\,\text{mH}$ in vehicle 2, and the distance between the vehicles is $d_2 = 0.1\,\text{km}$.

Given the overall electrical design of the considered ERS technology, the voltage ripple, caused by the 6-pulse passive rectifier, is approximately 70 V at voltage levels at approximately 600 V. The current ripple is around 25 A for the vehicles in interface D1-D2, where the current level is approximately 165 A for vehicle 1 and approximately 100 A for vehicle 2. These voltage and current ripple levels are not necessarily deemed problematic, provided they remain predictable, especially regarding the additive effects of multiple vehicles. However, if these ripples increase and require alterations to the design of the ERS power electronic interfaces onboard the vehicles, leading to the use of overly large, heavy passive components or excessively complex topologies, such increases could ultimately result in higher costs. Moreover, as will be shown later, there is a risk that the input filter design of the vehicles may interfere with each other, making it difficult to predict the exact voltage and current ripple levels supplied by the ERS. This simulation represents the nominal case, emulating the expected behavior if the ERS technology demonstrated here were applied to two vehicles with identical onboard ERS interfaces and different power consumption. Regardless of vehicle size and power consumption, each vehicle operating on the ERS must be designed to handle the voltage and current ripple from the ERS supply.

Figure 5.14 presents the simulated voltages (upper plot) and currents (lower plot) using the same parameters as those specified in Table 5.7 and Fig. 5.13, but with an inductor value of $L = 0.92\,\mathrm{mH}$ in vehicle 1. The voltage ripple in the upper plot is reduced from 70 V to 50 V at interface C, while the current ripple at this interface increases from 50 A to 80 A compared to the original simulation cases presented in Fig. 5.13.

Similarly, for vehicle 1, the voltage ripple is reduced from 50 V to 25 V, and the current ripple increases from 30 A to 60 A. However, for vehicle 2, the voltage ripple is also reduced to 25 V, while the current ripple decreases to 10 A. Thus, by reducing the inductance of the input filter in vehicle 1, the entire ERS supply is affected, particularly with respect to the current in the ERS supply at interfaces C and D1.

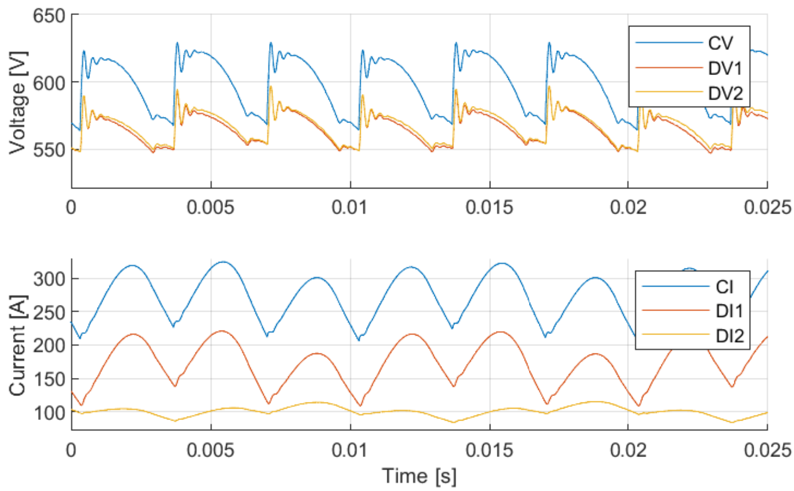

Figure 5.14: Simulated voltage (upper plot) and currents (lower plot) at interfaces C (blue), D1 (red), and D2 (yellow), where vehicle 1 (interface D1) draws 100 kW and vehicle 2 (interface D2) draws 50 kW. The parameter for the input filter is $L = 0.92\,\text{mH}$ in vehicle 1, $L = 1.15\,\text{mH}$ in vehicle 2, and the distance between the vehicles is $d_2 = 0.1\,\text{km}$.

Figure 5.15 presents the simulated voltages (upper plot) and currents (lower plot) using the same parameters as those in the original case shown in Table 5.7, with $L = 0.92\,\text{mH}$ in vehicle 1 and $\text{d}_2 = 2$ km. This simulation is designed to assess the impact of increased impedance on the ERS supply's voltage and current, resulting from the extended length of the electric road.

In the upper plot, the increased impedance of the electric road does not affect the waveform shape of the simulated voltages, apart from a constant voltage drop between the two vehicles due to the increased resistance between them. In the lower plot, the waveform shape of the current remains largely unaltered. Overall, this simulation demonstrates that the impedance of the electric road, considering the assumed length, does not significantly impact the ERS supply voltage and current. The electric road is too short and has too low impedance per unit length to noticeably affect the waveform shapes of voltage and current.

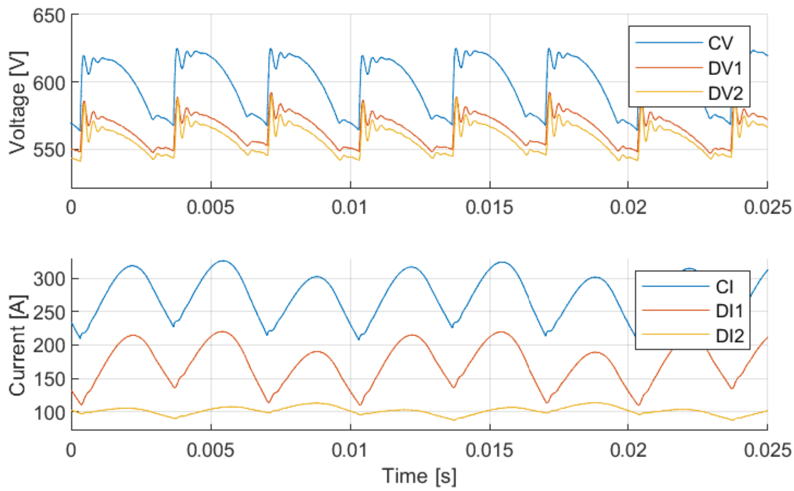

Figure 5.15: Simulated voltage (upper plot) and currents (lower plot) at interfaces C (blue), D1 (red), and D2 (yellow), where vehicle 1 (interface D1) draws 100 kW and vehicle 2 (interface D2) draws 50 kW. The parameter for the input filter is $L = 0.92$ mH in vehicle 1, $L = 1.15$ mH in vehicle 2, and the distance between the vehicles is $d_2 = 2$ km.

In Fig. 5.16, the simulated voltages (upper plot) and currents (lower plot) are presented using the same parameters as the original case shown in Table 5.7, but with L set to 2.06 mH in vehicle 1 and d_2 set to 0.1 km. With the increased inductance of the input filter in vehicle 1, the voltage ripple at interface C is increased to 80 V, while the current ripple at interface D1 for vehicle 1 decreases to 20 A but increases to 30 A for vehicle 2 at interface D2 compared to the nominal case in Fig. 5.13.

Figure 5.17 presents the same simulation as Fig. 5.16, but with an increased electric road length of 2 km between the vehicles ($d_2 = 2$ km). Similar to Fig. 5.15, the only difference is the increased constant voltage drop between the voltages $DV1$ and $DV2$ and there is no significant impact on either voltage or current ripple.

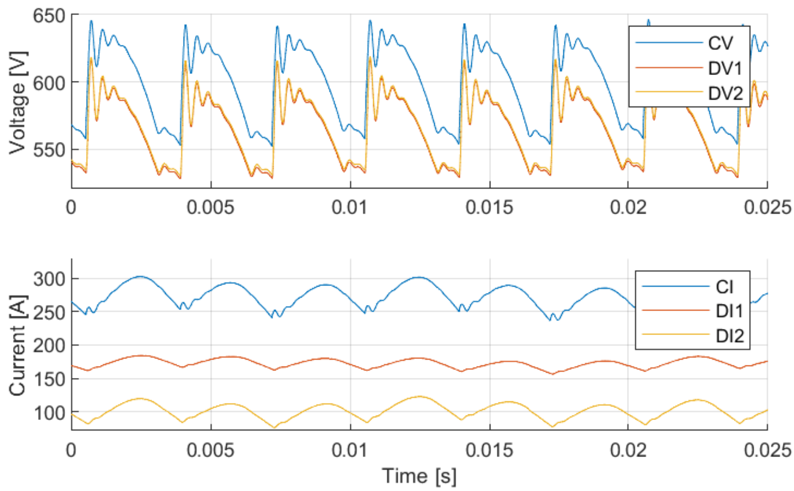

Figure 5.16: Simulated voltage (upper plot) and currents (lower plot) at interfaces C (blue), D1 (red), and D2 (yellow), where vehicle 1 (interface D1) draws 100 kW and vehicle 2 (interface D2) draws 50 kW. The parameter for the input filter is $L = 2.06$ mH in vehicle 1, $L = 1.15$ mH in vehicle 2, and the distance between the vehicles is $d_2 = 0.1$ km.

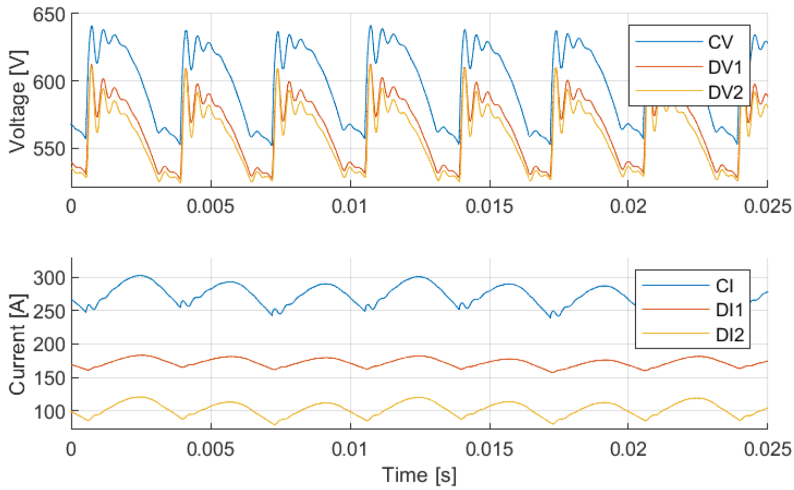

Figure 5.17: Simulated voltage (upper plot) and currents (lower plot) at interfaces C (blue), D1 (red), and D2 (yellow), where vehicle 1 (interface D1) draws 100 kW and vehicle 2 (interface D2) draws 50 kW. The parameter for the input filter is $L = 2.06$ mH in vehicle 1, $L = 1.15$ mH in vehicle 2, and the distance between the vehicles is $d_2 = 2$ km.

5.5.2 Influence of Vehicle Interface Design on Voltage and Current Ripple with 12-Pulse Passive Rectification

To mitigate the issues associated with conductive EMI within the ERS supply, it is essential to reduce voltage and current ripple. This subsection introduces the approach to implement a 12-pulse passive rectifier instead of the existing 6-pulse passive rectifier. Apart from this alteration, the model structure remains identical to the previously presented simulation cases, as originally illustrated in Figs. 5.10 and 5.11.

In Fig. 5.18, a simulation of voltage (upper plot) and current (lower plot) at interfaces C and D of two vehicles charging from the same ERS with a 12-pulse passive rectifier is presented. Similar to Fig. 5.13, the distance between the feeding point and vehicle 1, d_1, is 2 km and the distance between the two vehicles, denoted as d_2, is 0.1 km. The inductance L in vehicle 1 (100 kW) and 2 (50 kW) is set to 1.15 mH. By implementing the 12-pulse passive rectifier, the voltage ripple is significantly reduced to only 25 V at interface C, while the current ripple is decreased to less than 5 A. The only notable variations in voltage and current arise from the simulated grid voltages being modelled as unbalanced, as shown in Table 5.1.

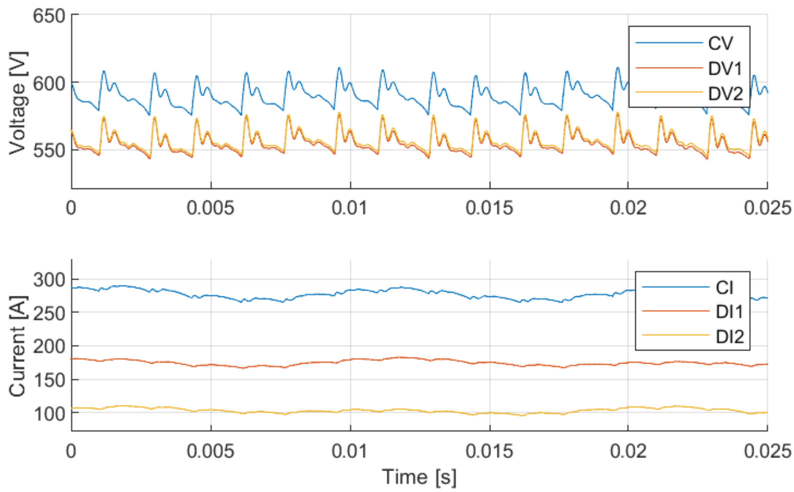

Figure 5.18: Simulated voltage (upper plot) and currents (lower plot) at interfaces C (blue), D1 (red), and D2 (yellow), where vehicle 1 (interface D1) draws 100 kW and vehicle 2 (interface D2) draws 50 kW. The 6-pulse passive rectifier is exchanged to a 12-pulse passive rectifier. The parameter for the input filter is $L = 1.15$ mH in vehicle 1, $L = 1.15$ mH in vehicle 2, and the distance between the vehicles is $d_2 = 0.1$ km.

In Fig. 5.19, the same simulation is executed as presented in Fig. 5.18, but with the inductor parameter L set to 0.92 mH in vehicle 1. As previously shown in Fig. 5.14, this alteration increases the current ripple and reduces the voltage ripple, and in this instance, similar effects are also observed. However, these effects are significantly less prominent because the voltage and current ripple are greatly reduced by the 12-pulse passive rectifier.

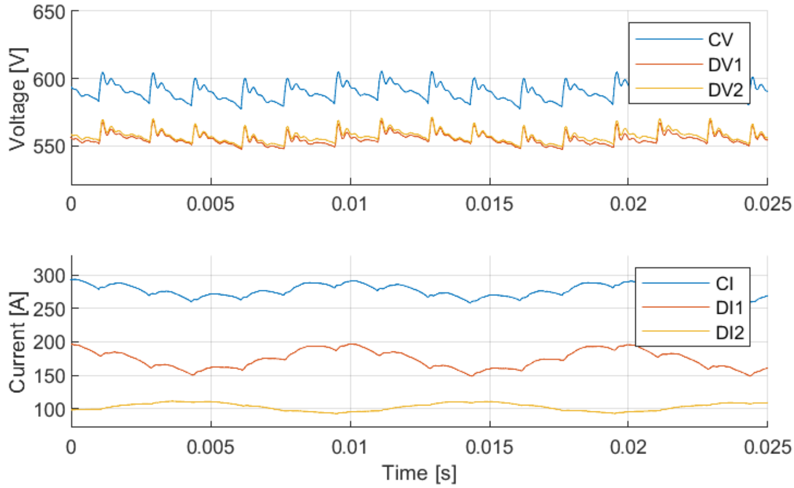

Figure 5.19: Simulated voltage (upper plot) and currents (lower plot) at interfaces C (blue), D1 (red), and D2 (yellow), where vehicle 1 (interface D1) draws 100 kW and vehicle 2 (interface D2) draws 50 kW. The 6-pulse passive rectifier is exchanged to a 12-pulse passive rectifier. The parameter for the input filter is $L = 0.92$ mH in vehicle 1, $L = 1.15$ mH in vehicle 2, and the distance between the vehicles is $d_2 = 0.1$ km.

In Fig. 5.20, the same simulation is executed as presented in Fig. 5.18, but with the inductor parameter L set to 2.06 mH in vehicle 1. As discussed in Fig. 5.16, increasing the inductor will raise the voltage ripple while decreasing the current ripple, which is also observed in Fig. 5.16. However, this effect is less pronounced, with the voltage ripple increasing to roughly 30 V peak-to-peak, while the current ripple remains minimal in relation to the current level.

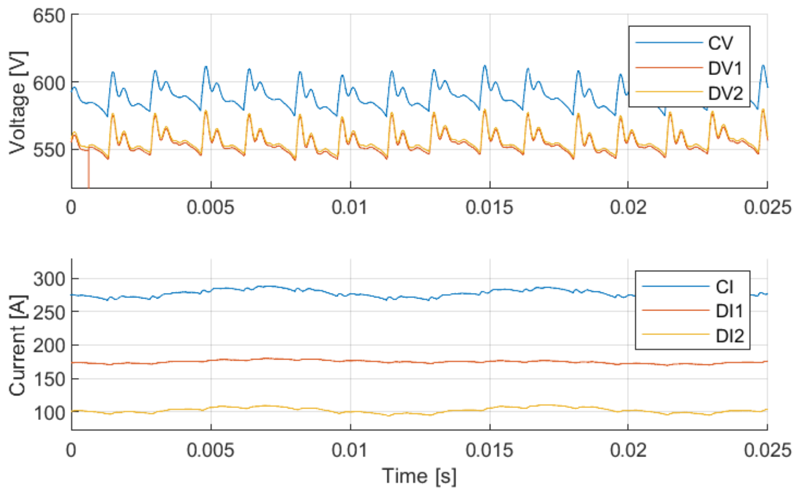

Figure 5.20: Simulated voltage (upper plot) and currents (lower plot) at interfaces C (blue), D1 (red), and D2 (yellow), where vehicle 1 (interface D1) draws 100 kW and vehicle 2 (interface D2) draws 50 kW. The 6-pulse passive rectifier is exchanged to a 12-pulse passive rectifier. The parameter for the input filter is $L = 2.06$ mH in vehicle 1, $L = 1.15$ mH in vehicle 2, and the distance between the vehicles is $d_2 = 0.1$ km.

In order to further reduce the impact of voltage and current ripple, an active filter can be used or an active front end can be implemented instead of the 6- and 12-pulse passive rectifiers. This change could reduce the impact of conductive EMI on the ERS supply and the power grid. By deploying this type of topology, the problems concerning increased voltage and current ripple caused by variations in input filter impedance can be greatly reduced, as the ERS supply voltage and current would exhibit even less ripple than with the 12-pulse passive rectifier. Additionally, by carefully designing the ERS supply to have low voltage and current ripple, the required size and weight of passive filter components onboard the vehicles can be reduced as well.

However, further assessments of conductive EMI with mitigating strategies such as active filters and active front ends, in conjunction with more than two vehicles, are the subject of future work and are outside the scope of this thesis. Regardless, this evaluation suggests that implementing mitigating strategies may be essential, depending on the design choices related to the rectifier station topology and the vehicle ERS interface topology.

5.5.3 Assessment of ERS-Induced Harmonics on the Power Grid

To evaluate the harmonics in the conductive EMI caused by the ERS and its impact on the power grid, the IEEE 519 standard is utilized as a reference [97]. Accordingly, the phase voltage and current at interface A are analyzed using Fast Fourier Transform (FFT) to quantify the harmonics.

According to the standard, the harmonic limits for current are determined by the "maximum demand load current (fundamental frequency component) at the Point of Common Coupling (PCC)." This current is derived from maximum billing periods, such as 15 or 30 minutes, rather than instantaneous peak values. As a result, for ERSs, the harmonics are calculated based on this maximum billing, indicating an average load over the specified time frame. This presents challenges for the standard's application, given that the load (current I_L) on the ERS is influenced by the traffic characteristics and thus the type and number of vehicles utilizing it. Nonetheless, the harmonic limits and Total Harmonic Distortion (THD) presented in [97] are utilized as guidelines to evaluate the magnitude of simulated voltages and currents, rather than as strict limits.

Fig. 5.21 presents the simulated phase voltage and current at interface A for two simulation cases: the plots on the left correspond to 6-pulse passive rectification, while those on the right correspond to 12-pulse passive rectification. This analysis corresponds to the simulation case in which two vehicles draw 100 kW and 50 kW from the ERS, as presented in Figs. 5.13 and 5.18, using the parameters listed in Table 5.7, specifically, $L = 1.15\,\text{mH}$ for both vehicles and $d_2 = 0.1\,\text{km}$. The top row of plots displays the phase voltage in the time domain at interface A, and the third row displays the phase current in the time domain. The FFT plots in the second row display the voltage harmonics at interface A, while the bottom row shows the current harmonics. In both cases, the y-axis represents the relative amplitude of the 50 Hz fundamental frequency, and the x-axis presents the harmonics.

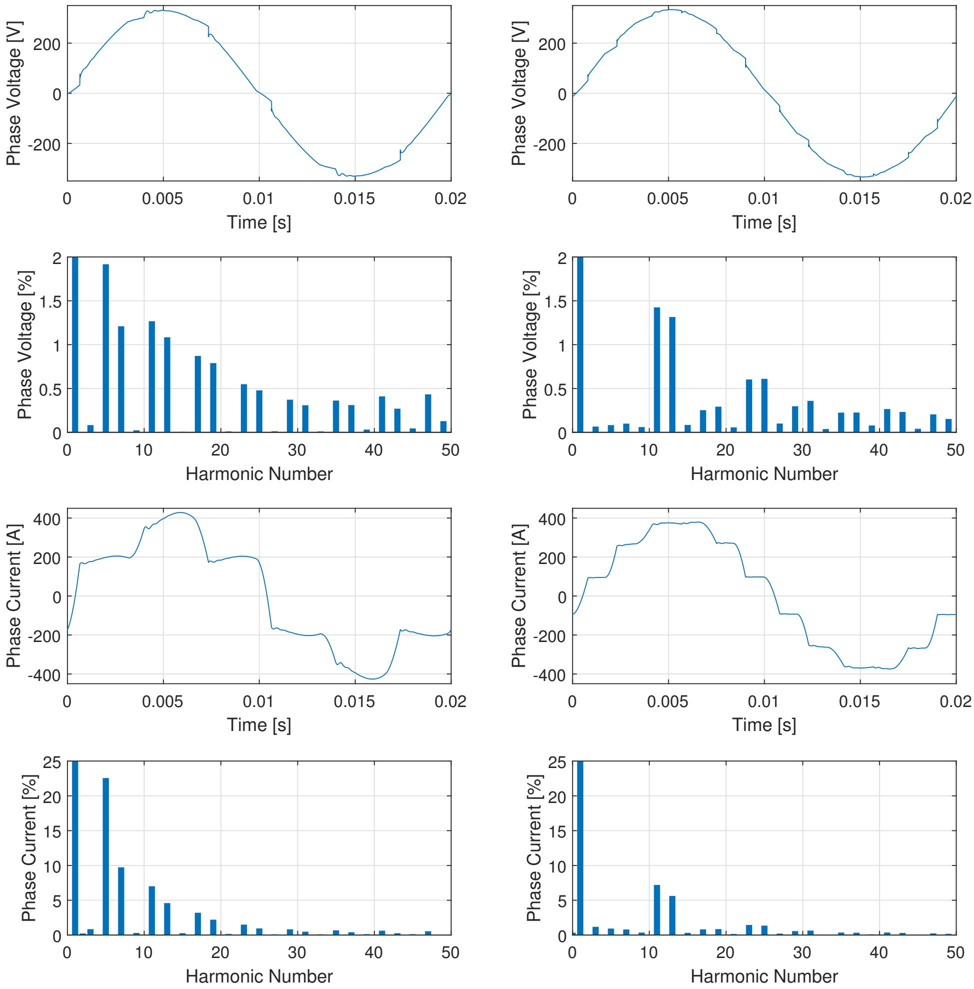

Figure 5.21: Simulated phase voltage and current at interface A with two vehicles drawing power from the ERS (100 kW and 50 kW). The left column of plots shows results for a 6-pulse passive rectifier, and the right column corresponds to a 12-pulse rectifier. The upper four plots show the phase voltage: the top row in the time domain, and the second row its corresponding FFT relative to the fundamental frequency of 50 Hz. The lower four plots show the phase current: the third row in the time domain, and the bottom row its corresponding FFT.

For the 6-pulse passive rectifier, as presented in the two upper left plots in Fig. 5.21, the simulated voltage remains below the prescribed THD limit of 5% established by the IEEE 519 standard. In contrast, the simulated current, depicted in the two lower left plots, significantly exceeds the predefined 4% limit for the odd harmonics from the 3rd to the 11th, particularly for the 5th and 7th harmonics, which exceed 22% and 9%, respectively.

The simulated voltage with the 12-pulse passive rectifier, presented in the two upper right plots of Fig. 5.21, remains within the IEEE 519 standard's 5% THD limit, as no harmonic components exceed this value. In contrast, the simulated current, presented in the two lower right plots, exceeds the established 4% limit for the odd harmonics from the 3rd to the 11th, but only for the 11th harmonic, where it exceeds 6%.

While the current harmonic distortion from the conductive EMI generated by the ERS at interface A exceeded the limits outlined in IEEE 519, and accounting for that there are numerous other standards the ERS grid connection must comply with, this evaluation should be considered preliminary. The evaluation highlights the problem of conductive EMI at the ERS grid connection, caused by the ERS. The results indicate that a more sophisticated rectifier station design, possibly incorporating an active rectifier, may be necessary to ensure compliance with IEEE 519. However, a more thorough investigation is needed to determine whether such a rectifier topology is required by assessing the expected mean load current over the specified timeframes of 15 or 30 minutes.

5.5.4 Recommended Strategies Concerning Conductive EMI

Although the choice of passive rectifiers, such as the 6-pulse and 12-pulse rectifiers, may seem obsolete in light of currently available technologies for various types of active rectification, particularly given their ability to offer low voltage and current ripple in the ERS supply as well as control of active and reactive power, there are still advantages to passive rectification.

- First, passive rectification relies solely on passive components, eliminating the need for supplied power or dependence on the control of the rectification. This characteristic contributes to the robustness and reliability of passive rectifiers due to the absence of active components.

- Second, passive rectifiers are generally expected to be more cost-effective than their active counterparts. In the ERS perspective they only require an ERS transformer (with two secondary windings and two three-phase full-bridge rectifiers in the 12-pulse case), whereas active rectifiers necessitate additional components such as a three-phase inverter (with its control unit and power supply) and grid-side passive filters.

The results related to passive rectification, although they may seem outdated in the context of the more likely adoption of active rectification for future ERS systems, still illuminate concerns regarding conductive EMI, particularly in terms of voltage and current ripple within the ERS supply. As illustrated in the scenarios with the 12-pulse passive rectifier, the associated voltage and current ripple are minimal. However, it is important to recognize that active rectification will still exhibit some degree of voltage and current ripple, which may increase due to the design of vehicles' onboard ERS interfaces. Consequently, it is necessary to determine how stringent the requirements for voltage and current ripples should be. The effects of multiple vehicles with different input filters in their ERS interfaces are not yet fully investigated and could have a significant impact on voltage and current ripple. In addition, reducing voltage and current ripple is expected to lead to smaller and lighter passive filter components in the vehicles. This represents a topic for future research, falling outside the scope of this thesis.

Chapter 6

Modelling Electrical Safety

6.1 Introduction

Given the nature of an ERS as a high-voltage and high-power infrastructure, it inherently poses several safety hazards, particularly the risk of electrocution of human beings and animals as well as exposure to hazardous voltages. One reason for these hazards is the lack of a reliable protective earth connection to the vehicles' chassis.

This chapter explores the safety concerns associated with touch events, defined as instances when a person makes physical contact with an object or structure linked to the ERS that is not intended to be hazardous. Two specific aspects of electrical safety related to touch events are analyzed: (I) human contact with a vehicle connected to the ERS, and (II) human contact with the exposed electric road exterior intended for deployment on public roads. These aspects are evaluated by establishing and using a simulation model that is validated using experimental results from the ERS demonstrator. The validation of the simulation model presented in this chapter extends the work presented in [43].

A human body model, as defined in [49, 98], is used to evaluate the body current levels that may result from various touch events. The model consists of resistors and capacitors representing the impedance of a typical human body. It is important to emphasize that the purpose of this model is not to precisely determine safety margins concerning the severity of a hazardous touch event but rather to model and understand the phenomena associated with hazardous touch events.

For a BEV not adapted for ERS operation, the TVS is floating, meaning there is high impedance between the TVS and electrical ground. The isolation between the high-voltage poles and the chassis is designed to prevent any touch events that could create a conductive path between these high-voltage poles. In contrast, for a vehicle adapted for ERS, the critical safety concern when a person makes physical contact with the vehicle's chassis is ensuring that the chassis remains electrically isolated from the high-voltage poles of both the TVS and the ERS supply. This isolation is crucial to mitigate safety risks, as contact with one of the high-voltage poles in the ERS could result in current flowing through the human body to electrical ground. The challenge lies in consistently ensuring that the vehicle chassis, which includes all accessible parts that a person may touch without crawling beneath it—because the high-voltage components of the current collector, sliding contacts, and active segments of the electric road are located underneath the vehicle—remains electrically isolated from the high-voltage poles. Additionally, if an isolation fault causes a deviation in the impedance between the chassis and a high-voltage pole, the vehicle must be immediately disconnected from the ERS to prevent safety hazards.

Given that the electric road is intended for deployment in diverse environments, including those with extreme weather conditions, it is essential to ensure that the exterior of the electric road remains safe to touch at all times. Typically, the exteriors and accessible parts of all power grid-connected electrical equipment are either connected to electrical ground or isolated from the electrical poles of the device, thereby minimizing the risk of hazardous touch events. Regarding the electric road, as previously discussed in Chapter 2, Section 2.2, the exterior of the electric road is electrically grounded at the rectifier station. However, as with all grounded systems, maintaining a low impedance to ground is crucial to ensure functionality of the grounding system. Consequently, the safety concerns associated with touch events, specifically regarding the impedance of the negative pole of the ERS, are evaluated and tested under various operating conditions to ensure that electrical safety is maintained at all times.

6.1.1 The Human Model

In this chapter, the impedance of a human body, as defined by the standard IEC 60990:2016 [98], is used to analyze phenomena related to touch events involving a person. Fig. 6.1 depicts the human model, which consists of a parallel connection of resistor $R_s = 1.5\,\mathrm{k}\Omega$ and capacitor $C_s = 0.22\,\mu F$, connected in series with resistor $R_b = 0.5\,\mathrm{k}\Omega$. Resistor R_s and capacitor C_s are intended to replicate the impedance of the skin, while resistor R_b represents the internal resistance of the human body. In standard IEC 60990:2016 [98] several variants of this human model are outlined, which are applied based on the touch event and measurement scenario, including correction factors related to the frequency of the current present. The human model presented in Fig. 6.1 is selected for all measurements and modelling in the subsequent sections. This choice is made for the sake of simplification, with the focus being on capturing the fundamental phenomena of touch events.

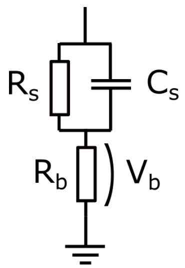

Figure 6.1: The chosen human model for evaluating touch events.

Assessing the impact and severity of hazardous electrical touch events is complex, as outlined in [49, 98]. Generally, the severity of such events is related to both the duration of exposure, measured in ms, and the magnitude of the current, measured in mA (in RMS for AC). Currents between 0.5 and 20 mA AC RMS with exposure times ranging from 0 to 500 ms correspond to the threshold of immobilization. At this level, the muscular contractions are intense enough to prevent voluntary movement as long as the current is flowing. The standard [49] defines an RMS value of 10 mA for AC as the maximum touch current at which an adult can still release the object when it is under voltage. Currents exceeding 20 mA with exposure times over 500 ms can cause difficulty in breathing and reversible disturbances in heart function. Currents above 100 mA with exposure durations over 500 ms can potentially lead to burns, cellular damage, and cardiac and respiratory arrest.

6.1.2 Chassis Voltage Hazards in Electric Vehicle Charging

In a conventional static charger, the BEV chassis is connected to the protective earth via the charging port in the BEV and the charging cable. In the event of an isolation fault between the high-voltage poles of the TVS and the vehicle chassis, the charger's RCD is triggered. This mechanism mitigates the risk of the chassis being exposed to an elevated voltage. However, in the context of a conductive ERS, there is no reliable direct electrical ground connection between the vehicle chassis and the ERS. In the unlikely scenario where an isolation fault exposes the BEV chassis to high voltage, if a human body in contact with electrical ground also touches the chassis, current will flow through the human body to electrical ground. The current will then return via the ERS supply ground connection to the ERS supply, as illustrated in Figs. 6.2 and 6.3.

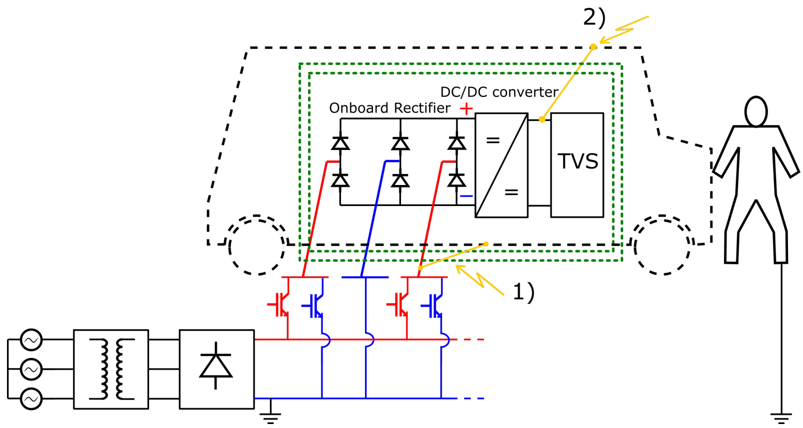

Figure 6.2: A BEV equipped with an ERS interface is connected to an ERS supply. Both the BEV's TVS and the ERS interface are double insulated, as indicated by the green elements in the figure. In the figure, 1) represents an isolation fault between the chassis and the ERS supply, while 2) represents an isolation fault between the chassis and the TVS.

The issue of an elevated voltage on a vehicle's chassis is addressed through two different methods. Firstly, the implementation of double insulation ensures enhanced safety. Double insulation means that all high-voltage components are equipped with an additional layer of supplementary insulation on top of the basic insulation, as outlined in [48]. Fig. 6.2 illustrates a BEV in which double insulation is applied to both the ERS interface and the TVS. The electric bus which is the main vehicle when conducting measurements in the ERS demonstrator is outfitted with double insulation. All components of the TVS, including the ERS power electronic interface, current collector, and associated arms, are required to maintain double insulation relative to the vehicle chassis.

In the event of an isolation fault between the arms of the current collector and the chassis, as shown in fault 1), or between the chassis and the high-voltage pole of the TVS, as depicted in fault 2), the fault must be severe enough to breach both layers of insulation. In cases where a conductive object or debris, possibly mixed with saltwater from the road, contacts an active segment of the ERS or an arm of the current collector along with the vehicle chassis, there is a risk that the chassis could be elevated to a high voltage. This fault is illustrated in 1) in Fig. 6.2. This risk is present in an ERS as they are designed for public roads, where conductive materials such as trash, aluminum cans, or packed snow mixed with salt may accumulate beneath the vehicle.

The risk of elevated chassis voltage may also arise from an internal isolation fault within the TVS, specifically between the positive pole and the vehicle chassis, as shown in fault 2). In such an event, if the chassis becomes energized and a person comes into contact with it, electrical current will flow through the human body to the ground, returning to the rectifier station.

The second measure to ensure a high isolation is the use of a galvanically isolated DC/DC converter between the high-voltage poles of the BEV's TVS and the ERS supply, as discussed in [36]. This configuration allows for less stringent insulation resistance requirements [48], as the TVS remains electrically floating with respect to the ground. Compared to a design that applies double insulation, this approach can significantly reduce the additional volume required onboard the vehicle. Fig. 6.3 illustrates a BEV where a galvanically isolated DC/DC converter is implemented.

It is important to note that the ERS interface must still be double insulated to ensure electrical safety. This is crucial because, in the event of an isolation fault between the chassis and the arm of the current collector, as illustrated by fault 1), the chassis voltage could be elevated, and the resulting current could flow through a human in contact with the vehicle's chassis. However, in the case of an isolation fault between the TVS pole and the chassis, as shown in fault 2), the current will not flow through the human body since the TVS is not galvanically connected to the ERS supply. Therefore, double insulation is not required for this part of the BEV circuit.

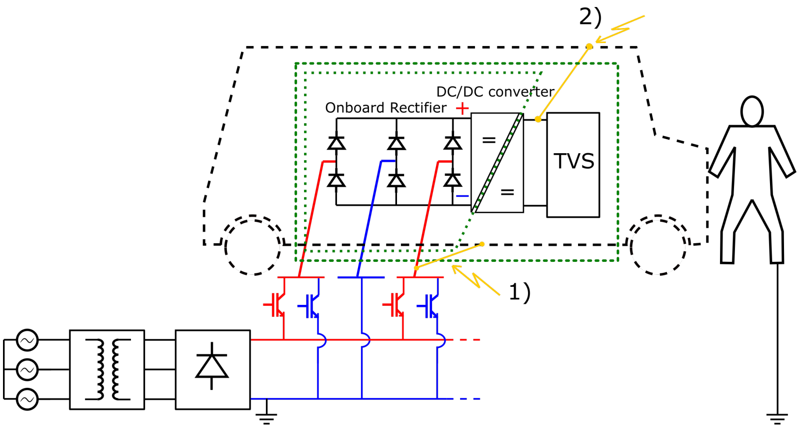

Figure 6.3: A BEV equipped with an ERS interface is connected to an ERS supply. The BEV's TVS is galvanically isolated from both the ERS interface and the ERS supply through an isolated DC/DC converter. Only the ERS interface is double-insulated, as indicated by the green elements in the figure. In the figure, 1) represents an isolation fault between the chassis and the ERS supply, while 2) represents an isolation fault between the chassis and the TVS.

In addition to these measures, BEVs are generally equipped with an IMS that monitors the impedance between the poles of the TVS and the chassis. An IMS can be adapted for ERS deployment to detect elevated chassis voltage and actively disconnect the BEV from the ERS supply, thereby mitigating the risk of hazardous voltages. In such cases, the IMS would monitor impedance variations between the high-voltage poles, from the arms of the current collector and the TVS to the chassis. Upon detecting an isolation fault, indicated by a significant change in impedance between the chassis and a high-voltage pole, the IMS would activate, disconnecting the vehicle from the ERS supply. Prompt detection and disconnection are crucial aspects of IMS operation, as time is a critical factor in mitigating harmful electric hazards, with longer exposure leading to more severe health consequences, as detailed in [49].

6.1.3 Experimental Methods for Characterizing the Vehicle's Chassis Voltage

During the EVR project, numerous attempts were made to assess the voltage of the bus' chassis. This measurement presented significant challenges due to several factors. First, assessing the chassis voltage required establishing a connection between the bus chassis, a measurement instrument, and electrical ground. Since the bus was in motion, it was necessary to use a long cable to connect the chassis to the measurement instrument and electrical ground at the rectifier station, which posed practical difficulties. Second, the long cable inadvertently acted as an antenna, making it highly susceptible to EMI. Third, since the chassis is electrically floating with respect to ground, meaning there was a very high impedance between the chassis and ground, measuring the chassis voltage with respect to ground with high-impedance instruments (as most voltmeters are) proved difficult. A high-impedance voltmeter used to measure a high-impedance voltage leads to a measurement setup that is highly susceptible to EMI, as both the voltmeter and the voltage being measured exhibit minimal current flow.

Several measurements were conducted to refine the measurement methodology progressively. Measurements were performed repeatedly under diverse weather conditions, including both wet and dry environments, to ensure the reliability and robustness of the results. To address the issue of conducting measurements with a high-impedance instrument, the human model was used to lower the impedance path to ground, which allowed for higher current flow, thereby reducing the impact of EMI and improving the reliability of the voltage measurements with the high-impedance instrument. Fig. 6.4 illustrates the measurement setup used for assessing the voltage of the vehicle's chassis. While the bus is drawing power from the ERS, both statically and in motion, a human model is connected between the ground connection of the rectifier station and the bus chassis. The human model is connected as close to the rectifier station as possible, while a long coaxial cable, with its shield grounded in the rectifier station, is used to connect the human model to the vehicle's chassis. This method proved to introduce the least amount of EMI into the measurements. As detailed in the standard [98], the voltage V_b across the resistor R_b is measured, and in this case, a PicoScope 4444 [81] was used.

It is important to note that the figure is intended to highlight the physical distances related to the measurement setup. Despite these distances, the setup maintains the correct impedance between the human model and the rectifier station's ground connection. The measurement setup reflects a touch event by a human, as the impedance of the coaxial cable is very low, rendering the physical distance between the human model and the vehicle negligible in terms of added impedance. Similarly, during a touch event, the ground resistance between the human body and the rectifier station is assumed to be very low, validating the choice of connecting the human model directly to ground at the rectifier station.

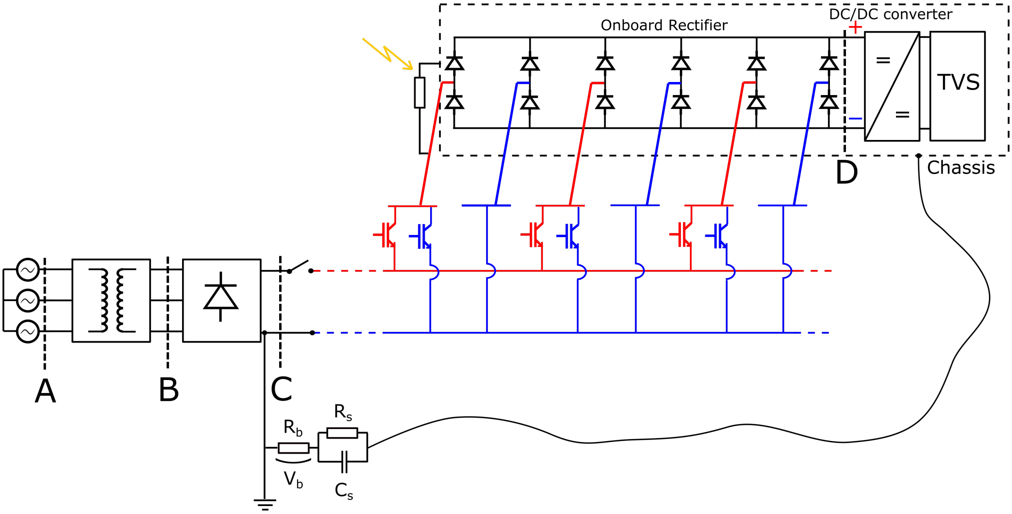

Figure 6.4: The measurement setup for assessing the chassis voltage of the bus involves connecting a human model, grounded at the rectifier station, to the bus chassis via a long coaxial cable. Isolation faults are introduced between the chassis and the arm of the current collector to evaluate their effect on the chassis voltage.

To evaluate the impact of isolation faults, two resistors $11\,\mathrm{k\Omega}$ and $100\,\mathrm{k\Omega}$ were used, representing 1.1% and 10% of an assumed $1\,\mathrm{M\Omega}$ isolation between the chassis and high-voltage pole in a BEV. These values were based on measurements taken from the bus adapted for ERS operation, as presented in Section 2.2. The resistors were alternately connected between the chassis and one of the arms in the current collector, as shown in Fig. 6.4. These values were chosen to replicate the possible presence of conductive objects, debris, or salty snow on public roads, which could introduce such impedances between the BEV chassis and high-voltage pole of the ERS supply.

Measurements without isolation faults were first conducted to serve as a reference for comparing the effects of induced faults. However, during each measurement session, the same waveform shape and magnitude were consistently observed, indicating that the bus chassis exhibited an elevated voltage relative to ground. Simultaneously, the development and establishment of a simulation model intended to simulate the elevated voltage of the chassis was in progress. This model was subsequently used to investigate and understand the observed phenomenon. By adding capacitors between the high-voltage poles of the TVS and the vehicle chassis in the model, the measured voltage was accurately replicated in the simulation model. Fig. 6.5 illustrates the locations of these parasitic capacitors that contribute to this phenomenon. The elevated voltage observed across the human body is caused by the charging and discharging of these capacitors.

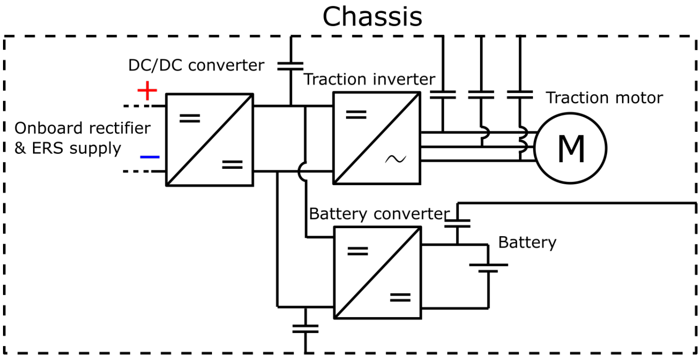

Figure 6.5: A conceptual view of the bus's TVS illustrates the parasitic capacitors connected between the BEV chassis and the high-voltage poles of the DC-link, as well as to the output of the TVS subsystems.

To validate the presence of these parasitic capacitors, measurements were conducted on both the bus and a separate drivetrain from a passenger BEV using an impedance analyzer [83]. Estimating and measuring these parasitic capacitors, especially in a complex electrical system like the bus TVS, proved challenging as these parasitics are highly dependent on the structure, topology, and physical layout of the components within the specific vehicle's TVS. Consequently, different vehicles are expected to exhibit this phenomenon to varying degrees. Although not covered in the scope of this thesis, preliminary analysis of measurements on a passenger car drawing power from the ERS demonstrator also exhibited a current flowing through the human model.

6.1.4 Voltage Hazards on the Exposed Exterior of the Electric Road

Given that the ERS is designed for deployment in a range of environments, including wet conditions and areas where road salt is present, which increase the risk of electric shock, it is essential to assess the electrical safety performance of the exposed ERS exterior voltage relative to electrical ground. The negative conductor of the SER, along with the cable connecting the electric road and the rectifier station, is designed with a larger cross-sectional area compared to the positive conductor. This design choice is intended to mitigate the risk of hazardous voltage drops in the negative conductor, which is exposed externally. It is essential to evaluate whether any voltage drops in the electric road's negative conductor could present a hazard to humans or animals.

Fig. 6.6 illustrates this safety issue, depicting a BEV, in the form of a truck, drawing power from an electric road with an arbitrary length, connected to a rectifier station. In the lower part of the figure, a simplified equivalent circuit diagram of the ERS setup is presented. In this circuit, the DC voltage source U_{DC} represents the rectifier station, variable resistors $R_{ER}+$ and $R_{ER}-$ denote the positive and negative conductors of the electric road, respectively (along with their aggregated resistance including the cable between the electric road and rectifier station), and the variable resistor R_{Load} represents the load of the BEV drawing power from the ERS. The negative and positive conductors are indicated in blue and red colors, respectively, with the negative pole connected to the electric road exterior to illustrate the design of the considered ERS technology.

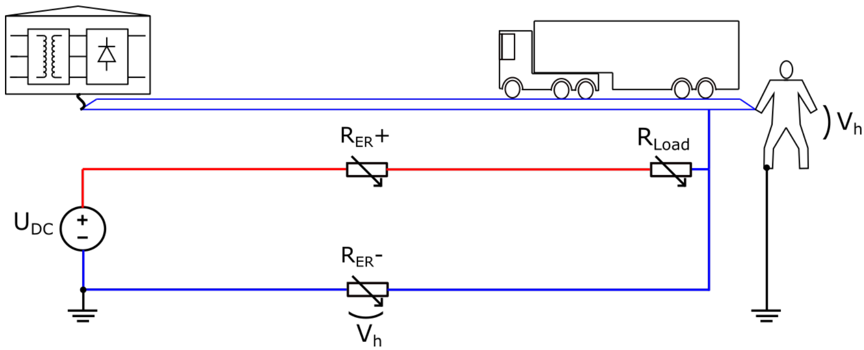

Figure 6.6: Conceptual circuit illustrating the electrical safety concerns during a touch event on the electric road exterior while a vehicle draws power from an ERS. The upper illustration represent the physical ERS setup and components corresponding to the simplified circuit shown below.

As the truck draws power from the electric road and current flows through the circuit, voltage drops occur in the electric road conductors. For $R_{ER}-$, this voltage drop, denoted V_h, is between the load and ground. If a human body contacts the exterior of the electric road near the BEV drawing power from it, the human body will be exposed to the same voltage drop, denoted V_h, as that in the electric road conductor. Consequently, as long as the resistance of $R_{ER}-$ remains low, the voltage drop will also be low and thus not hazardous to touch. Ultimately, the magnitude of the voltage drop, denoted V_h, depends on the current drawn by the BEV and the length of the electric road.

6.1.5 Experimental Methods for Characterizing Voltage on Exposed Electric Road Exteriors

To evaluate the impact of elevated voltage relative to ground on the electric road exterior, measurements were conducted on the ERS demonstrator. Fig. 6.7 illustrates the measurement setup used to assess the voltage level of the negative conductor of the electric road with respect to ground. During these measurements, the bus was drawing power from 100 meters of electric road, denoted as L in the figure. A Picoscope 4444 [81] was used to measure the voltage between the exterior of the electric road (the negative conductor), denoted V_h, located just behind the bus, and a copper bar hammered into the ground, which served as the electrical ground connection.

Although a more ideal measurement setup would involve using a human model connected to the electrical ground at the rectifier station, as illustrated in Fig. 6.4, the presented and employed measurement setup still yielded adequate results for assessing the magnitude of the current flowing through the human body. During the development of the measurement setup used to evaluate the vehicle's chassis voltage, as shown in Fig. 6.4, it was found that using a grounded copper bar for the ground connection, instead of the rectifier station's ground, and omitting the human model, had a minor impact on the DC voltage levels and the corresponding low-frequency components. The primary focus of this assessment is on the DC voltage and low-frequency content of the electric road exterior voltage, specifically to determine whether the current through the body when touching the electric road exterior can reach harmful levels as defined in the adhering standards [49]. Given this context, the described measurement setup was considered adequate for the assessment.

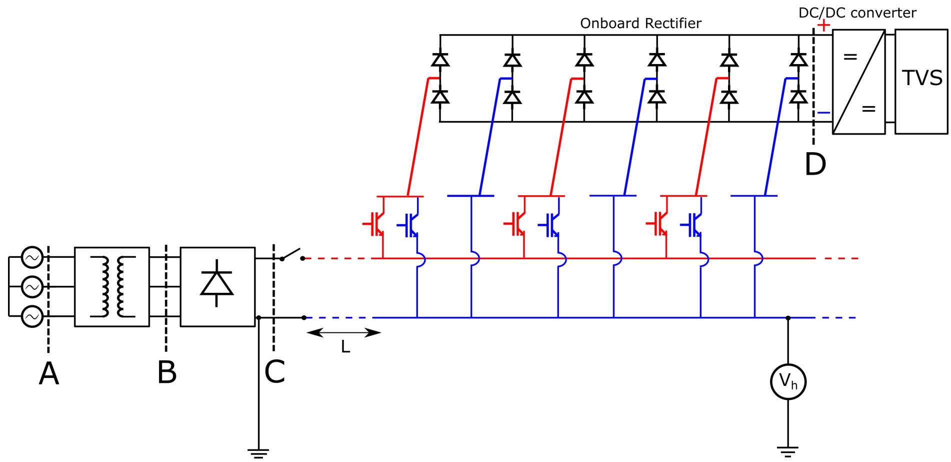

Figure 6.7: Measurement setup for assessing the voltage of the electric road exterior with respect to ground. The bus draws power from the ERS demonstrator while the voltage V_h between the electric road exterior and the electrical ground, positioned just behind the bus, is measured.

6.2 Modelling

The phenomena related to the elevated voltage of the vehicle chassis are attributed to capacitive coupling between the chassis and the output of the onboard converters. Consequently, the time resolution required to model these phenomena is related to the switching frequency of the converters. Therefore, the model presented in Chapter 5, Section 5.2, is deemed appropriate for simulating these phenomena. This model is validated for the ERS demonstrator during normal operation and is capable of performing simulations at a timescale of 0.1 ms, which exceeds the range of switching frequencies for the onboard converters in the bus' TVS. Subsequent subsections detail modifications to the original model presented in Chapter 5 to enable it to address the electrical safety issues related to elevated chassis potential and the voltage of the electric road exterior. Considering that the model presented in Chapter 5 shows an error margin of less than 10%, it is expected that this model is capable of accurately simulating both the voltage of the BEV chassis and the voltage of the electric road exterior.

The modelling of electrical safety issues in this chapter is not intended as a tool for quantifying the fatality or danger of a specific event but rather to provide insight into the factors influencing these phenomena and to identify which parameters affect their magnitude. Consequently, the accuracy of the model should be assessed not only by the magnitude of the error but also by the degree to which the waveform shape and magnitude in simulations align with those observed in actual measurements.

6.2.1 Model Adjustments for Simulations of Chassis Voltage

To accurately model the parasitic capacitive effects that occur when a human model contacts a BEV chassis while the vehicle is drawing power from an ERS, it is necessary to introduce capacitors between the BEV's high-voltage poles and chassis. This subsection presents modifications to the vehicle circuit models originally presented in Section 5.2.4 in Chapter 5.

In Fig. 6.8, the circuit model for the vehicle's ERS interface is illustrated. The model from Fig. 5.3 is extended with two resistors, R_{DC+} and R_{DC-}, as well as two capacitors, C_{DC+} and C_{DC-}, placed at the DC-link (capacitor C_6) between the high-voltage poles of the TVS and the BEV chassis. The values for these parameters are specified in Table 6.1. The resistors represent the aggregated isolation resistance between the positive and negative poles of the BEV TVS and the chassis and the capacitors represent the parasitic capacitive coupling between chassis and the high-voltage poles of the DC-link.

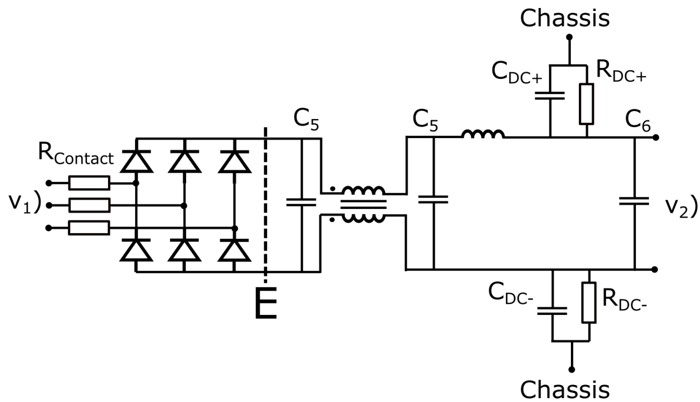

Figure 6.8: Circuit model of the vehicle ERS interface adjusted for modelling the vehicle's chassis voltage.

Table 6.1: Simulation parameters for the vehicle ERS interface circuit model.

Vehicle ERS interface circuit model parameters		
Parameter	*Unit*	*Value*
C_{DC+}	nF	18.5
C_{DC-}	nF	18.5
R_{DC+}	MΩ	1
R_{DC-}	MΩ	1

Although the isolation resistance is expected to vary greatly depending on external factors such as humidity and weather conditions, a nominal value of 1 MΩ is chosen for all isolation resistance parameters in this chapter. Measurements conducted during the EVR project using an isolation tester revealed that this parameter choice was within the range of 1 MΩ. The parasitic coupling between the high-voltage poles of the DC-link in the TVS and the bus chassis was measured using an impedance analyzer [83]. This parasitic capacitance is expected to be one of the largest in the TVS, as the DC-link has a large surface area exposed to the chassis and acts as a connecting node for all subsystems in the TVS. Fortunately, the measurement of this parasitic capacitance was successful, providing a relatively constant capacitive impedance over a wide range of frequencies when using the impedance analyzer.

In Fig. 6.9, the adjusted circuit model for the battery system is illustrated, extended with a parasitic capacitor and isolation resistor between the output of the converter and BEV chassis. The values of this capacitor and resistor are detailed in Table 6.2. The original battery system circuit model is presented in Fig. 5.4.

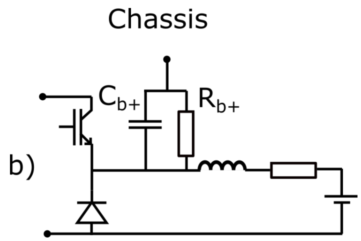

Figure 6.9: Circuit model of the battery system adjusted for modelling the vehicle's chassis voltage.

Table 6.2: Simulation parameters for the battery system circuit model.

Battery system circuit model parameters		
Parameter	*Unit*	*Value*
C_{b+}	nF	1.6
R_{b+}	MΩ	1

Fig. 6.10 presents the adjusted circuit model of the drivetrain from Fig. 5.5, where parasitic capacitors and isolation resistors are introduced between the BEV chassis and the output of the traction inverter. The parameter values for these components are detailed in Table 6.3. All three positive capacitors and isolation resistors, denoted C_{d+} and R_{d+}, are assigned identical values at the output of the converter.

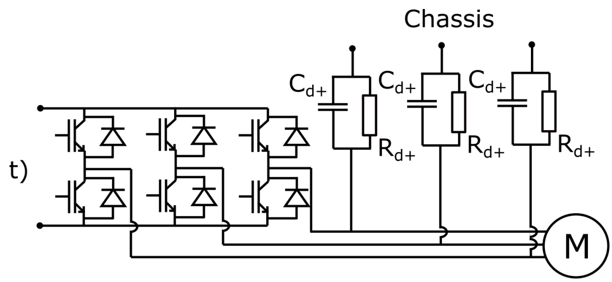

Figure 6.10: Circuit model of the drivetrain adjusted for modelling the vehicle's chassis voltage.

Table 6.3: Simulation parameters for the drivetrain circuit model.

Drivetrain circuit model parameters		
Parameter	*Unit*	*Value*
C_{d+}	nF	1.2
R_{d+}	MΩ	1

To validate the magnitude of these parasitic capacitors, measurements were conducted using an impedance analyzer [83] both on the bus and on a separate traction inverter and corresponding machine located in a laboratory environment from a passenger car. Although the conducted measurements were rudimentary, they confirmed the presence of parasitic capacitance, with magnitudes ranging from 10 to 200 nF depending on the measurement setup and frequency. The final parasitic capacitance values used for model validation, as presented in Tables 6.2 and 6.3, were adjusted during the model calibration process. These adjustments were necessary to achieve accurate model behavior, even though the initial values were based on measurements from the bus, the separate drivetrain, and previous published work regarding parasitic capacitance [99]. Additional work is needed to refine measurement methods for assessing these parasitics and to better understand the influence of physical layouts and topology on these parasitic effects.

To evaluate the impact of electrical safety concerning the BEV chassis voltage, the human model previously presented in Fig. 6.1 is integrated into the chassis of the vehicle's ERS interface, battery system, and drivetrain circuit models, as depicted in the block diagram in Fig. 6.11, where the chassis is represented by a dotted black rectangle. In addition to the human model, an isolation fault block is incorporated to represent the induced isolation faults of 11 kΩ and 100 kΩ, which are introduced in both the measurements and the model, as illustrated in Fig. 6.4. This block diagram outlines the model structure that is utilized in all simulations related to the BEV chassis voltage.

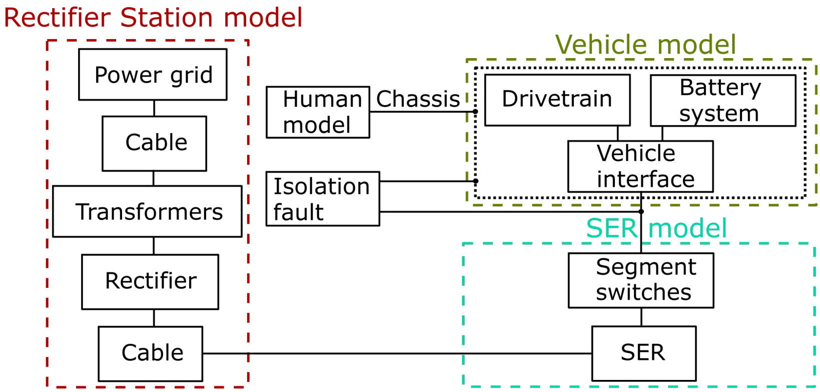

Figure 6.11: Block diagram of the simulation model's structure which is used to assess electrical safety concerns related to the BEV chassis voltage.

6.2.2 Model Adjustments for Simulations of Voltage on the Electric Road Exterior

To assess the voltage of the electric road exterior, the original SER circuit model in Fig. 5.2 from Section 5.2 is adjusted to include a voltmeter, as illustrated in Fig. 6.12, reflecting the employed measurement method. To evaluate the severity and effects on the human body, subsequent simulation scenarios presented in this chapter include a human model, presented in Fig. 6.1. Apart from incorporating the human model connected to the negative pole of the SER circuit model, the overall model structure for both validation and simulation cases remains consistent with that used for BEV chassis voltage simulations, as illustrated in Fig. 6.11, excluding the location of the human model and the isolation fault resistor. Simulations concerning the voltage of the electric road exterior focus on scenarios involving increased vehicle power draw and extended electric road length to simulate worst-case conditions that could result in potentially hazardous voltage levels affecting the human body.

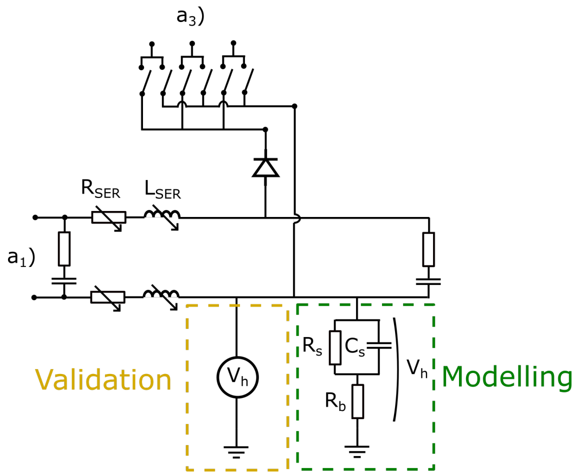

Figure 6.12: The circuit model of the SER, extended with a voltmeter for validation and a human model for subsequent simulation cases.

6.3 Model Validation of the Vehicle's Chassis Voltage

The model is validated using experimental results obtained from the ERS demonstrator with the electric bus. This section presents the validation of the model when simulating the voltage of the vehicle's chassis, comprising three distinct validation cases: one with no induced isolation faults between the chassis and the positive pole, one with an isolation fault of 100 kΩ, and a final case with an isolation fault of 11 kΩ.

The validation process includes assessing the voltage of the bus' chassis under both static and dynamic charging conditions. Static charging is evaluated when the bus draws 40 kW, while dynamic charging is evaluated when the bus draws 100 kW. During static charging, only the battery converter is active, affecting the voltage V_b in the human model. In contrast, during dynamic charging, both the battery converter and the traction inverter are active, thus affecting the voltage V_b in the human model compared to the static charging case.

The timing of static and dynamic charging events differs between measurements and simulations to demonstrate the model's capability to replicate the capacitive coupling phenomenon between the chassis and the TVS for both the battery converter and the traction inverter. However, it is important to note that this difference should not be interpreted as an indication that the model can accurately replicate phenomena occurring on a timescale of seconds. Since the model operates on a ms timescale, the precise timing of charging events in the order of seconds or fractions of seconds is not critical for these simulations. The model is configured to simulate a constant speed during dynamic charging; in this case, the bus is assumed to travel at 18 km/h without accounting for acceleration or deceleration. Consequently, the lower plots in the subsequent figures presented in this subsection illustrate static charging followed by an instantaneous transition to dynamic charging at 18 km/h, primarily to demonstrate the model's ability to simulate both static and dynamic charging conditions.

6.3.1 Validation of Elevated Chassis Voltage due to Capacitive Coupling

Fig. 6.13 presents data for both the measured (upper plot) and simulated (lower plot) voltage V_b (over R_b in the human model, as defined in the standard [98]), related to the left y-axis. The right y-axis corresponds to the red line, which displays the current I_b, measured in the upper plot and simulated in the lower plot, flowing through the human model. I_b is presented as an RMS value with an additional moving average filter applied with a 50 ms window. This approach is employed because the current values for I_b are defined as RMS in [49].

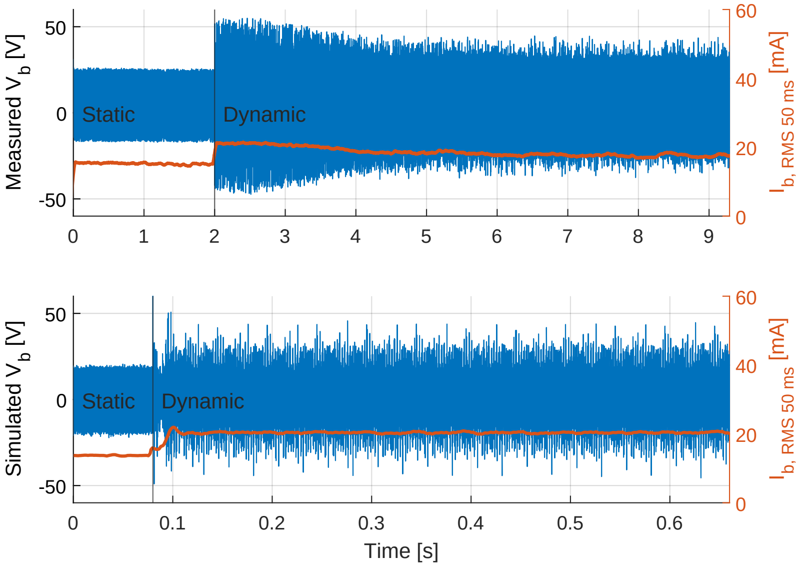

Figure 6.13: Measured (upper plot) and simulated (lower plot) voltage V_b across the resistor R_b in the human model, shown by blue lines related to the left y-axis, when the bus is drawing power from the ERS both statically (40 kW) and dynamically (100 kW). Current through the human body I_b, with a moving RMS value filtered with a 50 ms window, is represented by red lines related to the right y-axis.

In the measurements (upper plot), the bus remains stationary and draws power from the ERS between 0 and 2 seconds, while it is in motion and drawing power from 2 to 9.2 seconds. Note that the voltage V_b and the corresponding current I_b increase and then decrease as dynamic charging starts between 2 and 4 seconds. Given the complexity of the bus's TVS, the exact cause of this phenomenon remains unclear, particularly since it occurs on a timescale of seconds rather than milliseconds, which is beyond the scope of the simulation model's intended timescale. However, one possible explanation is that additional parasitic capacitors associated with subsystems and their corresponding converters become active when dynamic charging begins. These capacitors, connected to the bus's TVS, become charged, leading the voltage V_b across the resistor R_b in the human model to exhibit a waveform similar to that of a current charging a capacitor in an RC circuit, with a time constant on the order of several seconds. This hypothesis is supported by subsequent measurements, where the introduction of isolation faults between the arm in the current collector and the chassis affected this phenomenon, indicating that the RC filter's time constant is altered.

The upper plot in Fig. 6.14 presents a zoomed view at 1 second from the upper plot in Fig. 6.13, showing a timeframe of 3 ms during which the bus is charging statically from the demonstrator. The lower plot in Fig. 6.14 shows a simulation designed to replicate the voltage V_b during static charging, wherein the battery converter is active, as detailed in Fig. 6.9. The model successfully simulates the basic waveform shape with reasonable accuracy, and the absolute values are closely aligned with the measurements. The voltage V_b originates from the charging and discharging of parasitic capacitors between the TVS poles and the chassis. Thus, the magnitude of V_b is independent of the drawn power but rather depends on the absolute voltage level across these parasitic capacitors, which is not influenced by the vehicle load. The waveform shape reflects the charge and discharge cycles of the parasitic capacitors between the chassis and the output of the active subsystems in the bus TVS.

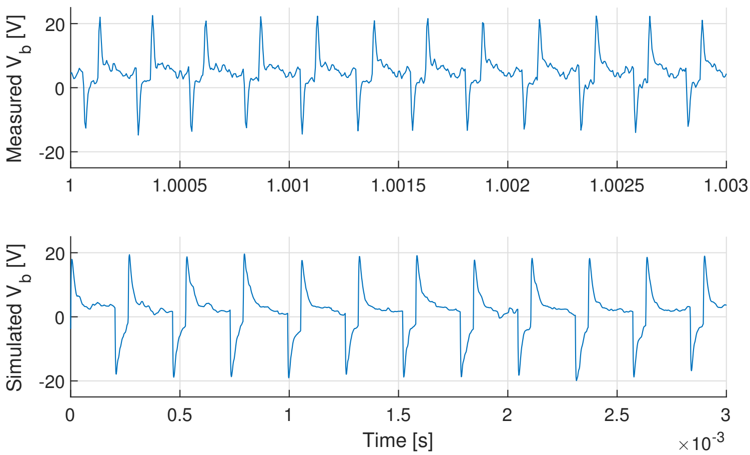

Figure 6.14: Measured (upper plot) and simulated (lower plot) voltage V_b across the resistor R_b in the human model when the bus is drawing power from the ERS statically (40 kW).

The upper plot in Fig. 6.15 presents a zoomed-in view of a 5 ms interval at the 7-second mark from the upper plot in Fig. 6.13, showing the measured and simulated (lower plot) voltage V_b during dynamic charging, with the bus driving at approximately 18 km/h along the electric road. As depicted in the drivetrain circuit model in Fig. 6.10, the system includes three output points of the inverter, each alternating between 0 V and 650 V, in contrast to the battery converter, which has only one such point as shown in Fig. 6.9. Consequently, the charging and discharging of the parasitic capacitors to the chassis from the traction inverter and battery converter vary in time and move in and out of phase with each other, resulting in an interference-based waveform shape for V_b. Due to this variability in the waveform shape of V_b during dynamic charging, the model's ability to replicate both the waveform shape and magnitude is less precise compared to the static charging case. Nevertheless, the model successfully captures the overall waveform shape and phenomena observed in the measurements.

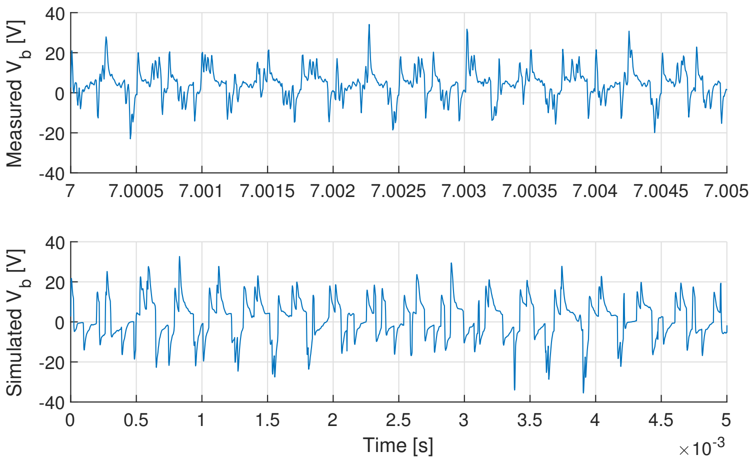

Figure 6.15: Measured (upper plot) and simulated (lower plot) voltage V_b across the resistor R_b in the human model when the bus is drawing power from the ERS dynamically (100 kW).

In Table 6.4, RMS values of I_b filtered with a moving average filter with a 50 ms filter window, representing the current flowing through the human model, are presented for both static and dynamic charging conditions, based on measurements and simulations. The models accuracy in predicting I_b in RMS is deemed adequate. Specifically, the model exhibits an error of 13% during static charging and 18% during dynamic charging. For static charging, as presented in Fig. 6.14, this difference is mainly attributed to the lower voltage level after the charging of the parasitic capacitors, the average DC-offset voltage (for instance, between 0.05 and 0.2 ms in the lower plot), where the simulated voltage is 2 V, compared to 5 V in the measurement (upper plot), leading to a reduced value of I_{b} in the simulations. In the case of dynamic charging, this difference primarily arises because the discharge time of the simulated voltage V_b is longer than that observed in the measurements, resulting in an overestimation of the RMS value in the simulations.

Although the model performs well in accurately replicating the hazardous current I_{b}, it is not yet sufficiently refined to reliably estimate safety risks based on the RMS values outlined in standards. In terms of the actual severity of the measured current I_b, utilizing the prescribed human model presented in Fig. 6.1, the current levels of 15 and 17 mA are associated with immobilization, previously discussed in Section 6.1.1 of this chapter. Beyond the prescribed 10 mA threshold, an adult may no longer be able to release an object carrying this current. It is important to note that the effect of these parasitic capacitors are specific to each BEV. However, additional measurements—though not included in this thesis—suggest that similar phenomena are not exclusive to the bus, but are also observed in other vehicles.

Table 6.4: Measured and simulated values of current flowing through the human model.

Simulation result - no isolation fault			
Result	*Unit*	*Value*	
		Static	Dynamic
Measured I_b	$\mathrm{mA}_{\mathrm{RMS},\,50\,\mathrm{ms}}$	15	17
Simulated I_b	$\mathrm{mA}_{\mathrm{RMS},\,50\,\mathrm{ms}}$	13	20

Fig. 6.16 presents a conceptual simplified circuit of the ERS demonstrator with the aim to explain the factors influencing the phenomena related to parasitic capacitors and the voltage V_b across the human model. Through modelling, it was observed that the voltage V_b in the human model behaves similarly to a charge-discharge current in an RC circuit, where the capacitors C^+ and C^- are charged and discharged in response to the switched voltage. The circuit is based on an arbitrary buck converter representing a power electronic subsystem within the bus TVS while the bus is drawing power from an ERS. This simplified model includes U_{DC} to represent the ERS supply voltage, with all other circuits and impedances between the ERS supply voltage and the input of the buck converter omitted. C^+ represents the parasitic capacitor between the switched output of the converter and the vehicle's chassis (C_b+ from Fig. 6.9), while C^- denotes the aggregated parasitic capacitors between the high-voltage poles of the TVS

and chassis at the DC-link ($C_{\mathrm{DC}+}$ and $C_{\mathrm{DC}-}$ from Fig. 6.8). At the switching frequencies of the subsystems in the TVS, the DC-link capacitor (C_6 from Fig. 6.8) acts as a short circuit, as it is much larger than the parasitic capacitors $C_{\mathrm{DC}+}$ and $C_{\mathrm{DC}-}$. Thus, C^- represents the sum value of $C_{\mathrm{DC}+}$ and $C_{\mathrm{DC}-}$, as they are connected in parallel if the DC-link capacitor is regarded as a short-circuit. The load side of the buck converter comprises an inductor and a DC voltage source. The elements C_s, R_s, and R_b represent elements of the human model, as previously presented in Fig. 6.1.

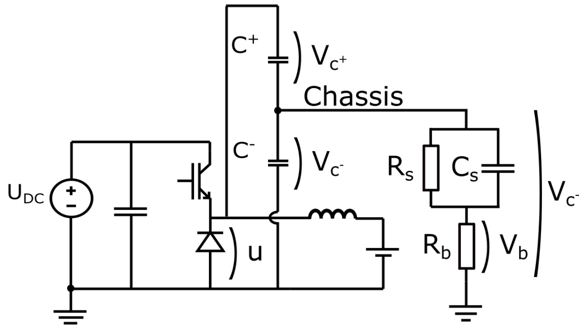

Figure 6.16: Simplified circuit of an arbitrary subsystem within a BEV TVS, incorporating a buck converter, designed to illustrate the phenomena associated with the voltage V_b across the human model and the parasitic capacitors between the chassis and TVS.

When the transistor in the buck converter begins to conduct, the voltage u is applied across both the load and the parasitic capacitors. This voltage transient will cause the parasitic capacitors C^+ and C^- to be charged. The applied voltage U_{DC} is divided across each parasitic capacitor through voltage division. The voltage V_{C^-}, which is applied across C^-, is also applied across the human model, as the human model is connected in parallel with C^- and ground. As C^+ and C^- charge, a corresponding charging current flows through the human model. Given that C^+ and C^- are significantly smaller than C_s, the human model can be approximated as a resistance (R_{b}) during this brief interval when the voltage is applied across the parasitic capacitors. Consequently, the parasitic capacitors C^+ and C^-, in conjunction with the human model, function as an RC circuit, where the voltage V_b behaves similarly to a charging current (as the voltage V_b is linearly proportional to the current flowing through the human model). Conversely, when the transistor ceases to conduct and the voltage u across the load is turned off, the load current supplied to the battery freewheels through the diode in the circuit and the capacitors partly discharge through the human model, resulting in a negative discharge current and, in turn, a negative voltage V_b.

To facilitate a clearer understanding of the circuit, it is useful to initially consider a simplified model in which the human model is excluded. In this scenario, the current flowing through the capacitors can be described by Eqs. (6.1) and (6.2), where the currents i^+ and i^- are equal, leading to the expression in Eq. (6.3).

During the transistor's turn-on (or turn-off) event, the change in the converter's output voltage can be described by the sum of the rates of change of the voltages across capacitors C^+ and C^-, as described in Eq. (6.4). During the switching event, which occurs over a switching period t_{sw}, this expression can be approximated according to Eq. (6.5), which simplifies to Eq. (6.6).

By incorporating this with Eq. (6.3), the voltage difference dV_{C^-} can be described by the formula in Eq. (6.7). Reintroducing the human model into the circuit reveals that the voltage difference dV_{C^-} is parallel to the capacitor C^-, and hence, this voltage is applied across the human model. Therefore, the simplified circuit analysis leading to Eq. (6.7) provides insight into the parameters influencing the magnitude of V_b.

$$C^- \frac{dV_{C^-}}{dt} = i^- \tag{6.1}$$

$$C^+ \frac{dV_{C^+}}{dt} = i^+ \tag{6.2}$$

$$\frac{dV_{C^-}}{dV_{C^+}} = \frac{C^+}{C^-} \tag{6.3}$$

$$\frac{du}{dt} = \frac{dV_{C^+}}{dt} + \frac{dV_{C^-}}{dt} \tag{6.4}$$

$$\frac{U_{DC}}{t_{sw}} = \frac{dV_{C^+}}{t_{sw}} + \frac{dV_{C^-}}{t_{sw}} \tag{6.5}$$

$$U_{DC} = dV_{C^-} + dV_{C^+} \tag{6.6}$$

$$dV_{C^-} = U_{DC} \frac{C^+}{C^+ + C^-} \tag{6.7}$$

6.3.2 Validation of Elevated Chassis Voltage due to Isolation Faults

To further assess the effects of elevated voltage on the chassis of a BEV when isolation faults occur between the chassis and high-voltage poles of the TVS or ERS supply, the model was validated under these conditions. Isolation faults were introduced between one arm of the current collector and the bus chassis using resistors, R_{f}, with values of $100\,\mathrm{k}\Omega$ and $11\,\mathrm{k}\Omega$, as presented in Section 6.1.3. Consequently, as the arm made contact with a segment activated with positive high-voltage, the voltage of the BEV chassis was elevated with respect to ground.

These variations in isolation resistance per pole are expected to influence the DC offset voltage of V_b, as the isolation resistances per pole (R_{DC+} and R_{DC-}) form a voltage divider to the chassis, as illustrated in Fig. 6.8. The isolation fault R_{f} affects this voltage divider when connected in parallel.

100 kΩ Isolation Fault

In Fig. 6.17, both measured (top) and modelled (bottom) values of the voltage V_b across the resistor R_{b} in the human model are presented for an isolation fault of $100\,\mathrm{k}\Omega$. As previously discussed, the measurements and simulations are not synchronized on a time scale of seconds. The lower plot serves to illustrate the model's ability to model static charging and dynamic charging at a constant speed of 18 km/h. In the measurement, the voltage V_b increases when the current collector arm comes into contact with a segment with a positive voltage due to the induced isolation fault. The acceleration of the bus can be observed by noting that the duration of each period of elevated voltage shortens over time. However, the model, which only simulates a constant speed, fails to capture this phenomenon since it is not designed to account for speed variation.

The model is limited in its ability to represent variations in isolation resistance, as the increase in voltage V_b is minimal when the arm in the current collector is connected to a positive segment in the ERS, as shown in the lower plot. In the measurement (upper plot), it is observed that when the arm in the current collector, connected to the chassis, makes contact with a segment of negative voltage (0 V) during static charging, the isolation fault does not elevate the voltage of the BEV chassis. This is due to an error in the experimental setup for this measurement, as the arm with the isolation fault in the current collector should have been in contact with a positive segment in the ERS. If the experimental setup had been as intended, the arm with the isolation fault would have been connected to a positive segment (650V), and an elevated chassis potential would have been observed during static charging. During dynamic charging, at approximately 9.4 s, the arm with the isolation fault comes into contact with a segment at a positive voltage (650 V), resulting in an increase of the voltage V_b. This occurs because the current is divided between the positive ERS supply pole and the human model via the BEV chassis. However, the isolation fault of 100 kΩ does not appear to be significant, as the impact on V_b and the current I_b is minimal, with only a small change in I_b of a few mA in the measurement.

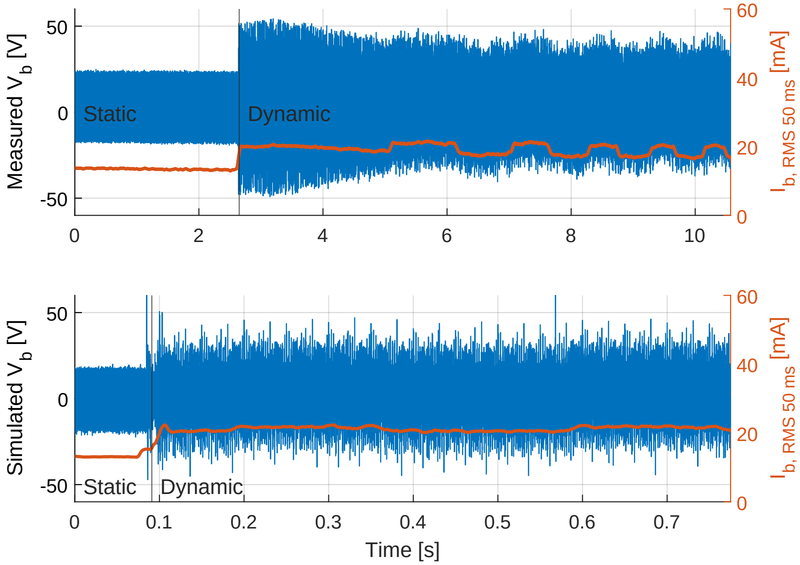

Figure 6.17: Measured (upper plot) and simulated (lower plot) voltage V_b across the resistor R_b in the human model, shown by blue lines related to the left y-axis, when the bus is drawing power from the ERS both statically (40 kW) and dynamically (100 kW) with an isolation fault of 100 kΩ present. Current through the human body I_b, with a moving RMS value filtered with a 50 ms window, is represented by red lines related to the right y-axis.

The upper plot in Fig. 6.18 provides a zoomed-in view of a 3 ms interval at the 2-second mark during static charging, corresponding to the upper plot in Fig. 6.17, where the vehicle is charging statically with an isolation fault of 100 kΩ. The simulation (lower plot) is configured such that the arm of the current collector, which has an isolation fault to the bus chassis, makes contact with a negative segment in the electric road, analogous to the conditions of the measurement (upper plot). Since the isolation fault occurs between the chassis and the current collector arm while the arm is in contact with a negative segment of the electric road, both V_b and I_b remain unchanged, matching the values observed in the absence of an isolation fault, as shown in Fig. 6.14.

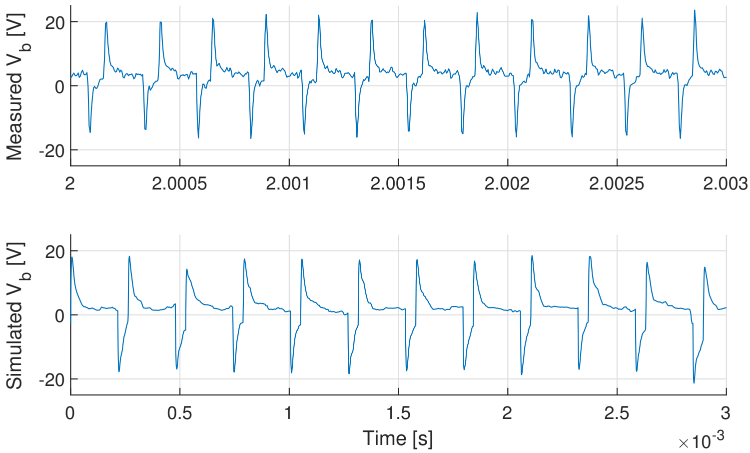

Figure 6.18: Measured (upper plot) and simulated (lower plot) voltage V_b across the resistor R_b in the human model when the bus is drawing power from the ERS statically (40 kW) with an isolation fault of 100 kΩ present.

In Fig. 6.19 the upper plot illustrates a zoomed-in view of a 5 ms interval at 10.3 s, taken from the upper plot of Fig. 6.17, during dynamic charging. The lower plot in Fig. 6.19 presents a simulation of the same event. At 10.3 s, the arm in the bus's current collector makes contact with a positive segment in the electric road (650 V), causing the voltage V_b to increase with a DC offset, resulting from the voltage division across the isolation resistances between the TVS poles and the chassis. The simulation is similarly configured, ensuring that the arm in the current collector makes contact with a positive segment in the electric road, thereby replicating the conditions of the measurement. Similar to the original scenario without induced isolation faults, presented in Fig. 6.15, the model performs well in this case as both the waveform shape and magnitude of the simulated and measured voltages correlate closely as the DC offset voltage resulting from the induced isolation fault has an insignificant impact.

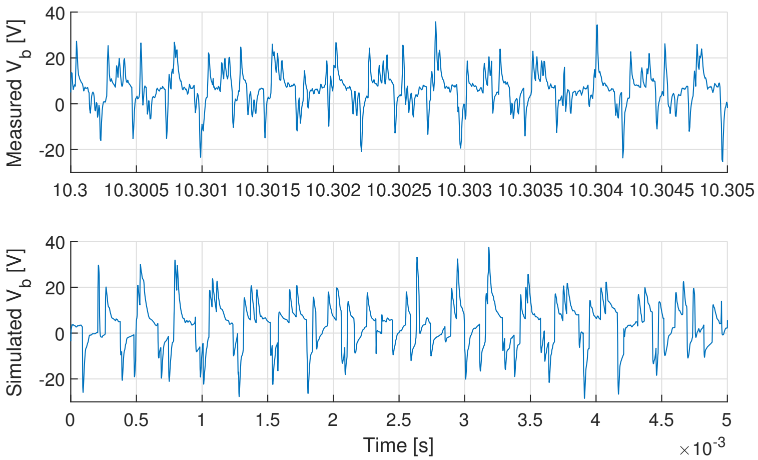

Figure 6.19: Measured (upper plot) and simulated (lower plot) voltage V_b across the resistor R_b in the human model when the bus is drawing power from the ERS dynamically (100kW) with an isolation fault of 100 kΩ present.

The current through the human body I_b in RMS filtered with a moving average filter with a 50 ms window is presented for both measurement and simulation during both static and dynamic charging in Table 6.5. Generally, compared to the no-fault case presented in Table 6.4, there are no significant changes in the results for static charging. This is due to the fact that, as shown in the measurements, the arm with an isolation fault was in contact with a negative segment, as previously discussed. Consequently, there are no differences in the static case with a 100 kΩ isolation fault compared to the static case with no induced isolation faults. However, due to minor natural variations in the measurements, I_b is reduced to 14 mA during static charging.

During the measurements of dynamic charging, when the arm with the isolation fault contacts a positive segment, thereby elevating the chassis potential, the current I_b increases from 17 mA to 21 mA compared to the baseline case with no isolation faults. The model's limited capability to emulate small alterations in isolation resistance becomes evident when comparing the simulated values of I_b during dynamic charging in Table 6.5 with those in Table 6.4. An isolation fault of 100 kΩ results in a 4 mA increase during dynamic charging in the measurement, compared to the case without induced isolation faults, while in the simulation, it results in an increase of only 1 mA. Although the model appears to be very accurate during dynamic charging, its accuracy should be regarded as coincidental. This is because the original value without isolation faults was an overestimation of I_b, while the increase due to a 100 kΩ isolation fault represents an underestimation.

Table 6.5: Measured and simulated values of current flowing through the human model.

Simulation result - 100 kΩ isolation fault			
Result	*Unit*	*Value*	
		Static	Dynamic
Measured I_b	$\mathrm{mA_{RMS,\,50\,ms}}$	14	21
Simulated I_b	$\mathrm{mA_{RMS,\,50\,ms}}$	13	21

11 kΩ Isolation Fault

Fig. 6.20 presents measurements (upper plot) and simulations (lower plot) of the voltage V_b when the bus has an isolation fault of 11 kΩ between one arm of the current collector and the BEV chassis. With such a significant alteration in isolation resistance, the voltage V_b increases significantly due to the substantial increase of the BEV chassis voltage. In both measurements and simulations, the arm with the isolation fault makes contact with a positive segment during static charging and disconnects from a positive segment at 1.8 s in the measurement (upper plot). Thus, compared to the original case without an isolation fault, an offset of 22 V is introduced when the bus is in contact with segments that have a positive voltage of 650 V.

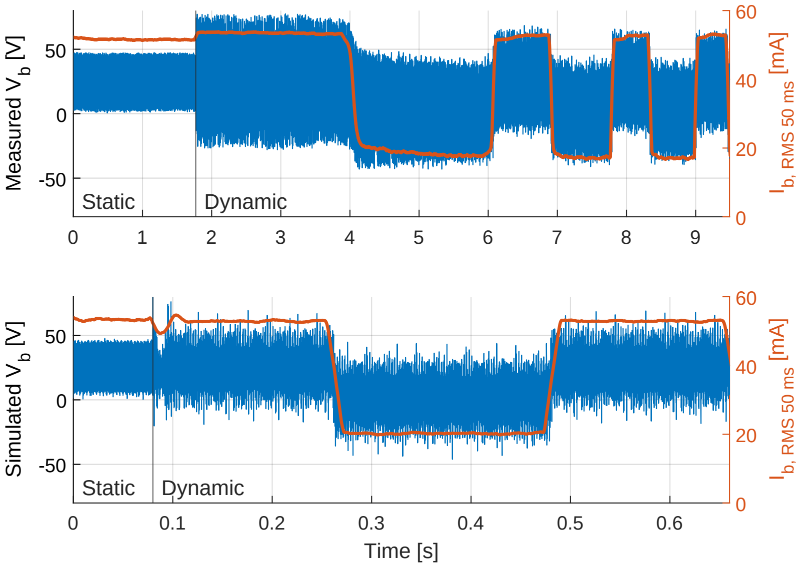

Figure 6.20: Measured (upper plot) and simulated (lower plot) voltage V_b across the resistor R_b in the human model, shown by blue lines related to the left y-axis, when the bus is drawing power from the ERS both statically (40 kW) and dynamically (100 kW) with an isolation fault of 11 kΩ present. Current through the human body I_b, with a moving RMS value filtered with a 50 ms window, is represented by red lines related to the right y-axis.

The upper plot in Fig. 6.21 provides a zoomed-in view of 3 ms at 1 s from the upper plot in Fig. 6.20. The isolation fault of 11 kΩ increases the BEV chassis voltage, resulting in an approximate 22 V DC offset in the voltage V_b across the human model. The lower plot, which shows a simulation of static charging, exhibits the same offset, indicating that the model accurately replicates the magnitude of this isolation fault. It is important to note that the waveform shape and the original peak-to-peak values of V_b are maintained, suggesting that the charge and discharge characteristics of the parasitic capacitors between the chassis and BEV TVS are unaffected by this isolation fault. Additionally, the magnitude of the isolation fault results in measured and simulated current levels (I_b) that are considered hazardous, potentially leading to cardiac and respiratory arrest. This underscores that while capacitive coupling can be hazardous, a severe isolation fault poses an even greater risk.

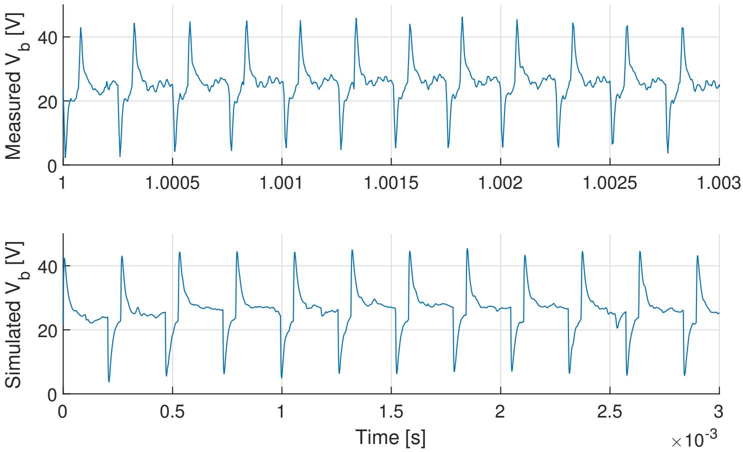

Figure 6.21: Measured (upper plot) and simulated (lower plot) voltage V_b across the resistor R_b in the human model when the bus is drawing power from the ERS statically (40 kW) with an isolation fault of 11 kΩ present.

The upper plot in Fig. 6.22 presents a zoomed-in in view of 5 ms at 8 s from the upper plot in Fig. 6.20. Similar to the situation during static charging in Fig. 6.21, the same off-set voltage of 22 V is present in the measurement and the original waveform shape of the voltage V_b is intact.

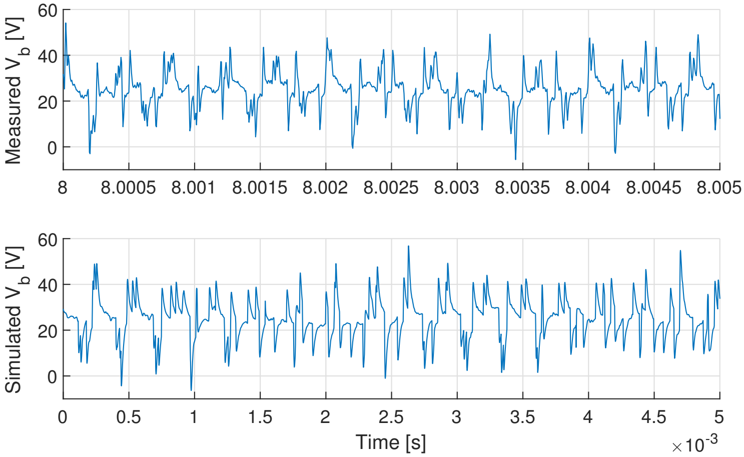

Figure 6.22: Measured (upper plot) and simulated (lower plot) voltage V_b across the resistor R_b in the human model when the bus is drawing power from the ERS dynamically (100kW) with an isolation fault of 11 kΩ present.

In Table 6.6, values of I_b in RMS filtered with a moving average filter with a 50 ms filter window are presented for both measured and simulated cases with an isolation fault of 11 kΩ. At this level of isolation fault, the model presents excellent performance; during static charging, the measured value is 51 mA and the modelled value is 52 mA. During dynamic charging, the measured and simulated value is 52 mA. In conclusion, the validation of the model with respect to isolation faults demonstrates that the model is capable of accurately replicating phenomena related to the BEV chassis. The model's accuracy is greater for larger isolation alterations than for smaller ones.

Table 6.6: Measured and simulated values of current flowing through the human model.

Simulation result - 11kΩ isolation fault			
Result	*Unit*	*Value*	
		Static	Dynamic
Measured I_b	$\mathrm{mA}_{\mathrm{RMS},\,50\,\mathrm{ms}}$	51	52
Simulated I_b	$\mathrm{mA}_{\mathrm{RMS},\,50\,\mathrm{ms}}$	52	52

6.4 Model Validation of Voltage on the Electric Road Exterior

To assess and model the impact of elevated voltage on the exposed electric road exterior, a validation of the model's capability to simulate this phenomenon at three different levels of drawn power was conducted. Fig. 6.23 presents a measurement of the bus charging dynamically on the ERS demonstrator, starting 100 m away from the feeding point (and the rectifier station) and accelerating towards it. The blue line, associated with the left y-axis, represents the voltage V_h, which is the voltage between the electric road exterior just behind the bus and ground, as illustrated in Fig. 6.6. The right y-axis is associated with the orange dotted line which displays the drawn power from the bus, and the dotted-dashed line which represents the current drawn by the bus in interface C (see Fig. 2.13).

Note that V_h is -0.07 V and not zero when the bus starts to accelerate. This is believed to be due to a 48 V power supply that feeds all the transistors, LEDs, and microprocessors in the electric road, which share its positive pole (0 V) with the negative pole (0 V) of the electric road, as presented in [41]. Thus, the negative pole of the 48 V power supply is at -48 V with respect to ground. Consequently, as the power supply continuously feeds all

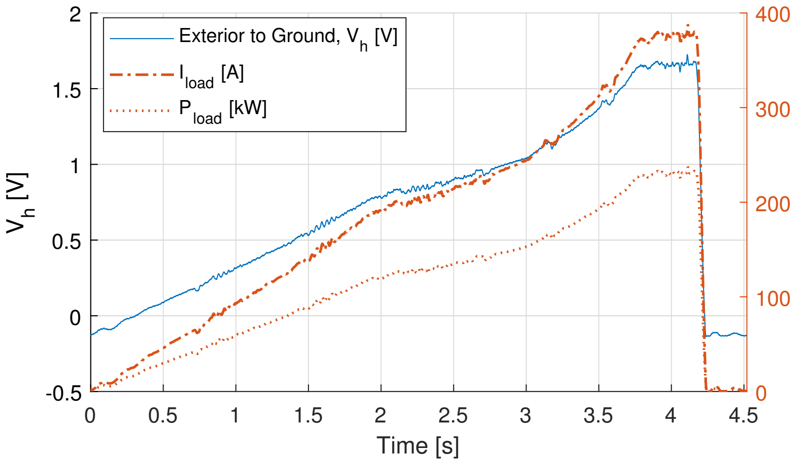

Figure 6.23: Measurement of the bus drawing power at the ERS demonstrator. The blue line represent the voltage between electric road exterior and electrical ground, V_h, related to the left y-axis. Red lines represent current (dotted-dashed) and power (dotted) drawn by the bus related to the right y-axis.

the transistors, LEDs, and microprocessors, there is always a small negative voltage drop in the negative pole of the electric road with respect to ground when the electric road is active and connected to the 48 V power supply.

As detailed in Fig. 6.6, the voltage drop (V_h) over R_{ER-} depends on two factors: the resistance of R_{ER}, which is related to the length of the electric road, and the current through the conductors, which consequently relates to the power drawn by the bus. The measurement shows that the primary cause for the increased voltage to ground V_h is the increased drawn power and current, as the electric road length and resistance in the negative conductor of the electric road do not change rapidly while the bus accelerates up to 20 km/h between 0 to 4.2 s. At 4.2 s, when the bus loses its connection with the electric road, the voltage to ground, drawn power, and current are instantly reduced.

The upper plot in Fig. 6.24 presents a zoomed-in view of 20 ms at 0.67 s when the bus is drawing 63 A from the electric road in interface C. The lower plot shows a simulation provided by the model for the same scenario, where the bus is drawing 63 A from 100 m of electric road. Although the waveform shape of the measured and simulated voltage to ground is somewhat similar, the simulated voltage exhibits higher oscillations. This is believed to originate from that the model lacks dampening from resistive elements, as the voltage in the model oscillates more than the measured voltage. Consequently, the peak-to-peak magnitude of the modelled voltage is greater than that of the measured voltage. Despite this, the mean values of the waveforms are similar, with the measured value corresponding to a mean of 0.17 V and the simulated value to 0.18 V, resulting in a 5.5% error between the model and measurement for this level of drawn power.

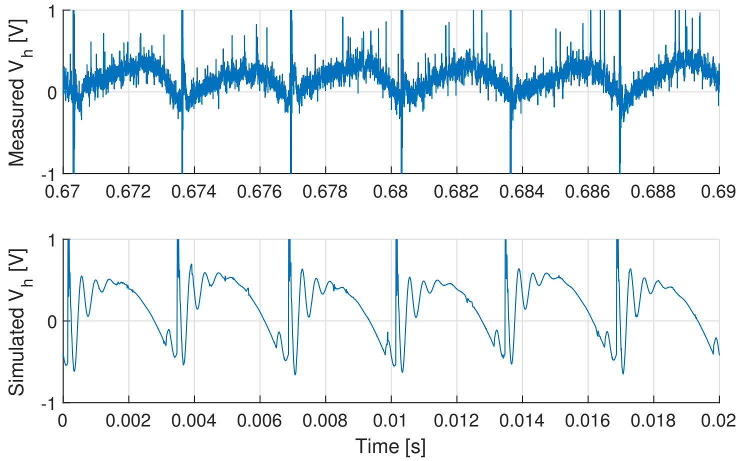

Figure 6.24: Zoomed-in view of 20 ms at 0.67 s from Fig. 6.23, showing the measured (upper plot) and simulated (lower plot) voltage V_h between the electric road exterior and ground.

The recurring peaks observed in the measurement waveform are unknown but are believed to be attributed to the reverse recovery phenomenon of the diodes in the rectifier station. However, since this phenomenon occurs over timescales of μs and does not significantly impact the average voltage, it is disregarded in this analysis. The focus of this validation is on average values and general waveform shape at timescales larger than a few tens of milliseconds.

The upper plot in Fig. 6.25 illustrates a zoomed-in view of 20 ms at 2.43 s from Fig. 6.23, when the bus is drawing 210 A from the electric road in interface C. The lower plot presents a simulation of the same scenario, with the bus drawing 210 A from 100 m of electric road. Generally, the waveform shape of the voltage V_h in the measurements (upper plot) is quite similar to the 63 A case shown in the previous figure. However, the model exhibits slightly more oscillations as the drawn current increases. Despite this, the model demonstrates a reasonable level of accuracy, with the offset voltage increasing to comparable levels in both the measurements and the simulation. The mean voltage V_h at 210 A is 0.87 V in the measurement and 0.65 V in the simulation, resulting in a 25% error between the model and the measurement.

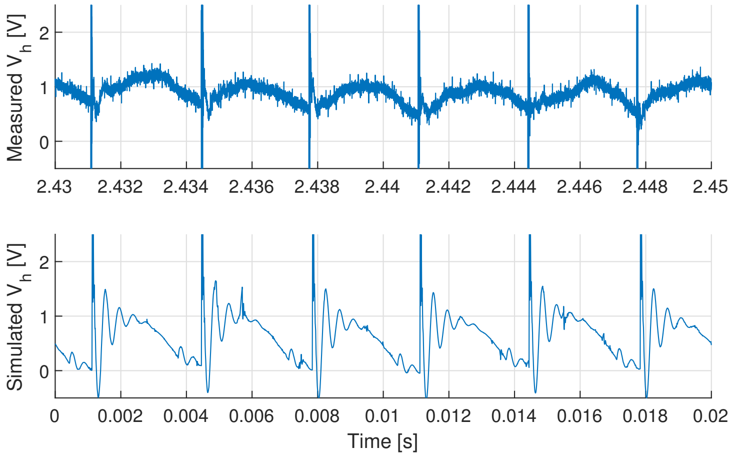

Figure 6.25: Zoomed-in view of 20 ms at 2.43 s from Fig. 6.23, showing the measured (upper plot) and simulated (lower plot) voltage V_h between the electric road exterior and ground.

The upper plot in Fig. 6.26 provides a zoomed-in view of 20 ms at 3.9 s from Fig. 6.23, when the bus is drawing 375 A from the electric road in interface C. The lower plot presents a simulation of the same scenario, with the bus drawing 375 A from 100 m of electric road. Similar to Fig. 6.25, the waveform shape is very similar when the current is increased to 375 A, as shown in the lower plot of Fig. 6.26. However, for this high current level, the offset voltage between the measurement and simulation deviates more. The mean voltage V_h is 1.68 V in the measurement and 1.12 V in the simulation, resulting in a 33% error between the measurement and the model.

To conclude, the model error increases with higher currents. The deviation in V_h between measurements and simulations can be attributed to the fact that the impedance of the ground is disregarded in the model. For currents as low as 63 A, the model error is 5.5%, whereas at a drawn current of 375 A, the error increases to 33%. Although the waveform shape of the model appears to oscillate more than in the measurements, the general phenomenon of elevated voltage in the electric road exterior with respect to ground is replicated adequately, albeit with an underestimation at higher current levels.

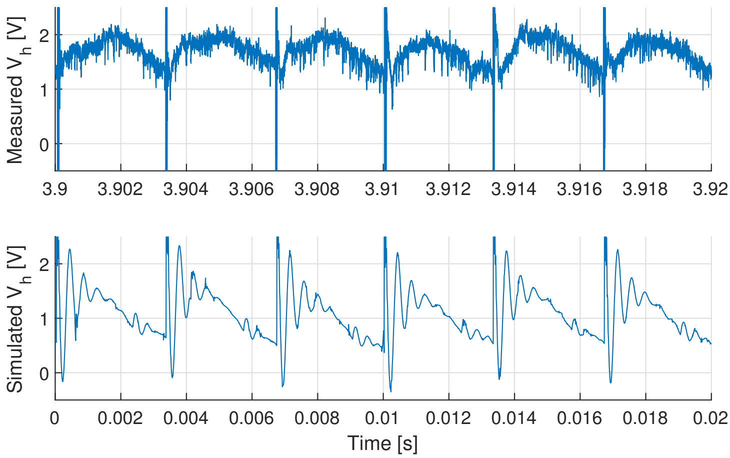

Figure 6.26: Zoomed-in view of 20 ms at 3.9 s from Fig. 6.23, showing the measured (upper plot) and simulated (lower plot) voltage V_h between the electric road exterior and ground.

6.5 Electrical Safety Simulation Scenarios

This section presents simulation scenarios addressing electrical safety, specifically examining the voltage V_b and current I_b in the human model caused by parasitic capacitance and isolation faults in the BEV chassis. The impact of the parameters related to parasitic capacitance and isolation faults is first modeled separately, and then their combined impact is assessed. Subsequently, simulations addressing the elevated voltage of the electric road exterior and its effect on a human model are presented and discussed.

6.5.1 Simulations of Elevated Chassis Voltage - Parameters

Due to the nature of parasitic capacitive coupling in the BEV chassis, which is largely dependent on the specific structure and topology of the vehicle's TVS, it is likely that different vehicles will exhibit this phenomenon to varying extents. Preliminary measurements of the magnitude of these parasitics suggest that the parameters chosen for the model are of the correct order of magnitude. However, given the difficulty in accurately estimating these parasitics and their variability between vehicles, a set of six simulations was performed to assess their impact on the human model.

The parameters C_{b+}, C_{d+}, C_{DC+}, and C_{DC-} presented in Tables 6.1 to 6.3, are varied during these simulations which comprise both static and dynamic charging. The parasitic capacitors connected to the output of the TVS subsystems C_{b+} and C_{d+} are altered by a factor denoted k_{c^+} and the capacitors at the DC-link (C_{DC+} and C_{DC-}) are altered by a factor denoted k_{c^-}. The reason for this choice is that, at the time resolution of the switching instances of the converters in the TVS, the capacitors C_{DC+} and C_{DC-} effectively act as the main parasitic capacitor between the negative pole of the active subsystem and the chassis, as previously discussed at the end of Section 6.3.1 related to Fig. 6.16. Besides the nominal estimated values ($k_{c^+} = 1$ and $k_{c^-} = 1$), different simulations are conducted assuming both half ($k_{c^+} = 0.5$ and $k_{c^-} = 0.5$) and double ($k_{c^+} = 2$ and $k_{c^-} = 2$) the parasitic capacitances (see Tables 6.7 and 6.8). Throughout these simulations, the remaining parameters are kept unchanged from the validation of the model as originally detailed in Tables 6.1 to 6.3.

Table 6.7: Parasitic capacitor variation factors and their corresponding parameter values.

Simulation parameters - capacitor factors				
Parameter	*Value*	*Parameter*	*Unit*	*Value*
k_{c^+}	0.5	C_{b+} C_{d+}	nF	0.8 0.6
k_{c^+}	1	C_{b+} C_{d+}	nF	1.6 1.2
k_{c^+}	2	C_{b+} C_{d+}	nF	3.2 2.4
k_{c^-}	0.5	C_{DC+} C_{DC-}	nF	9.25 9.25
k_{c^-}	1	C_{DC+} C_{DC-}	nF	18.5 18.5
k_{c^-}	2	C_{DC+} C_{DC-}	nF	37 37

Table 6.8: Simulation parameters for different simulations of variations in parasitic capacitors.

Simulation parameters			
Simulation	*Parameter*	*Value*	
Capacitive coupling 1	k_{c^+}, k_{c^-}	0.5	1
Capacitive coupling 2		1	0.5
Capacitive coupling 3		0.5	0.5
Capacitive coupling 4		2	1
Capacitive coupling 5		1	2
Capacitive coupling 6		2	2

To further assess the impact of isolation faults between the ERS supply and the BEV chassis, isolation fault resistances of 1 kΩ, 5 kΩ, 10 kΩ, 50 kΩ, 0.1 MΩ, and 0.5 MΩ (as detailed in Table 6.9) were introduced between one arm of the current collector and the BEV chassis in the simulations. For each simulation, both static and dynamic charging conditions were assessed while a human model was connected to the BEV chassis.

Table 6.9: Simulation parameters for different simulations of variations in isolation fault resistances.

Simulation parameters - isolation faults		
Parameter	*Unit*	*Value*
Fault 1		
Isolation fault resistance, R_f	kΩ	1
Fault 2		
Isolation fault resistance, R_f	kΩ	5
Fault 3		
Isolation fault resistance, R_f	kΩ	10
Fault 4		
Isolation fault resistance, R_f	kΩ	50
Fault 5		
Isolation fault resistance, R_f	MΩ	0.1
Fault 6		
Isolation fault resistance, R_f	MΩ	0.5

To continue the assessment with elevated voltage of the BEV chassis, a set of six simulations were conducted combining altered parasitic capacitance with induced isolation faults. The parasitic capacitors with $k_{c^+} = 2$ and $k_{c^-} = 1$ (simulation Capacitive coupling 4) were selected as this combination had the most significant increase in the magnitude of V_b. The same isolation fault resistances as detailed in Table 6.9 were chosen to evaluate the combined impact of the altered parasitic capacitance and isolation faults.

6.5.2 Simulations of Elevated Voltage on the Electric Road Exterior - Parameters

The electric road exterior is originally designed to mitigate issues concerning hazardous touch events, ensuring that it does not expose persons or animals to hazardous voltage levels relative to ground. To assess this risk, simulations are conducted using the validated model with a human model connected to the electric road exterior. As presented in Fig. 6.6, the two main factors that impact the voltage with respect to ground for the electric road exterior are: 1) the length of the electric road and 2) the power drawn by the vehicle. In an attempt to examine some extreme worst-cases, two simulations are conducted, Scenario 1 and Scenario 2. In this evaluation, the impedance of the ground is assumed to be zero.

In Scenario 1 the simulation involves two BEVs, which we assume are 20 m long trucks but with the same vehicle parameters as presented in Section 5.2.4, drawing 350 kW each over a 1.24 km stretch of electric road, as illustrated in Fig. 6.27. The distance from the feeding point to the first truck is 1 km (denoted d_1) and the distance between the trucks is 0.2 km (denoted d_2). The voltage to ground over a human model, V_h, is measured just behind the last truck in the model. To accommodate the total drawn power of the trucks, five parallel transformers are required (see Fig. 5.1 in Section 5.2).

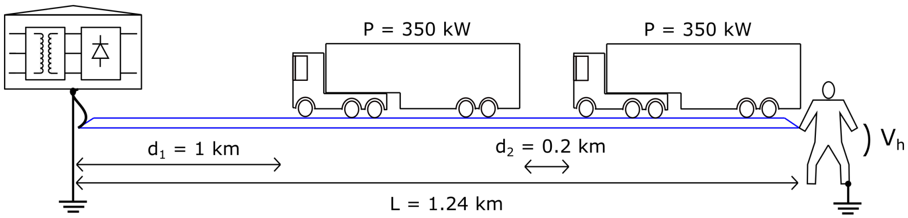

Figure 6.27: Overview of the simulation cases Scenario 1 and 2 where the voltage V_h across a human model, connected between the exterior of the electric road and electrical ground, is measured while two BEVs draw 350 kW each from a 1.24 km long electric road.

In Scenario 2, the simulation retains the same electric road length and power draw from the trucks but halves the resistance of the positive conductor while doubling the resistance of the negative conductor. This modification represents a doubling of the positive conductor's cross-sectional area and a halving of the negative conductor's cross-sectional area while retaining the combined total cross-sectional area for both conductors. This design alteration allows for reduced losses in the electric road, which is particularly beneficial for high-power draw scenarios, as presented in Fig. 4.2 and discussed in the introduction in chapter 4. However, increasing the resistance of the negative conductor also increases the voltage drop between the electric road exterior and ground.

6.5.3 Simulations of Elevated Chassis Voltage due to Capacitive Coupling - Results

Fig. 6.28 illustrates six simulations of the voltage V_b during the static charging of the bus, with each simulation employing different parasitic chassis capacitor parameters, as detailed in Tables 6.7 and 6.8. The upper plot displays simulations Capacitive Coupling 1-3, while the lower plot shows simulations Capacitive Coupling 4-6. The original case with no alterations to the parasitic capacitors ($\mathrm{k}_{c^+} = \mathrm{k}_{c^-} = 1$) is included for reference as brown dashed lines. In these simulations, with the bus remaining stationary and charging, only the battery converter is active in the bus TVS, drawing 40 kW. As presented in the simulations, the voltage V_b in the human model varies significantly with the selected adjustments to the parasitic capacitors.

The curves for $\mathrm{k}_{c^+} = 1, \mathrm{k}_{c^-} = 0.5$ (upper plot) and $\mathrm{k}_{c^+} = 2, \mathrm{k}_{c^-} = 1$ (lower plot) exhibit similar results, producing comparable ratios between the capacitors C^+ and C^- according to Eq. (6.7). Similarly, the curves for $\mathrm{k}_{c^+} = 0.5, \mathrm{k}_{c^-} = 1$ (upper plot) and $\mathrm{k}_{c^+} = 1, \mathrm{k}_{c^-} = 2$ (lower plot) also show comparable results for the same reason.

However, the simulations of $\mathrm{k}_{c^+} = 0.5$, $\mathrm{k}_{c^-} = 0.5$ and $\mathrm{k}_{c^+} = 2$, $\mathrm{k}_{c^-} = 2$ do not produce the same results. This discrepancy arises because a capacitor's stored energy increases with its capacitance, which generally results in a longer discharge time for a given load resistance— in this case, the human model. This behavior is observable in the negative voltage transients shown in Fig. 6.28, where the curve for $\mathrm{k}_{c^+} = 0.5$, $\mathrm{k}_{c^-} = 0.5$ exhibits a smaller amplitude and faster discharge time compared to the curve for $\mathrm{k}_{c^+} = 2$, $\mathrm{k}_{c^-} = 2$. However, during the positive transient, the curve for $\mathrm{k}_{c^+} = 2$,

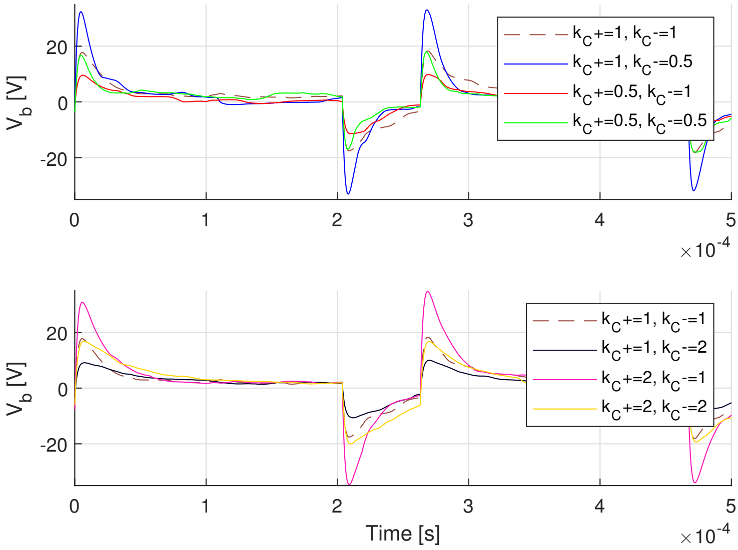

Figure 6.28: Simulated voltage V_b across the human model during static charging with varied parasitic capacitors, as detailed in Tables 6.7 and 6.8, where $\mathrm{k}_{c^+} = \mathrm{k}_{c^-} = 1$ represents the original case with no altered parameters.

$\mathrm{k}_{c^-} = 2$ is smaller than the curve for $\mathrm{k}_{c^+} = 0.5$, $\mathrm{k}_{c^-} = 0.5$ and the nominal curve of $\mathrm{k}_{c^+} = 1$, $\mathrm{k}_{c^-} = 1$. This is due to the fact that the duty cycle of the converter is too high to allow the larger capacitors in the case of $\mathrm{k}_{c^+} = 2$, $\mathrm{k}_{c^-} = 2$ to fully discharge through the human model before being recharged, resulting in a lower voltage prior to charge and consequently a lower peak in the transient compared to the curve for $\mathrm{k}_{c^+} = 0.5$, $\mathrm{k}_{c^-} = 0.5$ and the nominal curve of $\mathrm{k}_{c^+} = 1$, $\mathrm{k}_{c^-} = 1$.

Fig. 6.29 presents the simulations of the voltage V_b during dynamic charging. In this simulation, the bus draws 100 kW, and both the battery converter and the traction inverter are active in the TVS. As a result, the voltage V_b exhibits an increased number of transients due to the continuous charging and discharging of the parasitic capacitors in both the battery converter and the traction inverter.

Since the transients in V_b originate from the switching frequency and duty cycle of two unrelated converters (3.4 kHz for the traction inverter and 3.8 kHz for the battery converter, see Tables 5.4 and 5.5), the time intervals between these transients are partially unrelated. Due to variations in the parasitic capacitors (k_c^+ and k_c^-), the time constants of the transients are affected, which may cause these transients to superimpose, leading to

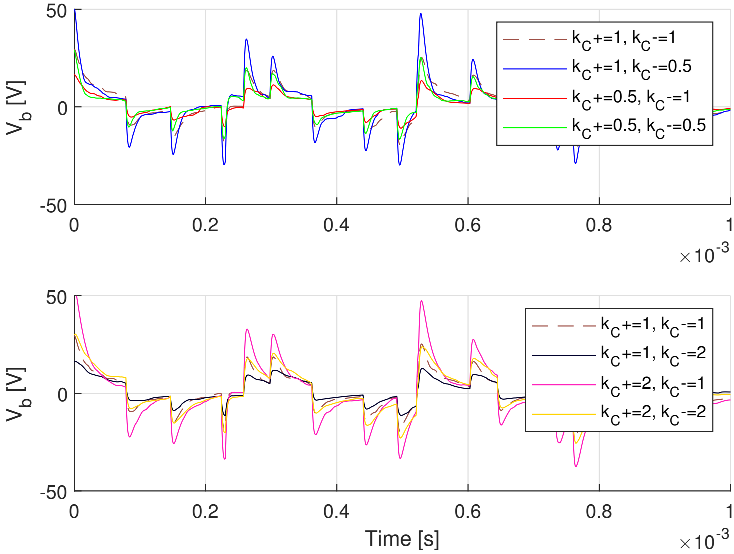

Figure 6.29: Simulated voltage V_b across the human model during dynamic charging with varied parasitic capacitors, as detailed in Tables 6.7 and 6.8, where $\mathrm{k}_{c^+} = \mathrm{k}_{c^-} = 1$ represents the original case with no altered parameters.

higher instantaneous levels of V_b. This effect is particularly noticeable in simulations involving combinations where $k_c^+ = 2$, $k_c^- = 2$, or both. In the worst case, simultaneous switching events—one from each converter—could cause two transient peaks in V_b to add up, as observed at 0 and 0.525 ms.

In Table 6.10, the current flowing through the human model, I_b, is presented for both static and dynamic charging scenarios. This includes the original simulation with no alterations to the parasitic capacitors ($\mathrm{k}_{c^+} = \mathrm{k}_{c^-} = 1$).

The results are consistent with the observations from these figures, indicating that the configurations $\mathrm{k}_{c^+} = 2, \mathrm{k}_{c^-} = 1$ and $\mathrm{k}_{c^+} = 1, \mathrm{k}_{c^-} = 0.5$ produce the highest values of I_b, while $\mathrm{k}_{c^+} = 1, \mathrm{k}_{c^-} = 2$ and $\mathrm{k}_{c^+} = 0.5, \mathrm{k}_{c^-} = 1$ yield the lowest values. These results are consistent with the voltage division described by Eq. (6.7). In addition, also similar to the previous observations in the figures, $\mathrm{k}_{c^-} = 0.5$ and $\mathrm{k}_{c^+} = 0.5$ result in lower RMS values compared to the original case of $\mathrm{k}_{c^-} = 1$ and $\mathrm{k}_{c^+} = 1$, due to lower currents which are caused by shorter discharge times. Conversely, for $\mathrm{k}_{c^-} = 2$ and $\mathrm{k}_{c^+} = 2$, the RMS values increase due to higher currents which are caused by longer discharge times. Although the model is not designed to evaluate the severity of I_b on the human body, it is important to note that all values, except for static charging in simulations Capacitive Coupling 1 and 3, exceed the 10 mA RMS threshold, above which an adult person cannot release an object while the current is flowing, as presented in Section 6.1.1. The results indicate that adjustments in parasitic capacitance can significantly affect I_b, either increasing or decreasing it.

Table 6.10: Simulation results of current flowing through the human model with varied parasitic capacitors.

Simulation results - varied parasitic capacitors					
Parameter	*Value*	*Result*	*Unit*	*Value*	
Capacitor factor		Human current		Static	Dynamic
No altered capacitive coupling					
k_{c^+}, k_{c^-}	1, 1	I_b	mA_{RMS}	13	20
Capacitive coupling 1					
k_{c^+}, k_{c^-}	0.5, 1	I_b	mA_{RMS}	8	12
Capacitive coupling 2					
k_{c^+}, k_{c^-}	1, 0.5	I_b	mA_{RMS}	18	26
Capacitive coupling 3					
k_{c^+}, k_{c^-}	0.5, 0.5	I_b	mA_{RMS}	10	15
Capacitive coupling 4					
k_{c^+}, k_{c^-}	2, 1	I_b	mA_{RMS}	24	34
Capacitive coupling 5					
k_{c^+}, k_{c^-}	1, 2	I_b	mA_{RMS}	9	13
Capacitive coupling 6					
k_{c^+}, k_{c^-}	2, 2	I_b	mA_{RMS}	16	24

6.5.4 Simulations of Elevated Chassis Voltage due to Isolation Faults - Results

To evaluate the impact of an isolation fault between the TVS and the BEV chassis as presented in Fig. 6.4, a series of six simulations were conducted in which the isolation fault resistance, R_f, was varied from 1 kΩ to 0.5 MΩ. Table 6.11 presents the simulation results for varying degrees of isolation faults. The current through the human model, I_b, in RMS was measured for both static and dynamic charging in each simulation. The selected values of R_f primarily serve as an indicator of the order of magnitude at which isolation faults become critically severe. For isolation fault resistance values R_f approaching 10 kΩ, the current flowing through the human body begins to reach the critical lethal thresholds, as specified in Section 6.1.1.

Note that in these simulations, I_b differs between static and dynamic charging. For Faults 4 through 6, which correspond to less severe isolation faults, I_b is lower during static charging compared to dynamic charging. This finding aligns with the previously presented results from the original case with no isolation faults or alterations to parasitic capacitors, as shown in Tables 6.4 and 6.10, and is mainly due to the increased number of charge and discharge of the parasitic capacitors during dynamic charging, which increases the RMS value of I_b. However, in simulation Fault 3, the current I_b is identical during both static and dynamic charging, whereas in simulations Fault 1-2, I_b is greater during static charging than dynamic charging. This occurs because the isolation fault in simulations Fault 1-3 is so severe that I_b begins to behave like a purely resistive load. Consequently, the waveform resembles the shape of a rectified current, driven by the 6-pulse passive rectifier in the rectifier station, which due to its 6-pulse ripple increases the RMS value of I_b. This effect is more prominent during static charging than dynamic charging and becomes increasingly noticeable from simulation Fault 3 to 1, resulting in the RMS values of I_b being equal for static and dynamic charging in simulation Fault 3.

Table 6.11: Simulation results of current flowing through the human model with varied isolation resistance faults.

Simulation results - isolation faults						
Parameter	*Unit*	*Value*	*Result*	*Unit*	*Value*	
Isolation fault resistance			Human current		Static	Dynamic
			Fault 1			
R_f	kΩ	1	I_b	mA_{RMS}	218	205
			Fault 2			
R_f	kΩ	5	I_b	mA_{RMS}	94	91
			Fault 3			
R_f	kΩ	10	I_b	mA_{RMS}	56	56
			Fault 4			
R_f	kΩ	50	I_b	mA_{RMS}	18	23
			Fault 5			
R_f	MΩ	0.1	I_b	mA_{RMS}	15	21
			Fault 6			
R_f	MΩ	0.5	I_b	mA_{RMS}	14	20

Given the observed impact of parasitic capacitive coupling between the BEV TVS and BEV chassis, the combination of this phenomenon with isolation faults is further evaluated. A conservative approach is adopted, thus the most severe case is selected which is simulation Capacitive Coupling 4 from Table 6.10, as it resulted in the most significant increase in I_b.

The same isolation faults outlined in Table 6.11 are used to examine the combined effects of isolation faults with the enhanced influence of parasitic capacitors.

Table 6.12 presents six simulations that display values of I_b during both static and dynamic charging, with the inclusion of isolation faults and the increased influence of parasitic capacitance. For isolation Faults 4–6, the impact on the current I_b is minimal. However, for isolation faults in the range of 1–10 kΩ, corresponding to Faults 1–3, I_b exhibits a slight increase of 2–6 mA across all results compared to those in Table 6.11. This increase is attributable to the contribution of the altered parasitic capacitors. The reason that the parasitics do not produce a consistent increase in I_b in every simulation is that each isolation fault alters the waveform of I_b slightly. For more severe isolation faults, the waveform begins to approximate that of a purely resistive load, resembling the shape of a rectified current while still reflecting the influence of the parasitic capacitors.

To conclude, severe isolation faults have a significantly greater impact on the current through the human body compared to the effect of capacitive coupling between the TVS and the BEV chassis. The increase in I_b due to altered parasitic capacitive couplings diminishes as the altered isolation resistance increases.

Table 6.12: Simulation results of current flowing through the human model with varied isolation resistance faults and altered parasitic capacitors.

Simulation results - isolation faults and altered parasitic capacitors								
Parameter	*Unit*	*Value*	*Parameter*	*Value*	*Result*	*Unit*	*Value*	
Isolation fault resistance			Capacitor factor		Human current		Static	Dynamic
Fault 1								
R_f	kΩ	1	k_c+, k_c-	2, 1	I_b	mA_{RMS}	219	207
Fault 2								
R_f	kΩ	5	k_c+, k_c-	2, 1	I_b	mA_{RMS}	96	96
Fault 3								
R_f	kΩ	10	k_c+, k_c-	2, 1	I_b	mA_{RMS}	59	62
Fault 4								
R_f	kΩ	50	k_c+, k_c-	2, 1	I_b	mA_{RMS}	26	36
Fault 5								
R_f	MΩ	0.1	k_c+, k_c-	2, 1	I_b	mA_{RMS}	24	35
Fault 6								
R_f	MΩ	0.5	k_c+, k_c-	2, 1	I_b	mA_{RMS}	24	34

6.5.5 Strategies for Mitigating Elevated Voltage on Vehicle's Chassis

For future BEVs designed for ERS deployment, it is essential to address the issue of elevated chassis voltage with respect to ground. While the presented values of I_b may not pose immediate harm under typical operating conditions or during regular service, certain scenarios could lead to a hazardous increase in I_b. The current I_b is influenced by various factors, including the contact area of the skin with the object carrying the voltage and environmental conditions such as humidity. In an ERS, there is a risk if an individual comes into contact with the BEV chassis under unfavorable conditions, such as a rainy day with high moisture levels on the chassis, and the person is standing in a puddle or another wet environment that enhances electrical contact between the person and the ground. Under such conditions, as presented in the results of this chapter, I_b can reach harmful levels. Moreover, even if I_b does not attain fatal levels, it may still reach values that are noticeably unpleasant. The sensation of current flow through the body is highly uncomfortable and should be regarded as a design flaw if ERSs and BEVs permit such occurrences.

As previously discussed in this chapter, one mitigating strategy for addressing elevated chassis voltages is to implement an IMS specifically designed for BEVs intended for ERS operation. This IMS should be sufficiently fast to detect elevated levels of chassis voltage and capable of disconnecting the BEV from the ERS supply if such an event occurs. If effectively implemented, this IMS could potentially mitigate issues related to isolation faults. However, the challenge of parasitic capacitive coupling must also be addressed and monitored during the design phase of the BEV or during retrofitting of a vehicle adapted for ERS operation. Therefore, parasitic capacitive couplings should be minimized, monitored, and accounted for as part of the design phase.

An additional strategy could involve deploying a galvanically isolated DC/DC converter between the vehicle's ERS interface and the vehicle's TVS, as previously discussed and illustrated in Fig. 6.3. The use of such a DC/DC converter is intended to interrupt the current path of I_b from the ground to the rectifier station and back to the vehicle's TVS. However, preliminary analysis of measurements from a passenger car drawing power from the ERS demonstrator equipped with a galvanically isolated DC/DC converter suggests that this approach does not fully resolve the issue. It is suspected that I_b may still flow through parasitic capacitive coupling within the supposedly galvanically isolated DC/DC converter. Further investigation is needed to assess the effectiveness of this strategy and to establish the necessary requirements and standards for managing parasitic capacitive coupling between the TVS converters' outputs and the chassis, or possibly within the galvanically isolated DC/DC converter if deployed.

6.5.6 Simulations of Elevated Voltage on the Electric Road Exterior - Results

The electric road exterior is designed to mitigate issues related to touch events, ensuring that the voltage on the exterior does not pose a hazard with respect to ground. To thoroughly assess these risks, simulations were conducted using the validated simulation model.

The upper plot in Fig. 6.30 illustrates Scenario 1 with the simulated voltage $V1_h$ across the entire human model and ground presented in Section 6.5.2. Although the accuracy of the model diminishes with increasing power draw, as demonstrated during model validation in Figs. 6.24 to 6.26, these simulations are designed to evaluate whether the voltage to ground can reach levels that can cause noticeable or harmful currents to flow through the human body. The mean voltage to ground in Scenario 1 is approximately 11 V, which results in a current (I_b) of approximately 6 mA through the human body.

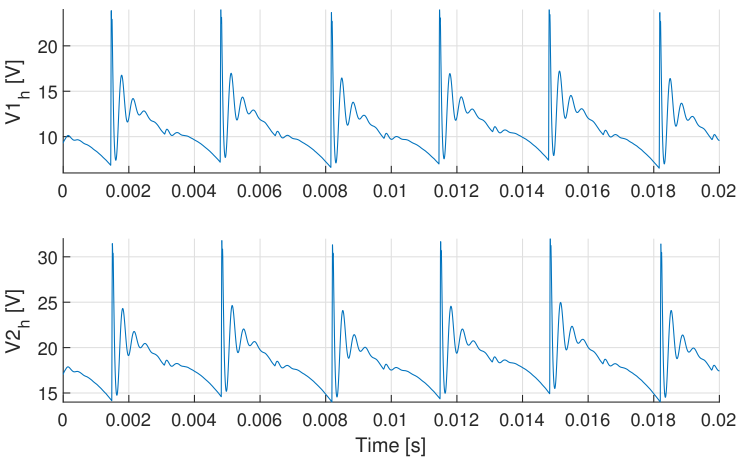

Figure 6.30: Simulations of the voltage V_h between the electric road exterior and the ground across the human model. The upper plot represents Scenario 1, where two BEVs draw 350 kW each from 1.24 km of electric road. The lower plot represents Scenario 2, which is identical to Scenario 1 but with increased resistance in the negative conductor of the electric road.

The lower plot in Fig. 6.30 illustrates Scenario 2 with the simulated voltage $V2_h$ under the same conditions as the upper plot, with the exception that the resistance of the positive conductor is halved while the resistance of the negative conductor is doubled as presented in Section 6.5.2.

Although the voltage briefly peaks above 30 V, the average voltage is 19 V, which corresponds to a current (I_b) of 10 mA. For both Scenario 1 and Scenario 2, the current is below 30 mA DC, which pertains to the likelihood of muscular contractions and usually no harmful physiological electrical effects, according to the standard [49]. Note that V_h in these simulations corresponds to a DC current, and thus relates to the corresponding DC values in the standard, making it less harmful compared to similar AC values of I_b previously presented, which were related to the elevated voltage of the vehicle chassis. Given that the resulting current I_b is too low to inflict any critical harm on the human body, and assuming that people typically do not remain stationary on a public road, especially one with traffic, the voltage V_h poses a minor issue compared to the greater safety risk of potential collisions on a public road.

Chapter 7

Conclusions and Future Work

In this thesis, the electrical properties of conductive electric road technology are evaluated based on measurements conducted on an ERS demonstrator developed by the company Elonroad. Among the electrical properties of conductive ERS, the thesis focuses on the following main areas:

- The electrical characteristics of the sliding contact.
- The power capabilities, losses, and efficiency of the system.
- The presence of conductive EMI within the ERS supply and its impact on the power grid.
- Electrical safety concerning both the vehicle chassis of vehicles drawing power from the ERS and the exposed external structure of the electric road itself.

This chapter presents the main conclusions of this thesis and provides suggestions for future work.

7.1 Conclusions

ERSs offer many benefits in facilitating a green transition for the transport sector, primarily due to their ability to supply power to vehicles while in motion, which could potentially reduce the size of onboard batteries. The technology holds the potential for widespread deployment at both national and international levels, such as providing ERS access on the most traffic-intensive routes in Sweden or within the European road network (TEN-T). Additionally, the results presented in this thesis could be interpreted as demonstrating the potential of conductive ERS for applications beyond public roads, focusing on more industry-oriented settings such as container terminals at ports or heavy vehicle operations in mines, due to the technology's high efficiency and high power capabilities. As modern conductive ERS is still an emerging technology, its most suitable areas and applications are not yet fully determined. The results of this thesis highlight both the technical possibilities and limitations of conductive ERS technology. These factors must be carefully considered when planning and procuring future ERS expansions, as well as when evaluating the applications for which the technology is most appropriate. The findings also indicate that the technology is not yet mature enough for full deployment in some areas, such as the results concerning the performance of the sliding contact discussed in Chapter 3, and the electrical safety challenges presented in Chapter 6.

While the electrical sliding contact is a well-established technology for energy transfer in various applications, conductive ERS introduces a new application with distinct conditions that require it to be designed and adapted accordingly. The results presented in Chapter 3 highlight that the underlying factors influencing the sliding contact, adapted for conductive ERS, are still unknown. Moreover, the sliding contact, comprising metallic brushes as implemented in the demonstrator, requires improvements, as poor contact was frequently observed in the measurements of current distribution in the current collector with the trailer. The poor performance of the sliding contact comprising metallic brushes is further evident in the frequent occurrence of arcing, as observed during experiments with the RTR. Stable energy transfer to the vehicle can be facilitated by using a current collector with more than three arms, where multiple arms provide redundancy to maintain stable contact. This design allows a parallel contact to take over the current load if one sliding contact performs poorly, significantly reducing the risk of impacting the quality of the load current. However, if poorly performing sliding contacts are not monitored or addressed, they can lead to excessive losses and arcing. Arcing presents a significant risk to the ERS and its surroundings, as it may generate conducted and radiated EMI, potentially jeopardizing the operation of the ERS and causing non-compliance with EMC standards.

The results of contact resistance and arcing from the RTR and the demonstrator, where brushes were used as sliding contacts, suggest that future sliding contact designs should prioritize a dedicated suspension system for the sliding contact itself. In the RTR, contact resistance and arcing were highly sensitive to minor variations in the forces exerted on the brushes, likely due to the sliding contacts being mounted in a rigid system without suspension. Furthermore, alternative sliding contact designs should be explored, as the brushes exhibited poor performance, particularly in terms of stable contact resistance, high contact resistance, and arcing during tests with the RTR. Metallic blocks or more advanced designs, possibly involving rotating metallic wheels, could be considered as potential alternatives. While issues such as arcing, high contact resistance, and significant variations in contact resistance were frequent, these problems are expected to diminish with advancements in suspension systems and improved sliding contact designs.

Concerning electrical safety, as presented in Chapter 6, further work is needed to fully explore the electrical safety challenges related to the vehicle's chassis during ERS operation and how they can be mitigated. These problems originate from the overall physical layout and design of the vehicle's TVS, particularly the parasitic capacitive coupling between the output of the TVS converters and the vehicle's chassis, rather than solely from the vehicle's ERS interface. Parasitic capacitive coupling should be minimized and monitored during the design phase of the vehicle's TVS. Consequently, the involvement of EV manufacturers will be necessary to address these issues, as they cannot be resolved solely by ERS manufacturers. This involvement from EV manufacturers may present an additional obstacle to achieving widespread acceptance of future ERS deployments.

Moreover, to ensure electrical safety for vehicles operating on a conductive ERS, it is vital that onboard electrical safety systems are adapted for ERS operation. This includes monitoring for potential isolation faults and other fault modes, which should be mitigated by rapidly disconnecting the ERS supply from the vehicle.

Regarding conductive EMI, as presented in Chapter 5, the results highlight that the occurrence of conductive EMI and its effects within the ERS supply and the ERS power grid connection are highly dependent on the design and topology of the rectifier station supplying power to the electric road. In addition, the results show that the conductive EMI within the ERS supply depends on the design of the input filters in the vehicles' onboard ERS interfaces. These findings suggest that standardization is necessary regarding voltage and current ripple levels when designing the input filters of the ERS interfaces in vehicles. By selecting more sophisticated designs for the rectifier station, such as active rectification, the voltage and current ripple is expected to be minimized. However, even with active rectification, it remains uncertain how the aggregated effects of multiple vehicles, each with varying input filter designs, will ultimately impact the voltage and current ripple within the ERS.

In Chapter 4, the power capabilities and efficiency of the considered ERS technology are examined with respect to traffic characteristics in urban, rural, and highway scenarios, where the technology demonstrates a system efficiency between the ERS power grid connection and the vehicle exceeding 93% in these deployment scenarios. Additionally, the chapter explores design choices and alterations of ERS subsystems and components and how they can be selected in relation to various traffic conditions to ultimately improve the performance of the ERS in terms of power capabilities, resulting losses, and overall system efficiency. The results highlight that, to minimize losses and maintain high system efficiency, the design of the ERS must account for traffic characteristics. By tailoring the ERS to handle the anticipated traffic load, excessive losses can be avoided, and the overall cost of the ERS can be reduced as its components and subsystems are accurately designed to match the expected power load.

With respect to traffic characteristics involving a high total power draw, such as intense traffic conditions with a high number of vehicles and substantial power consumption (for example, to handle truck congestion on highways), improvements in the power capacity of the ERS components and subsystems are required for the considered ERS technology. One such improvement is increasing the cross-sectional area of the main conductors in the electric road. Many of the suggested design alterations presented for this scenario in Chapter 4 have not yet been implemented in reality and are likely to require intensive research and development efforts, along with associated costs. Another strategy to accommodate this scenario is to limit the power drawn per vehicle, thereby reducing the charge power supplied to the vehicle battery and instead focusing the power on auxiliary systems and propulsion. The anticipated development efforts and costs associated with improving the ERS subsystems and components in the first strategy can then be redirected towards a broader deployment of the ERS, thus increasing overall ERS access, although with lower power capabilities. It remains unclear which of these two strategies is most effective and suitable for real-world ERS scenarios. However, it is expected that the suitability of these strategies will depend on the specific ERS deployment scenario, considering factors such as traffic characteristics, vehicle power demands, and the power capabilities of the ERS grid connection.

To conclude, although conductive ERS show great potential in many respects, a number of key challenges remain. This thesis addresses several of these challenges, and in the subsequent section, recommendations for solving some of them are presented in the form of future work.

7.2 Future Work

This section presents the main suggested areas for future work based on the results presented in this thesis which encompass the following main areas:

- **The Sliding Contact:** As demonstrated in the results presented in Chapter 3, additional research and development efforts are required to optimize the sliding contact adapted for conductive ERS. This is crucial as the whole concept relies on the energy transfer facilitated by the sliding contact. The sliding contact must exhibit increased reliability, availability, energy efficiency as well as minimal occurrence of arcing. To achieve this, a more comprehensive understanding of the factors impacting contact resistance and arcing is necessary.

  While this thesis has made initial contributions to the research field of sliding contacts consisting of metallic brushes adapted for conductive ERS by providing an order of magnitude for contact resistance and highlighting its variability in terms of contact resistance and arcing, further research is needed. Additional experiments are required to isolate the specific factors that affect voltage drop, contact resistance, and frictional forces in the sliding contact. These experiments should be conducted in a laboratory environment, possibly using an RTR. In parallel, further measurements are necessary on a real ERS to validate that the laboratory experiments accurately replicate the conditions present in a real ERS.

To improve the reliability of the results provided by the RTR presented in Chapter 3, the setup must either be replaced or upgraded, as its mechanical system currently lacks the precision required to generate consistent results with low variation and to conduct experiments at higher rotational speeds (corresponding to vehicle speeds present in highway deployment scenarios) and potentially higher currents. Additionally, an experimental setup capable of measuring arcing directly, rather than relying on visual observations, is essential for a better understanding of how arcing impacts the sliding contact. The suggested improvements to the RTR, in combination with replicating experiments and employing statistical methods, such as t-tests and ANOVA, are expected to yield results that can isolate the factors influencing arcing and contact resistance.

- **Power Capabilities, Losses, and System Efficiency:**

  Apart from further improving the accuracy of the employed simulation model, future work regarding the ERS power capabilities, losses, and system efficiency entails three main areas:

  1. Further simulations that implement real-time power control for each vehicle drawing power from the ERS will allow the system to be optimized in terms of minimizing losses. This includes enabling vehicles operating on the electric road to draw more power near the feeding point of the electric road (close to the electric road's connection to the rectifier station) in order to minimize overall losses in the ERS, as well as limiting the maximum power drawn from a specific rectifier station and actively distributing the required power to vehicles based on their power draw for propulsion and auxiliary systems, as well as their SoC levels. Furthermore, it is suggested that a priority system be implemented in future simulations, granting selected vehicles priority charging over others drawing power from the ERS. This prioritization could be based on business models or SoC levels while still ensuring sufficient power for propulsion and auxiliary systems in lower-priority vehicles. By conducting these suggested simulation scenarios, the potential of the power control aspects in improving ERS performance in terms of power capabilities and losses can be evaluated.
  2. A detailed assessment examining whether the suggested design alterations of ERS subsystems and components are feasible and practically viable, especially those related to higher power draw

scenarios corresponding to highway deployment, involving multiple trucks operating on an ERS. This includes, for instance, whether the cross-sectional area of the conductors in the electric road can be increased and what impact this would have on the overall design of the ERS.

3. Cost-effectiveness analysis, which compares the costs of the suggested design alterations of ERS subsystems and components and determines which of them are most effective. Moreover, the suggested design alterations that allow for increased power capabilities of the ERS are further compared with the alternative of a lower-power-drawn ERS design which allows for more widespread deployment of ERS.

- **Conductive EMI:** In addition to improving the accuracy of the simulation model for conducting simulations of conductive EMI outlined in Chapter 5, further simulations involving an active rectifier topology in the ERS rectifier station are required to fully assess whether this rectifier station design can minimize voltage and current ripples within the ERS. These simulations are proposed to include an active rectifier topology in the rectifier station along with multiple vehicles, where the input filter design parameters of the vehicles' onboard ERS interfaces are varied to assess the cumulative effects of these filters on the voltage and current ripple within the ERS supply. The results are aimed to contribute to establishing thresholds for voltage and current ripples within the ERS supply, which could serve as a basis for the standardization of voltage and current ripple levels within the ERS supply.

- **Electrical Safety:** To ensure electrical safety for vehicles operating on a conductive ERS, two primary areas of future work remain related to touch events involving the vehicle's chassis. First, a deeper understanding is needed of the factors influencing parasitic capacitive coupling in automotive applications, particularly between the vehicle chassis and the TVS in vehicles adapted for conductive ERS operation. To assess this, further impedance measurements in a controlled laboratory environment are required, using a vehicle where components such as converters, enclosures, and cables can be removed and disassembled to isolate the factors that most significantly influence capacitive coupling. Second, it is necessary to explore potential methods for mitigating the effects of parasitic capacitive coupling, with the implementation of filters designed to eliminate hazardous currents leading to touch events being a possible solution. This approach may include transformers in the vehicle's onboard ERS interface, which provide galvanic isolation between the ERS supply and the vehicle, thereby possibly obstructing the flow of hazardous currents, and active filters that utilize a current source to actively cancel out the hazardous currents associated with touch events. The proposed mitigation strategies, involving the deployment of filters, are recommended to be evaluated through simulations using the simulation model presented in Chapter 5 and 6.

Both areas of suggested future work concerning touch events involving the vehicle's chassis could contribute to the standardization of parasitic capacitive coupling thresholds for BEVs adapted for conductive ERS operation. Although the use of a galvanically isolated DC/DC converter may interrupt the hazardous currents path, initial analysis of measurements where this is tested indicate that this approach does not fully resolve the issue. This is suspected to be due to parasitic coupling in the isolating transformer of the DC/DC converter. Further investigation is necessary to refine this strategy and establish effective standards to address these challenges.

Lastly, and possibly most critical, a real-time monitoring and fault detection system needs to be developed for vehicles operating on conductive ERS. This system should be capable of rapidly disconnecting the vehicle from the ERS supply upon detecting an increase in the chassis voltage.

References

[1] IPCC, The Intergovernmental Panel on Climate Change, March 2025. [Online]. Available: https://www.ipcc.ch/.

[2] International Energy Agency, Global EV Outlook 2023, March 2025. [Online]. Available: https://www.iea.org/reports/global-ev-outlook-2023.

[3] Congressional Research Service, Battery Minerals Report, March 2025. [Online]. Available: https://crsreports.congress.gov/product/pdf/R/R47227.

[4] Mongabay, Environmental Impact of EV Battery Scaling, March 2025. [Online]. Available: https://news.mongabay.com/2023/09/study-tricky-balancing-act-between-ev-scale-up-and-mining-battery-metals/.

[5] Amnesty International, Cobalt and Copper Mining for Batteries, March 2023.
[Online]. Available: https://www.amnesty.org/en/latest/news/2023/09/drc-cobalt-and-copper-mining-for-batteries-leading-to-human-rights-abuses/.

[6] Sustainability by Numbers, Cobalt Mining Overview, March 2025. [Online]. Available: https://www.sustainabilitybynumbers.com/p/cobalt.

[7] Earth.org, Environmental Impact of Battery Production, March 2025. [Online]. Available: https://earth.org/environmental-impact-of-battery-production/.

[8] Norwegian EV Association, Battery Electric Vehicles in Norway, March 2025.

[Online]. Available: `https://elbil.no/om-elbil/elbilstatistikk/`.

[9] Statista, Passenger Cars in Germany, March 2025.
[Online]. Available: `https://www.statista.com/statistics/810662/passenger-cars-stock-germany/`.

[10] Statista, Road Network in Germany, March 2025.
[Online]. Available: `https://www.statista.com/statistics/449832/germany-length-of-road-network-by-road-type/`.

[11] Hao Wu. A survey of battery swapping stations for electric vehicles: Operation modes and decision scenarios. *IEEE Transactions on Intelligent Transportation Systems*, 23(8):10163–10185, 2022. doi: 10.1109/TITS.2021.3125861.

[12] Francisco J. Márquez-Fernández, Joschka Bischoff, Gabriel Domingues-Olavarría, and Mats Alaküla. Assessment of future ev charging infrastructure scenarios for long-distance transport in sweden. *IEEE Transactions on Transportation Electrification*, pages 1–1, 2021. doi: 10.1109/TTE.2021.3065144.

[13] Siemens Archive, Werner von Siemens history: Elektromote, March 2025.
[Online]. Available: `https://web.archive.org/web/20090322024807/http://w4.siemens.de/archiv/de/innovationen/mobil.html#2`.

[14] KAIST OLEV Project, March 2025. [Online]. Available: `https://www.kaist.ac.kr/newsen/html/news/?mode=V&mng_no=3960`.

[15] Philippe Veyrunes, Patrick Duprat, and Jean-Luc Hourtane. Ground-level feeding systems from rail to road. In *2017 IEEE Transportation Electrification Conference and Expo, Asia-Pacific (ITEC Asia-Pacific)*, pages 1–4, Aug. 7-10 2017. doi: 10.1109/ITEC-AP.2017.8080778.

[16] Bombardier Primove, March 2025.
[Online]. Available: `https://dcstreetcar.com/wp-content/uploads/2020/10/Section-D-Part-6-723-830-pagesred.pdf`.

[17] Ansaldo Tramwave, March 2025. [Online]. Available: `https://www.railjournal.com/news/ansaldo-sts-reveals-tramwave/`.

[18] Jakob Rogstadius. Interaction effects between battery electric trucks, electric road systems and static charging infrastructure, (in swedish), March 2025.
[Online]. Available: http://www.diva-portal.org/smash/get/diva2:1712747/FULLTEXT03.pdf.

[19] Takamitsu Tajima. Study of 450-kw conductive ers at 150km/h. In *3rd Electric Road Systems Conference*, pages 1–7, May 7-8 2019.

[20] David Wenander and Mats Alaküla. Reducing the environmental impact of large battery systems with conductive electric road systems—a technical overview. *World Electric Vehicle Journal*, 15(2), 2024. ISSN 2032-6653. doi: 10.3390/wevj15020059. URL https://www.mdpi.com/2032-6653/15/2/59.

[21] David Wenander, Francisco J. Márquez-Fernández, and Mats Alaküla. Efficiency evaluation of a conductive electric road system with respect to traffic characteristics. *IEEE Transactions on Vehicular Technology*, 73(4):4694–4704, 2024. doi: 10.1109/TVT.2024.3362533.

[22] ENRX Website, March 2025. [Online]. Available: https://www.enrx.com/en.

[23] Electreon Website, March 2025. [Online]. Available: https://www.electreon.com/.

[24] Electreon picture, March 2025.
[Online]. Available: https://electreon.com/projects/elina-balingen.

[25] Vahid Zahiri Barsari, Duleepa J. Thrimawithana, and Grant A. Covic. An inductive coupler array for in-motion wireless charging of electric vehicles. *IEEE Transactions on Power Electronics*, 36(9):9854–9863, 2021. doi: 10.1109/TPEL.2021.3058666.

[26] Elonroad Website, March 2025.
[Online]. Available: http://elonroad.com/.

[27] Evias Website, March 2025.
[Online]. Available: https://evias.com/.

[28] Evias picture, March 2025.
[Online]. Available: https://www.koha.net/en/auto/93428/electrified-roads-Swedish-project-can-reduce-the-cost-of-electric-vehicles.

[29] Siemens Website, March 2025.
[Online]. Available: https://assets.new.siemens.com/siemens/assets/api/uuid:5e482791-554d-4d84-84f8-943eab9e4be9/background-ehighway-solution-e.pdf.

[30] Siemens eHighway picture, March 2025.
[Online]. Available: https://www.cnet.com/roadshow/news/germany-ehighway-hybrid-trucks-electricity/.

[31] Evolution Road Project Website, March 2025. [Online]. Available: https://www.evolutionroad.se/en/.

[32] Wasim Shoman, Sten Karlsson, and Sonia Yeh. Benefits of an electric road system for battery electric vehicles. *World Electric Vehicle Journal*, 13(11), 2022. ISSN 2032-6653. doi: 10.3390/wevj13110197. URL https://www.mdpi.com/2032-6653/13/11/197.

[33] Gabriel Domingues. *Modeling, Optimization and Analysis of Electromobility Systems*. PhD thesis, Division of Industrial Electrical Engineering and Automation, Lund University, Lund, Sweden, 2018. URL https://lucris.lub.lu.se/ws/portalfiles/portal/53514836/Gabriel_Domingues_webb.pdf.

[34] Philip Abrahamsson. *Thermal Management of Conductive Electric Road Systems*. PhD thesis, Division of Industrial Electrical Engineering and Automation, Lund University, Lund, Sweden, 2020. URL https://lup.lub.lu.se/search/files/86528059/Thermal_Management_of_Conductive_Electric_Road_Systems.pdf.

[35] Kil Young Lee, Florian Bühs, Dietmar Göhlich, and Sangyoung Park. Towards reliable design and operation of electric road systems for heavy-duty vehicles under realistic traffic scenarios. *IEEE Transactions on Intelligent Transportation Systems*, 24(10):10963–10976, 2023. doi: 10.1109/TITS.2023.3280948.

[36] Anton Karlsson. *Electric drive and charging system for heavy vehicles: Solutions based on Electric Road Systems*. PhD thesis, Division of Industrial Electrical Engineering and Automation, Faculty of Engineering, Lund University, 2022. URL https://lup.lub.lu.se/search/files/114434961/thesisAK_print.pdf.

[37] Anton Karlsson and Mats Alaküla. Conductive electric road localization and related vehicle power control. *World Electric Vehicle Journal*, 13(1), 2022. ISSN 2032-6653. doi: 10.3390/wevj13010022. URL https://www.mdpi.com/2032-6653/13/1/22.

[38] Francisco J. Márquez-Fernández, Sönke Schuch, Lars Lindgren, and Mats Alaküla. Electric safety challenges with a conductive electric road system—chassis potential modeling and measurement. *World Electric Vehicle Journal*, 10(2), 2019. ISSN 2032-6653. doi: 10.3390/wevj10020030. URL `https://www.mdpi.com/2032-6653/10/2/30`.

[39] Swedish Transport Administration, Traffic Data Portal, March 2025. [Online]. Available: `https://bransch.trafikverket.se/en/startpage/`.

[40] Zhe Huang, Francisco J. Márquez-Fernández, Yury Loayza, Avo Reinap, and Mats Alaküla. Dynamic thermal modeling and application of electrical machine in hybrid drives. In *2014 International Conference on Electrical Machines (ICEM)*, pages 2158–2164, 2014. doi: 10.1109/ICELMACH.2014.6960483.

[41] David Wenander, Philip Abrahamsson, Francisco J. Márquez-Fernández, and Mats Alaküla. Measuring electric properties of a conductive electric road. In *2021 AEIT International Conference on Electrical and Electronic Technologies for Automotive (AEIT AUTOMOTIVE)*, pages 1–6, 2021. doi: 10.23919/AEITAUTOMOTIVE52815.2021.9662755.

[42] David Wenander, Francisco J. Márquez-Fernández, and Mats Alaküla. Modelling of power flow and losses in a conductive electric road system. In *2022 IEEE Vehicle Power and Propulsion Conference (VPPC)*, pages 1–6, 2022. doi: 10.1109/VPPC55846.2022.10003398.

[43] David Wenander, Francisco J. Márquez-Fernández, and Mats Alaküla. Modelling electric transients in a conductive electric road system. In *2023 AEIT International Annual Conference (AEIT)*, pages 1–6, 2023. doi: 10.23919/AEIT60520.2023.10330352.

[44] David Wenander, Francisco J. Márquez-Fernández, and Mats Alaküla. Measurements of the electric properties of the current collector in a conductive electric road. In *2024 ELEKTRO (ELEKTRO)*, pages 1–6, 2024.

[45] Philip Abrahamsson, David Wenander, Mats Alaküla, Francisco J. Márquez-Fernández, and Gabriel Domingues-Olavarría. Automatic static charging of electric distribution vehicles using ers technology. In *2020 IEEE Transportation Electrification Conference & Expo (ITEC)*, pages 1191–1196, 2020. doi: 10.1109/ITEC48692.2020.9161573.

[46] Swedish Transport Administration, Sweden's First Permanent Electric Road, March 2025.
[Online]. Available: https://www.trafikverket.se/vara-projekt/projekt-i-orebro-lan/sveriges-forsta-permanenta-elvag/.

[47] Møre Transformers Specifications, March 2025.
[Online]. Available: https://moretrafo.no/produkter/500-kva/.

[48] Electrically propelled road vehicles — Safety specifications — Part 3: Electrical safety, ISO 6469-3:2021, March 2025.
[Online]. Available: https://www.iso.org/.

[49] Effects of current on human beings and livestock, IEC 60479, March 2025.
[Online]. Available: https://www.iec.ch/.

[50] Solaris Trollino 12 Specifications, March 2025.
[Online]. Available: http://trollino.mashke.org/.

[51] MCC USB-1808X Multifunction Data Acquisition Device, March 2025.
[Online]. Available: https://www.mccdaq.com/pdfs/manuals/USB-1808X.pdf.

[52] LEM, CV 3-500 Voltage Sensor, March 2025.
[Online]. Available: https://www.lem.com/sites/default/files/products_datasheets/cv_3-500_v12.pdf.

[53] LEM, CV 3-1000 Voltage Sensor, March 2025.
[Online]. Available: https://www.lem.com/sites/default/files/products_datasheets/cv_3-1000_v17.pdf.

[54] LEM, LF 505-S Current Sensor, March 2025.
[Online]. Available: https://www.lem.com/sites/default/files/products_datasheets/lf_505-s.pdf.

[55] LEM, IT 605-S Current Sensor, March 2025.
[Online]. Available: https://www.farnell.com/datasheets/2150004.pdf?_gl=1*nq1qrf*_gcl_au*MTUxNjgxNTQ5My4xNzQyNzI0MTAx.

[56] LEM, IT 405-S Current Sensor, March 2025.
[Online]. Available: https://www.lem.com/sites/default/files/products_datasheets/it_400-s_ultrastab.pdf.

[57] LEM, DVL 250 Voltage Sensor, March 2025.
[Online]. Available: https://www.lem.com/en/product-list/dvl-250.

[58] Vishay, High Precision Resistors, March 2025.
[Online]. Available: https://www.vishay.com/en/resistors-fixed/res-tol-less-pt01/.

[59] Riedon, High Precision Resistors, March 2025.
[Online]. Available: https://riedon.com/resistors/wirewound.

[60] Rigol, DM3068 Multimeter, March 2025.
[Online]. Available: https://int.rigol.com/Images/DM3068_Datasheet_EN_tcm7-2884.pdf.

[61] Velleman Power Supply, March 2025.
[Online]. Available: https://cdn.velleman.eu/downloads/2/ps3010ps3020gbnlfresd.pdf.

[62] R. Holm and E. Holm. *Electric Contacts: Theory and Application*. Springer-Verlag, 1967.

[63] Yoshitada Watanabe. Sliding contact characteristics between composite materials containing layered solid lubricants and carbon. *Wear*, 155(2):237–249, 1992. ISSN 0043-1648. doi: https://doi.org/10.1016/0043-1648(92)90084-L. URL https://www.sciencedirect.com/science/article/pii/004316489290084L.

[64] L. Dong, G.X. Chen, M.H. Zhu, and Z.R. Zhou. Wear mechanism of aluminum–stainless steel composite conductor rail sliding against collector shoe with electric current. In *16th International Conference on Wear of Materials*, number 1, pages 598–603, 2007. doi: 10.1016/j.wear.2007.01.130. URL https://www.sciencedirect.com/science/article/pii/S0043164807004218.

[65] Surajit Midya, Dierk Bormann, Ziya Mazloom, Thorsten Schutte, and Rajeev Thottappillil. Conducted and radiated emission from pantograph arcing in ac traction system. In *2009 IEEE Power & Energy Society General Meeting*, pages 1–8, 2009. doi: 10.1109/PES.2009.5275833.

[66] Tamura, Current Sensor, March 2025.
[Online]. Available: https://www.tamuracorp.com/electronics/jp/pdf/2015/02_L34SxxxD15_e.pdf.

[67] DATAQ, Data Logger, March 2025.
[Online]. Available: https://www.dataq.com/resources/pdfs/datasheets/di-2108-p-usb-daq-datasheet.pdf.

[68] Wangang Wang, Anping Dong, Guangning Wu, Guoqiang Gao, Lijun Zhou, Bo Wang, Yi Cui, Donglai Liu, Dajian Li, and Tianzhi Li. Study on characterization of electrical contact between pantograph and catenary. In *2011 IEEE 57th Holm Conference on Electrical Contacts (Holm)*, pages 1–6, 2011. doi: 10.1109/HOLM.2011.6034815.

[69] D.K. Lawson and T.A. Dow. The sparking and wear of high current density electrical brushes. *Wear*, 102(1):105–125, 1985. ISSN 0043-1648. doi: https://doi.org/10.1016/0043-1648(85)90094-8. URL https://www.sciencedirect.com/science/article/pii/0043164885900948.

[70] RTR Load Cell, March 2025.
[Online]. Available: http://www.htc-sensor.com/products/94.html.

[71] RTR Load Cell Amplifier, March 2025.
[Online]. Available: https://statinst.com/index.php?route=product/product&product_id=92.

[72] RTR Data Logger, March 2025.
[Online]. Available: https://www.ni.com/docs/en-US/bundle/crio-9012-9014-user-manual/resource/crio-9012-9014-user-manual.pdf?srsltid=AfmBOootvezqqn1a56WwYSQftrWApyB9OWvYUDbtw1LpI1zUH95r_dxc.

[73] RTR Logg Module, March 2025.
[Online]. Available: https://www.ni.com/sv-se/shop/model/ni-9220.html?srsltid=AfmBOoow-MaYPbMxDfQCv4qUtGD2uV1W9a8DW-9v4r4X6mLfntRXYy6S.

[74] RTR Voltage Measurement, March 2025.
[Online]. Available: https://www.ti.com/lit/ds/symlink/iso224.pdf?ts=1621748353932.

[75] TESCAN, Scanning Electron Microscopy, March 2025.
[Online]. Available: https://www.tescan.com/product/sem-for-materials-science-tescan-mira/.

[76] Yu Mei, Zeng-Jun Zhou, and H. L. Luo. Electrical resistivity of rf-sputtered iron oxide thin films. *Journal of Applied Physics*, 61(8): 4388–4389, 04 1987. ISSN 0021-8979. doi: 10.1063/1.338431.

[77] ThoughtCo, Table of Resistivity, March 2025.
[Online]. Available: https://www.thoughtco.com/table-of-electrical-resistivity-conductivity-608499.

[78] Transportation Research Board. Tires and passenger vehicle fuel economy: Informing consumers, improving performance – special report 286, March 2025.
[Online]. Available: https://nap.nationalacademies.org/catalog/11620/tires-and-passenger-vehicle-fuel-economy-informing-consumers-improving-performance.

[79] Power Supply, March 2025.
[Online]. Available: https://mastechpowersupply.com/files/public/manuals/Manual_HY3010EX_new.pdf.

[80] Shunt Resistor, March 2025.
[Online]. Available: https://docs.rs-online.com/9a31/0900766b813bb937.pdf.

[81] Picotech Website, March 2025.
[Online]. Available: https://www.picotech.com/download/datasheets/picoscope-4444-data-sheet.pdf.

[82] Giorgio Rizzoni. *Principles and Applications of Electrical Engineering*. McGraw-Hill Science/Engineering/Math, 2005.

[83] HIOKI, Impedance Analyzer, March 2025.
[Online]. Available: https://shop.hioki.eu/IM3570-IMPEDANCE-ANALYSER/IM3570.

[84] MathWorks, Simulink Model Component Three-Phase Transformer Inductance Matrix Type (Two Windings), March 2025.
[Online]. Available: https://se.mathworks.com/help/sps/powersys/ref/threephasetransformerinductancematrixtypetwowindings.html.

[85] Nissan, Nissan Leaf 24kWh Specifications, March 2025.
[Online]. Available: https://ev-database.org/car/1019/Nissan-Leaf-24-kWh.

[86] Tesla Semi-Truck Specifications, March 2025.
[Online]. Available: https://www.drive.com.au/news/first-tesla-semi-truck-delivered/.

[87] Tesla Semi-Truck Power Consumption, March 2025.
[Online]. Available: https://www.electrive.com/2023/08/15/pepsico-cites-consumption-of-1-1-kwh-km-for-tesla-semi/.

[88] Open Infrastructure Map, March 2025.
[Online]. Available: https://openinframap.org/#7.87/56.266/14.083.

[89] ChargeFinder, March 2025.
[Online]. Available: https://chargefinder.com/se/search.

[90] Pei Zhang, Changqing Du, Fuwu Yan, and Jianqiang Kang. Influence of practical complications on energy efficiency of the vehicle's lithium-ion batteries. In *2011 International Conference on Electric Information and Control Engineering*, pages 2278–2281, 2011. doi: 10.1109/ICEICE.2011.5777025.

[91] Pengcheng Li, Qian Wang, Yuanliang, and Shuai Lu. Power conversion efficiency calculation models for electric vehicle fast charger system. In *2018 13th IEEE Conference on Industrial Electronics and Applications (ICIEA)*, pages 316–321, 2018. doi: 10.1109/ICIEA.2018.8397735.

[92] Rakesh Ramachandran, Jesper Nielsen, Morten Nymand, Nils Nageler, and Ronald Eisele. A 20 kw high power density isolated dc-dc converter for an on-board battery charger utilizing very-low inductive sic power modules. In *2020 IEEE Applied Power Electronics Conference and Exposition (APEC)*, pages 3503–3507, 2020. doi: 10.1109/APEC39645.2020.9124200.

[93] Rectifier Diode, March 2025.
[Online]. Available: https://www.semikron-danfoss.com/products/p/skkd-70116-07898755.

[94] Eduardo Espinosa, José Espinoza, Jaime Rohten, Roberto Ramirez, Marcelo Reyes, Javier Muñoz, and Pedro Melin. An efficiency comparison between a 18 pulses diode rectifier and a multi-cell afe rectifier operating with fcs — mpc. In *IECON 2014 - 40th Annual Conference of the IEEE Industrial Electronics Society*, pages 1214–1220, 2014. doi: 10.1109/IECON.2014.7048657.

[95] Saijun Mao, Tao Wu, Xi Lu, Jelena Popovic, and Jan Abraham Ferreira. Three-phase active front-end rectifier efficiency improvement with silicon carbide power semiconductor devices. In *2016 IEEE Energy Conversion Congress and Exposition (ECCE)*, pages 1–8, 2016. doi: 10.1109/ECCE.2016.7855515.

[96] PLEXIM, PLECS Manual, March 2025.
[Online]. Available: `https://www.plexim.com/download/documentation`.

[97] D.J. Carnovale T.M. Blooming. Application of ieee std 519-1992 harmonic limits. In *Conference Record of 2006 Annual Pulp and Paper Industry Technical Conference*, pages 1–9, March 2025. doi: 10.1109/PAPCON.2006.1673767.

[98] Methods of measurement of touch current and protective conductor current, IEC 60990, March 2025.
[Online]. Available: `https://www.iec.ch/`.

[99] Tim Williams. Characterisation of emissions due to power electronics heatsinks. In *2013 International Symposium on Electromagnetic Compatibility*, pages 616–621, 2013.

Printed by Media-Tryck, Lund 2025 NORDIC SWAN ECOLABEL 3041 0903

LUND UNIVERSITY

Division of Industrial Electrical Engineering and Automation
Department of Biomedical Engineering
Faculty of Engineering

ISBN 978-91-985110-4-8
CODEN: LUTEDX/(TEIE-1100)/1-269/(2025)